Bachelor Thesis

Stockholm University

Degree Project in Geology 30 hp

Cr-spinels in the Franklinian Mobile Belt: a geochemical record of Paleozoic tectonics

Malvina Forbes Halldén

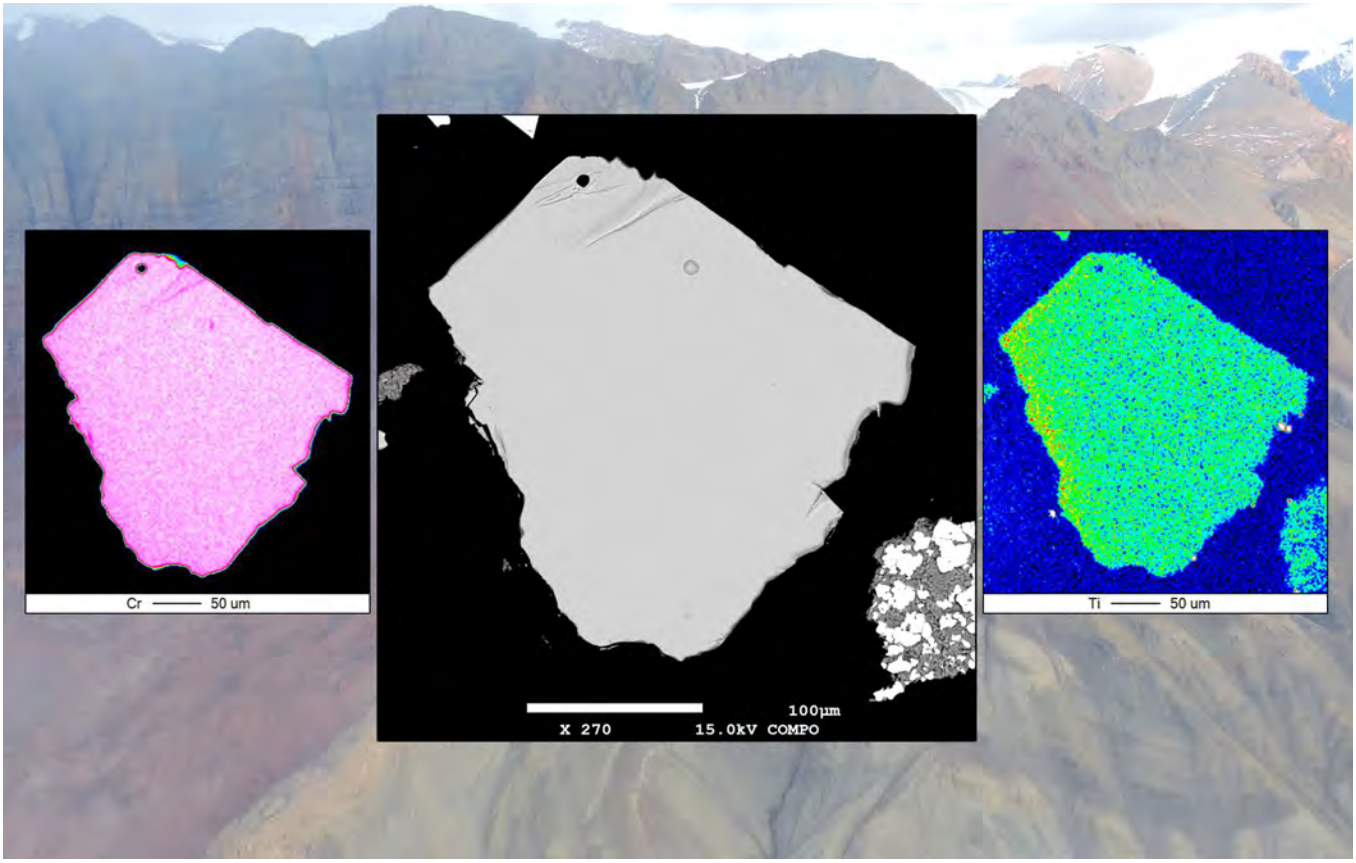

Stockholm 2019

Department of Geological Sciences
Stockholm University
SE-106 91 Stockholm

Abstract

The chemical compositions of Cr-spinel extracted from mafic and ultramafic rocks collected on Ellesmere Island in the Arctic Canadian Archipelago were obtained through electron microprobe analyses. The extensively altered rocks are sampled from rock units in the Franklinian Mobile Belt, which is representative of a Paleozoic tectonically active oceanic regime of which little is presently known. The evolutionary trend of the ocean basin may have changed when the exotic crustal fragments now called the Pearya terrane were accreted to the North American margin through poorly understood tectonic processes sometime prior to the Devonian. The results of the analysis are used to determine the tectonic setting associated with the rock units. The results reveal that the Cr-spinels predominantly have a supra-subduction zone geochemical signature, suggesting an island arc origin.

Introduction

This study uses the chemical compositions of Cr-spinels extracted from mafic and ultramafic Paleozoic rocks to determine the tectonic settings associated with geological units within the Franklinian Mobile Belt in the Arctic Canadian Archipelago (Figure 1). The rock samples were collected during the 2017 Circum-Arctic Structural Events – Expedition 19 to Ellesmere Island.

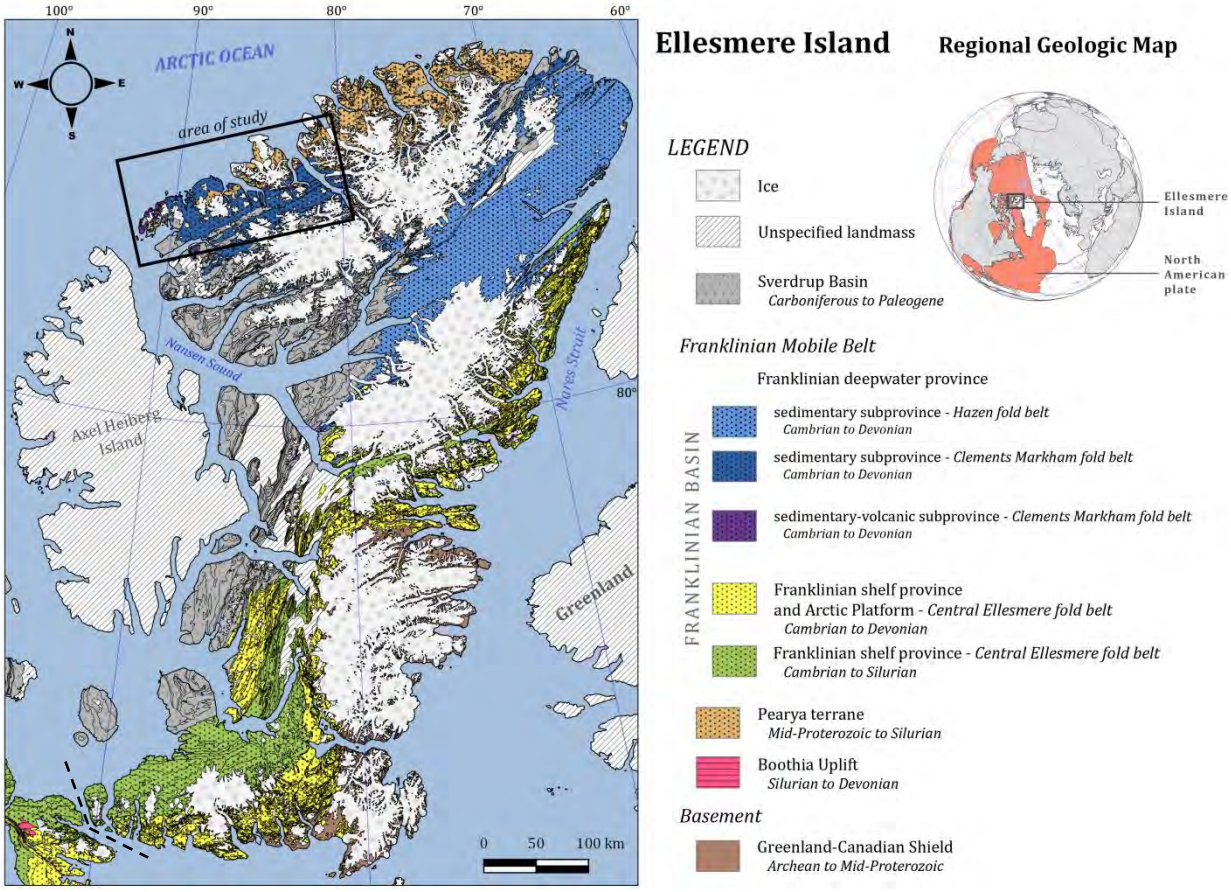

Figure 1 Regional geologic map of Ellesmere Island. *Datum: WGS84. Map projection: Lambert Conformal Conic; Central Meridian at 100°, standard parallels at 78°N and 73°N. Geodatabase: Geological Survey of Canada doi:10.4095/297416. Inset map (top right) projection: Azimuthal orthographic. Geodatabases: "Natural Earth" and Peter Bird's plate boundaries doi:10.1029/2001GC000252 (modified by Nordpil).* Note the area of study (outlined).

The northwestern coast of Ellesmere Island is covered by the exotic Pearya terrane (see generally Trettin, 1987; Klaper, 1992; Klaper & Ohta, 1993; Malone, 2012; Malone, McClelland, von Gosen & Piepjohn, 2018). The poorly studied area has experienced several major tectonic events and the sampled rocks are extensively metamorphosed (Trettin, 1998). Cr-spinel geochemistry is one of the few tools available for petrogenetic investigations after metamorphism (Habtoor, Ahmed, Akizawa, Harbi & Arai, 2017). Electron microprobe analysis was used to determine chemical compositions in the modest number of Cr-spinels that could be extracted from the altered rocks obtained in the area of study outlined in Figure 1.

The tectonic evolution of northern Ellesmere Island and the area of study is dominated by the accretion of the Pearya terrane (Malone, 2012). The Pearya terrane is composed of sutured crustal fragments in five recognized successions. Trettin (1987) suggested that the terrane was the only one of its kind that has been documented on the northern margin of the North American continent, although similar terranes have been documented on Northern Greenland and Svalbard (accord Bjørnerud, 1991; Klaper, 1992; Malone, 2012). The timing and manner of accretion onto the edge of the North American margin, the *in situ* Franklinian Basin, is still highly speculative but an upper constraint is placed on timing by the Late Devonian Ellesmerian orogeny that affected both basin and terrane.

The terrane borders the Clements Markham fold belt, which together with the easterly Hazen fold belt made up the deepwater province of the Franklinian Basin in the Paleozoic. The fault-bounded contact zone between the Clements Markham fold belt and the Pearya terrane records a steep metamorphic gradient up to amphibolite facies seemingly caused by underplating (Trettin, 1991; Klaper & Ohta, 1993). Regional metamorphic grades above greenschist facies are otherwise uncommon in the region (Bjørnerud, 1991; Trettin, 1991; Klaper & Ohta, 1993).

The Clements Markham fold belt is subdivided into an older (Cambrian to Silurian) and a younger succession (Silurian to Devonian). Enigmatic volcanics included in the older succession suggest tectonic activity prior to the accretion of Pearya and there is evidence of coeval Ordovician arc-type volcanism in the second and third successions of the Pearya terrane that most likely predate accretion (see Trettin, 1991; Estrada, Piepjohn, Henjes-Kunst & von Gosen, 2003; Malone, 2012; Malone et al., 2018). A lack of volcanic detritus in the Franklinian Basin shelf region that is represented by the Central Ellesmere fold belt indicates that this hypothetical arc system should have been located far offshore in the deepwater regime (i.e. the Clements Markham fold belt). The three fold belts and the Pearya terrane together make up the Franklinian Fold Belt on Ellesmere Island.

The coastal strip outlined in Figure 1 includes the two areas in which the sampled rocks used in this study were obtained. Both these areas are associated with the Pearya terrane and the Clements Markham fold belt. Klaper (1992) believed that the former deepwater province between the parallel Kulutingwak Fiord Fault Zone and the Emma Fiord Fault Zone might hold the key to understanding the early evolution of the Clements Markham fold belt and the sequence of events that led to the Pearya terrane accretion. Chemical, petrographical and micro-textural mineral data are presented for six samples from five different rock units within the Clements Markham Fold Belt and the Pearya terrane; three of which contained within the area of interest suggested by Klaper (1992). The results support an infant supra-subduction zone setting, possibly with an accretionary prism within the Emma Fiord Fault Zone.

This study was conducted during the fall semester of 2018 at Stockholm University (sample preparation, petrography, data reduction and writing) and at Memorial University of Newfoundland in Canada (electron microprobe analyses).

Background

Geochemistry

Cr-spinel as petrogenetic indicator

Cr-spinel crystallizes under a remarkably wide range of conditions and records the chemical evolution of its surrounding melt through a nuanced range of solid solution, making it a so-called 'petrogenetic indicator' (Irvine, 1965) of widespread investigative use. Being among the first mineral phases to crystallize, Cr-spinel is a ubiquitous accessory mineral in ultramafic and mafic rocks, with the exception of more basic cumulate-types due to the peritectic reaction between Cr-spinel and silicate melt to form Cr_2O_3-enriched clinopyroxene (e.g. Hulbert, 1997). Cr-spinels are also frequently encountered in sedimentary and metamorphic rocks due to its resistance to alteration (Barnes & Roeder, 2001).

The refractory nature of spinel and its complex crystal chemistry, both in terms of major and minor elements, makes it sensitive to crystal-melt equilibrium and disequilibrium processes (Barnes & Roeder, 2001). Cr-spinel is considered exceedingly resistant to post-magmatic alteration processes and metamorphism compared to other coeval high-temperature phases such as olivine (Barnes & Roeder, 2001). Cr-spinels are even known to occasionally survive low-grade metamorphism related to pervasive serpentinization, making it the only acknowledged primary mineral phase that can be used for petrogenetic interpretation in highly altered rocks (Barnes & Roeder, 2001).

Cr-spinel typically occurs as inclusions in other mafic minerals, and in metamorphic and metasomatic rocks, they are usually interpreted as relicts of an igneous stage (e.g. Arai, 1992; Barnes, 2000). While Cr-spinel serves as the main reservoir for chromium ($_{24}$Cr) in igneous rocks, it does not contribute significantly to the total concentration of any other element (e.g. Dick & Bullen, 1984; Kamenetsky, Crawford & Meffre, 2001). The wide range of compositional variations demonstrated among terrestrial spinels is attributable to a spectrum of igneous processes with superimposed metamorphic effects (Barnes & Roeder, 2001). Therefore, the chemistry of this particular mineral can potentially be used to gain valuable insight into the geotectonic provenance, metamorphic history, degree of partial melting and oxygen fugacity (fO_2) of its host.

Spinel chemistry

Spinels are a mineral group of isometric oxides arranged in a cubic close-packed crystal lattice (Deer, Howie & Zussman, 1992). The general chemical formula unit for members of the spinel group is AB_2O_4 where A and B represent "sites" occupied by cations (Lenaz, Rollinson & Adetunji, 2014). The spinel structure can either be *normal* or *inverse,* and in normal spinel structures, like Cr-spinel, trivalent cations in the B-site occupy half of the octahedral spaces and divalent cations in the A-site occupy one-eighth of the smaller tetrahedral spaces (Fulay & Lee, 2016). In inverse

spinel structures, all of the A-site cations and half of the B-site cations occupy the octahedral spaces and the other half the tetrahedral spaces and in such structures, the cation oxidation state is variable (Fulay & Lee, 2016).

All spinel compositions can be considered to plot somewhere inside a three-dimensional compositional space. A simplified version of the compositional space, which is based on the major chemical components, has been used to define different petrogenetic environments and alteration trends. This applied version of the compositional space is commonly referred to as the "spinel [compositional] prism" (e.g. Sigurdsson &Schilling, 1976). The prism can be described geometrically as two triangular prisms – the "ulvöspinel prism" for members of the so-called titanium subgroup and "magnetite prism" (Figure 2a) for all other members (e.g. Ferracutti, Ganuza, Bjerg & Castro, 2015). The vertices of the prisms define compositional end-members, e.g. Cr-spinel, and each side of either triangular prism translates to two-dimensional discrimination plots (e.g. Figure 2b) which are used for interpretation.

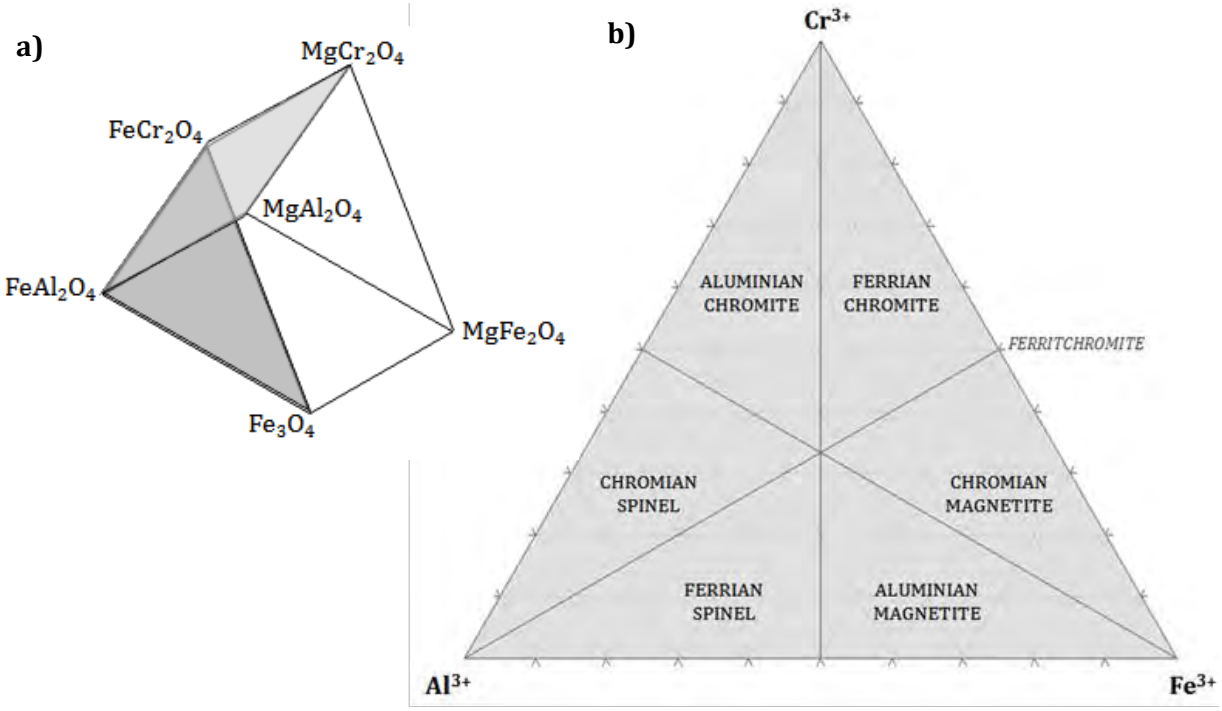

Figure 2 Spinel compositional prism. **a.** Magnetite prism based on Ferracutti, Gargiulo, Ganuza, Bjerg & Castro (2015). **b.** Ternary spinel classification diagram using B-site cations and nomenclature by Stevens (1944).

The most important spinel end-member for this study, Cr-spinel, roughly corresponds to spinels with compositions that plot inside the chromite group field using the ternary B-site cation classification diagram by Stevens (1944)(Figure 2b). In terms of the Cr-spinel end-member field or *chromite subgroup* (Ferracutti et al., 2015), the B-site is occupied by Cr^{3+}, with the A-site most commonly occupied by Mg^{2+} or Fe^{2+} in primary spinel. A noteworthy subgroup in the spinel family, the titanium subgroup, is comprised of inverse spinels that commonly form through substitution of Ti^{4+} into the B-site. Members of the titanium subgroup (mainly ulvöspinel and

qandilite) have the general formula $R^{2+}(Ti^{4+}R^{2+})O_4$ and are best regarded using the ulvöspinel prism.

In published literature, *chromite* is often loosely defined, and such minerals may also go under the names *chromian/chromium/chrome/chromiferous* spinel, thus being abbreviated *Cr-spinel*. It is worth mentioning that sometimes no distinction made between chromite and *Cr-rich* spinel, despite a given mineral being chemically closer to other end-members. Understanding that pure spinel end-members (e.g. magnetite) are more the exception than the norm is essential since spinels represent a solid solution of compositions that are highly dependent on the conditions under which they form (e.g. Barnes & Roeder, 2001) - one of the properties that makes them so useful to scientists. It may therefore be convenient to view the compositional space of spinel as a spectrum and accept that trying to classify a spinel mineral phase strictly is often as unnecessary as it is difficult. Herein, the term Cr-spinel will be used for compositions that correspond to chromian spinel, aluminian chromite and ferrian chromite that are distinct from *ferritchromite* (see section Spinel alteration) using the classification diagram in Figure 2b by Stevens (1944).

Great variation develops in spinels within the group of major elements during partial melting and fractional crystallization (e.g. Dick & Bullen, 1984). The most important variations stem from the substitutions of Al^{3+} <-> Cr^{3+} and Mg^{2+} <-> Fe^{2+} as the major elements Cr^{3+} and Mg^{2+} are strongly partitioned into the solid phase and Al^{3+} into the liquid (Dick & Bullen, 1984; Hulbert, 1997). Partitioning of Fe^{2+} between the spinel phase, silicate minerals and melt is strongly temperature dependent and the Fe^{2+}/Fe^{3+} ratio is sensitive to variations in oxygen fugacity (Dick & Bullen, 1984). Modest changes generated in the compositions of the major silicate phases by magmatic differentiation may produce more dramatic fluctuations in spinel compositions (Dick & Bullen, 1984).

Minor elements like Mn, Zn, Ni and Co are often found to substitute for the bivalent cations in the A-site (e.g. Barnes, 2000). During partial melting and fractional crystallization, minor and trace element concentrations demonstrate greater variations than the major elements, making the minor element configurations sensitive recorders of magmatic differentiation, interaction and melt-rock reactions (e.g. Barnes, 2000).

Spinel alteration

Spinel is sensitive to changes in the chemistry of intercumulus melt and silicate hosts during crystallization (e.g. Barnes, 1998; Barnes, 2000). Because of its sensitivity to subsolidus re-equilibration, any interpretation reliant on the assumption of a primary melt must be made with caution. Scowen, Roeder and Helz (1991) demonstrated that Cr-spinel, even completely enclosed in olivine, could still change its solidus composition by diffusion through olivine in a slowly cooling magma. Furthermore, Roeder and Campbell (1985) suggested that enclosed Cr-spinel may stay in contact with surrounding melt through microfractures produced by the differential thermal contraction between the two mineral phases.

Primitive mantle-derived melts, such as boninites, ophiolitic cumulates, kimberlites and komatiites, produce Cr- and Mg-rich Cr-spinels (Barnes & Roeder, 2001) but alteration processes can produce similar signatures (e.g. Arai, Shimizu, Ismail & Ahmed, 2006). During alteration, Cr is usually retained in Cr-spinel while easily liberated from the Cr-bearing silicates (Oze, Fendorf, Bird & Coleman, 2004), and though Cr^{3+} is only mobile over a limited distance, silicate host minerals may cause potentially misleading enrichments (e.g. Arai et al., 2006). The Al^{3+} <-> Cr^{3+} and Mg^{2+} <-> Fe^{2+} substitutions are often expressed as *mg#* ($Mg^{2+}/Mg^{2+}+Fe^{2+}$) and *cr# (*Cr/Cr+Al) respectively. The relationship between *mg#* and *cr#* that is commonly used to interpret Cr-spinel in igneous rocks is essentially strongly dependent on the subsolidus cooling history of the rocks *after* the igneous stage (Arai et al., 2011).

The best-known indicator of alteration in Cr-spinel is the presence of Fe-rich rims, or *ferritchromite* (Saumur & Hattori, 2013). These rims are practically Al- and Mg-free and variably depleted in Cr. The central region or *core* of Cr-spinel is presumed to preserve the most primitive composition and often is still sufficiently unaltered for most purposes (e.g. González-Jiménez, Kerestedjian, Proenza & Gervilla, 2009). The alteration state of the mineral must always be assessed before it is used for interpretation; particularly regarding petrogenesis. The state of alteration is usually assessed using the morphology and textural occurrence of the mineral grains in the rock, 2D element distribution maps and relative trace element concentrations. Trace elements such as Mn, for example, can be used to clarify ambiguous textural indications resulting from Mn^{2+} substituting for vacating Mg^{2+} in the Cr-spinel during alteration (e.g. Khedr & Arai, 2017).

Geological setting

Present-day Ellesmere Island in the Canadian Arctic Archipelago is situated on the northern sector of the North American plate near the North Pole (Figure 1, inset). Archean to Proterozoic crystalline basement rock of the Greenland-Canadian Shield is exposed along the island's southeastern coast and to the northwest lies the exotic Pearya terrane with a Grenville-age basement (ca. 1 Ga) shared with the Caledonides (e.g. Trettin 1991, 1998; Malone, 2012). The rifting of the Rodinian supercontinent that initiated the formation of the Proto-Pacific (*Panthalassa*) and Proto-Atlantic (*Iapetus*) oceans in the Neoproterozoic established an irregularly shaped passive continental margin on the eastern Laurentia (i.e. the present-day North American Craton of the North American plate)(Torsvik, Smethurst, Meert, van der Voo, McKerrow, Brasier, Sturt and Walderhaug, 1996) and the subsequent closure of the Proto-Atlantic ultimately resulted in the Taconic, Caledonian and Acadian orogenies (Monroe & Wicander, 2011). The Cryogenian rifting episode presumably resulted in extensive Laurentian diabase dike swarms (Trettin, 1991).

Early geological history

Not much is known about the early geological history of Ellesmere Island. It was not until 1953 that the Geological Survey of Canada performed its first geological survey of the northern coast (Trettin, 1998) and the region is an active area of research today. The anastomosing network of fault zones sub-parallel to the northern coastline (see Figure 3) is the result of its complex tectonic evolution, which was dominated by the accretion of the Pearya terrane, thought to have occurred sometime in the Silurian during the closing of the Iapetus Ocean (e.g. Malone, 2012). The Pearya terrane, which was first identified by Shuchert (1923), appears to have been accreted to the northern margin of Laurentia represented by the Neoproterozoic to Devonian Franklinian Basin at some point in the Late Silurian (Trettin, 1986, 1991; Trettin, Parrish & Roddick, 1992; Klaper & Ohta, 1993).

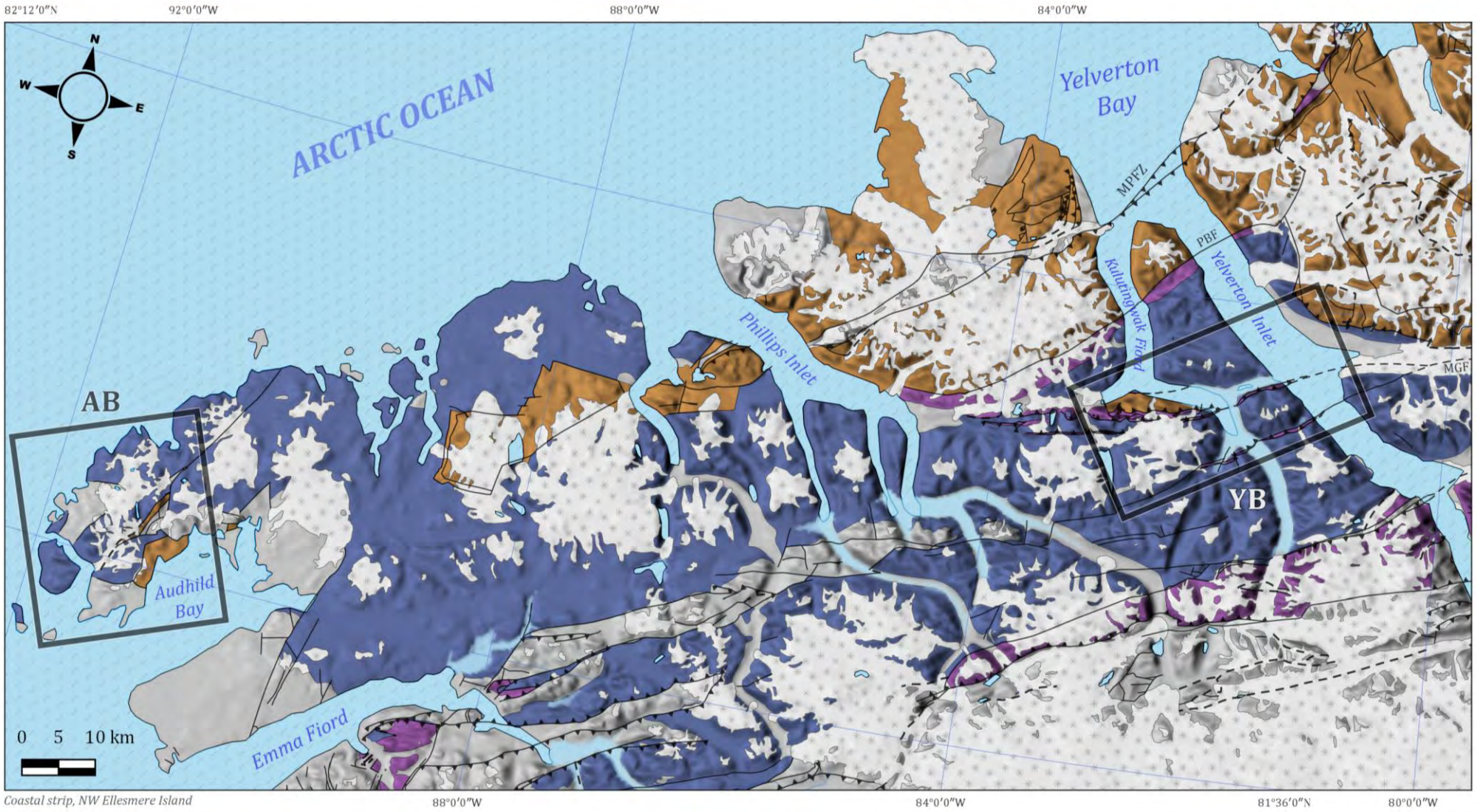

LEGEND

Clements Markham fold belt

- ***Succession A:*** *Cambrian to Silurian*
- ***Succession B:*** *Silurian to Devonian*
- Pearya terrane

- Ice
- Water
- Unspecified landmass

- Fault (motion unspecified)
- Assumed fault (motion unspecified)
- Thrust fault

Figure 3 Topographical and structural map of a circa 150 km long strip of the northwestern Ellesmere Island coast, colored after major Paleozoic geological units. Outlined sampling sites: AB = Audhild Bay (Figure 4a), YB = Yelverton Bay (Figure 4b). MPFZ = Mitchell Point Fault Zone, PBF = Petersen Bay Fault, MGF = M'Clintock Glacier Fault. *Hillshaded Digital Elevation Model: ArcticDEM. Geodatabase by Geological Survey of Canada. CRS = EPSG:3995*

The Franklinian Basin

Deposition in the Franklinian Basin began along the passive continental margin of Laurentia after rifting ca. 723 Ma, according to Malone et al. (2018) and references therein. Based on the works and interpretations of Trettin (1987, 1998) and Surlyk and Hurst (1984), the Franklinian Basin extended from northern Ellesmere Island to Northern Greenland, and associated deposits include the Franklinian shelf (Central Ellesmere fold belt, Figure 1) and a deepwater regime with two recognized subprovinces. The southeastern subprovince (Hazen fold belt, Figure 1) consists of Early Cambrian to Early Devonian sedimentary deepwater deposits and the northwestern subprovince (Clements Markham fold belt, Figure 1) of a mix of arc-type(?) volcanic rocks and Early Cambrian to Late Silurian shallow marine carbonates and deepwater sediments (e.g. Trettin, 1998). Basement rock of the Greenland-Canadian Shield outcrops in the southwestern territory of the island. The Arctic Platform that covers the basement rock is exposed west of the outcropping basement (Figure 1). The folded strata of the E-W trending Franklinian shelf are contiguous with the relatively undisturbed Cambrian to Devonian deposits of the Arctic Platform (Trettin, 1991). A clastic wedge deposited in a syntectonic foreland basin that includes sediments from the Pearya terrane conformably overlies the Franklinian shelf (Trettin, 1991; Malone et al., 2018).

The Franklinian Mobile Belt (Figure 1) incorporates the Franklinian shelf and deepwater subprovinces, the Pearya terrane, the Arctic Platform and the Late Silurian to Early Devonian Boothia Uplift (deposits not present on Ellesmere Island). Many have suggested that the northwestern deepwater province (Clements Markham fold belt) represents an offshore island arc that was still detached from the Laurentian passive continental margin prior to the accretion of the Pearya terrane. Compelling evidence of an Ordovician arc in the Franklinian Basin include shelf-parallel turbidite sequences found on Northern Greenland that indicate the presence of a northern barrier (Surlyk & Hurst, 1984) and the Ordovician to Silurian clastic sediments deposited on the approaching Pearya terrane prior to accretion, which are dominated by recycled basement rock and Ordovician arc material (Malone, 2012).

Surlyk and Hurst (1984) proposed that the Franklinian Basin expanded in several episodes by southward growth of the southern margin. It evolved from a narrow turbidite basin in the Early Cambrian to a wide, periodically stagnant turbidite basin before its evolution was disrupted during the Devonian-Early Carboniferous when the North Greenland Fold Belt took form during the Ellesmerian orogeny (Surlyk & Hurst, 1984). The Franklinian Mobile Belt is unconformably overlain by the Carboniferous to Paleogene Sverdrup Basin (Trettin, 1991), which covers most of the southeastern as well as certain central parts of Ellesmere Island (Figure 1).

The Pearya terrane

The Pearya terrane, fault-bounded by the Clements Markham fold belt along its eastern margin, consists of a series of polydeformed crustal fragments and is the only documented exotic terrane on the northern margin of Laurentia (Klaper, 1992; Trettin, 1992). The terrane's postulated Caledonian basement complex post-dates the age of basement of the Franklinian Basin by at least 1 Ga but other characteristics also speak of its exotic ancestry. Evidence of a mid-Ordovician orogeny, comparable to the M'Clintock orogeny in age and character, is recorded by an angular unconformity between Lower and Upper Ordovician strata in the Pearya terrane (e.g. Bjørnerud, 1991). The equivalent geologic record of the Franklinian Basin comprises carbonate deposition on the shelf and shale on the continental slope, with no evidence of the deformation or the clastic wedge that would accompany orogenesis (Stouge, Harper, Boyce & Christiansen, 2012). Silurian strata in the Pearya terrane record regional amphibolite facies metamorphism, which sets it apart from the rest of the Arctic Archipelago in which metamorphism has peaked at sub-greenschist grade. Furthermore, Neoproterozoic detrital zircon spectra from the Svalbard and East Greenland Caledonides supports the links between Pearya and the Caledonides (Malone, 2012).

Trettin (1998) divided the Peary terrane into the following five tectono-stratigraphic units:

Succession I: Polydeformed, crystalline basement rock of Grenville-age in fault contact with the Clements Markham fold belt

Succession II: Neoproterozoic to Lower Ordovician metasediments and metavolcanics (rift-related) in fault contact with the Clements Markham fold belt

Succession III: Lower to Middle Ordovician arc-type metavolcanics and metasediments, including mafic-ultramafic complexes

Successions VI-V: Middle Ordovician to Upper Silurian nearly unmetamorphosed sediments and volcanics

All successions are separated by major faults or unconformities. The Ordovician M'Clintock orogeny, comparable in age and character to e.g. the Taconian orogeny (Trettin, 1998), resulted in emplacement of granitic plutons in the terrane, lower greenschist to lower amphibolite facies metamorphism imposed on successions I-III, an angular unconformity that separates succession II and III from the overlying Middle Ordovician to Silurian post-orogenic strata of succession IV and overthrusting of succession III over parts of succession II. Unmetamorphosed mafic dikes or dike swarms crosscut parts of successions I and II, suggesting emplacement that post-dates the M'Clintock orogeny. The paleogeographic location of the Pearya terrane prior to accretion onto Laurentia and the manner of accretion are as of today uncertain.

The Ellesmerian orogeny

The boundary zone between Pearya and the northwestern the Clements Markham fold belt exhibits a steep metamorphic gradient that reaches up to amphibolite facies (Bjørnerud, 1991; Klaper & Ohta, 1993). Klaper and Ohta (1993) suggested that the timing of the metamorphic event was related to the southeastward regional overthrusting of Pearya over the *in situ*

Clements Markham fold belt; the heated basement rock would then have resulted in Barrovian metamorphism of greenschist to lower amphibolite grade in the Silurian strata of the Clements Markham fold belt. Postkinematic growth of porphyroblasts that overprint the foliation of the Silurian and evidence of high pressures suggests that regional overthrusting as opposed to metamorphism by underplating of an accretionary prism caused a major thermal pulse that post-dated the deformation episode (Klaper & Ohta, 1993). The region south of the boundary has been proposed to accommodate remnants of the accretionary prism of a postulated Ordovician arc (Bjørnerud, 1991). Depositional overlap of the Pearya terrane and the Clements Markham fold belt indicate that the accretion may have occurred prior to the Early Silurian (e.g. Trettin, 1991). The Franklinian Mobile Belt accommodated both the Pearya terrane and Clements Markham fold belt by the Late Devonian to Early Carboniferous when it was subjected to intense crustal shortening during the Ellesmerian orogeny, which places a definite upper constraint on the timing of the accretion (Trettin, 1991). The extensive compression of the Ellesmerian orogenic event generated folding of the Clements Markham fold belt strata and dextral movement of Central Pearya (Trettin, 1991, 1998). A single episode of syn- to post-tectonic prograde metamorphism resulted from the Ellesmerian orogeny and was followed by uplift, cooling and associated retrogression, as suggested by the retrograde greenschist overprints that are common in large parts of Pearya (Klaper and Ohta, 1993). The Franklinian Basin subsequently closed in the Early Carboniferous as a result of the Ellesmerian orogeny, when Laurentia converged with an unknown crustal block (Trettin 1991; Malone, 2012).

Methods

Sampling

The map units referenced are defined by the Geological Survey of Canada (Trettin, 1998).

Audhild Bay site

Two ultramafic rock samples collected from the Kleybolte Fault Zone near Audhild Bay were supplied by T. Hadlari, Geological Survey of Canada. These samples begin with the prefix "17HSB- ". Sample 17HSB-3 was identified as schist and 17HSB-4 as (faulted) dunite from the Kleybolte Fault Zone. The samples were collected from the *ds* unit, which forms a ca. 1 km long strip of serpentinized ultramafic plutonics between two branches of the Kleybolte Fault Zone (Figure 4a). The unit has so far not been dated but is thought to be associated with the Maskell magmatic arc of the Pearya terrane. The relationship between the *ds* unit and the Audhild Bay Inlier (unit *pqc*) is currently unknown. Trettin (1998) speculated that the *ds* unit may be a sub-arc pluton or remnants of oceanic crust that represents a tectonic suture. Aside from the Pearya terrane fragments, the Kleybolte Peninsula is covered by Clements Markham fold belt succession B and younger units (Figure 3).

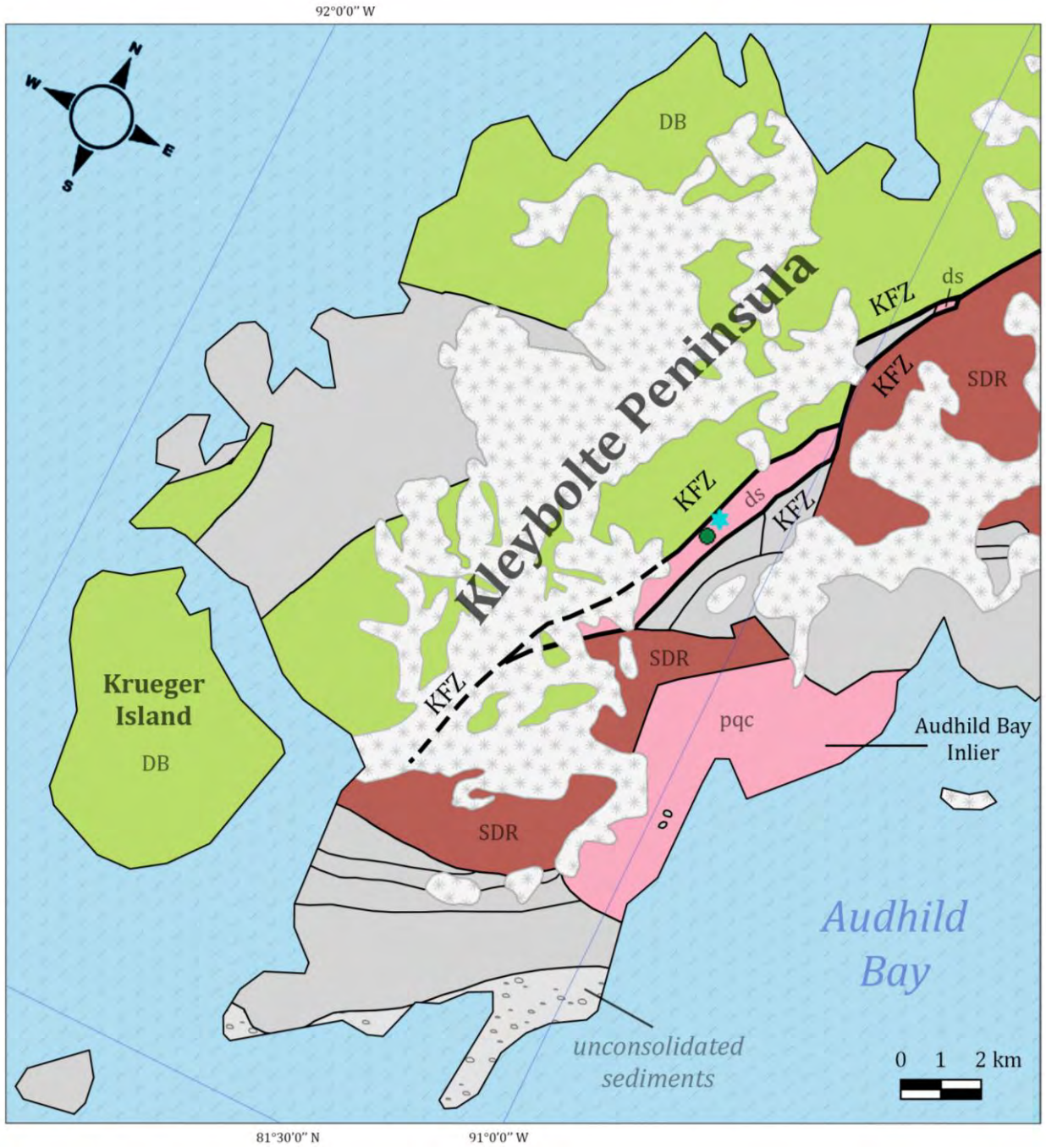

Clements Markham Fold Belt

Succession A

West-central belt

- OSv — Emma Fiord Fault Zone volcanics
- Unconsolidated sediments {*OSv*}

Northwestern belt

- SPI1 — Phillips Inlet Formation, member A
- OK1 — Kulutingwak Formation, member A
- OK2 — Kulutingwak Formation, member B
- OK — Kulutingwak Formation, *unspecified*
- Unconsolidated sediments {*OK*}

Succession B

- SDR — Danish River Formation
- Unconsolidated sediments {*SDR*}
- SL — Lands Lokk Formation
- Unconsolidated sediments {*SL*}
- DB — Bourne Complex

Pearya terrane

- pqc — Audhild Bay Inlier
- ds — Maskell assemblage
- sqc — Kulutingwak Inlier
- Unconsolidated sediments {*sqc*}

Other

- Unspecified landmass or unconsolidated sediments
- Water
- Ice
- Fault (motion unspecified)
- Assumed fault (motion unspecified)
- Thrust fault
- Sinistral transform fault
- *Northeastern Kulutingwak Anticlinorium*

Sampling sites

- VP17-01 ({*sqc*})
- VP17-04b (*OK1*)
- VP17-05b (*OSv*)
- VP17-15 (*OSv*)
- 17HSB-3 (*ds*)
- 17HSB-4 (*ds*)

Figure 4a. Geologic map of the Audhild Bay sampling site on the Kleybolte Peninsula. Note the location of the site for 17HSB-3 and 17HSB-4 in the *ds* unit between two branches of the Kleybolte Fault Zone (= KFZ). *Geodatabase by Geological Survey of Canada. CRS = EPSG:3995*

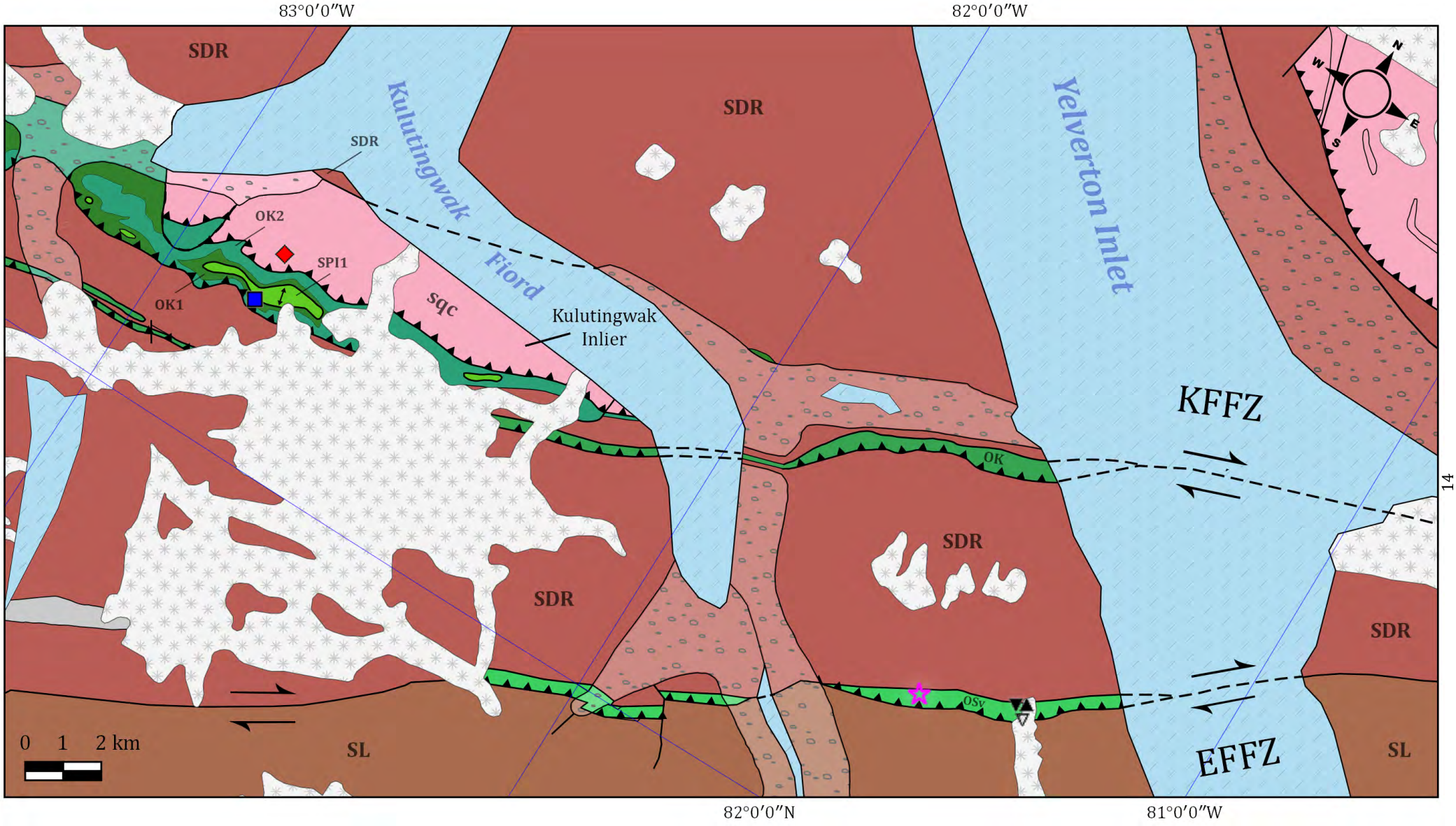

Figure 4b. Geologic map of the Yelverton Bay sampling site at the base of the Mitchell Point Peninsula. Note the locations of the sites of VP17-05b and VP17-15 in the *OSv* unit between two branches of the Emma Fiord Fault Zone (= EFFZ); the site of VP17-04b in the unit *OK1* outcropping in the Northeastern Kulutingwak Anticlinorium and the VP17-01 dike inside the *sqc* unit (Kulutingwak Inlier, Pearya terrane succession II) close to the faulted boundary zone between the Clements Markham fold belt and the Pearya terrane. KFFZ = Kulutingwak Fiord Fault Zone. Legend same as in Figure 4a. *Geodatabase by Geological Survey of Canada. CRS = EPSG:3995*

Yelverton Bay site

A total of four samples collected near Yelverton Bay were selected for analysis. These samples start with the prefix "VP17-". Sample VP17-01 was procured from a ca. 2 meters wide, semi-coarse phyric dike that intrudes the Kulutingwak Inlier (unit *sqc*) just north of the Kulutingwak Fiord Fault Zone (Figure 4b). The Kulutingwak Inlier is a dismembered fragment of the Pearya terrane (succession II) and comprises schist, phyllite, quartzite and marble. The dike cross-cuts the fabric of a calcareous-dolomitic schist attributed to the inlier (*sqc*)(Figure 5a).

Sample VP17-04b was a sub-rounded ultramafic clast attributed to the older member of the Kulutingwak Formation (unit *OK1)*(Figure 4b) that was hosted by carbonate breccia (Figure 5b). The unit outcrops in the Northeastern Kulutingwak Anticlinorium and is in fault contact with the younger member of the Phillips Inlet Formation (unit *SPI1*). The Phillips Inlet and Kulutingwak Formations together make up the Northwestern Clements Markham fold belt.

The West-central Clements Markham fold belt consists of a single unit, *OSv*, which outcrops in the Emma Fiord Fault Zone at the base of the Mitchell Point Peninsula (Figure 4b). The West-central belt unit, previously called the *Kulutingwak Fiord Assemblage*, hosts argillaceous sediments that have yielded post-Middle Ordovician conodonts and consists of a ca. 15km long steeply dipping volcanic belt that Trettin (1986) interpreted as island arc-derived. Sample VP17-05b came from a large volcanic fragment surrounded by dark-colored shale. There is a strong competence contrast between the volcanic fragment and the shale but both have undoubtedly experienced an episode of deformation that produced aligned fabrics in the form of elongation of the volcanic fragment and foliation in the shale (Figure 5c). Sample VP17-15 was collected east of VP17-05b from a unit interpreted as pillow lava. Some of those rocks were exceedingly deformed. Strain is highly partitioned onto less competent units (e.g. phyllitic conglomerates), but even the more competent units (pillow lava, sills) *in situ* were sheared. The sheared pillow lavas were variably vesicular and the pillows generally small (<20 cm) and elongate due to the shearing (Figure 5d). Sample VP17-15 constitutes one of the sheared pillows. The outcrop was cut by carbonate veins and vesicles were filled with carbonate and/or zeolite.

Klaper (1992) suggested that the igneous rocks in the West-central belt may represent an Ordovician island arc that predates the accretion of the Pearya terrane. Klaper (1992) further speculated that the region between the West-central and the Northwestern belt is relict ocean floor, covered by an accretionary prism of orogen-derived turdbidites (represented by units *SDR* and *SL*). Early structural, soft sediment features in the zone between the two belts are similar to turbidite structures observed in accretionary prisms in modern subduction zones and Bjørnerud (1991) suggested that the major folding and thrusting was related to the emplacement of the accretionary prism onto the continental margin.

Figure 5 Field photos from the sample sites in the Yelverton Bay area and description of lithological unit **a.** VP17-01 **b.** VP17-04b **c.** VP17-05b **d.** VP17-15

VP17-01 Sampling site {unit sqc} Pearya terrane, succession II

a) Sampled phyric dike. Note how the dike cuts the fabric of the calcareous-dolomitic schist of the *sqc* unit (contact = dashed line). The dike consists of semi-coarse, phyric diabase with large compositional variations, e.g. contains feldspar and pyroxene phenocrysts.

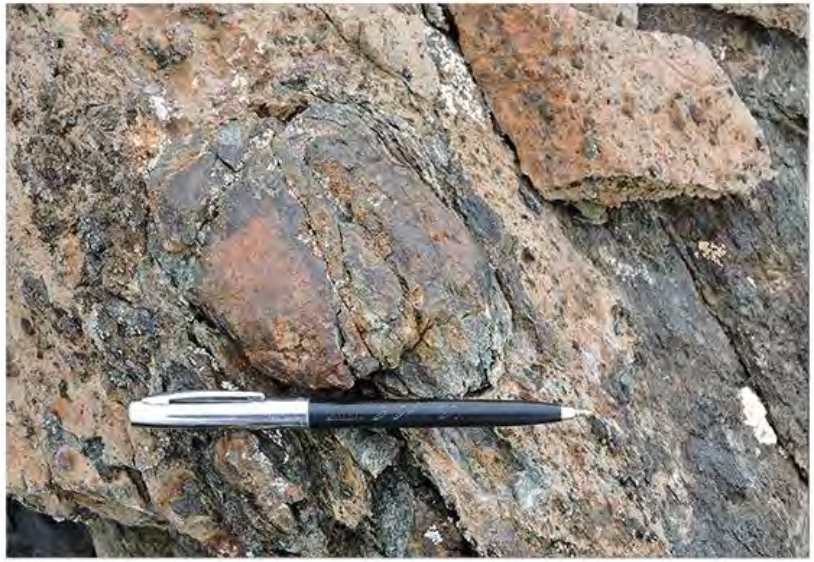

VP17-04b Sampling site unit OK1 Kulutingwak Formation A

b) Ultramafic clast protruding from carbonate breccia. Pen for scale.

VP17-05b Sampling site unit OSv West-central belt

c) Volcanic fragment surrounded by dark-colored shale was sampled. Note that the elongation of the volcanic fragment is parallel to the foliation of the shale. Hammer for scale.

VP17-15 Sampling site unit OSv West-central belt

d) Moderately deformed pillow lava with carbonate and/or zeolite amygdules that vary in size between individual pillows (examples outlined). Hammer for scale.

Petrography

A total of 17 samples were selected for processing after an initial microscope assessment of 28 thin sections: 23 thin sections from rocks from Yelverton Bay and 5 from Audhild Bay. A *Nikon Optiphot 2 POL* compound light microscope was used for the initial assessment. The strategy was to have multiple samples with high oxide-bearing potential representative of each rock unit observed in the field that could be attributed to or potentially related to the sedimentary-volcanic subprovince of the Franklinian deepwater regime. The assessment of each sample's oxide-bearing potential was based on either positive identification of translucent spinel or on the basis of the modal distribution of opaque minerals and their morphologies, reaction textures and associations with other primary and secondary minerals. The sample processing was prioritized accordingly.

Sample preparation procedure

Seven samples were ultimately selected for further analysis. Potential oxide grains were handpicked with a single-hair brush and placed inside markings on an adhesive surface covering a square of *Plexiglas*. The Ø25 mm grain mounts were cast in epoxy resin under vacuum, and later hand-polished at the Memorial University of Newfoundland for the electron microprobe. The mounts were coated with a carbon film of a thickness matching the standards used in the lab before being placed inside the electron microprobe instrument. A detailed description of the sample preparation process is available in Appendix A1.

The 17 selected samples were disintegrated to gravel with a jaw crusher and milled to fine sand using a stainless-steel mortar in a laboratory at Stockholm University. The sand was separated into heavy and light fractions using a gravity separation table with warm water. Additional purification of the heavy fractions was achieved by dry panning, removing magnetic minerals using a weak magnet and through heavy liquid mineral separation. The purified heavy fractions were assessed using a stereomicroscope.

Seven samples were ultimately selected for further analysis. Potential oxide grains were handpicked with a single-hair brush and placed inside markings on an adhesive surface covering square of Plexiglas. The Ø25 mm grain mounts were cast in epoxy resin under vacuum, and later hand-polished at the Memorial University of Newfoundland. The mounts were coated with carbon film of a thickness matching the laboratory's standard before they were inserted into the electron microprobe instrument.

Chemical analysis

SEM with WDS and EDS

The following section summarizes the fundamental principles behind the Scanning Electron Microscope (SEM) and the imaging techniques that were utilized prior to the chemical analysis. The summary is based on personal correspondence with the laboratory instructor Wanda Aylward and online resources developed by the Science Education Resource Center (SERC) at Carleton College[1].

A Scanning Electron Microscope (SEM) was used to locate, identify and document potential Cr-spinel grains on the grain mounts. The SEM is capable of producing high-resolution images of very small objects using a focused beam of electrons that is directed at the object. Thermal induction is used to produce the electron beam that is emitted by the 'electron gun' (Figure 6a). The electron gun is connected to a vacuum chamber (Figure 6b) containing a perforated anode (Figure 6c), which attracts the electrons.

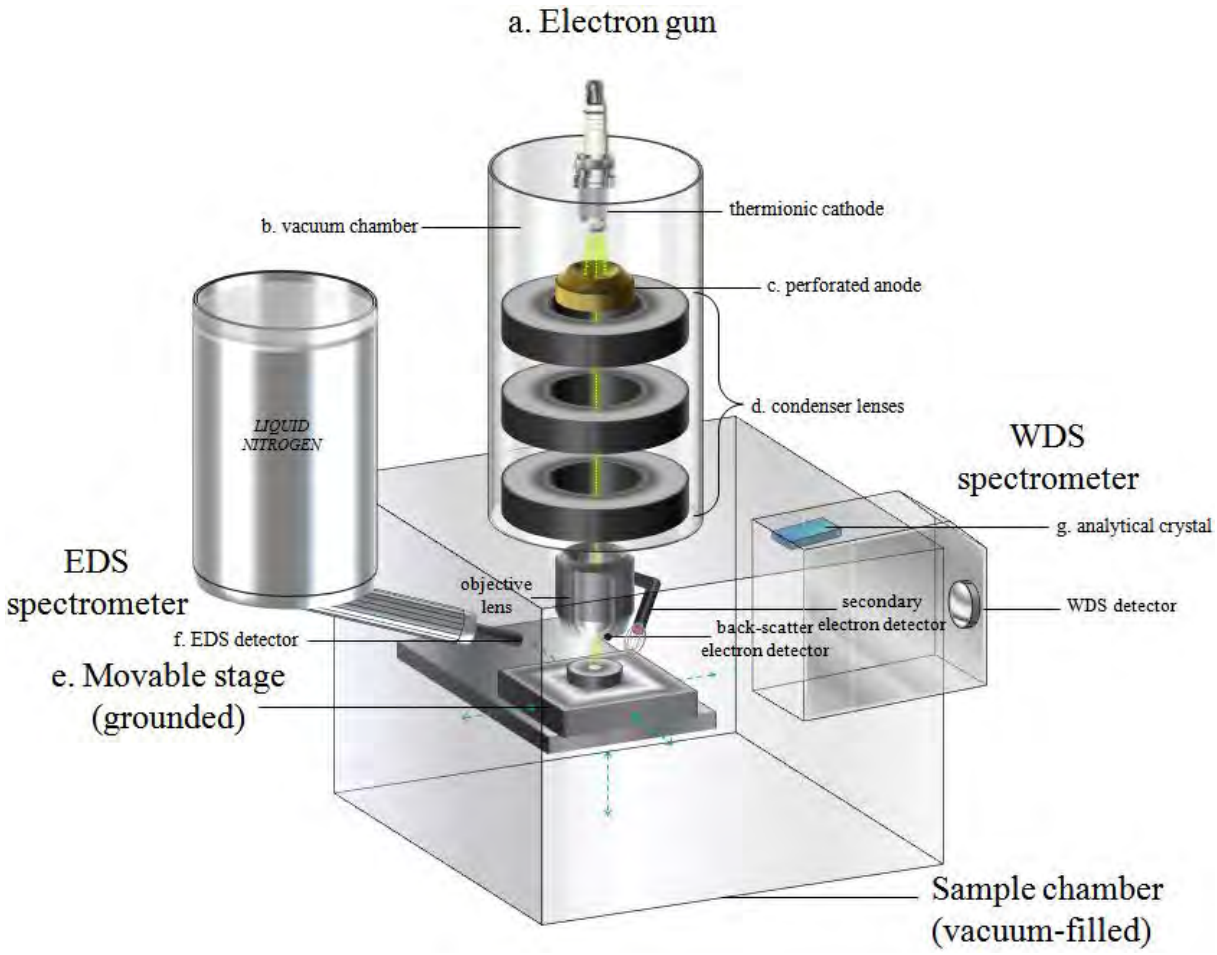

Figure 6 Simplified schematic of a Scanning Electron Microscope (SEM) with an EDS spectrometer and one WDS spectrometer filament.

[1] Science Education Resource Center. (2018, June 15). Electron probe micro-analyzer (EPMA). Retrieved January 1, 2019, from https://serc.carleton.edu/207669

Some of the electrons in motion pass through the aperture of the anode and continue through the vacuum towards the positively charged stage where the target (i.e. the grain mount) is mounted. A series of circular electromagnets called condenser lenses (Figure 6d) are used to focus the beam, analogous to the function of objective lenses in optical microscopes, before the beam passes through the objective lens aperture and reaches the target. Because nonconductive objects accumulate electrostatic charge, the target is covered with a conductive film that can be electrically grounded before being mounted on the movable stage (Figure 6e).

When the focused beam interacts with the target, several types of "signals" are emitted. The three types of signals that were utilized in this study include secondary electrons (SE), backscattered electrons (BSE) and X-rays. The secondary electrons are ejected from the atoms at the surface of the target when the absorbed energy of the beam electrons overcomes the surface energy barrier and are thus used to create a topographical image. The backscattered electrons are the reflected electrons from the beam. These are reflected both off the surface of the sample and below, when the energy of incoming electrons is high enough to penetrate. Because heavy elements (i.e. elements with a high atomic number) have a higher reflection coefficient than lighter elements, they appear brighter on the BSE image (if default settings are used). The diameter of the focused beam is much smaller than the generated image. The diameter is equivalent of the smallest feature that can be resolved and the circular area that the beam covers can be thought of as one "pixel" in the image that is generated by the scanning or "sweeping" of the beam from side to side to cover the fully illustrated area of the raster image. Though individual elements cannot be identified using only BSE, the image conveys information about the distribution of elements in the imaged target as a result of the contrasting reflection coefficients. Beam electrons with higher energy penetrate deeper into the target than those that are backscattered and can get trapped inside the object, resulting in ionization. The inner shell ionization causes transmission of so-called characteristic X-rays of whichever substance in the sample the electrons have interacted with. These X-rays are used to analyze the chemical compositions of single microscopic spots on the object (spot analysis).

The integrated Energy-Dispersive X-Ray Spectroscopy (EDS) system was used in "spot mode" to identify the mineral phases of interest by their characteristic X-ray signatures. The EDS detector's crystal (Figure 6f) absorbs the energy of the emitted X-rays from a single spot on the sample by ionization and converts the energy of the characteristic X-rays of different elements to electron volts in proportion to the absorbed energy. The software presents the result as an area plot of X-ray counts vs. keV, which is called an energy spectrum. The software isolates and labels the energy peaks with the corresponding element that would emit such a peak, and the shape or *signature* of the whole spectrum is often diagnostic of the mineral phase at that singular spot. Though relative abundances of individual elements in the form of peak heights can be discerned from the spectrum, these signals alone cannot be translated directly into quantities of individual elements or provide information on the internal chemical structure of the mineral. However, should a spectrum display relatively high peaks of the known major elements in Cr-spinel, it is a very good indication that the mineral is Cr-spinel. Should the spectrum also exhibit a

considerable peak of an (in spinel) undesirable element such as silica, the likelihood of this mineral being Cr-spinel is much lower. Ambiguous spectra were compared with online reference images[2].

Many elements have more than one energy peak. Some peaks of different elements are known to overlap, which is one of the limitations with EDS and all other techniques which rely on the characteristic X-rays. Other known limitations, which fortunately did not affect the purposes of this project, are that a) the EDS technique cannot be used to detect the lightest elements in the periodic table, and b) that peaks of whichever substance is used for coating will be omnipresent on the detection spectrum. Since the sample was coated in carbon, any carbon peaks had to be ignored due to their permanent presence.

Some grains in the sample, either considered representative of the sample as a whole or that were of particular interest, were picked out for Wavelength-Dispersive X-Ray Spectroscopy (WDS) mapping. This high-resolution 2D element distribution mapping provides an overview of chemical variations within grains and is an essential tool when it comes to understanding the nature of potential cryptic zoning. WDS is more precise than EDS and can detect lower concentrations of elements, although it is also unable to detect the lightest elements in the periodic table. The generated "2D maps" consist of a raster image of the mapped area with each pixel colored-coded with the intensity of the signal in that spot. These intensities, like the EDS spectrum peaks, cannot be directly translated into quantities of any element but instead illustrate variations in individual elements relative to the rest of the mapped area. Consequently, the number of elements that can be mapped is in practice limited by time and hardware capacity, as it is very time-consuming to create this raster-type spot analysis and different analytical crystals (Figure 6g) in the detector are needed for different elements. The elements that were selected for the purpose of this study were aluminum, magnesium, iron, chromium and titanium.

Electron microprobe analysis

The following section relates the fundamental principles of the electron microprobe technique to the application in this study. It includes two subsections that together summarize the analytical conditions (under Analytical method) and the data processing operation that is necessary due to limitations of the electron microprobe technique (under Stoichiometric method). The data processing operation, or algorithm for stoichiometric recalculations, is largely based on an online exercise[3] published by Prof. John B. Brady (Smith College). A step-by-step demonstration of the algorithm using data from this study is available in Appendix A2. The computer software End-Member Generator 8.0, which employs the same algorithm, was used to generate the recalculated values for this study's dataset.

[2] McGill University. (n.d.). Spectra of Energy Dispersive Spectrometry. Retrieved January 1, 2019, from http://www.eps.mcgill.ca/~lang/EDSSPEC/edshome.html

[3] Brady, J. B. (2019, March 11). Mineral Formulae Recalculation. Retrieved March 16, 2019, from https://serc.carleton.edu/research_education/equilibria/mineralformulaerecalculation.html

Analytical method. The chemical composition of spinel was determined using a JEOL JXA-8230 Electron Probe MicroAnalyzer at the Memorial University of Newfoundland, Canada. The instrument was equipped with a tungsten (W) filament cathode and five wavelength dispersive X-ray spectrometers (WDS), an energy dispersive X-ray spectrometer (EDS) and used the ZAF data reduction procedure for oxides. During quantitative spot analyses, the analytical conditions were 15 kV accelerating voltage, 20 nA electron beam current, 1 µm beam diameter, and 1.3 · 10-4 Pa vacuum. The ten elements selected for analysis were Fe, Mg, Al, Cr, Ti, Mn, Ni, V, Ca and Si. Peak interference corrections were made for Cr-V, V-Ti and Al-Cr, which are known to overlap and cause elevated measurement artifacts.

Spots for analyses were selected based on backscatter electron (BSE) and secondary electron (SE) imagery as well as EDS signatures. SEM with WDS was used to create elemental distributions maps of Al, Mg, Fe, Cr and Ti in on representative grains in each sample. During the analyses, standard checks on magnetite and crocoite were performed every ~20-30 points to track potential systematic errors and at the beginning and end of each run, and an additional standard check on magnetite was performed as well. Element standards, calibration parameters, mean detection limits, and standard deviations are displayed in Table 1.

	major elements				***minor elements***					
ELEMENT	Al	Mg	Fe	Cr	Ti	V	Mn	Ni	Ca	Si
Calibration standard	diopside	diopside	magnetite	*crocoite**	rutile	native V	rhodenite	pentlandite	diopside	diopside
Counting time, *seconds*	30	30	30	30	60	60	60	60	60	60
Analyzing crystal	TAP	TAP	LIFH	LIFH	LIFL	LIFH	LIFL	LIFL	PETL	TAP
Detection Limit (harm. mean), *wt.%*	0.005	0.004	0.006	0.009	0.007	0.009	0.005	0.006	0.002	0.004
Standard Deviation (harm. mean), *%*	1.0	1.4	9.7	0.3	16.8	0.5	3.4	6.0	19.2	8.0
* *secondary standard*										

Table 1 Analytical configuration and errors of the electron microprobe analysis.

Stoichiometric method. The electron microprobe software assumes that the entire iron content consists of the oxide FeO (i.e. Fe^{2+}) and generates a weight percentage for FeO based on this assumption. However, the ideal mineral formula for spinel is AB_2O_4 where A represents bivalent and B trivalent cations in normal spinels. Since iron may be present in spinels at both crystallographic sites, this assumption cannot be made, and measures must be taken.

Droop (1987) used a simple general equation for estimating the ferric content in ferromagnesian oxides and silicate minerals from electron microprobe data by assuming ideal stoichiometric proportions. It is dependent on the criterion that iron is the only element present among the analyzed oxides with variable valency and that oxygen is the only type of anion. By assuming a neutral electrostatic charge at each measured point and the ideal stoichiometric proportions of the spinel formula unit, the number of oxygen anions can be fixed as 4 exactly, and the sum of (unspecified) cations as exactly 3. Thus, by adjusting the relative proportions of Fe^{2+} and Fe^{3+}, charge balance can theoretically be achieved.

From the stoichiometric proportions, the mass of the two iron oxides can be determined by acknowledging the direct relationship between a) the (from measurements) calculated amount of substance for the given cation, n_c, in any detected oxide i, and b) the derived atomic proportion of the given cation normalized to the ideal sum of cations in the formula unit $p_{c,i}$:

$$\frac{n_{c,i}}{p_{c,i}} = \frac{n_{c,FeO}}{p_{c,FeO}} = \frac{n_{c,Fe2O3}}{p_{c,Fe2O3}}$$

Using this relationship, new weight percentages of the iron oxides can be determined from the initial electron microprobe data. With the following general formula, using Al_2O_3 as the oxide i for proportionality, the weight percent $W_{\%,x}$ of either of the iron oxides X is calculated through the formula:

$$W_{\%,x} = \left[\frac{c_{Al2O3} \cdot W_{\%,Al2O3}}{p_{c,Al2O3} \cdot M_{Al2O3}}\right] \cdot \frac{p_{c,x} \cdot M_x}{c_x}$$

The sum of all weight percentages, which should approach 100%, will change slightly compared to the initial sum that was generated by the electron microprobe software after the recalculation of the two iron oxides.

Data reduction. After weight percent recalculation following the stoichiometric algorithm, bad data were identified from high SiO_2 and anomalously high and low total weight percentages and consequently excluded. Cr-spinel should not contain any considerable amounts of SiO_2 so the highest accepted SiO_2 value was 1.776 wt.%. Generated total weight percentages far from 100% can mean that the mineral contains substantial amounts of additional oxide components not accounted for or that it does not follow the chemical framework of spinels (Aylward, pers. comm.). The range of the accepted total weight percentages is 92.075-104.573 wt.%. The cut-off values were generously chosen by discreet gaps in the dataset and are roughly comparable to those observed in published literature (e.g. compare SiO_2 = 1.41 wt.% in Lindsley, 1991).

Results

Petrography

Sample ID: 17HSB-3

Geographical coordinates *DDMM.mmm* (WGS84):	81°40.200' N 91°7.952' W
Map unit (by GSC):	*ds*
Rock type (from field comment):	Schist
Hand sample description:	Schistose, black and deep green-colored rock with crenulated cleavage. Relatively brittle. Figure 7a.
Hand sample photo:	
Thin section description:	Fabric: Foliated (schistose, crenulated) Textures and mineralogy: Ductile fabric consists of two interlaced phases: one is colorless and looks "dirty"; the other is greenish yellow and fibrous. The first phase appears more competent, judging by how it forms sigmoidal lenses which the other phase appears to flow around. Both display up to third order interference colors but the interference colors of the more competent phase are generally of lower order (i). Ductile, opaque bands and opaque pods conform with the fabric. A major shear band occurs roughly orthogonal to the orientation of the fabric (ii). Pod-like opaque accumulations with multiple (iii, Microscope image 1a) or isolated euhedral to subhedral opaques (iv, Microscope image 1b) occur away from the major shear band. Some of these pods as well as a few anhedral pseudomorphs (containing the competent phase) demonstrate pressure shadows conforming with the fabric of the groundmass (v, Microscope image 1c). The pods vary in shapes and sizes (Microscope image 1a-c) and are irregularly distributed. Anhedral, ductile opaque bands are omnipresent but mostly concentrated along the major shear band and generally associated with the less competent phase.

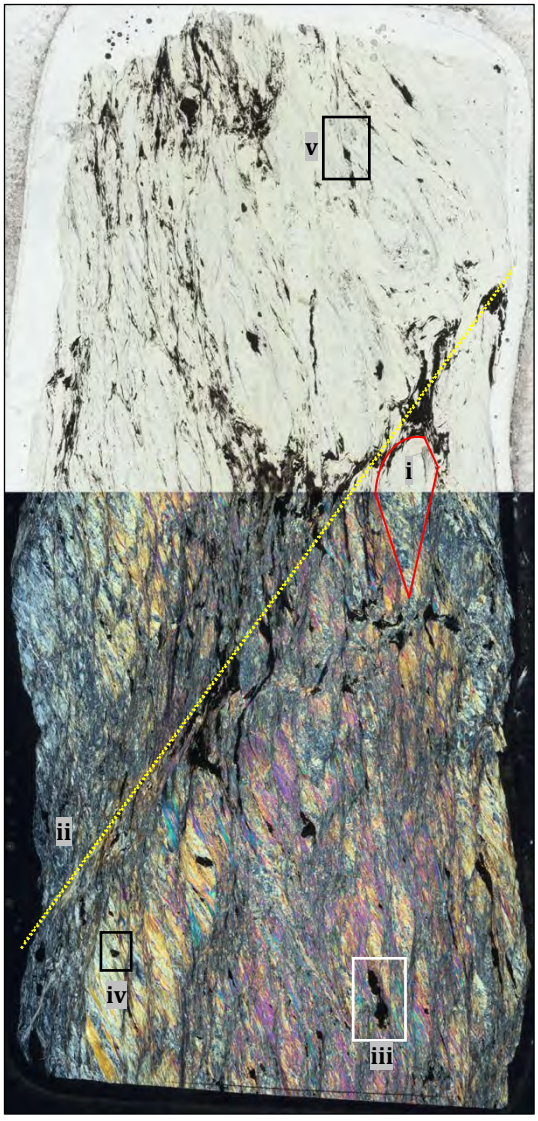

Thin section scan 17HSB-3 Top = PPL, bottom = XPL. FOV dimensions: 1.5 x 3.0 cm.

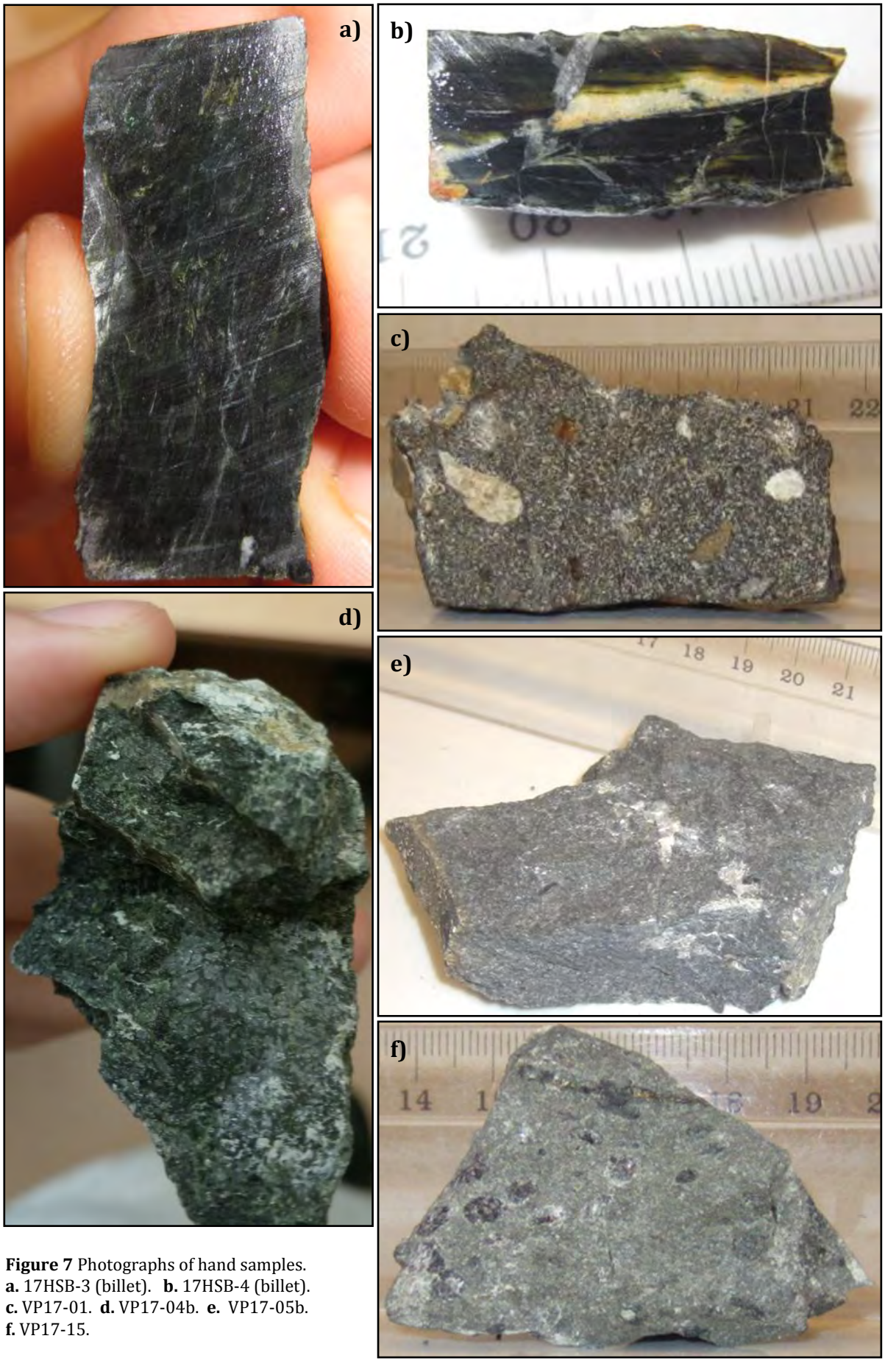

Figure 7 Photographs of hand samples.
a. 17HSB-3 (billet). **b.** 17HSB-4 (billet).
c. VP17-01. **d.** VP17-04b. **e.** VP17-05b.
f. VP17-15.

Microscope image 1. Three compound light microscope images (a-c) and one SEM backscatter electron image (d) for 17HSB-3.

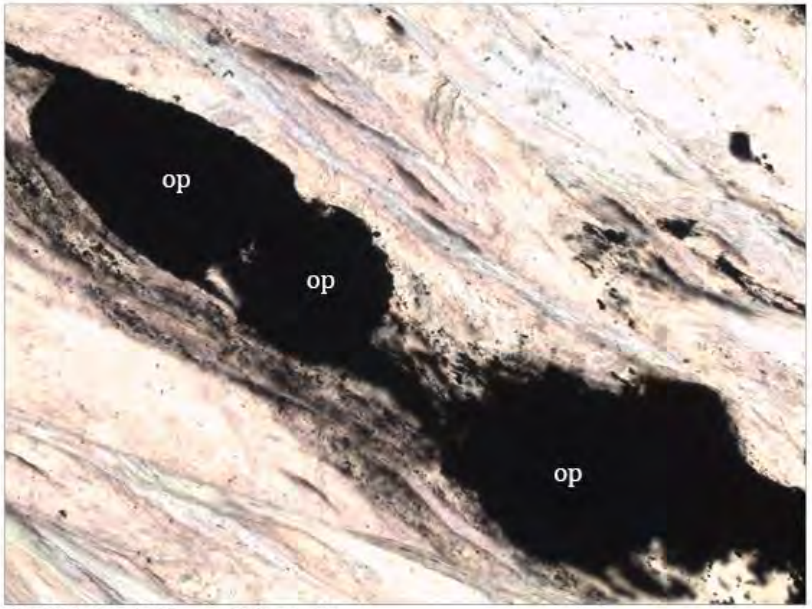

17HSB-3 ***PPL*** *FOV: 1.40 mm*

a) Pods with subhedral opaques along shear band. Note the competence contrast between the opaques and the schistose groundmass.

17HSB-3 ***PPL*** *FOV: 1.40 mm*

b) Relatively homogeneous groundmass of ductile shear bands with high order interference colors. The bands are interlaced with small lenses of deformed opaques. Note the pressure shadow (dotted outline) of the relatively undeformed but cracked subhedral opaque mineral.

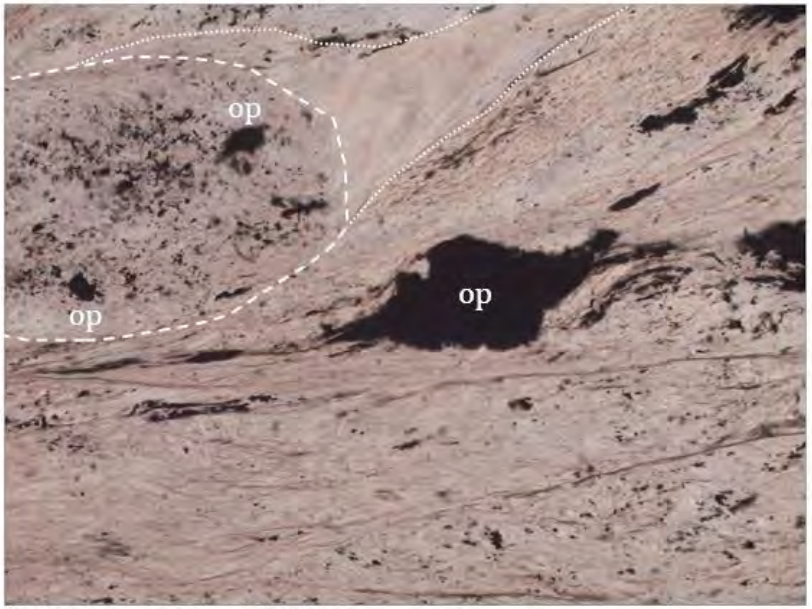

17HSB-3 ***PPL*** *FOV: 1.40 mm*

c) CENTER: Sigmoidal opaque pod aligned with shear bands. TOP LEFT CORNER: Competent pseudomorph (dashed outline) with intragranular opaques (potentially inclusions) and a pronounced pressure shadow (dotted outline).

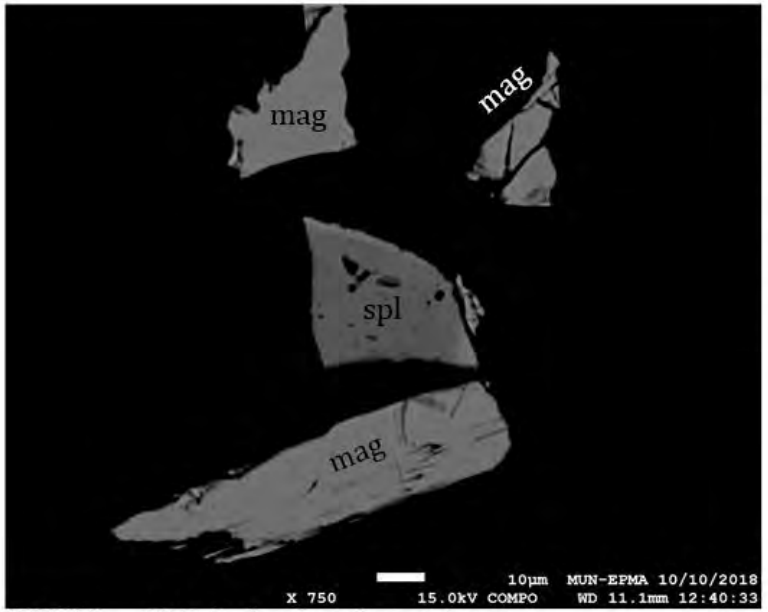

17HSB-3 ***SEM****: Backscatter electron image*

d) BSE image of the grain mount with Cr-rich spinel grain surrounded by magnetite. Note the compositional zoning along the top grain boundary and the bottom right edge.

Sample ID: 17HSB-4

Geographical coordinates	
DDMM.mmm (WGS84):	81°40.200' N 91°7.952' W
Map unit (by GSC):	*ds*
Rock type (from field comment):	Fault zone dunite
Hand sample description:	Melanocratic rock with some yellowish green bands with waxy luster. Banded, potentially of tectonized, faulted and veined with carbonate. Relatively brittle. Identified in the field as dunite. Thin section reveals that is has been fully serpentinized.
Hand sample photo:	Figure 7b.
Thin section description:	Fabric: Foliated (mylonitic, kinked) Textures and mineralogy: Ductile fabric consists of yellowish green serpentine striped with mylonitic, opaque shear bands with weak crenellations and kinks. More competent opaques form localized bulges or pods along the opaque shear bands (i, Microscope image 2a) and multiple grains can be occasionally be distinguished using reflected light within larger, winged pods (ii, Microscope image 2b). Discreet clusters of subhedral, opaque crystals can sometimes be discerned along shear bands (iii, Microscope image 2c). The display of interference colors of the serpentine is relatively uniform. The (ductile) mylonitic lineation is disrupted by one large, (brittle) crack (iv) roughly perpendicular to the lineation. Thinner carbonate veins likewise cut the fabric with a similar orientation (v). The fabric is markedly deformed and displaced along a shear zone (vi), which coalesces with a network of very fine-grained carbonate veins.

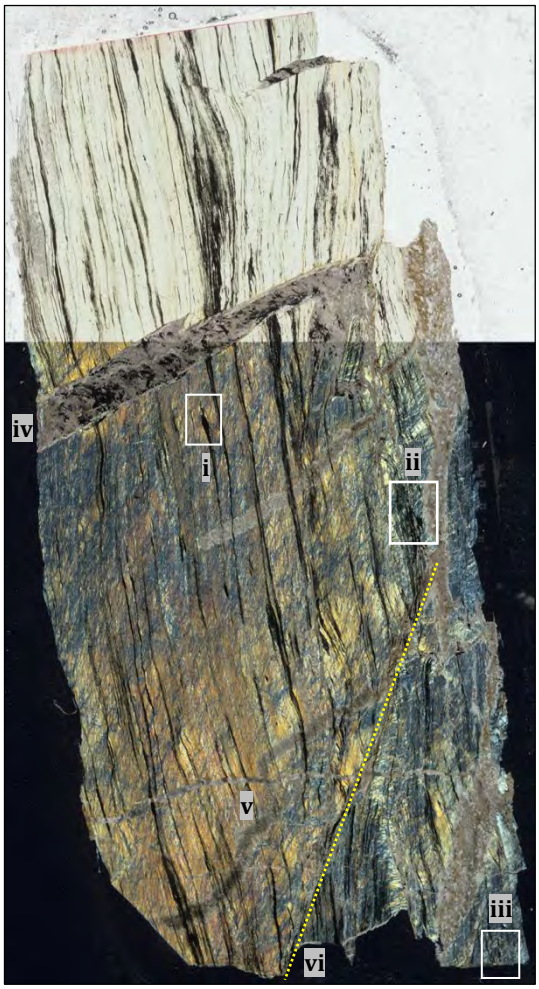

Thin section scan 17HSB-4 Top = PPL, bottom = XPL. FOV dimensions: 1.6 x 2.6 cm

Microscope image 2. Three compound light microscope images (a-c) and one SEM backscatter electron image (d) for 17HSB-4.

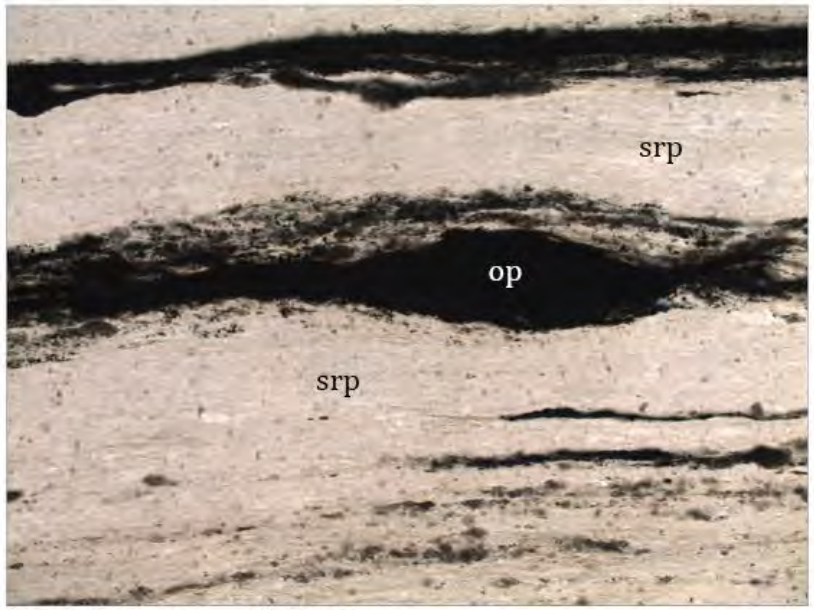

17HSB-4 ***PPL*** *FOV: 0.35 mm*

a) Winged, anhedral opaque pod inside a lightly kinked shear band segment of serpentine groundmass. Opaque pod appears as a lenticular, greyish mass in reflected light.

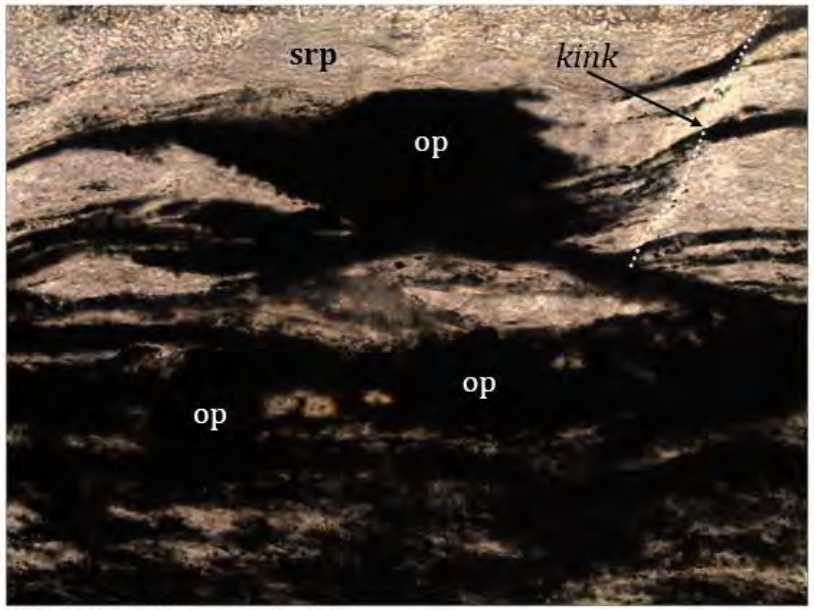

17HSB-4 ***PPL*** *FOV: 0.35 mm*

b) TOP: Winged, opaque pod along kinked serpentine shear bands. Reflected light reveals that the pod consists of three individual grains of the same type of mineral. BOTTOM: Opaque, indistinct mass that appears greyish colored under reflected light.

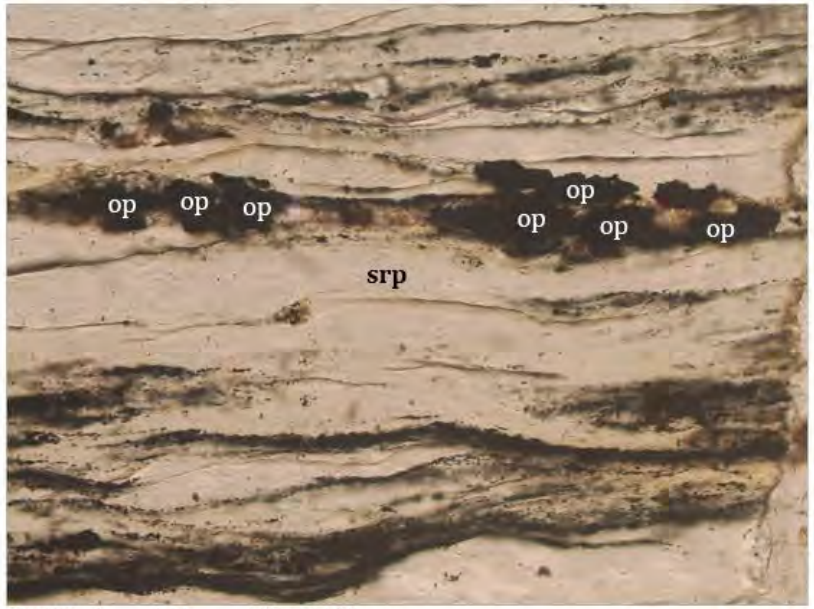

17HSB-4 ***PPL*** *FOV: 0.70 mm*

c) Lenticular clusters or aggregates of competent opaques inside shear bands of crenulated serpentine.

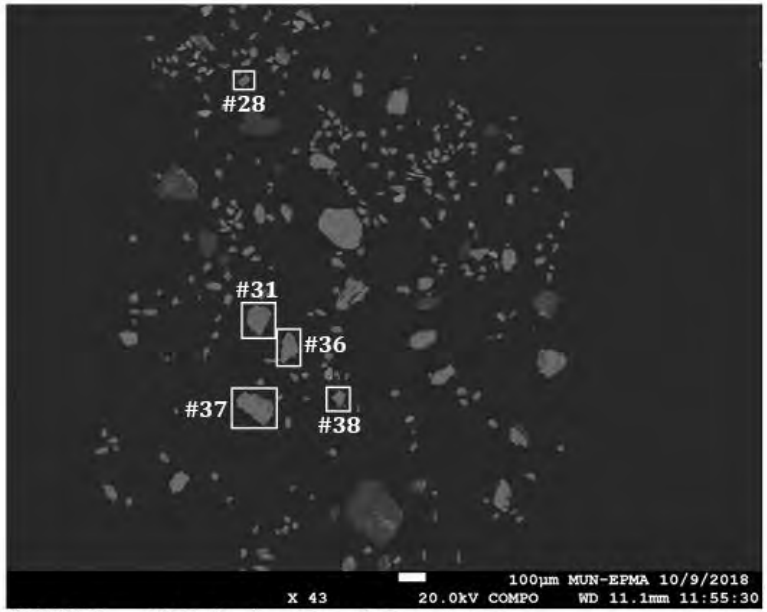

17HSB-4 ***SEM****: Backscatter electron image*

d) BSE image of the grain mount, marked with several of the analyzed spinel grains.

Sample ID: VP17-01

Geographical coordinates
DDMM.mmm (WGS84): 82°02.856' N 82°50.435' W
Map unit (by CGS): *{sqc}*
Rock type (from field comment): Basaltic dike cross-cutting *sqc* calcareous-dolomitic schist

Hand sample description: Phyric diabase with various megacrysts. The megacrysts vary in terms of size, shape and color. The rock is relatively compact and lacks foliation.

Hand sample photo: Figure 7c.

Thin section description:

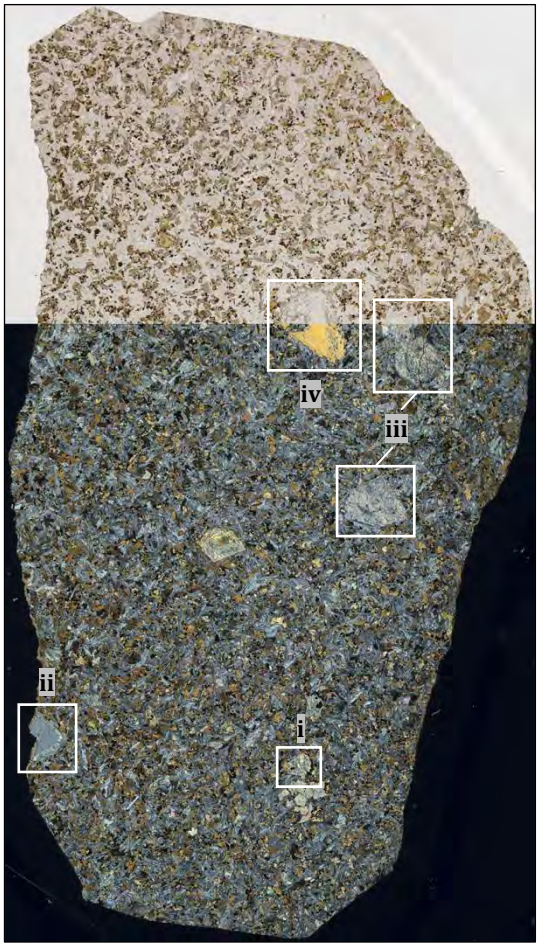

Thin section scan VP17-01 Top = PPL, bottom = XPL. FOV dimensions: 2.0 x 3.4 cm

Crystallinity: Holocrystalline.
Microstructure: Glomerphyric - fine-grained groundmass and medium-grained megacrysts.
Mineral assemblage:
Groundmass:
~40% *plagioclase* [interlocking, randomly oriented with polysynthetic twinning, partly sericitized].
~50% mafic equigranular (apart from opaques) glomerocrysts: *biotite* [iron-rich judging by the strong brown coloration, mildly chloritized along the edges (Microscope image 3b)], *clinopyroxene* [severely cracked, colorless to tan, often uralitized at edges (Microscope image 3a-c)], *hornblende* [brown , euhedral isolated grains or subhedral grains associated with pyroxene alteration (Microscope image 3a-c)], *rutile* [euhedral with 120° crystal faces or subhedral, deep reddish brown color, sometimes enveloping opaques (Microscope image 3b-c)], *olivine* [pseudomorphed to acicular bowlingite with third order interference colors, equant, yellowish], *opaques* [fine, euhedral to anhedral, concentrated around/on other mafics (Microscope image 3c) or as inclusions in rutile.

Megacrysts, mm scale: *olivine* [pseudomorphed to acicular bowlingite, yellowish, eqant and annealed glomerocrysts with localized reaction rims, occasionally with spinel inclusions (i, Microscope image 3a)], *feldspar* [equant with discontinuous concentric zoning (ii)], *unidentified* [subhedral pseudomorph with low relief (iii)], *tourmaline* [discontinuous concentric zoning, jagged grain boundary, partially envelops pocket of groundmass minerals (iv)].

Accessory: *spinel* [euhedral, brown-colored inclusions in pseudomorphed olivine (Microscope image 3a)], *carbonate* [interstitial].

Secondary textures: Sericitation [plagioclase, feldspar (preferentially of outer zone)], chloritization [biotite], uralitization [clinopyroxene], bowlingitization (olivine).

Comment: Hydrothermal alteration may have generated some of the megacrysts, e.g. tourmaline and feldspar. Discontinuous concentric zoning in tourmaline and feldspar may be cogenetic. Additional microscope images are available in Appendix B1.

Microscope image 3. Three compound light microscope images (a-c) and one SEM backscatter electron image (d) for VP17-01.

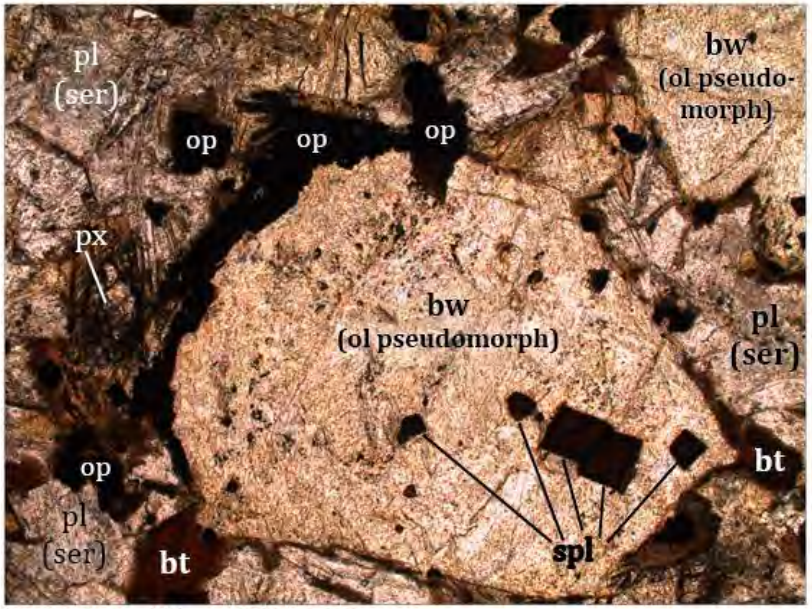

VP17-01 ***PPL*** *FOV: 1.40 mm*

a) Bowlingitized annealed olivine glomerocryst with translucent , euhedral brown-colored spinel inclusions. Note lack of opaque rims around the spinels. Glomerocryst is surrounded by partially seriticized plagioclase. Note reaction rim (biotite, opaques) where glomerocryst is in contact with altered pyroxene.

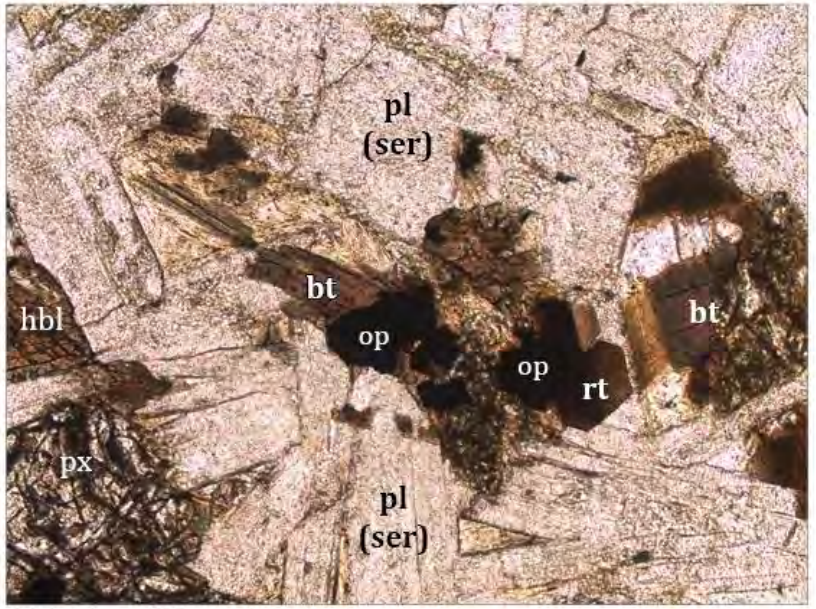

VP17-01 ***PPL*** *FOV: 0.70 mm*

b) CENTER: Cluster of mafic minerals and euhedral rutile in groundmass of randomly oriented and interlocking, plagioclase (partially sericitized). Note the chloritization of the biotite margins BOTTOM-LEFT CORNER: Colorless, altered and cracked clinopyroxene below a subhedral, brown hornblende phenocryst.

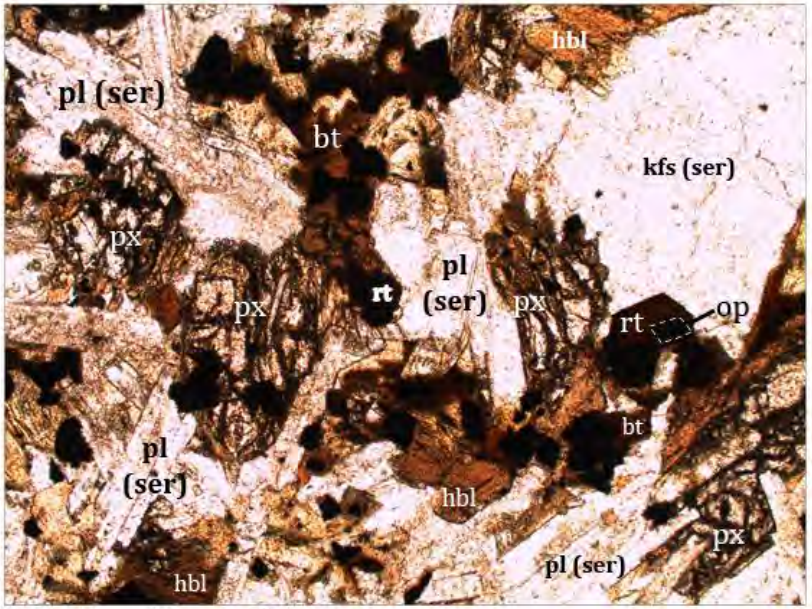

VP17-01 ***PPL*** *FOV: 1.40 mm*

c) Glomerophyric mafic minerals (altered clinopyroxene, hornblende, biotite, opaques) surrounded by plagioclase (partially sericitized). Note euhedral rutile with a euhedral, opaque inclusion (dashed outline) that is in contact with the mafics and a partially seriticized k-feldspar phenocryst or antecryst.

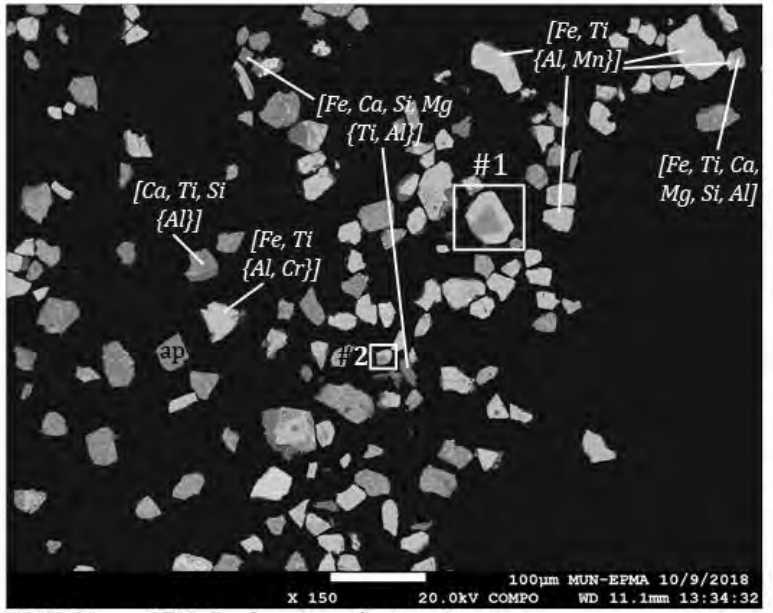

VP17-01 ***SEM****: Backscatter electron image*

d) Representative BSE image of the grain mount, marked with the analyzed spinel grains. Annotations on other grains show EDS peaks enclosed by [square brackets]: major peaks in *italic* and minor peaks in *{italic inside curly brackets}*. Note the compositional contrast between the rims and cores of grains #1-#2.

Sample ID: VP17-04b

Geographical coordinates	
DDMM.mmm (WGS84):	82°02.168' N 82°50.087' W
Map unit (by GSC):	*OK1*
Rock type (from field comment):	Pyroxenite
Hand sample description:	Greenish black rock with subtle fissile tendencies. Identified in the field as pyroxenite. Thin section reveals extensive chloritization and amphibole as opposed to pyroxenite, making it amphibolite in its current state. Figure 7d.

Hand sample photo:

Thin section description:

Thin section scan VP17-04b Right = PPL, left = XPL. FOV dimensions: 1.9 x 3.0 cm

Crystallinity: Holocrystalline.
Microstructure: Phaneritic or phyric, potentially cumulate.
Mineral assemblage:
Groundmass: Bimodal; green-colored chlorite (i) with anomalous bluish grey interference colors (Microscope image 4a) and globular, colorless chlorite with radial crystal (ii) habit and up to first order yellow interference colors (Microscope image 4b) – *groundmass interference colors not visible in thin section scan.*

Megacrysts: *amphibole* [multiple millimeters in size, randomly oriented, in disequilibrium, notably leucocratic – probably iron-poor, crystal habit prismatic for larger specimen and acicular for smaller].

Other: *opaques* [vermicular masses or subhedral clusters in groundmass (iii, Microscope image 2b) or more often concentrated as subhedral aggregates that conform to relict cleavages in altered amphibole (Microscope image 2c)], *unidentified* [prismatic, relief slightly higher than groundmass, one cleavage direction, anomalous blue interference colors, associated with green chlorite (Microscope image 4a)], *apatite* [accessory mineral, associated with groundmass].

Secondary textures: Chloritization.

Comment: The unidentified mineral may be bastite (serpentine group pseudomorph after clinopyroxene). The groundmass consists of patchy chlorite. The opaques concentrated in amphibole megacrysts (iv, v) are likely alteration products. Additional microscope images are available in Appendix B1.

Microscope image 4. Three compound light microscope images (a-c) and one SEM backscatter electron image (d) for VP17-04b.

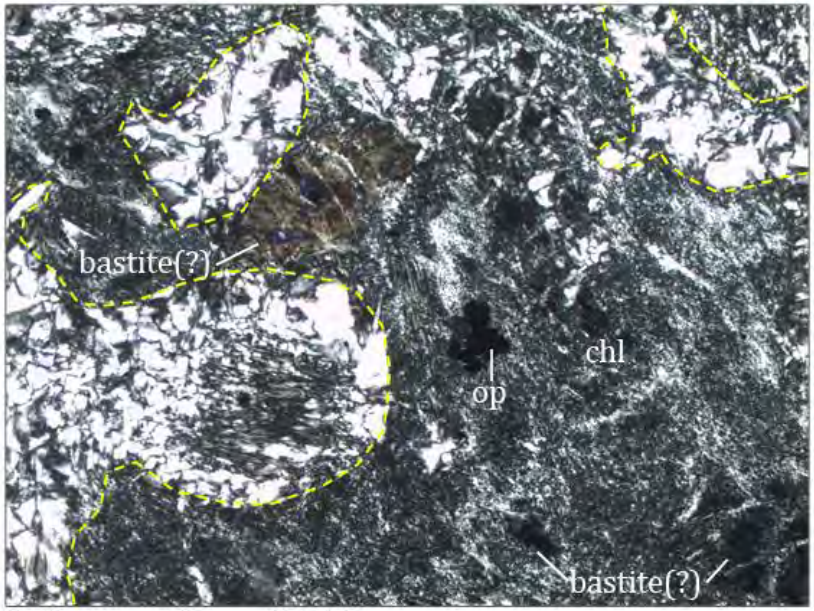

VP17-04b ***XPL*** *FOV: 5.60 mm*

a) Aggregate of subhedral opaques in chloritic groundmass. Groundmass also hosts aggregates of colorless chlorite with radial growth (dashed outline) and low relief bastite(?) pseudomorphs with anomalous blue interference colors (pseudomorphs only distinguishable in XPL)

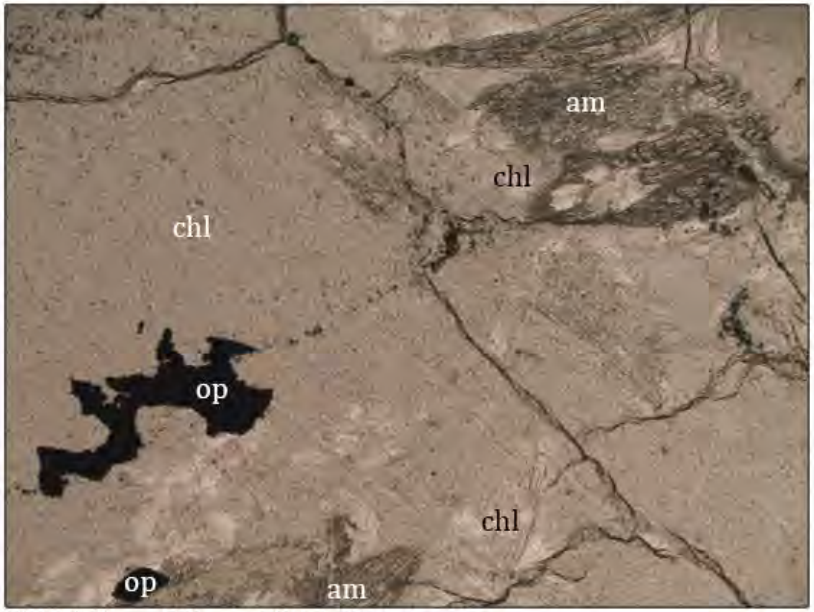

VP17-04b ***PPL*** *FOV: 1.40 mm*

b) Vermicular opaque mass associated with chlorite (both modes). Note that the acicular amphibole with medium relief form clusters associated with patches of colorless chlorite with radial growth.

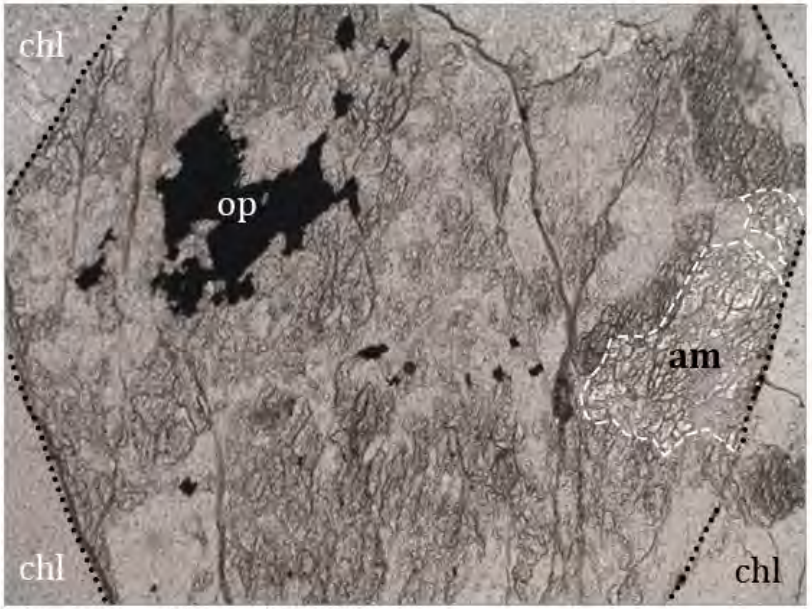

VP17-04b ***PPL*** *FOV: 0.70 mm*

c) Partial view of a euhedral and prismatic, largely altered amphibole (dotted outline) with a large accumulation of subhedral intragranular opaques. Note how the opaques conform to the amphibole cleavage. The least altered remnants of amphibole (outlined with dashes) is not associated with opaques.

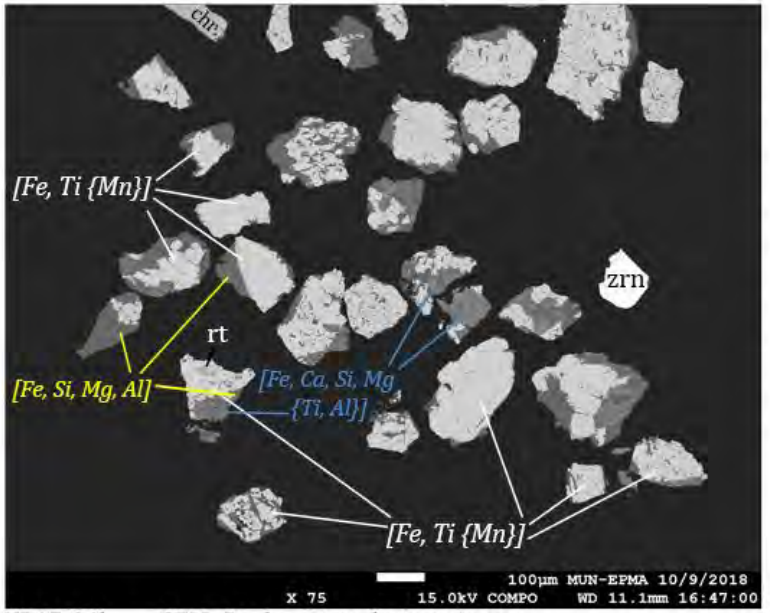

VP17-04b ***SEM****: Backscatter electron image*

d) BSE image of the grain mount. TOP LEFT: Part of one of the analyzed spinel grains. Annotation on other grains show EDS peaks [enclosed by square brackets]: major peaks in *italic* and minor peaks in *{italic inside curly brackets}*.

Sample ID: VP17-05b

Geographical coordinates
DDMM.mmm (WGS84): 82°02.230' N 81°28.724' W
Map unit (by GSC): *OSv*
Rock type (from field comment): Volcanogenic
Hand sample description: Medium grey, almost bluish-tilted compact rock with whitish carbonate veins. A brownish mineral is often associated with the carbonate margin. Contains some black phenocrysts (mm scale).

Hand sample photo: Figure 7e.

Thin section description:

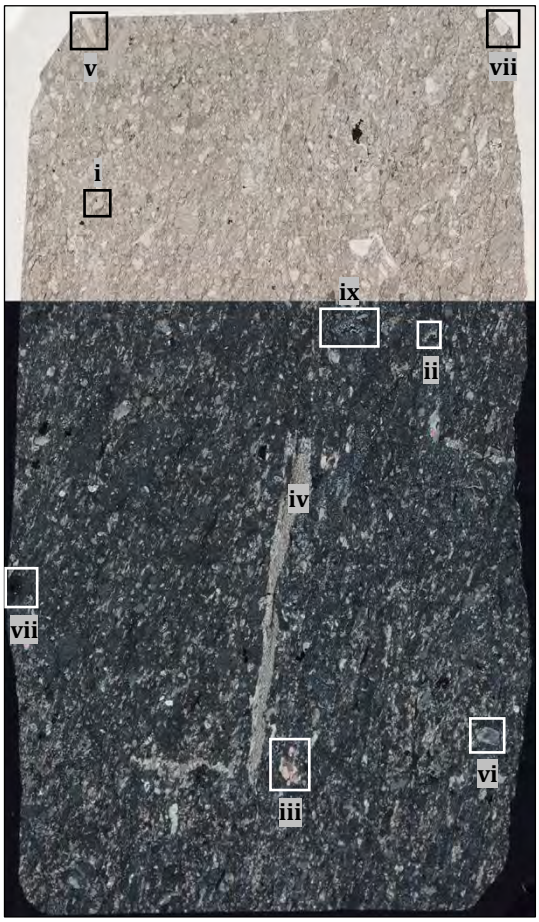

Thin section scan VP17-05b Top = PPL, bottom = XPL. FOV dimensions: 2.0 x 3.6 cm

Crystallinity: Hypocrystalline
Microstructure: Volcanogenic with superimposed protomylonitic texture. Contains entrained lithic volcanogenic fragments (Microscope image 5a) and xenocrysts (?).
Mineral assemblage:
Primary: Cryptocrystalline microlites and devitrified glass are omnipresent. Some subhedral opaques appear as inclusions in entrained fragments may also be primary (i, Microscope image 3a).

Secondary (?): *pyrite* [opaque, medium-sized and anhedral, often clustered, associated with carbonate (ii, Microscope image 5b]), *carbonate* [subhedral to anhedral grains with deformed cleavages or recrystallized pockets (iii) or fine-grained veins that conform with the lineation of the fabric (iv)], *opaques* [fine, interstitial and vermicular].

Xenocrysts (?): *feldspar* [isolated, with or without twinning (v, vi)], *quartz* [isolated, poikilitic (vii)], *spinel* inclusion [unaltered but cracked euhedral, translucent, brown-colored, armored by two altered mineral phases (vii, Microscope image 5c)], *unidentified oikocrysts* [altered crystalline remnants with rhombohedral crystal shapes differentiated by different orientations and display of anomalous blue interference colors].

Secondary textures: Some mineral grains are associated with pressure shadows and recrystallized porphyroclasts that contain e.g. plagioclase (ix).

Microscope image 5. Three compound light microscope images (a-c) and one SEM backscatter electron image (d) for VP17-05b.

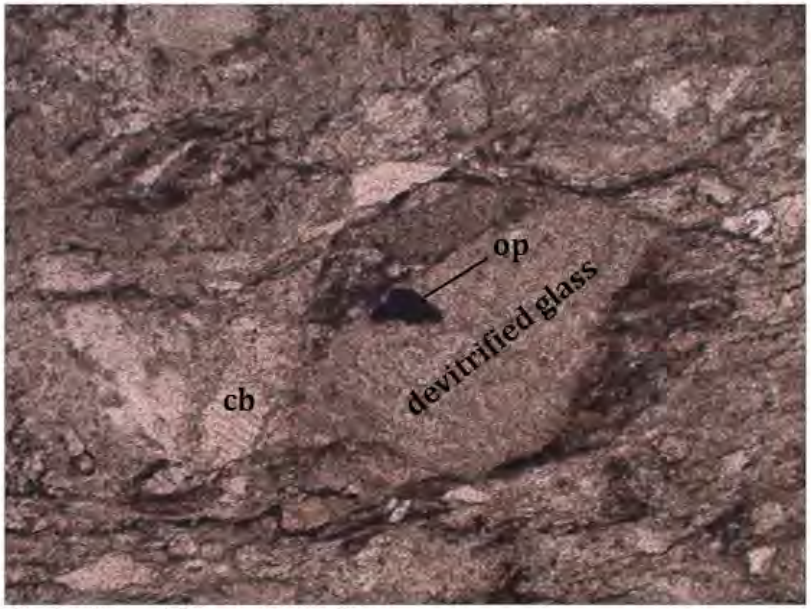

VP17-05b ***PPL*** *FOV: 0.70 mm*

a) Entrained lithic volcanic fragment consisting of devitrified glass and a subhedral opaque mineral grain.

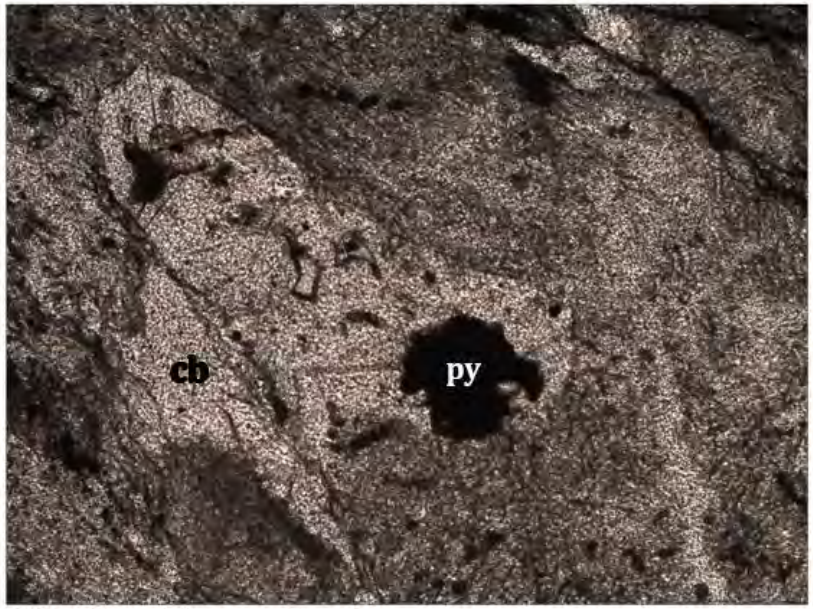

VP17-05b ***PPL*** *FOV: 0.35 mm*

b) Anhedral crbonate aggregate in groundmass associated with anhedral pyrite.

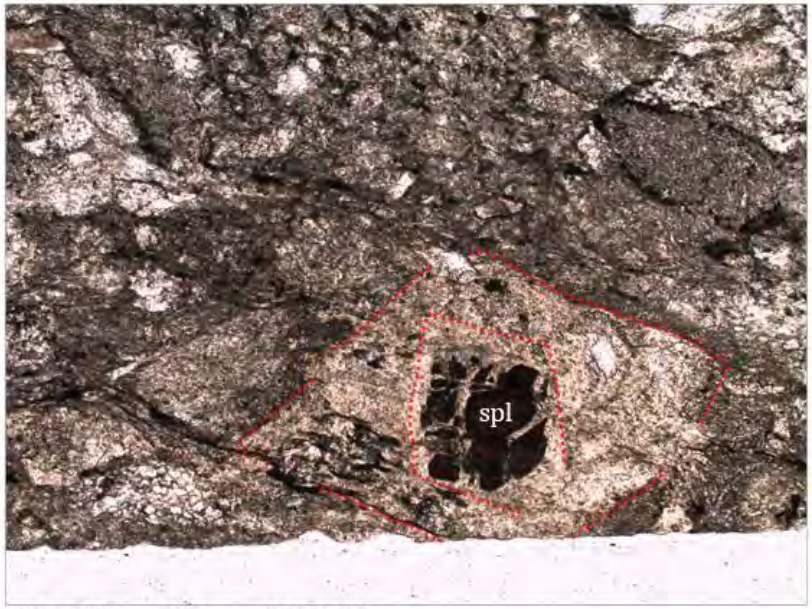

VP17-05b ***PPL*** *FOV: 0.70 mm*

c) Euhedral, translucent brown spinel double-armored by two extensively altered mineral phases (dotted outlines). Both phases exhibits anomalous blue interference colors with differentiating extinction and apparent roughly diamond-shaped morphologies. The spinel lacks notable signs of alteration along cracks.

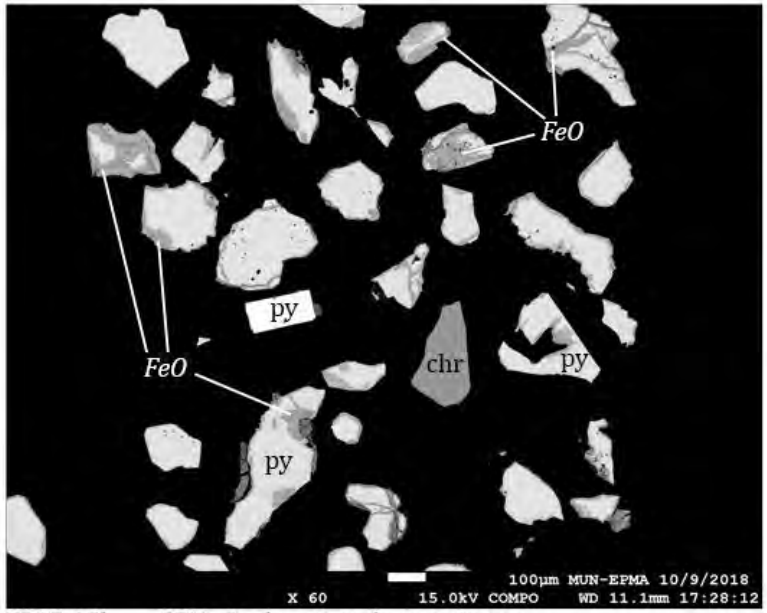

VP17-05b ***SEM****: Backscatter electron image*

d) BSE image of the grain mount, centered on the the only identified spinel grain. Note that the remaining grains consist solely of pyrite, often with iron oxide along cracks and grain boundaries.

Sample ID: VP17-15

Geographical coordinates *DDMM.mmm* (WGS84):	82°03.198 N 81°19.346' W
Map unit (by GSC):	*OSv*
Rock type (from field comment):	Deformed pillow lava
Hand sample description:	Medium grey rock with carbonate-filled vesicles (dark-colored, up to cm scale). Cut by some thin veins filled with either pyrite or carbonate.
Hand sample photo:	Figure 7f.
Thin section description:	Crystallinity: Hypocrystalline. Microstructure: Volcanogenic, highly vesicular with trachytic textures. Also contains entrained lithic fragments e.g. with a higher portion of devitrified glass (i). Mineral assemblage: Groundmass: *plagioclase* microlites and devitrified glass. Segregated into discreet lenticular structures with differentiating modes in terms of grains sizes (Microscope image 6a). Primary: *plagioclase* [trachytic, with polysynthetic twinning], *opaques* [very fine, disseminated in the groundmass (Microscope image 6b)], *spinel* [rare and very fine, translucent and brown-colored, disseminated in groundmass (Microscope image 6c)]. Secondary: *pyrite* [fine aggregates associated with carbonate and feldspar or as euhedral reaction rim accumulations]. Secondary textures: The groundmass and some amygdules are cut by a set of thin, fine-grained subparallel carbonate veins (ii). Two lenticular structures are cut off by the margin of the thin section have reaction rims (iii). The reaction rims are mostly made up of pyrite (Microscope image 6). Comment: Amygdules [semi-rounded, multiple millimeter sized] are diverse. One amygdule has concentric carbonate needles surrounded by radiating zeolite needles (iv). Another contains two generations of carbonate (v) in which one euhedral carbonate grain is surrounded by anhedral and locally deformed carbonate that fills the rest of the vesicle. The other carbonate amygdules display evidence of deformation, e.g. bent and kinked cleavages (vi) or annealed crystals with undulose extinction (vii). Additional microscope images are available in Appendix B1.

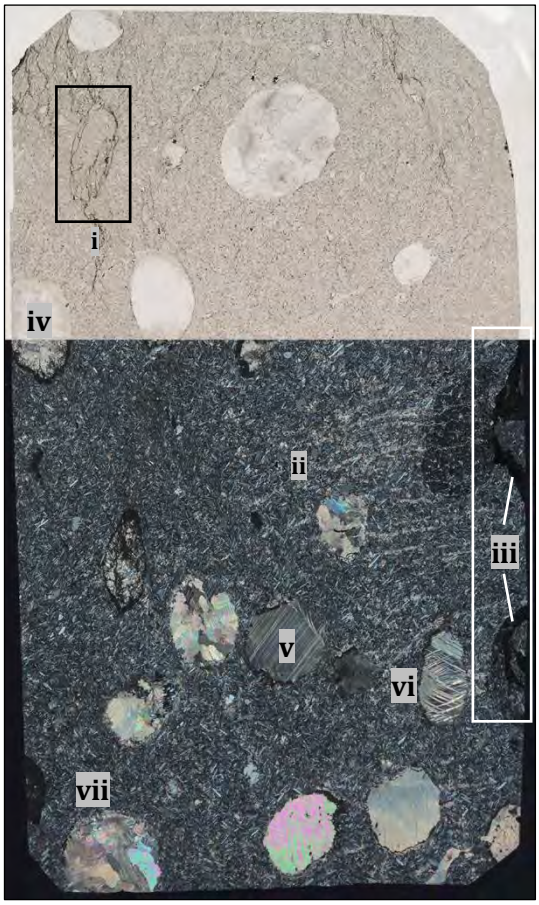

Thin section scan VP17-15 Top = PPL, bottom = XPL. FOV dimensions: 2.1 x 3.6 cm

Microscope image 6. Three compound light microscope images (a-c) and one SEM backscatter electron image (d) for VP17-15.

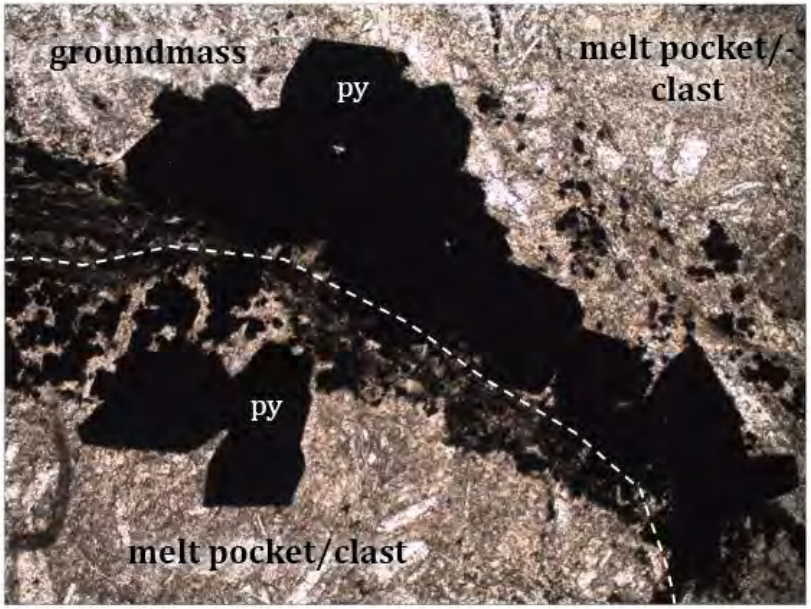

VP17-15 ***PPL*** *FOV: 0.70 mm*

a) Reaction rim around volcanic lens structure. The reaction rim consists of euhedral pyrite (opaque). The nucleation site of the pyrite appears to be a chill margin. Note the compositional differences between the two lenses and the groundmass. The lens at the top left corner completely lacks chill margin and a substantial reaction rim.

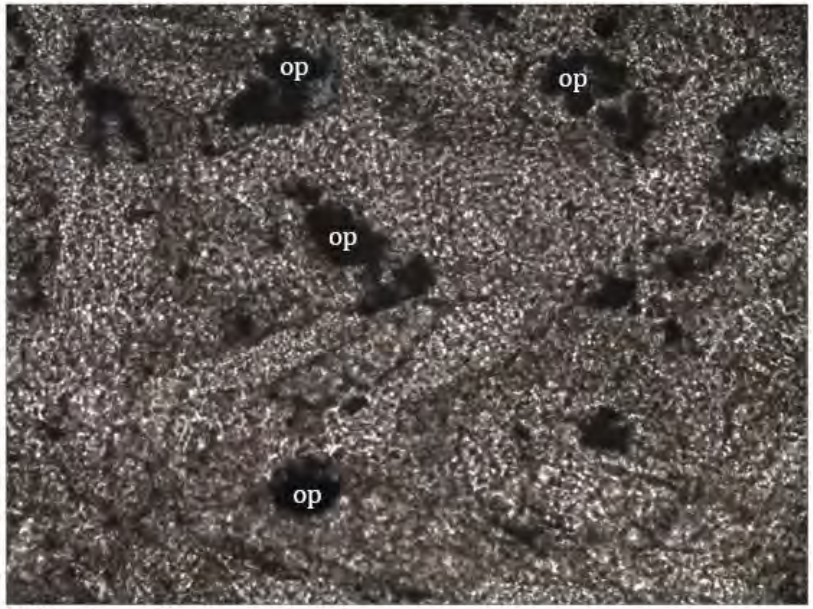

VP17-15 ***PPL*** *FOV: 0.35 mm*

b) Tiny, disseminated opaques in the groundmass.

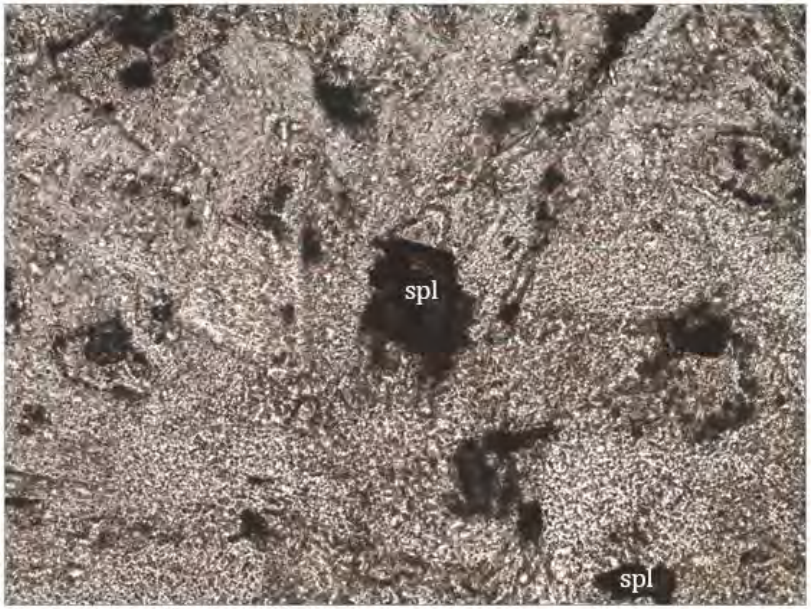

VP17-15 ***PPL*** *FOV: 0.35 mm*

c) Small, translucent brown spinel disseminated in the groundmass. Equivalent findings were made in certain lens structures.

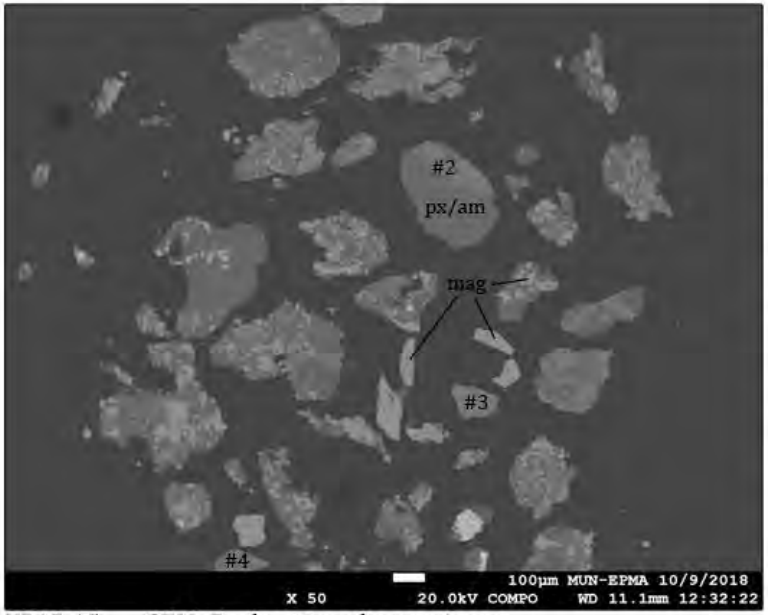

VP17-15 ***SEM****: Backscatter electron image*

d) BSE image of the grain mount, containing three of the analyzed spinel grains. Grains #2-#3 belong to generation X, grain #4 to generation Z. Note that grain #2 is an anhedral inclusion in pyroxene or amphibole.

Intragrain compositional variations

2D element distribution maps (Al, Cr, Fe, Mg and Ti), backscatter electron and secondary electron images of individual grains are presented in the form of collages (2D element distribution collages 1-9) and collages for one or two grains from each sample is provided. Note that the deformed pillow lava yielded seven subhedral to anhedral Cr-spinel grains among which there are three chemically discrete generations. The most Cr-rich generation is represented by four grains, the intermediate by two and the least Cr-rich by a single grain, and these generations are referred to as X, Y and Z respectively. 2D element distribution collage 9 presents a grain from generation X. Collages for generation Y are available in Appendix B2. These include the grain on the front page (generation Y). Appendix A2 also includes a collage from the second grain of the Kulutingwak Inlier intrusion (VP17-01).

The secondary electron images (reflecting topography of the grain surface) are marked with the positions of the electron microprobe spot analyses. Assuming that the surface topography is flat, the grayscale color variations in the backscatter electron images reflect compositional variations, with lighter colors indicating higher atomic numbers.

17HSB-3 Grain #16

Backscatter electron image of compositional variations

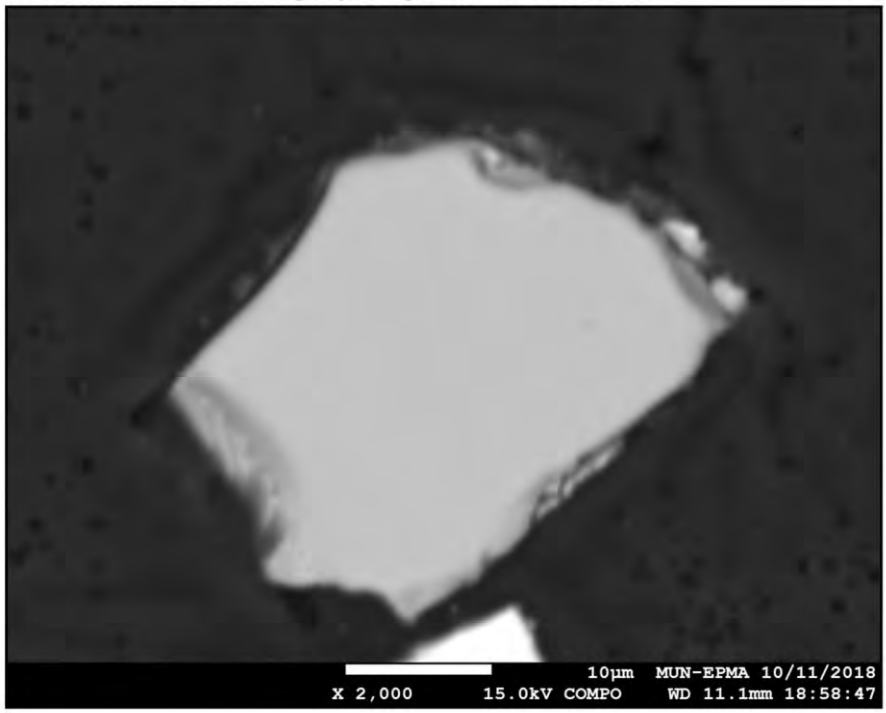

Secondary electron image (topography) with spot analyses positions

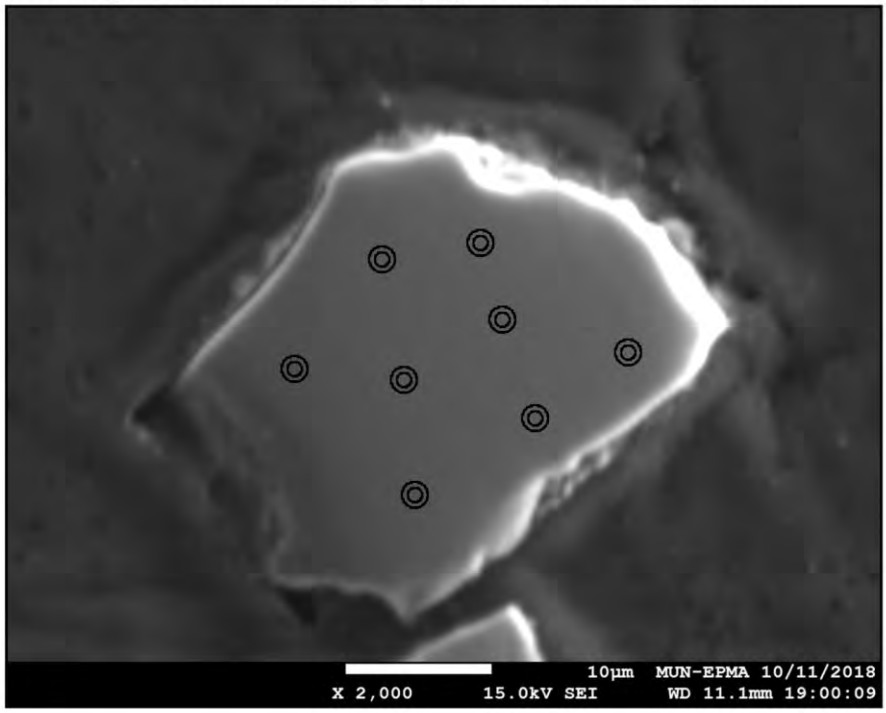

MAJOR ELEMENT X-RAY MAPS

Al ——— 10 um

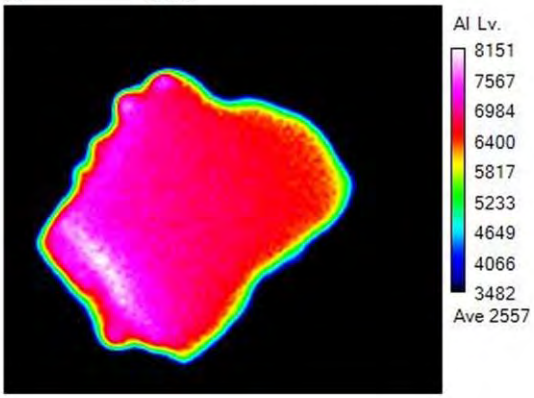

Cr ——— 10 um

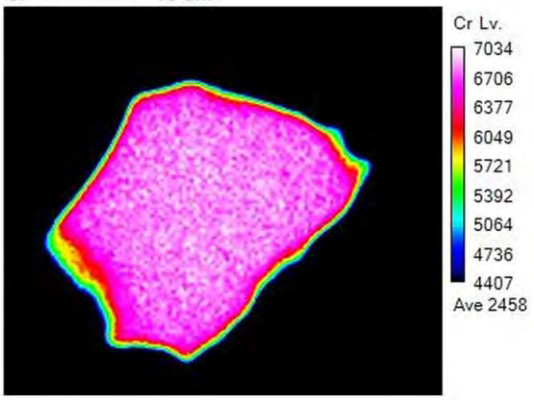

Fe ——— 10 um

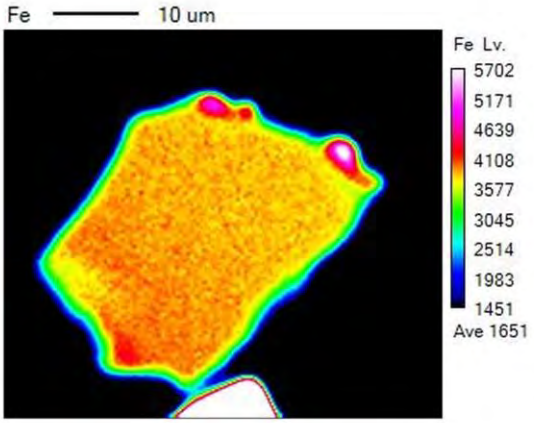

Mg ——— 10 um

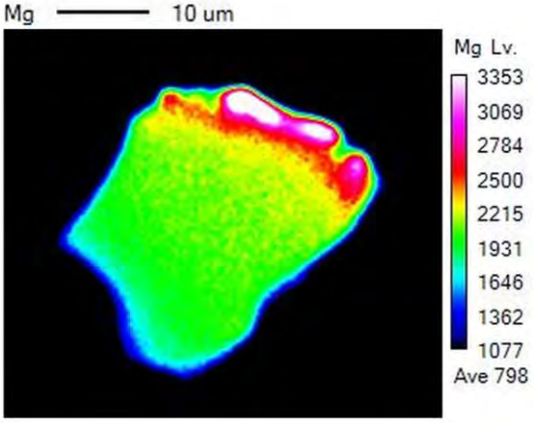

MINOR ELEMENT X-RAY MAPS

Ti ——— 10 um

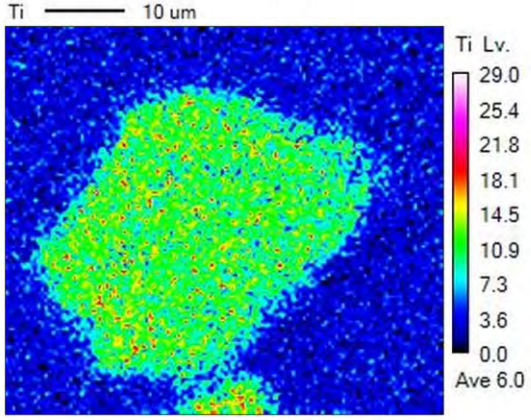

17HSB-3 Grain #17

Backscatter electron image of compositional variations

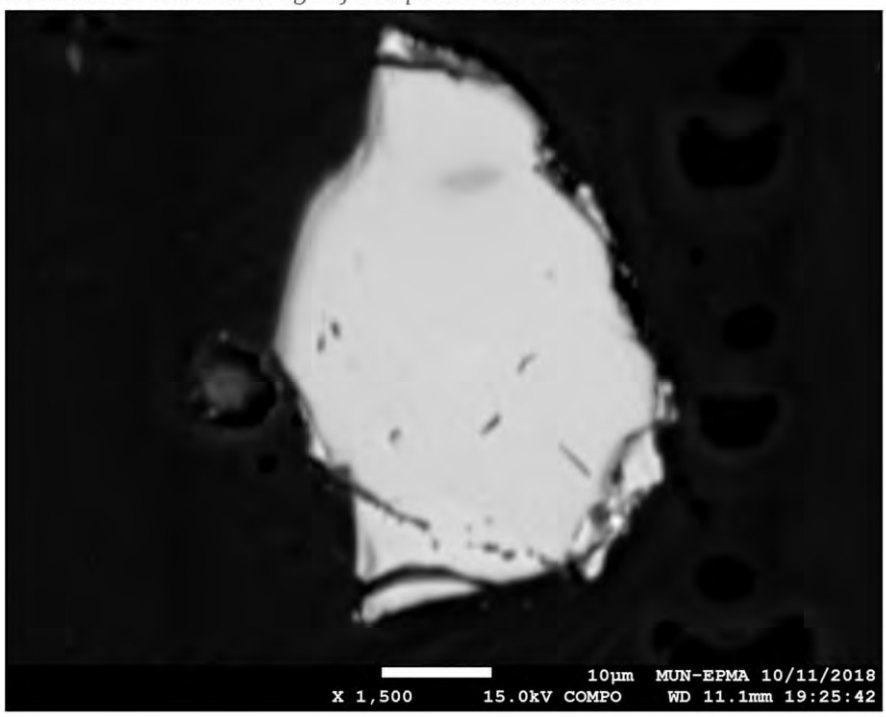

Secondary electron image (topography) with spot analyses positions

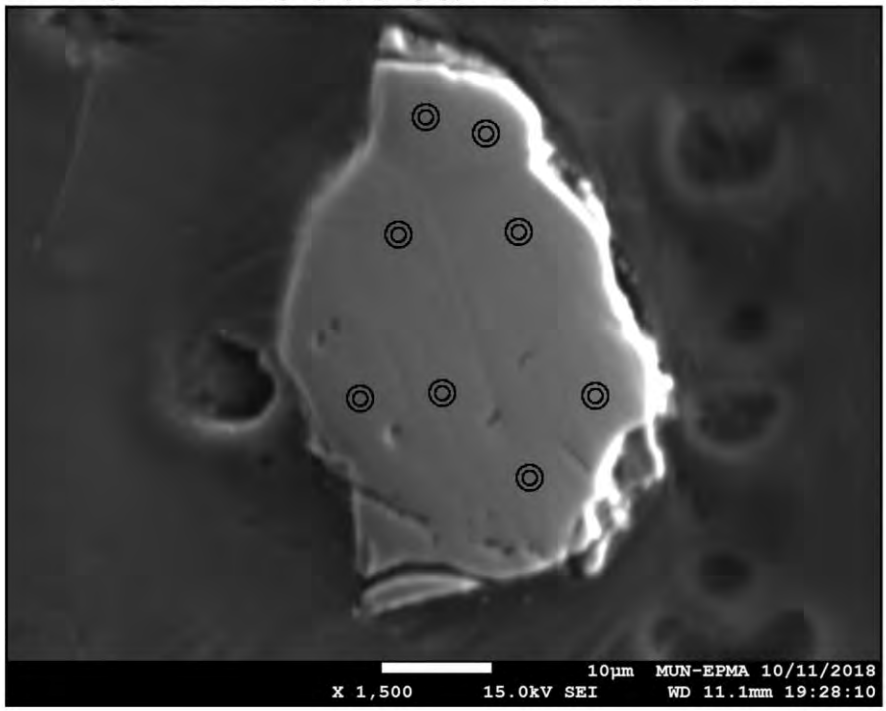

MAJOR ELEMENT X-RAY MAPS

Al — 10 um

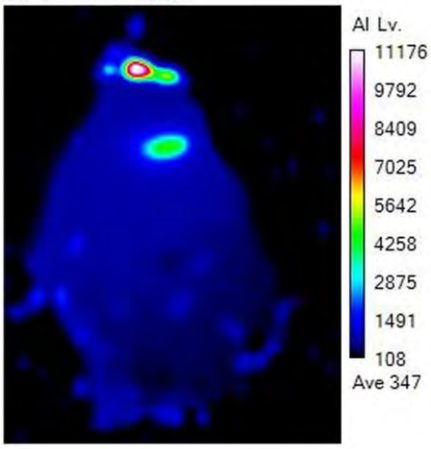

Cr — 10 um

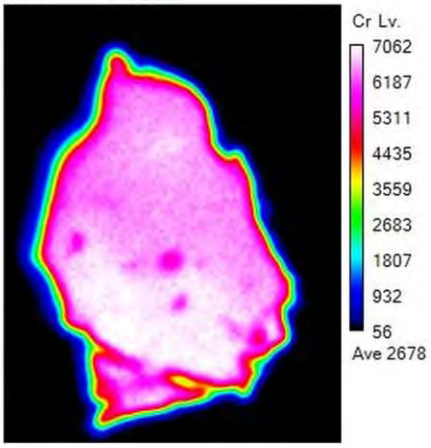

Fe — 10 um

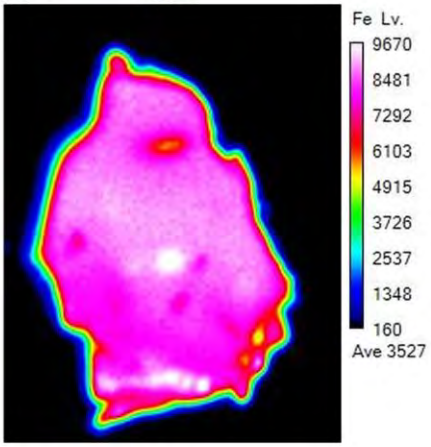

Mg — 10 um

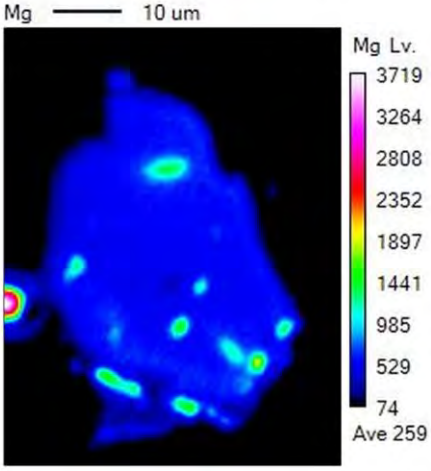

MINOR ELEMENT X-RAY MAPS

Ti — 10 um

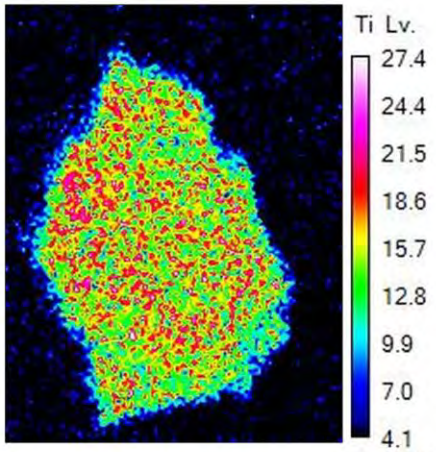

17HSB-4 Grain #31

MAJOR ELEMENT X-RAY MAPS

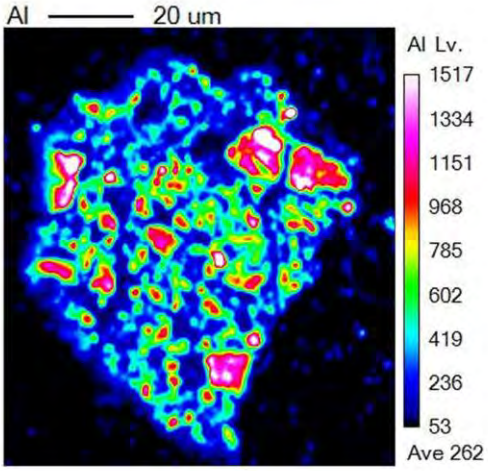

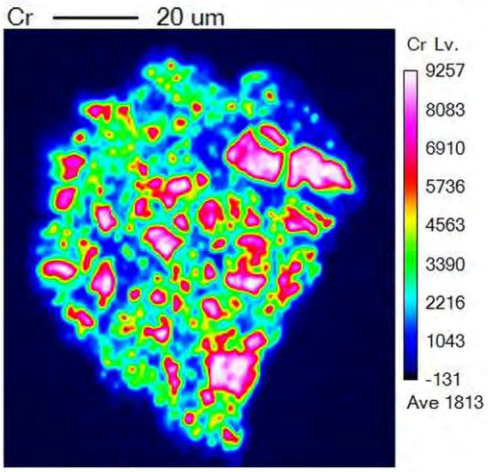

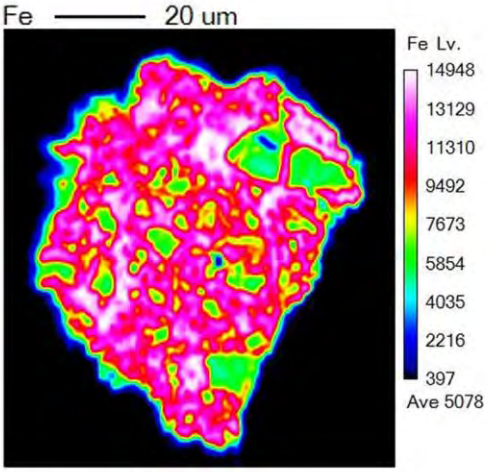

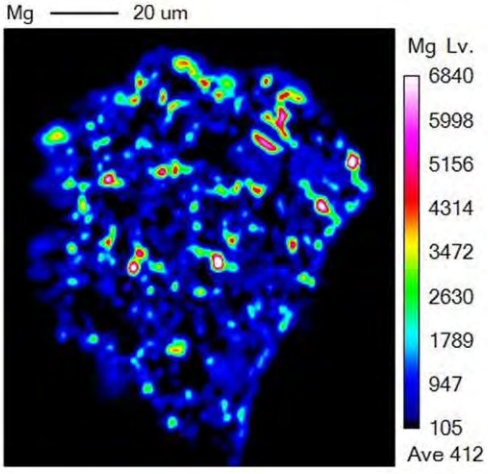

Backscatter electron image of compositional variations

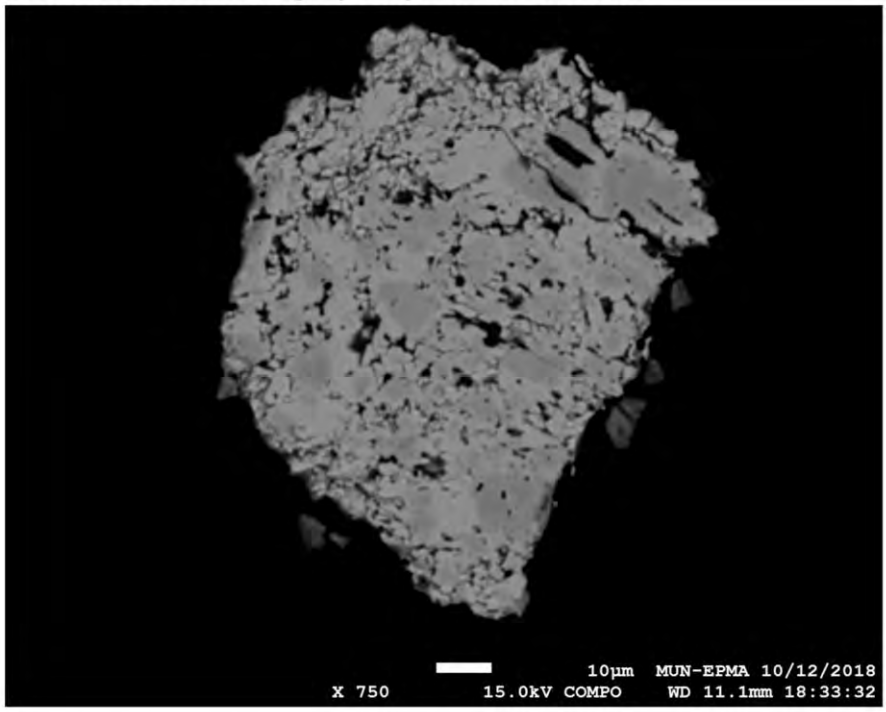

Secondary electron image (topography) with spot analyses positions

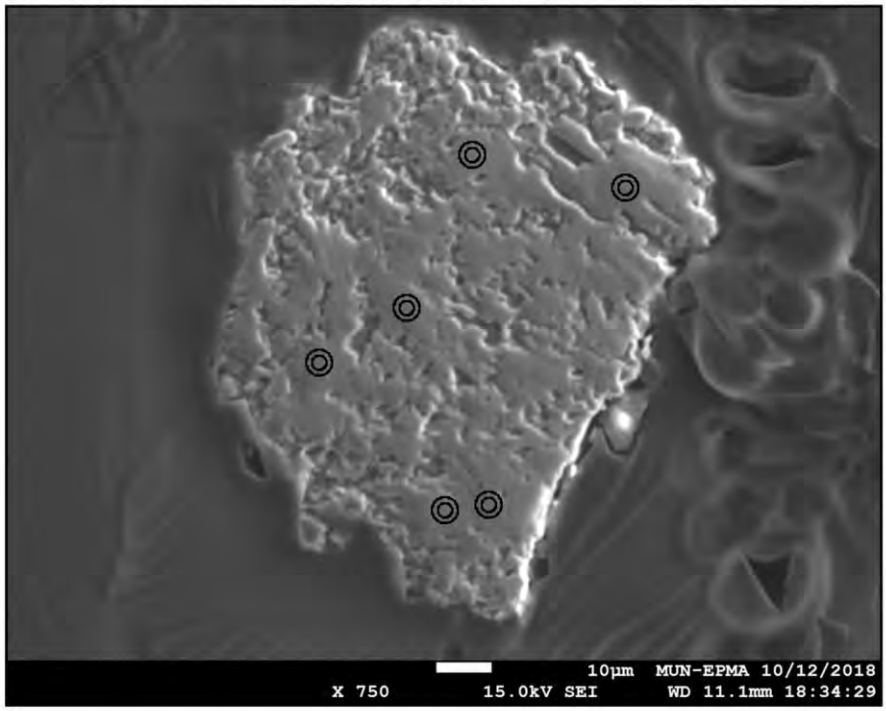

MINOR ELEMENT X-RAY MAPS

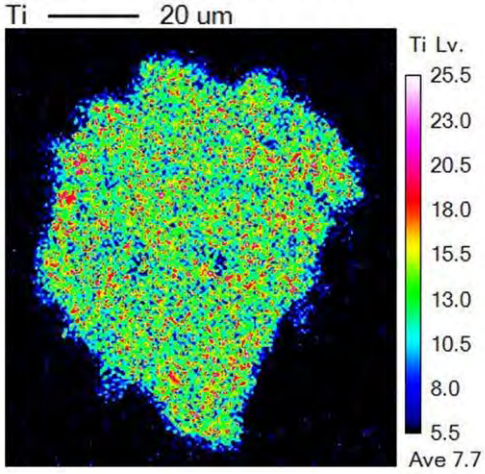

17HSB-4 Grain #36

Backscatter electron image of compositional variations

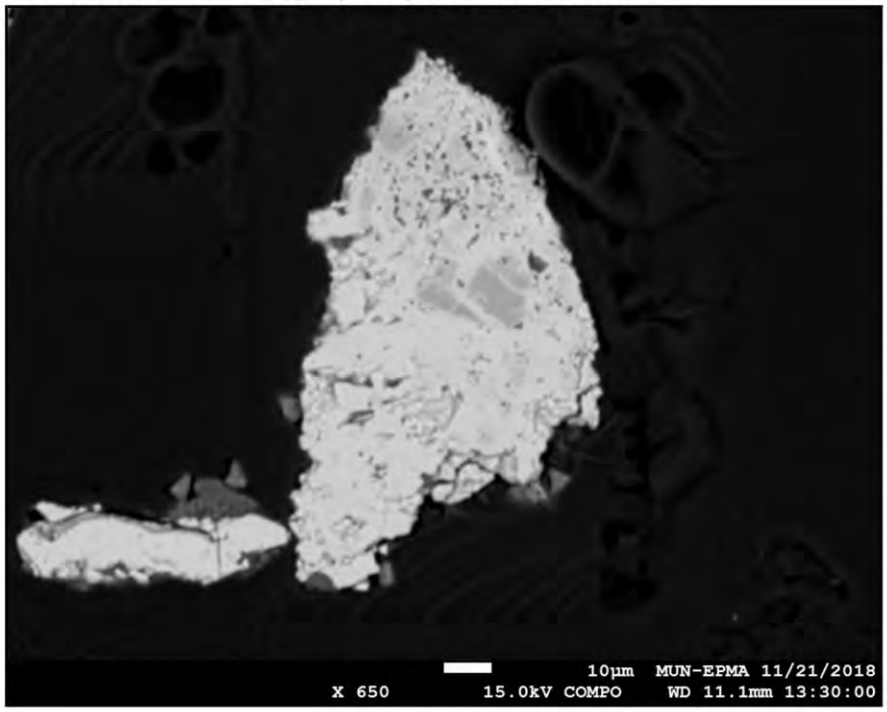

Secondary electron image (topography) with spot analyses positions

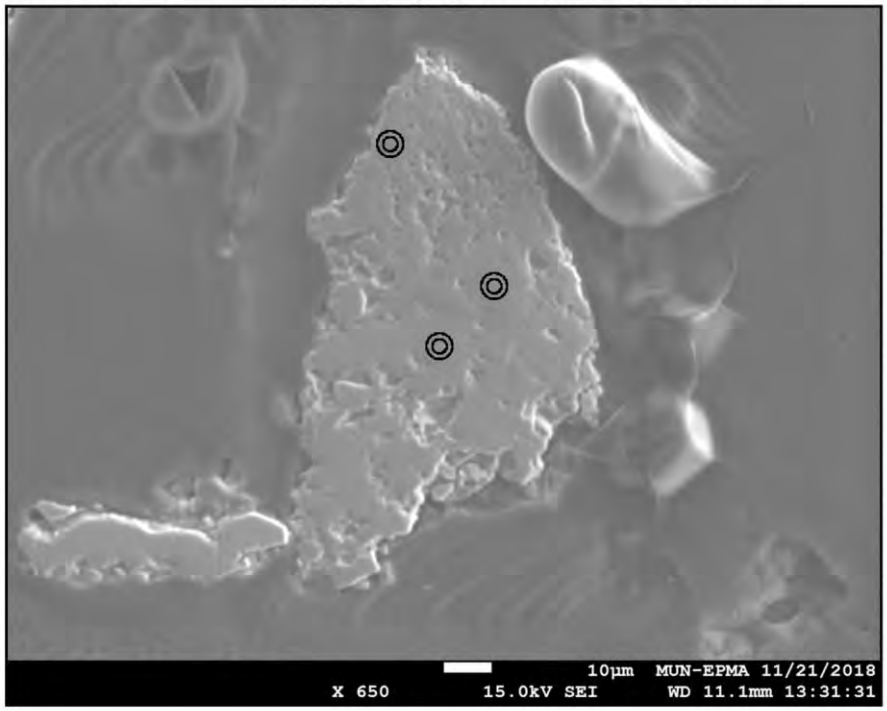

MAJOR ELEMENT X-RAY MAPS

Al ——— 20 um

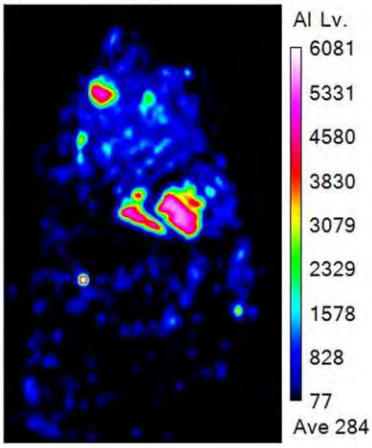

Cr ——— 20 um

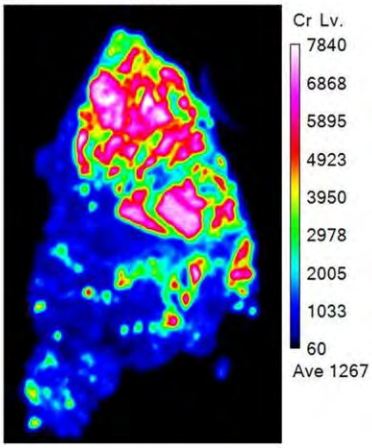

Fe ——— 20 um

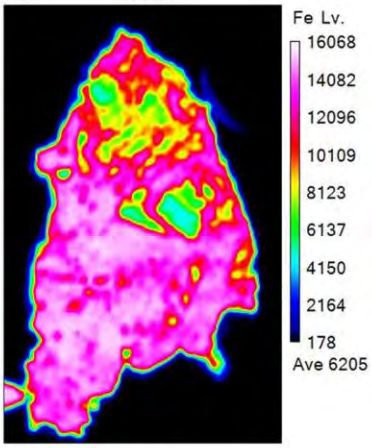

Mg ——— 20 um

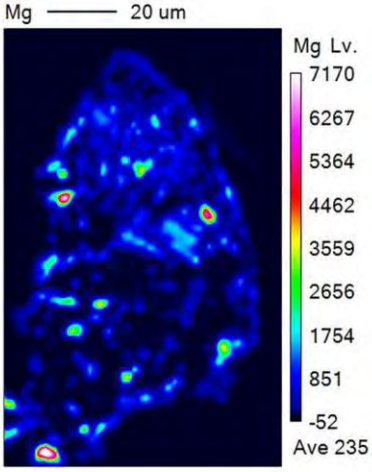

MINOR ELEMENT X-RAY MAPS

Ti ——— 20 um

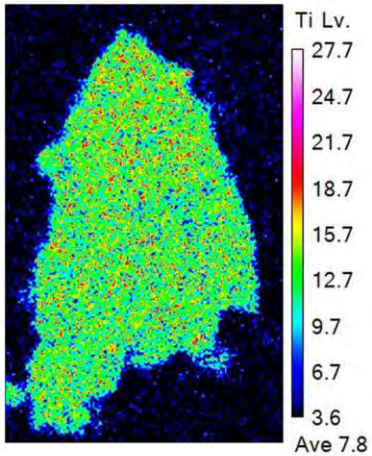

VP17-01 Grain #1

MAJOR ELEMENT X-RAY MAPS

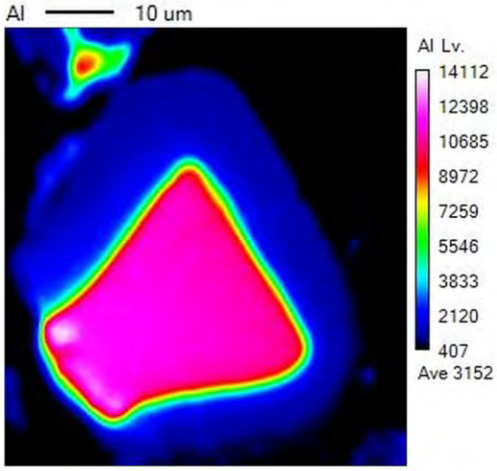

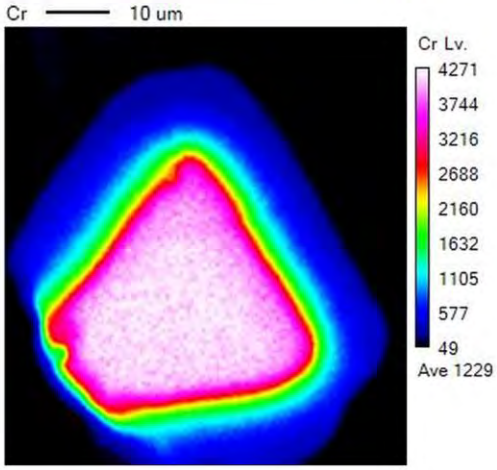

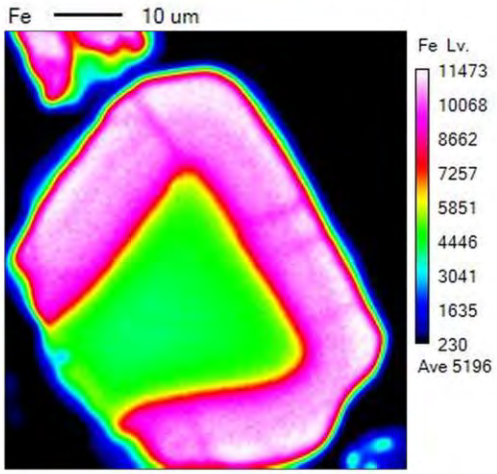

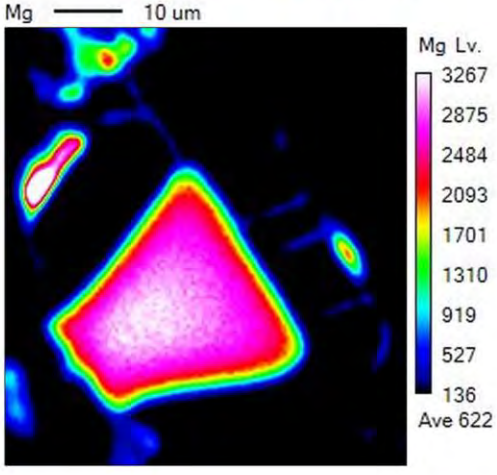

Backscatter electron image of compositional variations

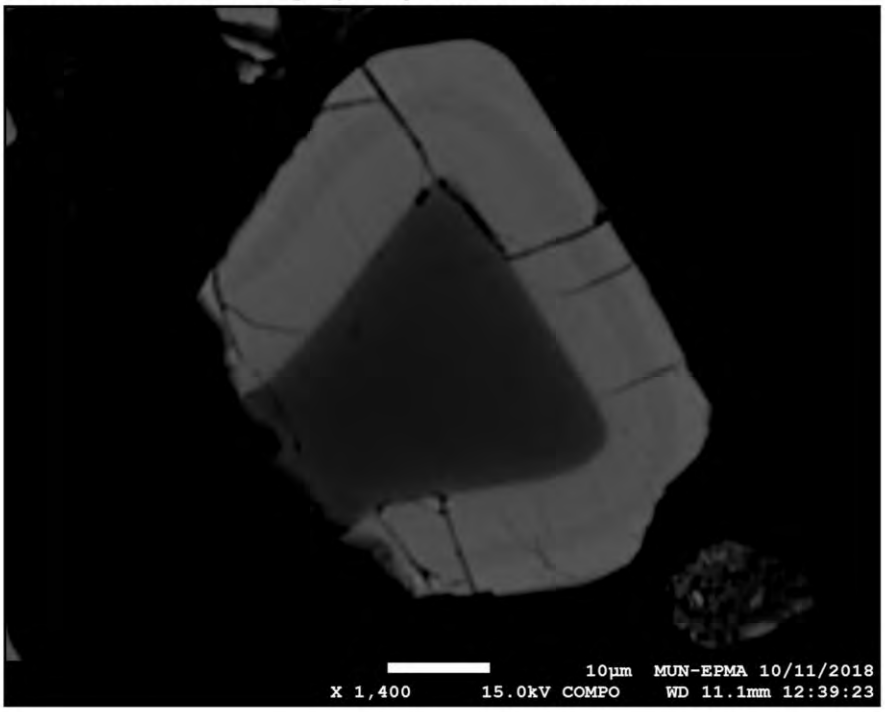

Secondary electron image (topography) with spot analyses positions

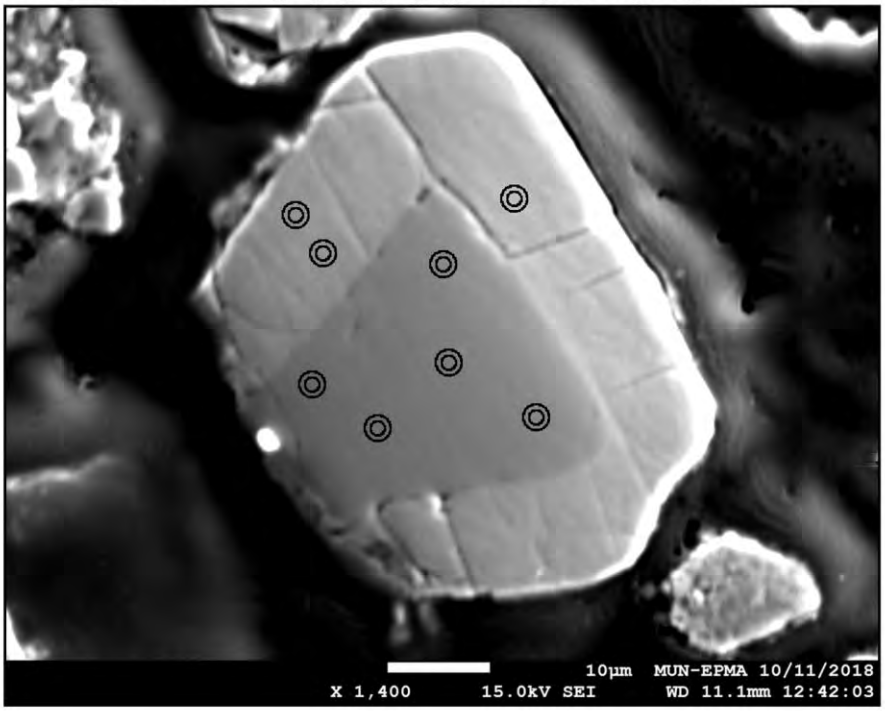

MINOR ELEMENT X-RAY MAPS

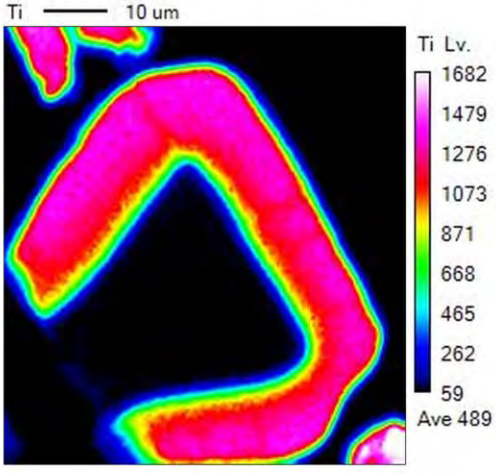

VP17-04b Grain #1

Backscatter electron image of compositional variations

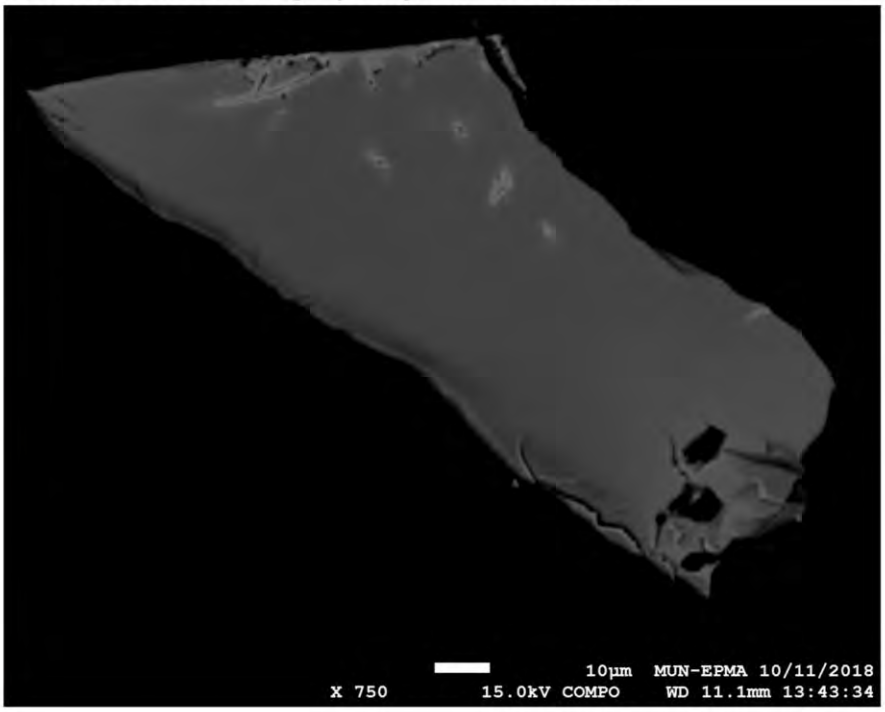

Secondary electron image (topography) with spot analyses positions

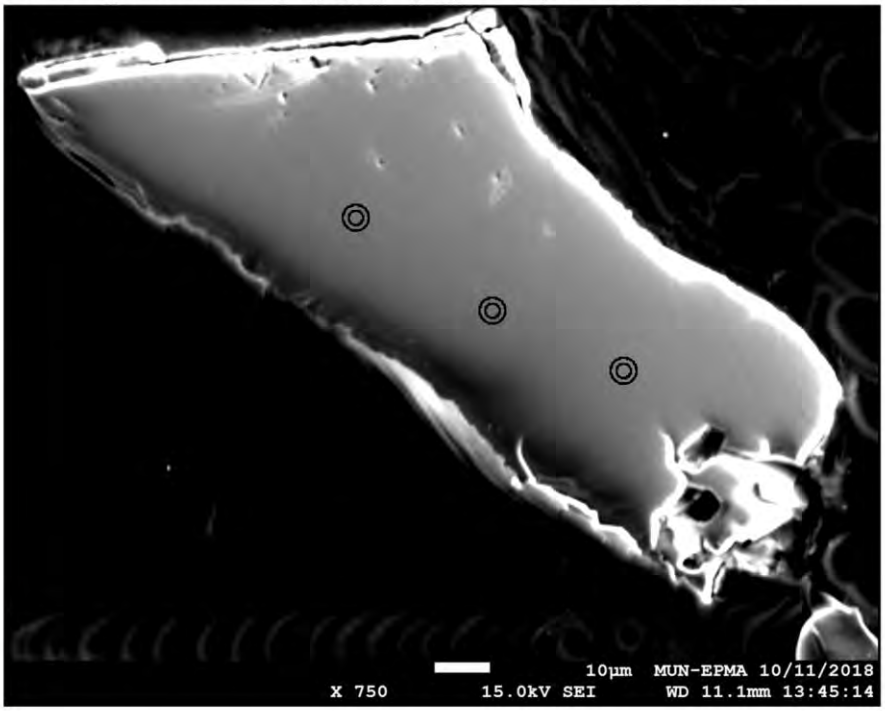

MAJOR ELEMENT X-RAY MAPS

Al ——— 20 um

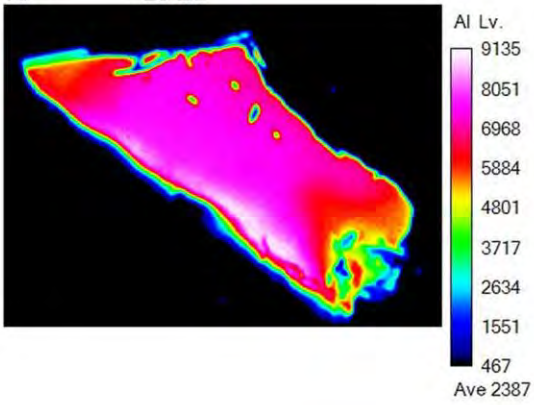

Cr ——— 20 um

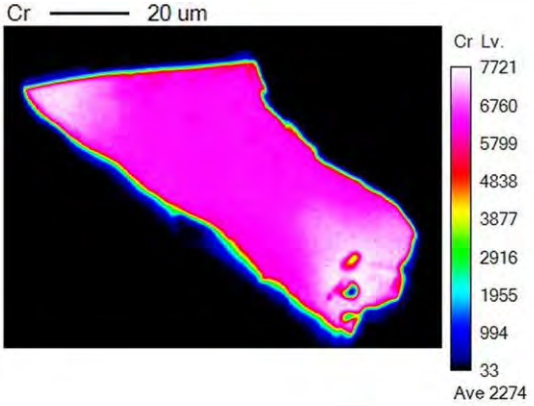

Fe ——— 20 um

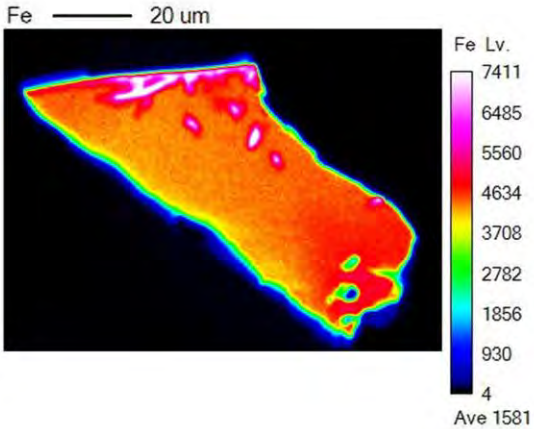

MINOR ELEMENT X-RAY MAPS

Mg ——— 20 um

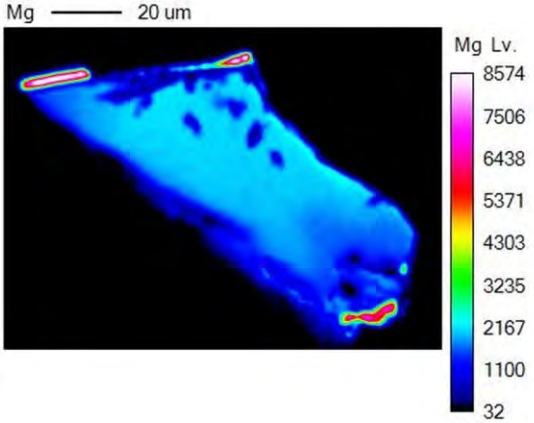

Ti ——— 20 um

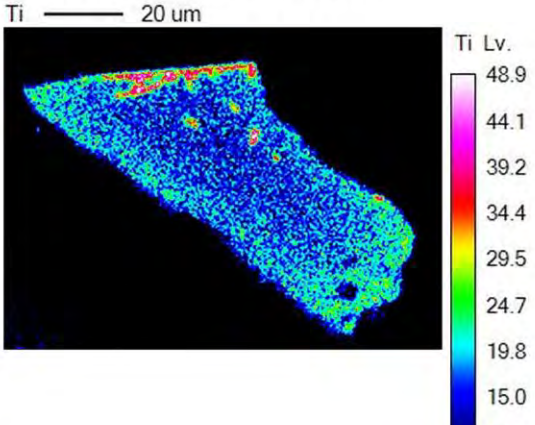

VP17-04b Grain #2

Backscatter electron image of compositional variations

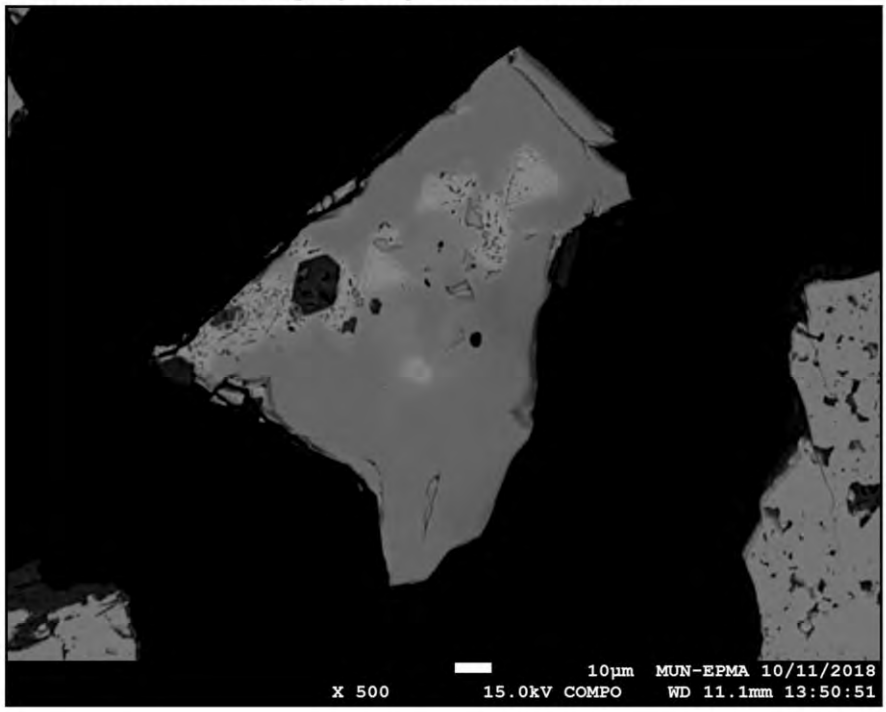

Secondary electron image (topography) with spot analyses positions

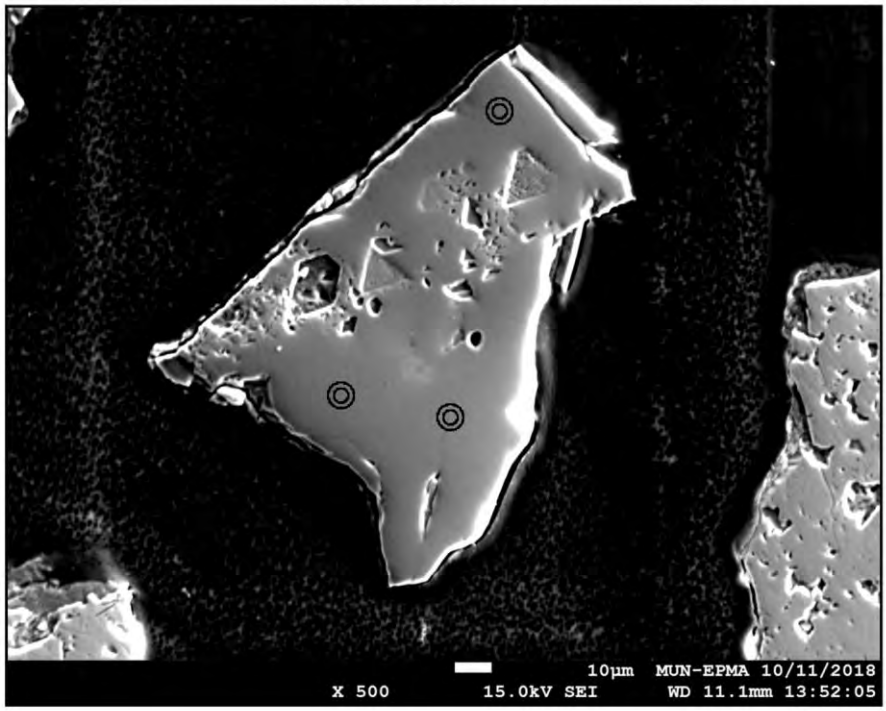

MAJOR ELEMENT X-RAY MAPS

Al —— 20 um

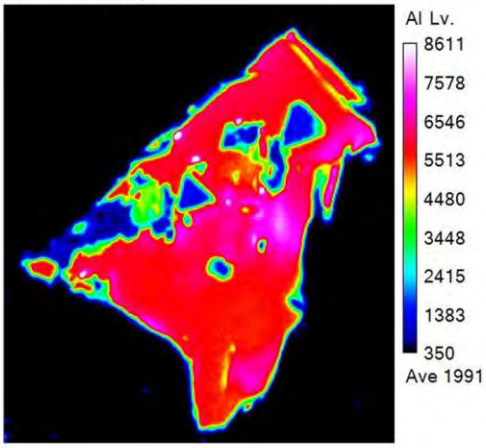

Cr —— 20 um

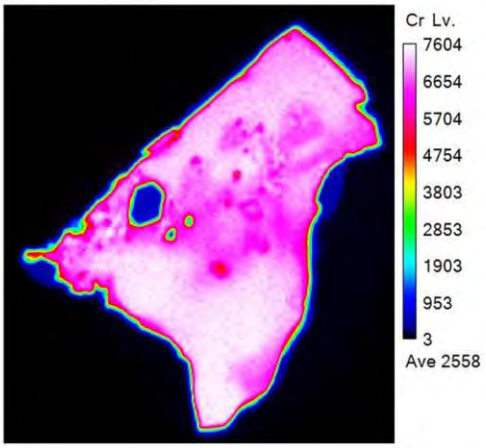

Fe —— 20 um

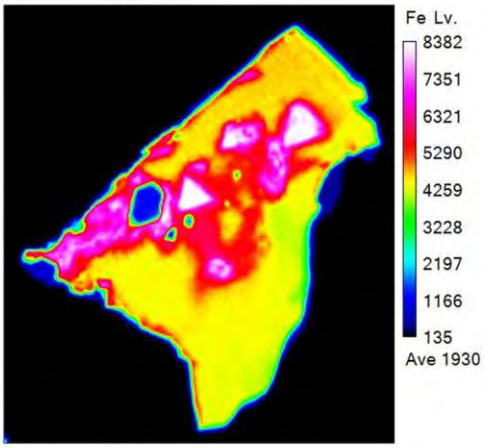

Mg —— 20 um

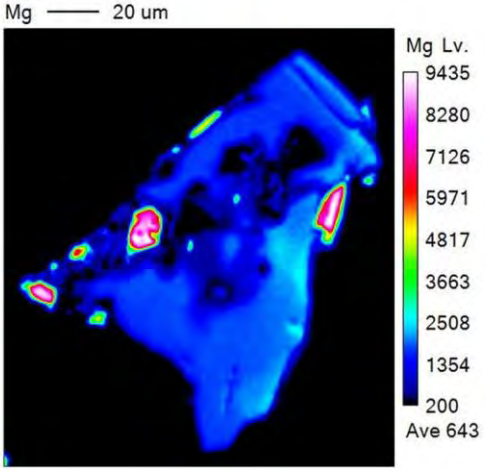

MINOR ELEMENT X-RAY MAPS

Ti —— 20 um

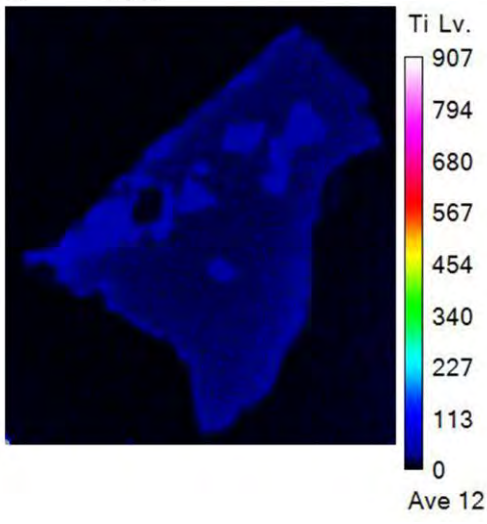

VP17-05b Grain #1

Backscatter electron image of compositional variations

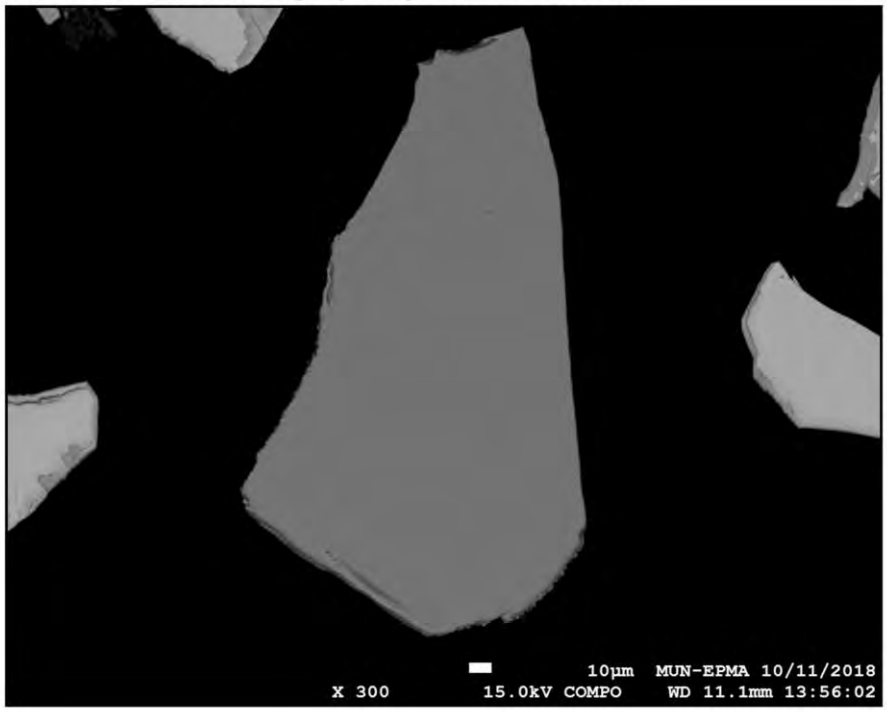

Secondary electron image (topography) with spot analyses positions

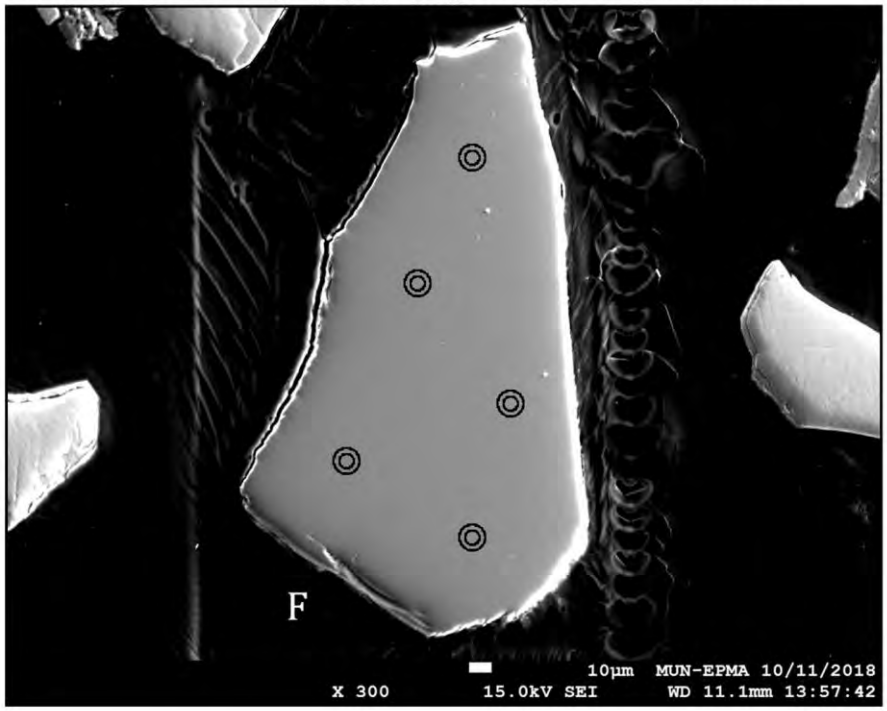

MAJOR ELEMENT X-RAY MAPS

Al ——— 50 um

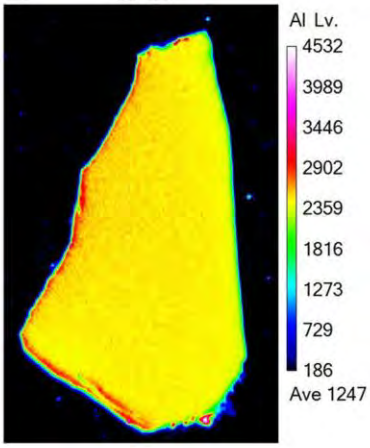

Cr ——— 50 um

Fe ——— 50 um

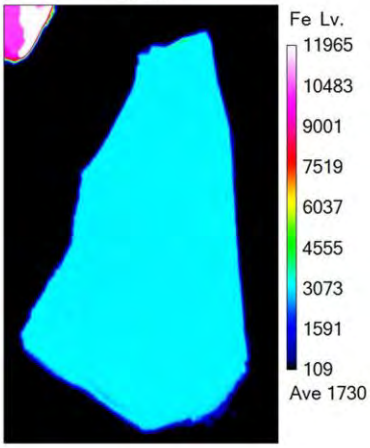

Mg ——— 50 um

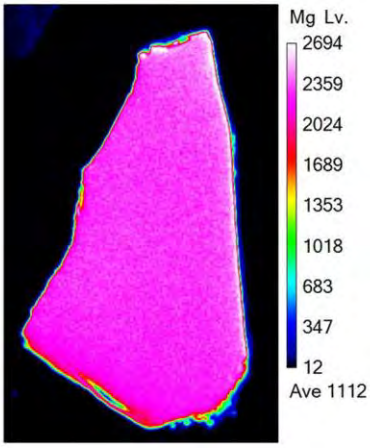

MINOR ELEMENT X-RAY MAPS

Ti ——— 50 um

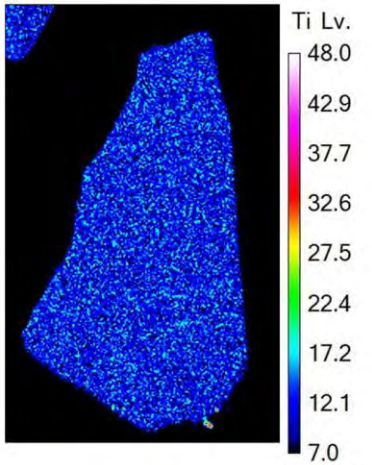

VP17-15 Grain #3

Backscatter electron image of compositional variations

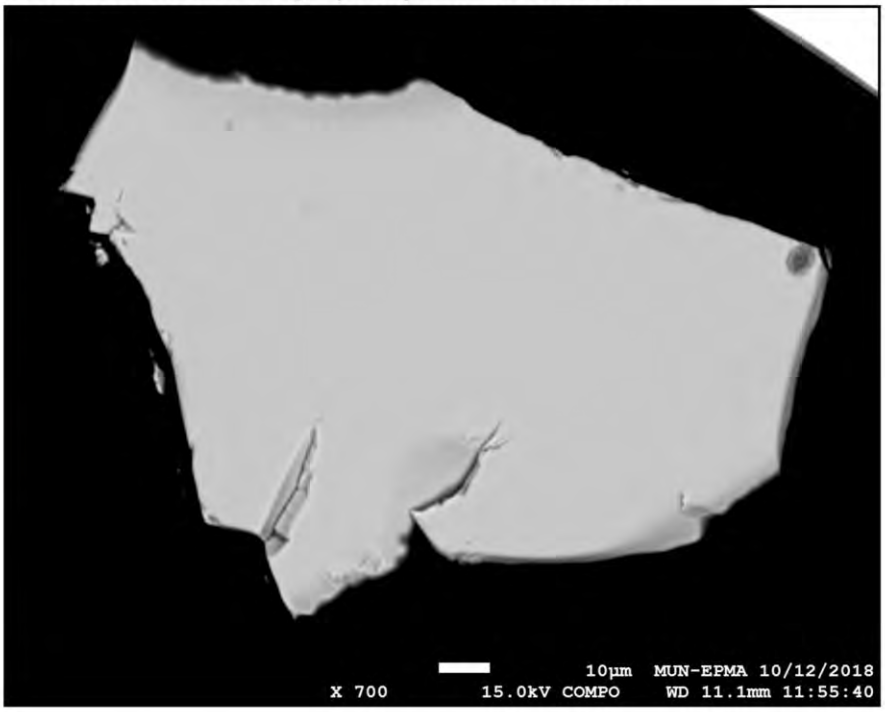

MAJOR ELEMENT X-RAY MAPS

Al —— 20 um

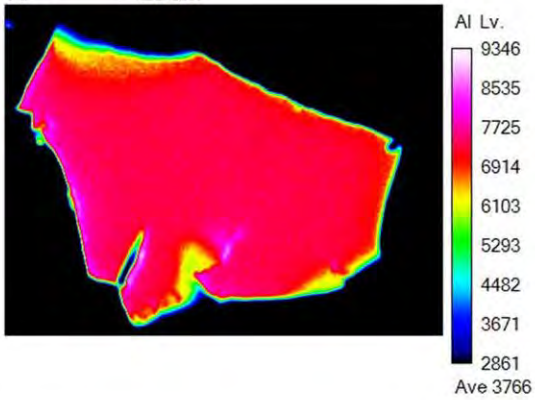

Cr —— 20 um

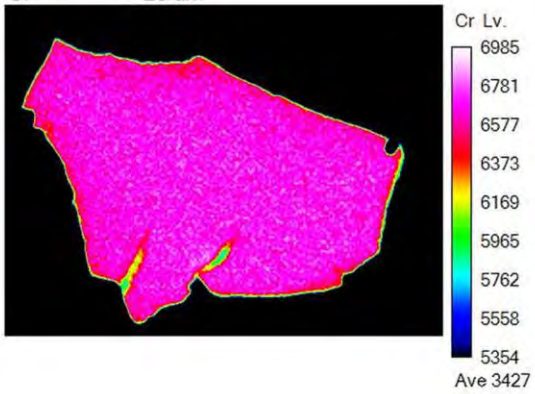

Secondary electron image (topography) with spot analyses positions

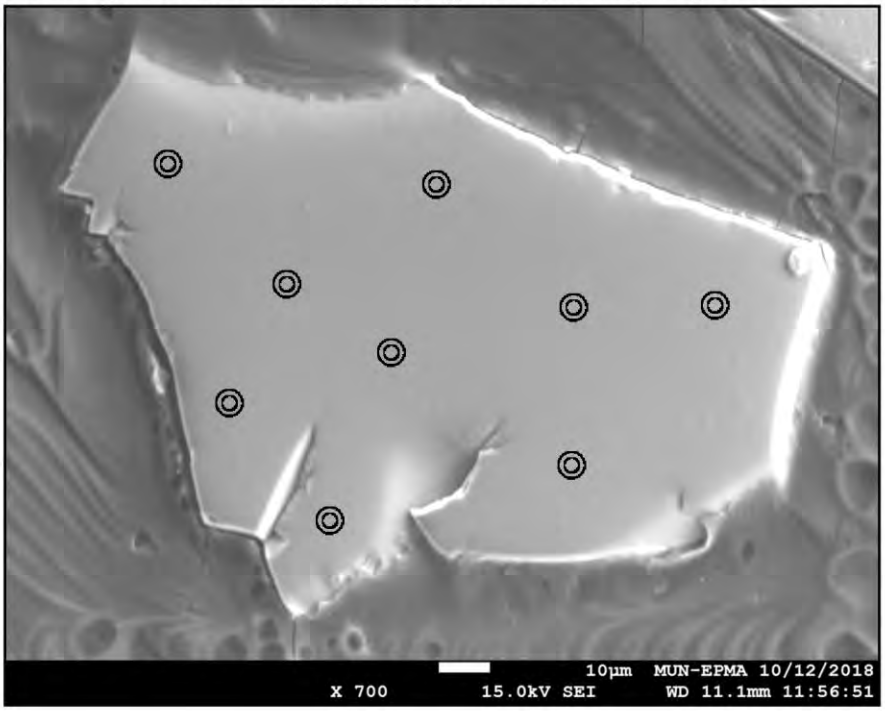

Fe —— 20 um

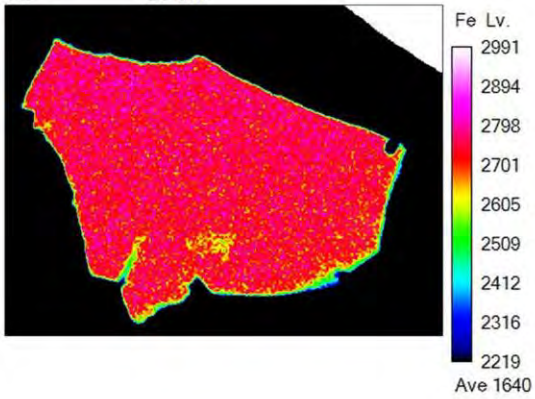

MINOR ELEMENT X-RAY MAPS

Mg —— 20 um

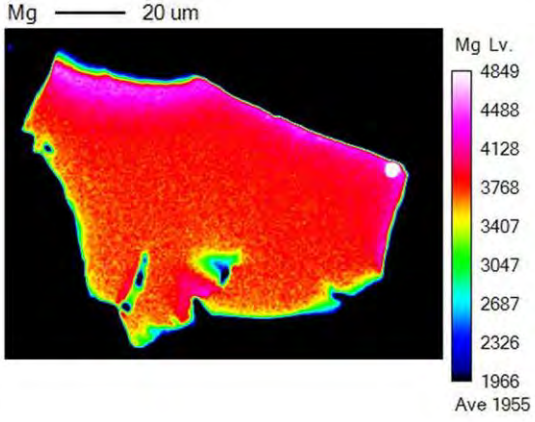

Ti —— 20 um

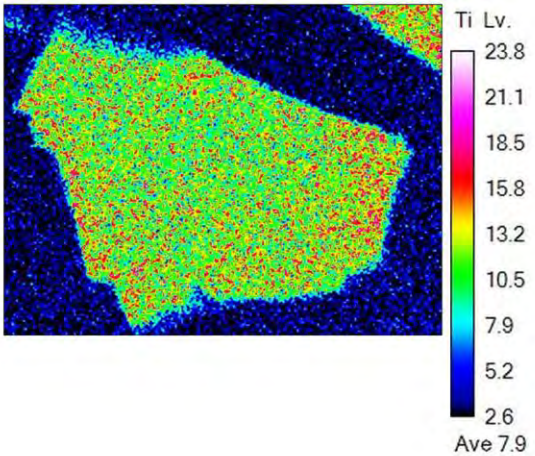

Chemical data of selected grains from electron microprobe analysis																														
		Measured oxide wt.% by electron microprobe analysis											Computed values																	
		major components				*minor components*							*oxide wt.% by EMG 8.0*			*cations per 4 oxygen atoms by EMG 8.0*													
Sample ID Grain no.	**Point**	**Al_2O_3**	**MgO**	**FeO_T**	**Cr_2O_3**	**TiO_2**	**V_2O_3**	**MnO**	**NiO**	**CaO**	**SiO_2**	**Total**	**FeO**	**Fe_2O_3**	**Total**	**Al^{3+}**	**Mg^{2+}**	**Cr^{3+}**	**Ti^{4+}**	**V^{3+}**	**Mn^{2+}**	**Ni^{2+}**	**Ca^{2+}**	**Si^{4+}**	**Fe^{2+}**	**Fe^{3+}**	**Fe^{2+}/Fe^{3+}**	**Y_{Fe3+}**	***cr#***	***mg#***
17HSB-3																														
#16																														
	1	22.71	7.63	23.23	43.65	0.02	0.20	0.43	0.03	0.00	0.01	97.92	22.89	0.39	97.96	0.867	0.368	1.117	-	0.005	0.012	0.001	-	-	0.620	0.009	68.889	0.005	0.563	0.372
	2	24.23	8.30	22.76	43.88	bdl	0.20	0.42	0.03	0.00	bdl	99.83	22.70	0.07	99.84	0.900	0.390	1.093	-	0.005	0.011	0.001	-	-	0.598	0.002	299.000	0.001	0.548	0.395
	3	25.46	8.82	22.38	43.59	0.03	0.22	0.42	0.05	bdl	0.02	100.99	22.39	0.00	100.99	0.928	0.407	1.066	0.001	0.006	0.011	0.001	-	0.001	0.579	-	-	0.000	0.535	0.413
#17																														
ferritchromite	*1*	0.95	2.47	48.17	41.97	0.07	0.19	1.97	0.20	0.01	0.01	96.02	25.50	25.20	98.54	0.042	0.138	1.239	0.002	0.006	0.062	0.006	-	-	0.796	0.708	1.124	0.356	0.967	0.148
ferritchromite	*2*	1.11	2.25	52.20	38.83	0.07	0.21	0.78	0.25	0.00	bdl	95.72	26.94	28.07	98.53	0.049	0.126	1.150	0.002	0.006	0.025	0.008	-	-	0.844	0.791	1.067	0.397	0.959	0.130
17HSB-4																														
#31																														
high *cr#* spinel	*3*	2.87	0.93	36.33	56.52	0.04	0.30	0.90	0.04	0.02	0.14	98.09	29.88	7.17	98.81	0.125	0.052	1.654	0.001	0.009	0.028	0.001	0.001	0.005	0.925	0.200	4.625	0.101	0.930	0.053
high *cr#* spinel	*4*	4.38	4.45	29.61	57.87	0.06	0.45	1.43	0.01	0.02	0.04	98.32	24.18	6.04	98.92	0.184	0.237	1.634	0.002	0.013	0.043	-	0.001	0.001	0.722	0.162	4.457	0.082	0.899	0.247
Cr-magnetite	*5*	0.05	bdl	88.05	5.47	bdl	0.03	0.04	0.19	0.01	0.09	93.93	31.09	63.30	100.27	0.002	-	0.166	-	0.001	0.001	0.006	-	0.003	0.996	1.824	0.546	0.916	0.988	0.000
#36																														
Cr-magnetite	*1*	0.01	0.05	88.93	3.50	0.02	0.05	0.03	0.26	bdl	0.03	92.88	30.60	64.83	99.37	-	0.003	0.107	0.001	0.002	0.001	0.008	-	0.001	0.990	1.887	0.525	0.946	1.000	0.003
altered Cr-spinel	*2*	18.64	6.58	26.72	45.98	0.01	0.20	0.85	0.04	0.01	0.03	99.05	23.86	3.18	99.37	0.721	0.322	1.193	-	0.005	0.024	0.001	-	0.001	0.655	0.079	8.291	0.040	0.623	0.330
altered Cr-spinel	*3*	19.05	5.62	28.07	44.13	0.01	0.17	1.04	0.01	0.01	0.03	98.15	24.95	3.47	98.50	0.746	0.279	1.160	-	0.005	0.029	-	-	0.001	0.693	0.087	7.966	0.044	0.609	0.287
VP17-01																														
#1																														
core	*1*	37.93	11.00	24.70	25.97	0.83	0.15	0.30	0.14	0.03	0.09	101.13	22.03	2.96	101.43	1.296	0.475	0.595	0.018	0.003	0.007	0.003	0.001	0.002	0.534	0.065	8.215	0.033	0.315	0.471
core	*2*	38.56	11.82	23.60	26.15	0.75	0.12	0.26	0.16	0.02	0.09	101.53	20.95	2.94	101.83	1.303	0.505	0.593	0.016	0.003	0.006	0.004	0.001	0.002	0.503	0.063	7.984	0.032	0.313	0.501
titanomagnetite rim	*8*	3.77	0.02	62.97	2.62	22.03	0.46	0.41	0.01	0.07	0.08	92.43	49.91	14.51	93.89	0.174	0.001	0.081	0.648	0.014	0.014	-	0.003	0.003	1.634	0.427	3.827	0.626	0.318	0.001
titanomagnetite rim	*9*	7.39	0.01	58.14	9.42	16.72	0.39	1.40	bdl	0.03	0.06	93.55	45.09	14.50	95.00	0.331	0.001	0.283	0.478	0.012	0.045	-	0.001	0.002	1.433	0.415	3.453	0.403	0.461	0.001
VP17-04b																														
#1																														
	1	21.45	6.89	26.73	44.49	0.10	0.34	0.30	0.13	0.00	bdl	100.44	24.76	2.19	100.66	0.809	0.328	1.125	0.002	0.009	0.008	0.003	-	-	0.662	0.053	12.491	0.027	0.582	0.331
	2	25.44	7.90	25.20	41.17	0.09	0.34	0.29	0.11	0.01	0.01	100.56	23.90	1.44	100.70	0.936	0.368	1.017	0.002	0.009	0.008	0.003	-	-	0.624	0.034	18.353	0.017	0.521	0.371
	3	25.94	8.22	24.99	41.08	0.11	0.33	0.30	0.12	0.02	0.02	101.13	23.67	1.46	101.28	0.946	0.379	1.005	0.003	0.008	0.008	0.003	0.001	0.001	0.613	0.034	18.029	0.017	0.515	0.382
VP17-05b																														
#1																														
	1	8.43	9.82	18.26	63.22	0.03	0.15	0.33	0.02	0.00	0.03	100.30	18.20	0.07	100.30	0.330	0.486	1.661	0.001	0.004	0.009	0.001	-	0.001	0.506	0.002	253.000	0.001	0.834	0.490
	2	8.56	9.97	18.21	62.78	0.02	0.15	0.35	0.03	0.00	0.02	100.08	17.88	0.37	100.12	0.335	0.494	1.649	0.001	0.004	0.010	0.001	-	0.001	0.497	0.009	55.222	0.005	0.831	0.498
	3	8.60	10.00	17.96	63.00	0.02	0.15	0.33	0.02	0.01	0.02	100.11	17.85	0.12	100.12	0.337	0.495	1.654	0.001	0.004	0.009	-	-	0.001	0.496	0.003	165.333	0.002	0.831	0.499
VP17-15																														
#3																														
generation X	*1*	25.95	14.75	16.04	43.92	0.05	0.20	0.20	0.15	0.00	0.04	101.30	13.81	2.48	101.55	0.906	0.652	1.029	0.001	0.005	0.005	0.004	-	0.001	0.342	0.055	6.218	0.028	0.532	0.656
generation X	*2*	26.79	15.28	16.03	43.76	0.11	0.23	0.22	0.18	bdl	0.02	102.63	13.54	2.77	102.91	0.920	0.664	1.008	0.002	0.005	0.005	0.004	-	0.001	0.330	0.061	5.410	0.031	0.523	0.668
#4																														
generation Z	*1*	33.27	15.40	16.25	37.03	0.27	0.21	0.19	0.15	0.01	0.04	102.81	14.62	1.80	102.99	1.113	0.651	0.831	0.006	0.005	0.005	0.003	-	0.001	0.347	0.038	9.132	0.019	0.427	0.652
generation Z	*2*	32.53	15.09	16.30	37.15	0.31	0.23	0.20	0.16	bdl	0.02	102.00	14.74	1.73	102.17	1.100	0.645	0.843	0.007	0.005	0.005	0.004	-	0.001	0.354	0.037	9.568	0.019	0.434	0.646
#6																														
generation Y	*1*	31.99	15.74	15.02	39.17	0.07	0.17	0.21	0.20	bdl	0.02	102.59	13.57	1.61	102.75	1.075	0.669	0.883	0.001	0.004	0.005	0.005	-	0.001	0.324	0.035	9.257	0.018	0.451	0.674
generation Y	*2*	31.84	15.61	14.79	39.36	0.06	0.21	0.21	0.19	bdl	0.02	102.29	13.66	1.26	102.41	1.074	0.666	0.890	0.001	0.005	0.005	0.004	-	0.001	0.327	0.027	12.111	0.014	0.453	0.671

Table 2 Chemical data of selected grains from each sample obtained from electron microprobe analysis, computed chemical values by End-Member Generator 8.0 and derivates. An extended version is available in Appendix B3.

[T] generated value by electron microprobe software assuming 100% FeO

End-Member Generator (EMG 8.0) assumes ideal stoichiometry: A_3O_4

cr# = $Cr^{3+}/Cr^{3+} + Al^{3+}$ a.p.f

mg# = $Mg^{2+}/Mg^{2+} + Fe^{2+}$ a.p.f

bdl = below detection limit

Graphical representation of analytical data

The six samples have been categorized into data groups based on potential common denominators in terms of their igneous and metamorphic histories (Table 3). These groups are treated separately in terms of compatible discrimination fields in most plots. Due to certain ambiguities regarding the nature of the spinel occurrences in the two West-central belt samples (VP17-05b and VP17-15), these make up their own data group, group A, in addition to being members of group B.

Table 3 Compositional groups from shared igneous and metamorphic history.

Group A: *Unaltered, volcanic spinel*	**Group B:** *Unaltered, plutonic spinel*	**Group C:** *Altered (?), plutonic spinels*
West-central belt (*OSv*) volcanic fragment: V*P17-05b* West-central belt (*OSv*) pillow lava: *VP17-15 (generations X, Y, Z)*	Kulutingwak Formation (*OK1*): *VP17-04b* West-central belt (*OSv*) volcanic fragment: V*P17-05b* West-central belt (*OSv*) pillow lava: *VP17-15 (generations X, Y, Z)* Kleybolte Fault Zone (*ds*) schist: *17HSB-3 (grain #16)*	Kulutingwak Inlier intrusion (*{sqc}*): *VP17-01* Kleybolte Fault Zone(*ds*) serpentinized dunite: *17HSB-4*

Alteration state. The minor element Mn can be used as a corroborating discriminant of primary and secondary/altered compositions in Cr-spinel. There is an antithetic variation between MnO (wt.%) and *mg#* in unaltered Cr-spinel from sub-amphibolite facies terrains owing to equilibration with surrounding olivine (Barnes, 1998) since Mn^{2+} may substitute for Mg^{2+} under metamorphic conditions. Barnes (1998) used a 'filter line' to discriminate between unaltered and weakly altered Cr-spinels from greenschist facies volcanic rocks, defined by the upper boundary of the area outlining the densest 80% of the data points in their extensive dataset. Analogously, Khedr and Arai (2017) compared MnO in relation to *cr#* in spinels from plutonic rocks and defined discrimination fields from a dataset consisting of primary and altered Cr-spinel in chromitite and serpentinite. The relative proportions of the trivalent B-site cations Cr^{3+}, Al^{3}+ and Fe^{3+} can be used to infer the metamorphic grade as aid when assessing the alteration state of spinels. The relative proportions of these trivalent end-members are not greatly modified by metamorphism up to lower amphibolite facies (Barnes, 2000).

The MnO component of the Cr-spinels in all samples but the serpentinized dunite from the Kleybolte Fault Zone indicate primary compositions (Plot 1a-b). However, elevated Mn concentrations in Cr-spinel are unlikely in the presence of carbonate (Barnes, 2000) and carbonate was present in the mineral assemblages of the Kulutingwak Inlier intrusion and both West-central belt samples (see Petrography), potentially making the Mn discriminant unreliable for these three samples.

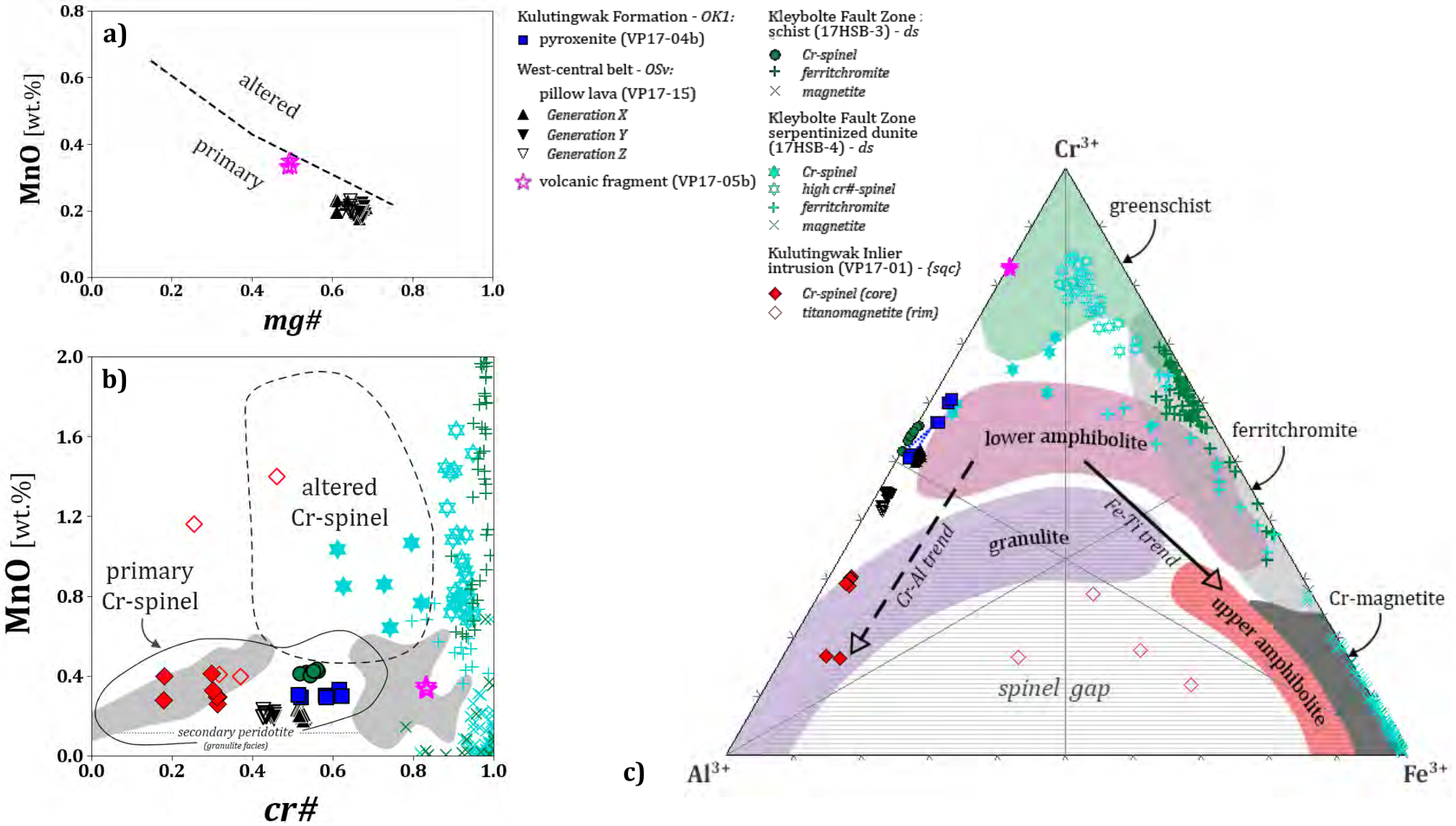

Plot 1 a. MnO versus *mg#*. For volcanic Cr-spinels. Filter line (dashed) from Barnes (1998). **b.** MnO versus *cr#*. For plutonic Cr-spinels. Fields for primary and altered Cr-spinel from Khedr and Arai (2017); Chilas Complex secondary peridotite (granulite facies) from Jagoutz et al. (2007). **c.** Cr^{3+}-Al^{3+}-Fe^{3+} ternary plot with metamorphic end-member fields. Fields for Cr-magnetite, greenschist, lower and upper amphibolite and granulite facies from Evans and Frost (1976) and Suita and Strieder (1996) as cited by González-Jiménez et al. (2009); ferritchromite from Habtoor et al. (2017); spinel gap and trend arrows from Barnes and Roeder (2001). Note the gap that divides the secondary peridotite field in b. where 3/6 samples plot.

While the compositions of the Kulutingwak Inlier intrusion and the West-central belt volcanic fragment plot inside the primary Cr-spinel field by Khedr and Arai (2017), the data also conforms with the secondary peridotite field defined by granulite facies rocks from the Chilas Complex (Plot 1b). The ternary plot supports granulite facies for the intrusion but no field observations of such a high metamorphic grade corroborate the notion. Unlike the intrusion, the volcanic fragment is not associated with the granulite facies field and the pillow lava spinels are not associated with any metamorphic field (Plot 1c). The Kulutingwak Formation pyroxenite spinels tentatively implicate lower amphibolite metamorphism in Plot 1c, which is supported by the mineral assemblage in thin section (see Petrography). Note that grain #2 compositions (represented by the three blue squares that are *not* connected by the blue line) plot closer to the lower amphibolite field than grain #1. Inferred from the MnO content and relative proportions of Cr^{3+}, Al^{3+} and Fe^{3+}, the Cr-spinels in data group B (group A is a subset of group B) are sufficiently unaltered to be used as tectonic indicators, though caution should be taken with the pyroxenite from the Kulutingwak Formation.

The rims compositions of the intrusion grains in Plot 1c (open diamonds) plot inside the so-called spinel gap, defined by a statistical region of low data density observed in terrestrial spinel compositions (e.g. Barnes and Roeder, 2001) because of their high concentrations of Ti. By using the ternary diagram from the ulvöspinel prism, the rims classify as titanomagnetite (Plot 2).

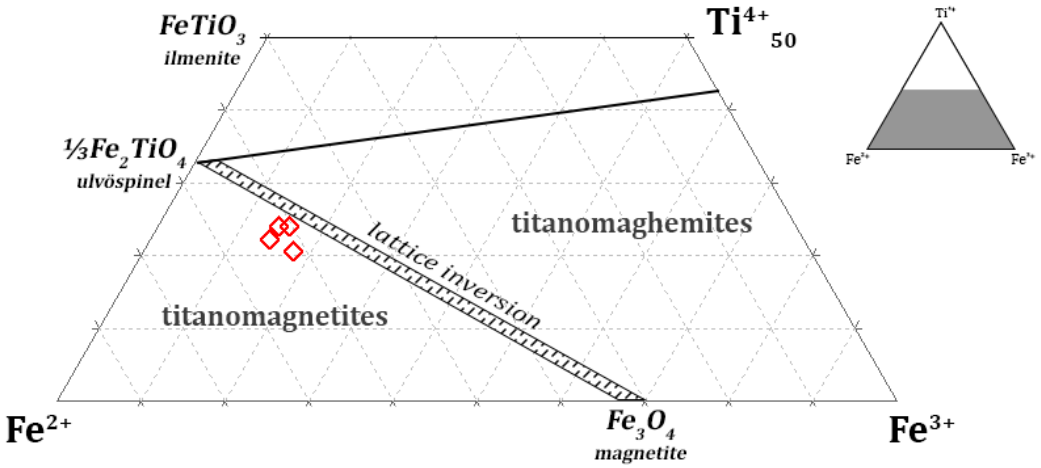

Plot 2 Ti^{4+}-Fe^{2+}-Fe^{3+} ternary plot from the ulvöspinel compositional prism. Modified from O'Reilley (1984). Open diamonds (red) = titanomagnetite rims from the Kulutingwak Inlier intrusion (VP17-01).

Igneous mode. Kamenetsky et al. (2001) used a large dataset of spinel analyses from a number of well-constrained tectonic settings to define tectonic discrimination fields and found that the Fe^{2+}/Fe^{3+} ratio in unaltered Cr-spinel was a useful discriminant for distinguishing between extrusive/volcanic and intrusive/plutonic modes of the host. In their dataset, plutonic spinels statistically had higher Fe^{2+}/Fe^{3+} ratios than volcanic spinels for the same proportions of the Al_2O_3 component. This discrepancy suggests the igneous mode must be determined to accurately

interpret tectonic setting from spinel chemistry. Furthermore, Kamenetsky et al. (2001) found that the Fe^{2+}/Fe^{3+} ratio in relation to Al_2O_3 was a useful discriminant of geochemical signatures of spinel from plutonic rocks associated with supra-subduction zones (SSZ) contra mid-ocean ridges. Generally speaking, the Fe^{2+}/Fe^{3+} ratios are higher and the Al_2O_3 proportions lower for SSZ-type peridotites than for MORB-type peridotites and for their volcanic equivalents, the Fe^{2+}/Fe^{3+} ratios are much lower because these tend to be much more oxidized (Plot 3a-c). However, the high Fe^{2+}/Fe^{3+} ratios of SSZ-peridotite spinels are most likely not a reflection of the melt oxidation state but the result of non-stoichiometry (see Kamperman, Danyushevsky, Taylor & Jablonski, 1996). Kamperman et al. (1996) found that the Fe^{2+}/Fe^{3+} ratios calculated assuming perfect stoichiometry in Cr-spinel from primitive subduction zone melts often extend to abnormally high values, which contradict the very nature of subduction zone petrogenesis as that would indicate highly reduced crystallization conditions. Thus, though the remarkably high Fe^{2+}/Fe^{3+} ratios exhibited by the Cr-spinels from the volcanic fragment in the West-central belt and the Kleybolte Fault Zone schist might indicate considerably less oxidized conditions than those expected in a volcanic source (Plot 3a-c), it is likely that this is the result of nonstoichiometry and not related to the oxidation state. Apparent highly reduced conditions have been found in rocks from arc regimes, like Conical Seamount close to the bow-shaped Mariana Trench in the forearc of the Izu-Bonin-Mariana arc system (Plot 3b). These rocks are actively being metasomatized by dense, high pH fluids derived from dehydration of the slab in the subduction zone (Parkinson & Pearce, 1998). SSZ-associated serpentinized peridotite in the East African Orogen (West Ethiopian Shield and Arabian-Nubian Shield) have also produced similarly high Fe^{2+}/Fe^{3+} ratios fields (Plot 3c).

Based on the high Fe^{2+}/Fe^{3+} ratios, the group A spinels should only be interpreted as potentially volcanic if it is in association with SSZ-type volcanism. The strong cryptic zoning in the pillow lava spinels from the West-central belt indicate that their source is indeed volcanic, as slower subsolidus cooling rates otherwise tend to mitigate chemical zoning (see Barnes & Roeder, 2001; Arai et al., 2011). The petrographical occurrence of the spinel in the West-central belt volcanic fragment suggests that it is likely a xenocryst and from the Fe^{2+}/Fe^{3+} ratios, the source appears to be plutonic.

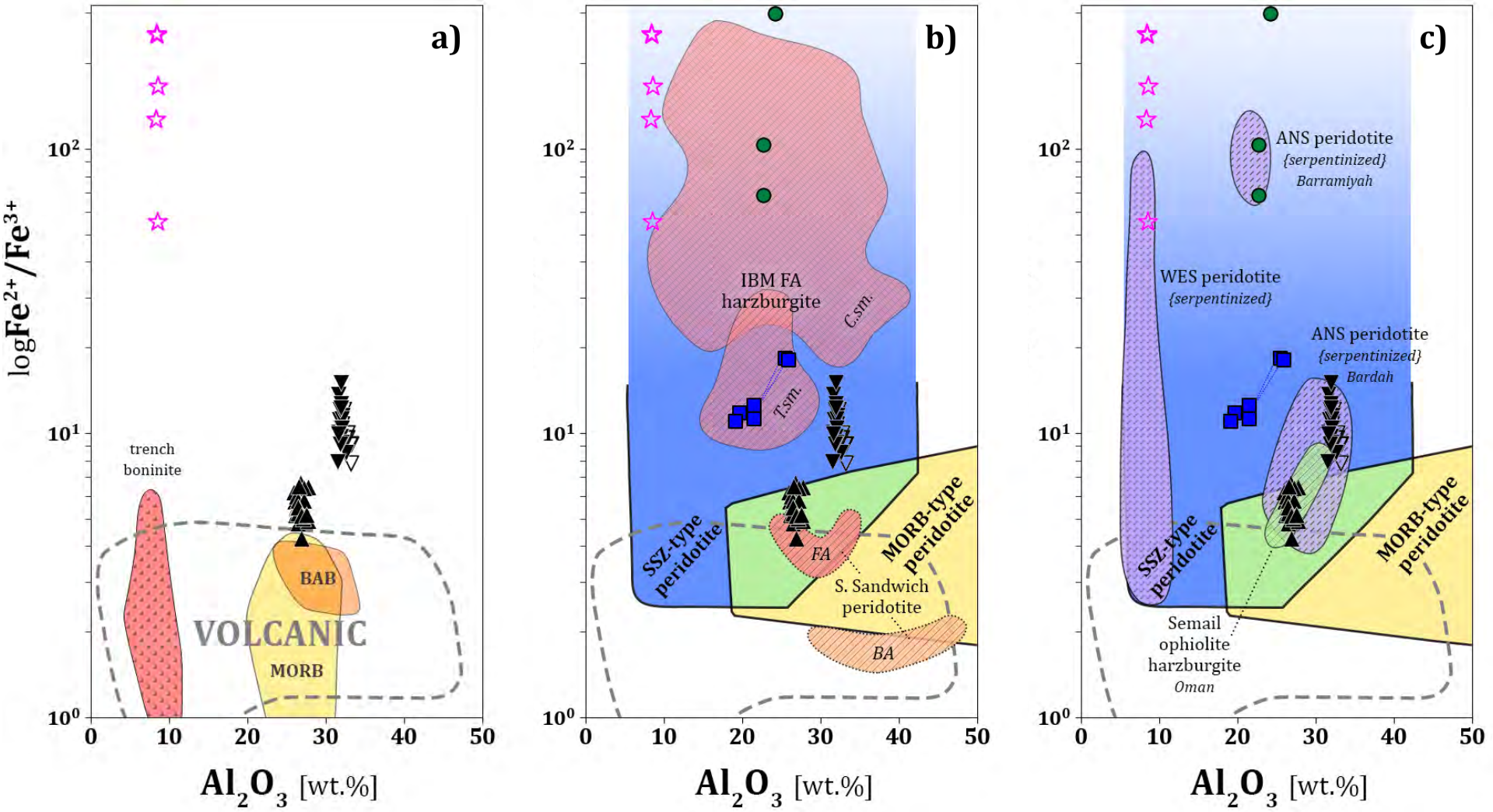

Plot 3 Fe^{2+}/Fe^{3+} versus Al_2O_3. Fields for **a.** volcanic spinel - dashed outline from Kamenetsky et al. (2001); Mid-Atlantic Ridge basalt (= MORB) from Sigurdsson and Schilling (1976) and Dick and Bryan (1978); Philippine Sea back-arc basin (= BAB) from Mattey et al. (1981); Tonga and Mariana trenches boninite from Sobolev and Danyushevsky (1993) and Bloomer and Hawkins (1987) respectively. **b.** volcanic spinel - dashed out line, SSZ- and MORB-type peridotites from Kamenetsky et al. (2001); Izu-Bonin-Mariana forearc (= IBM FA) harzburgite from Conical Seamount (= C.sm.) and Torishima Seamount (= T.sm.) in the Mariana arc and Izu-Bonin arcs respectively from Ishii et al. (1992); South Sandwich arc system (= S. Sandwich) forearc (= FA) and back-arc (= BA) peridotite from Pearce et al. (2000). **c.** Semail ophiolite (Oman) harzburgite from Pallister and Hopson (1981); West Ethiopian Shield (= WES) serpentinized peridotite (East African Orogen) from Blades et al. (2017); Arabian-Nubian Shield (= ANS) serpentinized peridotite (Wadi Al-Barramiyah and Wadi Bardah, northern East African Orogen in Egypt) from Khedr and Arai (2017). Blue dotted line connects data points from grain #1 in Kulutingwak Formation pyroxenite (VP17-04b). Note the variations within the West-central belt data. Legend same as in Plot 1.

Tectonic setting. The tectonic settings inferred from the Fe^{2+}/Fe^{3+} - Al_2O_3 relationship (Plot 3a-c) corroborate the results of the ternary plots (Plot 4a-c). The West-central belt pillow lava spinels are strongly affiliated with SSZ-related settings (Plot 3b-c, Plot 4b-c, Plot 5b-c). All generations essentially plot inside or nearby the forearc fields (Izu-Bonin-Mariana and South Sandwich arc systems) and the SSZ-related serpentinite from the Arabian-Nubian Shield (East African Orogen), displaying particular kinship with the Wadi Bardah serpentinized harzburgite (Plot 3c, Plot 5c). The Wadi Bardah serpentinite has been interpreted to represent a fragment of infant arc crust associated with seafloor spreading in the proto-forearc during subduction zone initiation (Khedr & Arai, 2017). The range of the tectonized mantle harzburgite from the southern Semail ophiolite (Oman) roughly extends over the same compositional range as the pillow lava spinels (Plot 3c, Plot 4c, Plot 5c). The well-studied Semail ophiolite is a typical SSZ-type environment in the sense that it exhibits both mid-ocean ridge and island arc-type characteristics, with the island arc-signature most pronounced in the northern parts (Arai et al., 2011 and references therein). This analogy is significant because mid-ocean ridge affinities are certainly pronounced in the pillow lava (e.g. Plot 4a). The volcanic fragment spinel plots at the edge of the Izu-Bonin-Mariana forearc field (Plot 4b) and is strongly associated with the West Ethiopian Shield field. The field represents data from the Abshala serpentinite, which has been interpreted as an accretionary mélange at a convergent boundary close to subduction initiation (Blades, Collins, Foden & Alemu, 2017). The Kulutingwak Formation pyroxenite spinel indicate a potential source that is nearly identical to that of the pillow lava's generation X at a point before leaching of Mg during lower amphibolite metamorphism (Plot 1c).

The *cr#-mg#* plot is perhaps the most frequently used tool for determining tectonic setting from spinel chemistry as well as visualizing associated compositional trends. The West-central belt volcanic fragment and Kleybolte Fault Zone schist Cr-spinels clearly follow the magma-mantle reaction trend (Plot 5c) that is defined by rapid decreases in *mg#* with increasing *cr#* (Aswad, Aziz & Koyi, 2011). With increasing degrees of partial melting in the mantle, Mg and Al become progressively less likely to go into the solid phase, thus causing increases in the relative proportions of Cr and Fe^{2+} in the Cr-spinel. The reaction trend is reversed in a cooling melt. The cryptic zoning that results from magma-mantle reaction is much more pronounced in the schist spinel than in the volcanic fragment spinel from the West-central belt, despite being much smaller (compare 2D element distribution collages 1 and 8). Neither the West-central belt pillow lava nor Kulutingwak Formation pyroxenite Cr-spinels follow the magma-mantle reaction trend, though all data group B samples follow the Cr-Al trend (Plot 1c), which has commonly been observed in ophiolites, oceanic peridotite, MORB and alpine-type intrusions (Barnes & Roeder, 2001). This trend stems from equilibration with the olivine phase at a constant temperature and composition (Barnes & Roeder, 2001). The high *cr#* spinels in the Kleybolte Fault Zone serpentinized dunite appear to follow the Fe-Ti trend in Plot 1c. The Fe-Ti trend, which has been attributed to evolving spinel compositions during fractional crystallization of olivine and pyroxene, which increase the Fe/Mg ratio and Ti content in the magma but this is likely not the case for these high *cr#* spinels, as their compositions appear to be secondary installments (Plot 1b, Plot 5b).

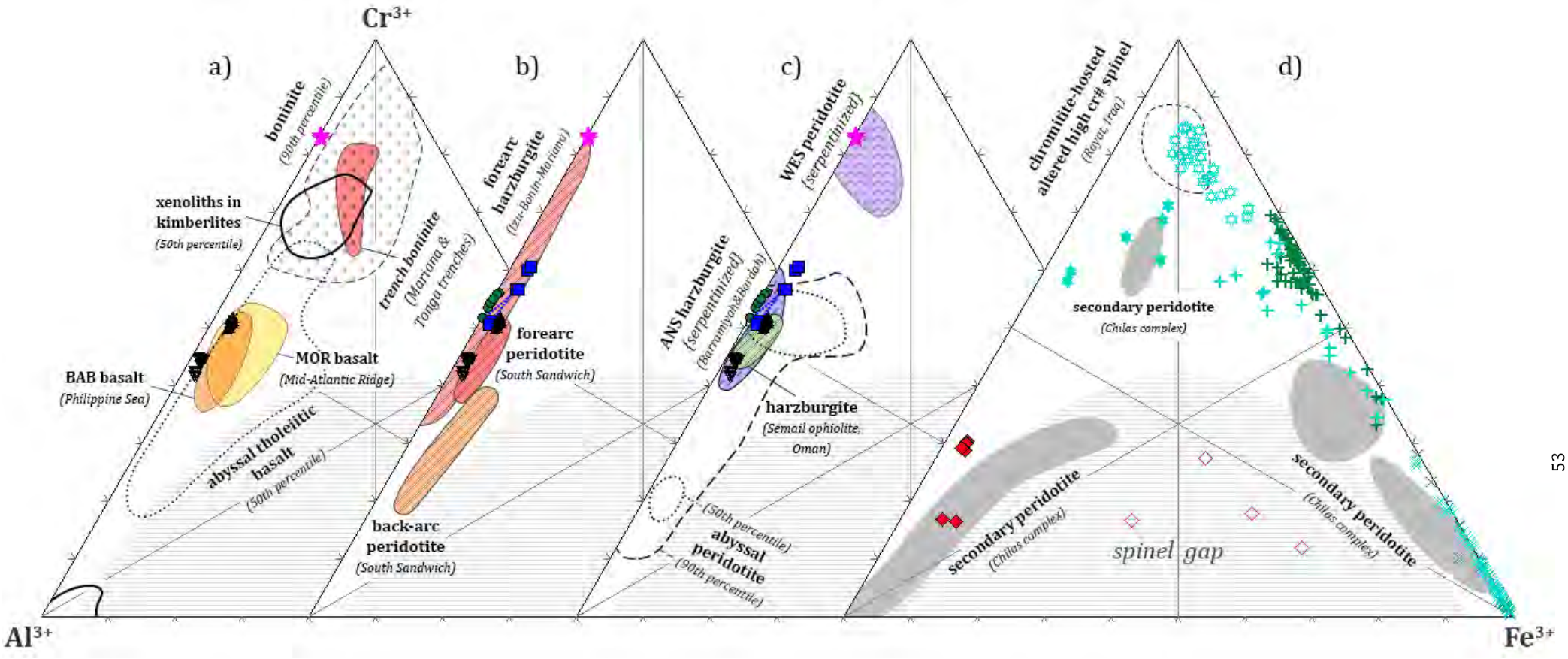

Plot 4 Cr^{3+}-Al^{3+}-Fe^{3+} ternary plot with tectonic discrimination fields. Fields for **a.** boninite (90th percentile) – dashed outline, abyssal tholeiitic basalt from ophiolites (50th percentile) – dotted outline and xenoliths (mantle nodules) in kimberlites (50th percentile) from the Barnes and Roeder (2001) published database; Mariana and Tonga trenches boninite, mid-ocean ridge (= MOR) basalt from the Mid-Atlantic Ridge and back-arc basin (= BAB) basalt from the Philippine Sea as in Plot 3a. **b.** forearc and back-arc peridotites from the South Sandwich and Izu-Bonin-Mariana arc systems as in Plot 3b. **c.** abyssal peridotite (50th percentile - dotted outline, 90th percentile - dashed outline) from the Barnes and Roeder (2001) published database; serpentinized harzburgite/peridotite from the East African Orogen (West Ethiopian Shield, Arabian-Nubian Shield) and Semail harzburgite as in Plot 3c. **d.** altered high *cr#* spinel (Iraq) from Arai et al. 2006; Chilas Complex secondary peridotite (granulite facies) as in Plot 1b. Legend same as in Plot 1.

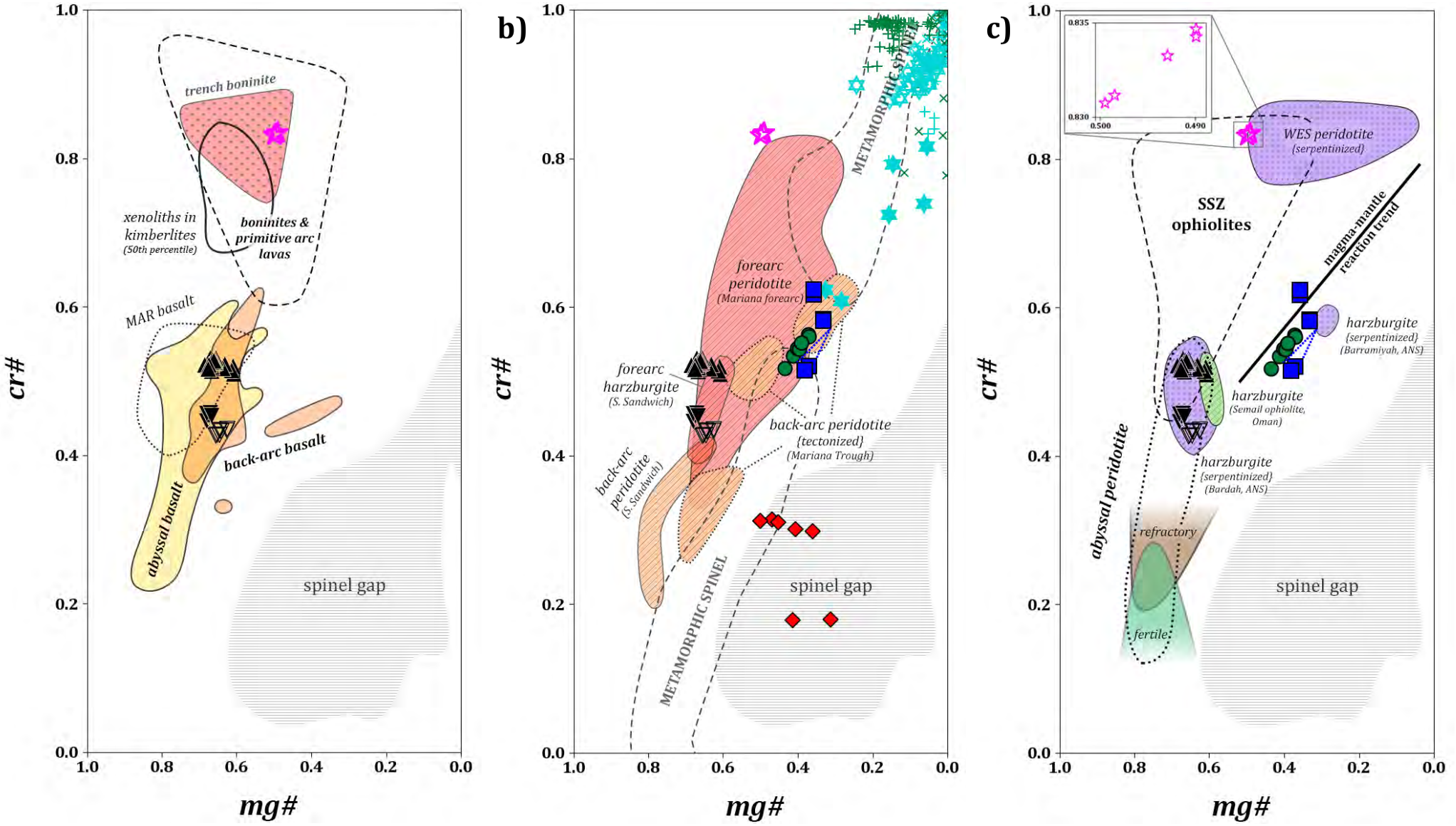

Plot 5 *cr#* versus *mg#.* Fields for **a.** abyssal basalt and back-arc basalt from Dick and Bullen (1984); boninites & primitive arc lavas - dashed outline from Bridges et al. (1995) and references therein; Mid-Atlantic Ridge (= MAR) basalt - dotted outline, trench boninite from the Mariana and Tonga trenches as in Plot 3a. **b.** Mariana forearc peridotite compiled from Taylor and Natland (1995) and Ishii et al. (1992); Mariana Trough tectonized back-arc peridotite - dotted outline from Taylor and Natland (1995); metamorphic spinel from Evans and Frost (1975); South Sandwich (=S. Sandwich) arc system forearc and back-arc peridotite as in Plot 3b. **c.** abyssal peridotite from Dick and Bullen (1984); fertile and refractory mantle from Zheng et al. (2001, 2007); SSZ ophiolites from Bridges et al. (1995) and references therein; serpentinized harzburgite/peridotite from the East African Orogen (WES = West Ethiopian Shield, ANS = Arabian-Nubian Shield) and Semail harzburgite as in Plot 3b. Magma-mantle reaction trend from Aswad et al. (2011). Spinel gap from Barnes and Roeder (2001). Blue dotted line connects data points from grain #1 in Kulutingwak Formation pyroxenite (VP17-04b). Legend same as in Plot 1.

Both high *cr#* spinel and Cr-spinels (open and filled hexagrams respectively) are associated with the upper metamorphic spinel field in Plot 7b, which roughly corresponds to the range of the alteration products Cr-magnetite and ferritchromite. The high *cr#* spinels are similar in character to altered spinels hosted by chromitite from an ophiolite mélange in northeastern Iraq (Plot 4d).

The TiO_2 of Cr-spinel is affected by the degree of partial melting/fractional crystallization. Evans and Wright (1972) demonstrated the correlation between Ti^{4+} content in Cr-spinel and magma differentiation: the more fractionated the basalt host, the more Ti-rich the Cr-spinel. A temperature drop at a fixed fO_2 will increase the Ti^{4+} concentration in the residual melt due to its incompatible nature, such that Ti^{4+} becomes progressively more enriched in the cooling magma (Hulbert, 1997). Cr^{3+} has a strong preference for the B-site in the spinel structure while Ti^{4+} has no site preference, making Ti^{4+} increasingly more likely to be incorporated into the spinel phase during fractional crystallization as Ti^{4+} becomes more available and may occupy either A- or B-sites (Hulbert, 1997). Pearce, Barker, Edwards, Parkinson and Leat (2000) modeled the partial melting trend curve of fertile MORB mantle (FMM) with 0.18 wt.% TiO_2 in Plot 6 assuming three stages of melting:

1. *Melting of a four-phase assemblage (lherzolite): olivine-clinopyroxene-orthopyroxene-spinel, up until the point of clinopyroxene's ultimate disappearance*
2. *Melting of the following three-phase assemblage (harzburgite): olivine-orthopyroxene-spinel, up until the point of orthopyroxene's ultimate disappearance*
3. *Melting of the two-phase assemblage (restitic dunite): olivine-spinel, which was not modeled to completion*

Using parameters for congruent and incongruent melting conditions, Pearce et al. (2000) found only a small difference in Ti concentrations in spinel from the retention of Ti in the residue generated under incongruent melting conditions. Higher Ti concentrations found in terrestrial spinel may therefore be interpreted as being a consequence of melt-mantle interaction through reaction or melt impregnation as opposed to the result of incongruent melting (Pearce et al., 2000).

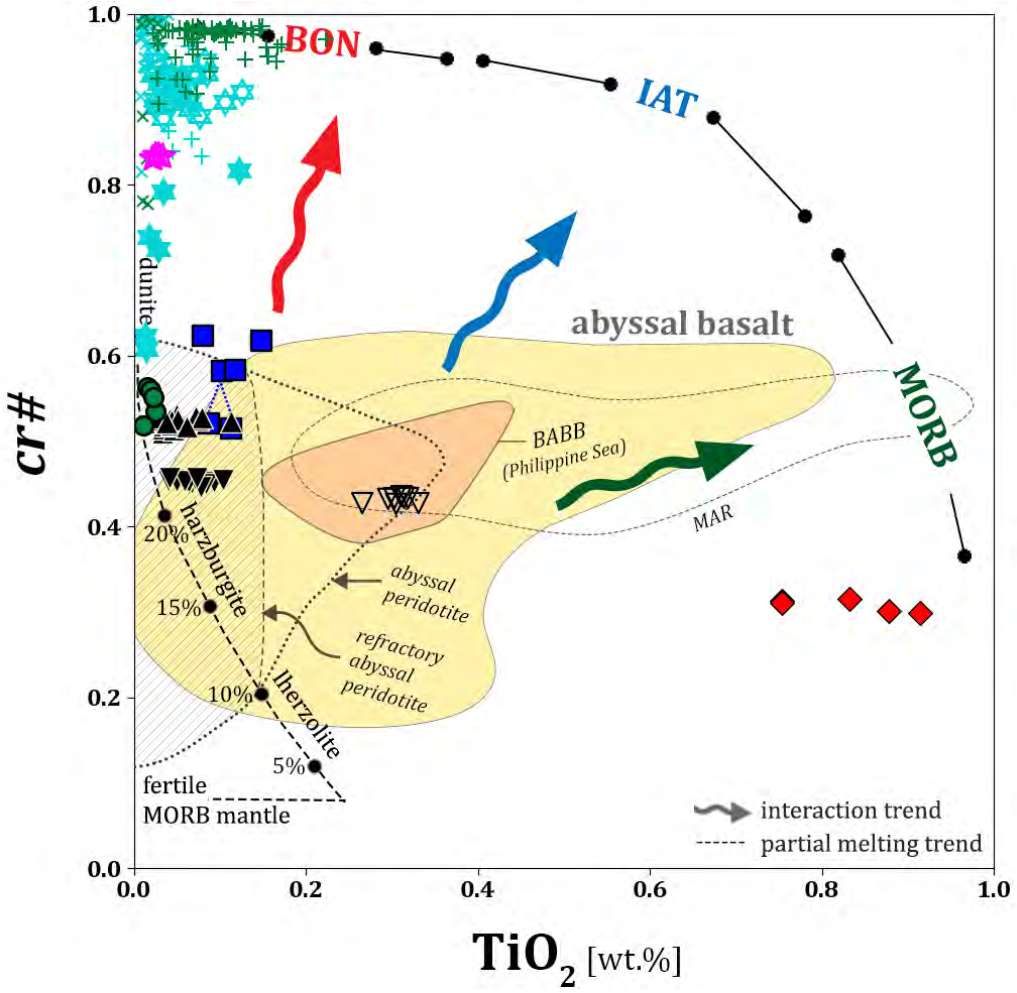

Plot 6 *cr#* versus TiO_2. Fields for abyssal basalt and abyssal peridotite - dotted outline from Dick and Bullen (1984); refractory abyssal peridotite - dashed outline from Kelemen et al. (1997) and references therein; mid-ocean ridge basalt (= MORB) from the Mid-Atlantic Ridge (= MAR) and back-arc basin basalt (BABB) from the Philippine Sea as in Plot 3a. End-members (BON = boninite, IAT = island arc tholeiite, MORB), partial melting trend and interaction trend arrows from Pearce et al. (2000). Legend same as in Plot 1.

The Kleybolte Fault Zone schist spinel clearly follows this partial melting/fractional crystallization trend in Plot 6. The high *cr#* and low TiO_2 suggest that the primitive sources of the Kleybolte Fault Zone schist and generations X and Y in the pillow lava were similar to the hypothetical FMM source that was assumed by Pearce et al. (2000)(Plot 6). Pearce et al. (2000) defined the interaction trends (colored arrows in Plot 6) using data from some well-defined tectonic settings as geochemical end-members to explain right-hand displacement of the partial melting curve and the evolutionary trajectories of data points that deviate from that of the curve. 'Interaction' in this case can be either in the form of magma impregnation or a reaction between melt and solid mantle/country rock. The pillow lava generations X and Y appear to have nucleated in a highly depleted source similar to that of the Kleybolte Fault Zone schist but, in contrast to the schist, instead clearly follow the MORB interaction evolutionary trend.

Kamenetsky et al. (2001) used defined discrimination fields of different tectonic settings in a TiO_2 versus Al_2O_3 plot intended to be used in combination with the Fe^{2+}/Fe^{3+} versus Al_2O_3 plot.

As in the Fe^{2+}/Fe^{3+} versus Al_2O_3 plot, overlap between many fields result from the polygenetic nature of many tectonic settings, e.g. SSZ-type peridotites and island arc (IA) volcanics, and IA-BABB-MORB; the BABB (back-arc basin basalt) signature is practically a combination of the IA volcanics' and MORB's signatures. The MORB interaction trend demonstrated by the West-central belt pillow lava spinels in Plot 6 is clearly detectable Plot 7a-b as a near-vertical trend approaching the MORB and BABB discrimination fields. Based on Kamenetsky et al. (2000)'s discrimination fields, it appears that generations X and Y conform with the plutonic SSZ-type peridotite field while generation Z is more ambiguous in regards to its igneous mode. It can be inferred from the near-identical Fe^{2+}/Fe^{3+} ratios of generations Y and Z (Plot 3a-c) that the igneous mode of generation Z should be the same as that of Y.

In Plot 7b, composition X evolves over a range that stretches from the field of serpentinized harzburgite from the Arabian-Nubian Shield to the fields for forearc harzburgites (Izu-Bonin-Mariana and South Sandwich arc systems) while crossing the field for tectonized harzburgite from the Semail ophiolite in the space between the other fields. Composition Y is associated with the same fields as composition X in this plot, with the exception of the Arabian-Nubian Shield field. Owing to its significantly higher TiO_2, composition Z contrastingly plots in the space between the fields for forearc and back-arc peridotites in the South Sandwich arc system. Additionally, composition Z plots near the overlap between those same fields in Plot 5b. Affiliations with the Wadi Bardah serpentinite (Arabian-Nubian Shield in the East African Orogen), tectonized mantle harzburgite of the southern Semail ophiolite (Oman) and forearc and back-arc peridotite (Izu-Bonin-Mariana and South Sandwich arc systems) are fairly consistent throughout the various plots that have been presented. While associations with the MORB/BABB fields are also evident, this is to a lesser extent (Plot 3a, Plot 4a, Plot 6, Plot 7a). Altogether, the support for a SSZ-associated tectonic setting of the pillow lava is strong.

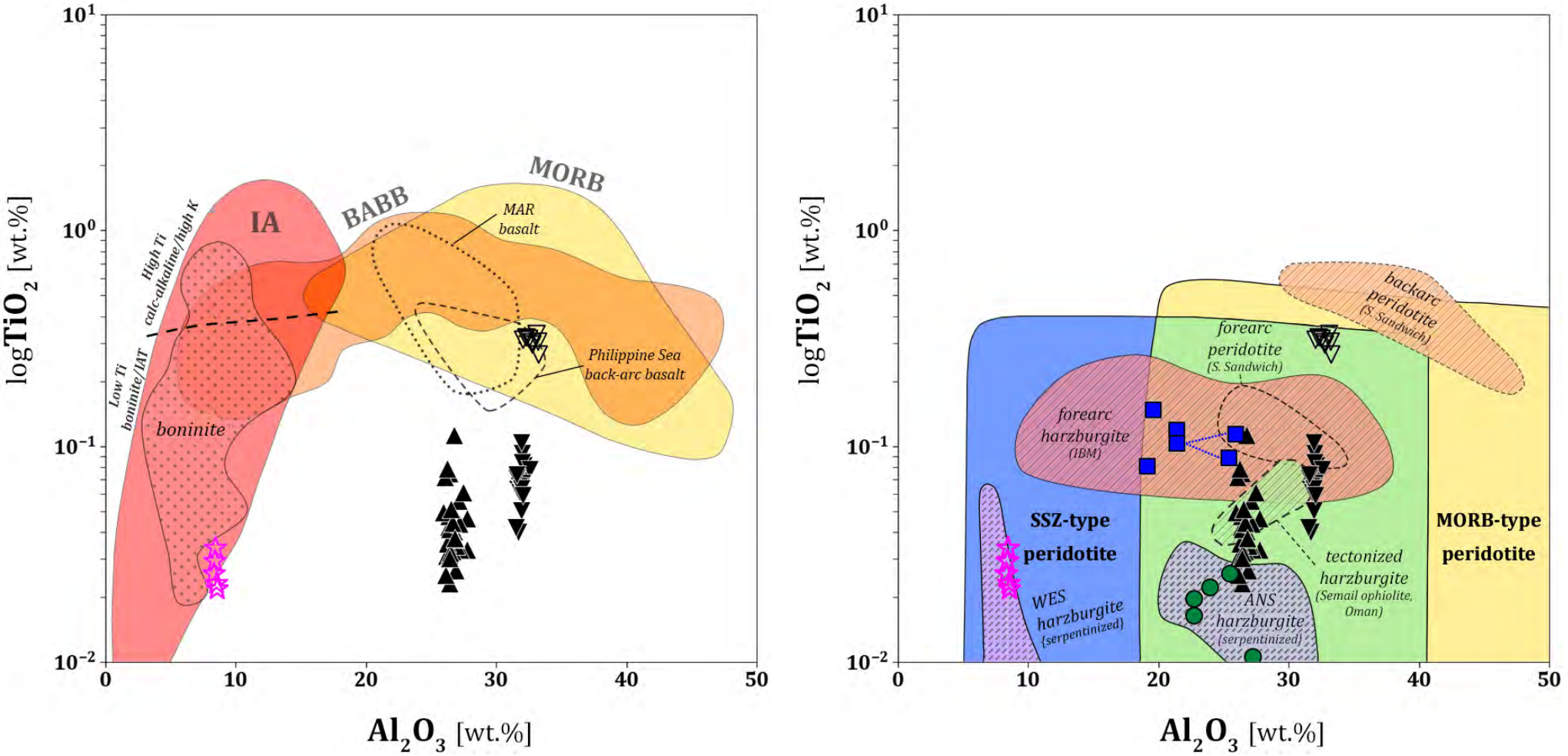

Plot 7 TiO_2 versus Al_2O_3. Fields for **a.** low- and high Ti island arc volcanics (= IA), back-arc basin basalts (= BABB) and mid-ocean ridge basalts (= MORB) from Kamenetsky et al. (2001); Mid-Atlantic Ridge (= MAR) basalt - dotted outline and Philippine Sea back-arc basalt - dashed outline as in Plot 3a; boninite - dotted pattern from GEOROC (available at: http://georoc.mpch-mainz.gwdg.de/georoc/). **b.** SSZ- and MORB-type peridotites from Kamenetsky et al. (2001); forearc and back-arc peridotites (IBM = Izu-Bonin Mariana and S. Sandwich = South Sandwich arc systems), serpentinized harzburgite from the East African Orogen (WES = West Ethiopian Shield, ANS = Arabian-Nubian Shield) and Semail tectonized harzburgite as in Plot 3b. Blue dotted line connects data points from grain #1 in Kulutingwak Formation pyroxenite (VP17-04b). Note logarithmic scale on the vertical axis. Legend same as in Plot 1.

Based on separation from the field for xenoliths in kimberlite (Plot 4a, Plot 5a) representing entrained mantle nodules, the spinel from the volcanic fragment in the West-central belt is more likely to have been generated in a SSZ-type setting, as suggested by the pillow lava from the same unit. This hypothetical SSZ setting shows is strongly affiliated with the Abshala serpentinite in the West Ethiopian Shield (Plot 3c, Plot 4c, Plot 5c, Plot 7b). The high *cr#* and low TiO_2 indicate a strongly depleted, probably dunitic magmatic source (Plot 6) and the compositional evolution is consistent with increasing degrees of partial melting of the mantle or alternatively fractional crystallization of a primitive mantle melt (Plot 5c). The Ti zoning (Plot 7b) is on a much smaller scale than the zoning exhibited by the pillow lava spinels (compare Plot 6) and could result from magma differentiation alone (see generally Evans & Wright, 1972). The spinels from both West-central belt samples resemble spinels from rocks that have been interpreted to reflect SSZ initiation.

The Kleybolte Fault Zone schist spinel is similar to spinels from the Mariana forearc (e.g. Plot 3b) and tectonized peridotite from the contemporary back-arc of the Mariana arc (the so-called Mariana Trough). However, it should be noted that the schist spinel is significantly more depleted than the Mariana arc spinels (compare TiO_2 in Plot 7b). The schist spinel evolved through partial melting of restitic mantle or through crystal fractionation of a mantle-derived melt that was generated through a high degree (>>20 %) of partial melting of FMM (Plot 6). The schist spinel is also affiliated with the discrimination field defined by serpentinized harzburgite spinels from the island arc-associated Wadi Al-Barramiyah of the Arabian-Nubian Shield (Plot 3c, Plot 4c, Plot 5c, Plot 7b).

The Kulutingwak Formation pyroxenite spinels have experienced some degree of alteration from lower amphibolite facies metamorphism (Petrography, Plot 1c). The most considerable effect of this type of metamorphism is Mg leaching and elevated Fe^{2+} concentrations as a consequence of an exchange between Cr-spinel and coexisting silicates (Barnes, 2000). This would mostly affect Fe^{2+}/Fe^{3+} ratios and *mg#,* potentially making the plots that depend on these variables unreliable (Plot 3 and Plot 5). It is also possible that there has been some Al leaching due to metamorphic exchange between Cr-spinel and chlorite but the effect of such is often restricted (see Barnes, 2000).

The cores of the spinels from the Kulutingwak Inlier intrusion are associated with secondary peridotite from granulite facies rocks (Plot 1b, Plot 4d) and the granulite facies metamorphic discrimination field in Plot 1c. In Plot 5b, the cores plot in the spinel gap. The serpentinized dunite Cr-spinels from the Kleybolte Fault Zone have alarmingly high MnO contents (Plot 1b) and are moderately affiliated with the secondary peridotite from granulite facies rocks in Plot 4d. Additionally, the Cr-spinels appear to approach compositions of the high *cr#* spinels in the same sample that are likewise associated with altered spinel (Plot 4d). The Kulutingwak Inlier intrusion and Kleybolte Fault Zone serpentinized dunite spinels are most likely too altered to be interpreted in the terms of tectonic provenance, which therefore will not be attempted.

Discussion

High degrees of alteration in the sampled rock units make evidence of Ellesmere's early tectonic history hard to come by, but Cr-spinel is one of the few minerals that may survive under metamorphic conditions while preserving its primary chemistry. The chemical analyses conducted during this study have indeed returned some results that can be interpreted in terms of petrogenesis, though admittedly, the quantity of usable data is low. Three out of the four Yelverton Bay samples only yielded 1-2 grains each and all but a single grain in the Kleybolte Fault Zone schist from the Audhild Bay site were altered to ferritchromite and Cr-magnetite (Plot 1c). The Kleybolte Fault Zone serpentinized dunite yielded a substantial amount of ferritchromite and Cr-magnetite as well as some altered high c*r#* spinel (Plot 4d). Due to the sparsity in data, interpretations for most samples are currently highly speculative. Nonetheless, the consensus of the available data strongly indicates a supra-subduction zone setting, with signatures comparable to rocks from the East African Orogen, and the Izu-Bonin-Mariana arc system to a lesser extent.

Kulutingwak Inlier intrusion – VP17-01

The Kulutingwak Inlier has been attributed to succession II of the Pearya terrane, which consists of Neoproteozoic to Lower Ordovician metasediments and rift-related metavolcanics. The subvolcanic, phyric diabase dike that was sampled intrudes the Kulutingwak Inlier but the timing is uncertain. The two grains that possessed Cr-spinel compositions in the grain mount comprise two distinctive spinel phases (2D element distribution collage 5): a Cr-spinel core and a titanomagnetite rim (Plot 2). The compositions of the cores as well as the presence of the titanomagnetite rim indicate that metamorphic conditions imposed on rock have altered the spinels to a degree where they no longer possess primary chemical compositions and are therefore not suitable as tectonic indicators. The core compositions conform with granulite facies altered spinel (Plot 1c) and secondary spinel in granulite facies rocks (Plot 4d) to a lesser extent in addition to being affiliated with the metamorphic spinel field and the spinel gap in Plot 5b. The relatively low MnO content in the cores is likely more indicative of the presence of carbonate than of primary compositions. As elevated MnO contents are restricted to essentially carbonate-free rocks with low metamorphic *mg#* (see Barnes, 2000), interstitial accessory carbonate observed in thin section and fact that the dike intrudes calcareous-dolomitic schist (Figure 5a) likely explain why our fall within the primary Cr-spinel field by Khedr and Arai (2017) in Plot 1b.

Kleybolte Fault Zone schist (*ds*) – 17HSB-3

Only one grain in the Kleybolte Fault Zone schist classifies as Cr-spinel but this grain appears to have survived alteration completely. For instance, the grain exhibits primary igneous zoning that

stems from the strongly linked divalent and trivalent substitutions of Mg^{2+} -> Fe^{2+} and Al^{3+} -> Cr^{3+} (see Dick & Bullen, 1984; Hulbert, 1997). While the grain does exhibit the magma-mantle reaction trend in Plot 5c, it is not obvious from the grain's morphology whether the compositional trend evolved from partial melting or fractional crystallization. Preservation of strong cryptic zoning expressed as great compositional variations within the small grain (~30 μm), indicates a lack of subsolidus equilibration and so, a rapid cooling rate (Barnes, 1998; Barnes 2000) despite extremely high Fe^{2+}/Fe^{3+} ratios. Thus, it is possible that the protolith of the schist was actually volcanic and carried this spinel grain directly from a primitive source to the surface. Alternatively, the spinel is an entrained xenocryst from an initially rapidly cooled source, if the *ds* map unit represents a sub-arc pluton as Trettin (1998) tentatively proposed. The cryptic zoning is expressed in the plots as an antithetic relationship between *cr#* and *mg#* (Plot 5b-c). Furthermore, there appears to be a linear relationship between *cr#* and TiO_2 (Plot 6, Plot 7b). Primary compositions are corroborated by the relatively low MnO content (Plot 1b).

The grain in question is not associated with the alteration product ferritchromite (2D element distribution collage 1), which was otherwise the dominant mineral phase in the grain mount (e.g. Plot 1c). Ferritchromite rims require oxidizing conditions (González-Jiménez et al., 2009) and the ferritchromite and the abnormally high Fe^{2+}/Fe^{3+} ratios generated by the Cr-spinel strongly indicate a SSZ-type setting. The grain consistently demonstrates affinities with island arc-associated serpentinized harzburgite from the Arabian-Nubian Shield; namely the Wadi Al-Barramiyah area in the Arabian-Nubian Shield (Blades et al., 2017). It is also associated with the forearc field represented by Conical Seamount near the Mariana arc and tectonized back-arc peridotites in the Izu-Bonin-Mariana arc system to a lesser extent.

The source of the Kleybolte Fault Zone schist spinel was more depleted than the Izu-Bonin-Mariana source is, as reflected by the relatively Ti-rich spinels procured from the Izu-Bonin-Mariana forearc peridotite (Plot 7b), which may reflect differentiating arc evolution stages. Many SSZ ophiolites represent fragments of forearc lithosphere due to the likelihood of obduction in proximity to the convergent margin (Stern, 2010). The forearc preserves the infant arc lithosphere (juvenile crust) and seafloor spreading in the relatively thin proto-forearc (forearc rifting as opposed to back-arc rifting) may produce less fractionated and fluid-contaminated (ergo oxidized) melts than magmatism associated with mature arcs (Stern, 2010). As the arc matures, the crust under the island arc or *magmatic front* thickens and primitive melts are progressively more fractionated and diversified over the vertical distance en route to the surface as the distance increases with the thickness of the crust (Stern, 2010). The subsequent magma evolution of mature arc melts is associated assimilation of continental crust, magma mixing with slab-derived partial melts and metasomatism by slab-derived fluids in addition to fractional crystallization of mantle-derived partial melts (Stern, 2010). The Izu-Bonin-Mariana arc system may be more mature than the alleged Ordovician (?) Franklinian Basin arc that the Clements Markham fold belt spinels represent. Note that there is very little evidence of pre-existing abyssal oceanic crust in the Izu-Bonin-Mariana forearc plutonics, despite having evolved in an intraoceanic setting (Taylor & Natland, 1995). Subduction is

thought to have initiated ~45 Ma (Parkinson & Pearce, 1998) and the infant stage only lasts ~5-10 Myr (Stern, 2010).

The primitive source of the schist spinel is similar in composition to primitive source of the generation X pillow lava spinel (West-central belt) and closely resemble a depleted FMM source (with 0.18% TiO_2), as modeled by Pearce et al. (2000). Unlike composition X, the compositional data from the schist follows the partial melting curve. A high partial melting degree (>>20%) is inferred from the partial melting curve (Plot 6). The contrasting evolutions of the schist spinel contra the West-central belt spinels in terms of Ti in clearly demonstrated in Plot 7b, where there is a linear relationship between Ti and Al_2O_3.

Kleybolte Fault Zone serpentinized dunite (*ds*) – 17HSB-4

The dunite was tectonized at some point and developed shear bands through ductile deformation. Polyphase deformation is required for the development of the kinks and crenellations in the shear fabric (see Petrography). Eventually, the mode of deformation changed from ductile to brittle, as inferred from faults and cracks. The carbonate-rich fluids that invaded through the cracks were contemporaneous with serpentinization, judging by the apparent equilibrium between carbonate veins and serpentine in the thin section. The serpentinization was either syn- or post-tectonic, as indicated by the relatively uniform display of interference colors.

The most primitive Cr-spinel compositions belong to the only Cr-spinel grain with euhedral morphology (2D element distribution collage 4). The grain is surrounded by Cr-magnetite, which is not the product of alteration based on the sharp compositionaö contrast between the two phases (compare with the gradational boundary in 2D element distribution collage 3). However, it is strongly suggested that even this grain has been substantially altered. Cr-spinel MnO contents in excess of 0.50 wt % are uncommon and considered to result from alteration (e.g. Barnes 2000) and all Cr-spinels in the serpentinized dunite have high MnO contents (>0.50 wt.%) (Plot 1b). The high *cr#* spinel compositions (open hexagrams in Plot 4d) that resemble the altered spinels from Rayat in northeastern Iraq (Arai et al., 2006) plot outside the altered Cr-spinel field by Khedr and Arai (2017) in Plot 1b only on account of their augmented *cr#*; the remaining Cr-spinels (solid hexagrams) plot inside. These Cr-spinel data do not group in the manner of the high *cr#* spinels, but judging by the trajectory of the data range in Plot 4d, the Cr-spinels are evolving towards the compositional grouping of the high *cr#* spinels. The altered Cr-spinels, therefore, most likely represent earlier stages of alteration. Moreover, the Cr-spinels are associated with the upper part of the metamorphic spinel in the *cr#* versus *mg#* plot (Plot 5b). During metamorphism above lower amphibolite facies, Al and Mg from the Cr-spinel margin can depart from the grain through fluids and form e.g. chlorite, leaving Fe^{2+} and Cr^{3+} behind and effectively depleting the spinel of Mg (Barnes, 2000). Combined with the significant loss of Al resulting from equilibration with fluids at temperatures above 550° C (see Barnes, 2000), the high *cr#* and low *mg#* are installed.

West-central belt volcanic fragment (*OSv*) – VP17-05b

The deformation that produced the foliation in the less competent shale that hosted the volcanic fragment and the protomylonitic texture was unidirectional based on shear sense indicators in thin section (e.g. pressure shadows). The opaques in the thin section that could be identified with confidence were all sulfides, but the possibility that some of the smaller opaques are some type of spinel cannot be ruled out. The grain mount is likewise dominated by sulfides, but for the one subhedral and relatively homogeneous aluminian Cr-spinel grain (see Petrography). The single Cr-spinel grain that could be identified in thin section is euhedral and translucent and so, likely representative of the aluminian Cr-spinel in the grain mount as low iron content (see Table 2) is consistent with translucent spinel (see Raith, Raase & Reinhardt, 2012). Though cracked, the grain has retained its crystal shape and based on the lack of alteration along cracks and grain margins and the produced chemical compositions, it appears that the grain has survived alteration completely. The volcanic texture of the rock, the presence of entrained volcanic fragments and the textural occurrence of the grain in thin section complicates the interpretation of the chemical composition as the grain is not directly linked to the groundmass nor associated with any autochthonous mineral phases. It is likely that the grain is a xenocryst and possibly not representative of the sampled volcanic rock. The cryptic zoning, that is much less pronounced than in e.g. the pillow lava spinels and the Kleybolte Fault Zone schist spinels, infers a slower subsolidus cooling rate, consistent with a plutonic source. Plot 6 suggests that the source was highly restitic.

On the SEM images, it is not obvious from the grain's morphology if any of its margins represent crystal faces, though one side in particular has potential. This side is marked F in SE image in 2D element distribution collage 8. It is remarkably straight and parallel to the apparent concentric cryptic zoning, suggesting that crystal face represents a relatively Mg-poor margin of an Mg-rich core. The cryptic zoning is barely perceptible on the element distribution maps since the variation in concentrations are minuscule over the extent of the grain (<100 μm) but they are detectable in e.g. the inset in Plot 5c. The strong antithetic variation between *cr#* and *mg#* is consistent with primary igneous zoning. The two data points with nearly identical compositions and the highest *cr#* are at an equal distance from the aforementioned potential crystal face.

Though the compositions are pretty similar to spinels in boninite (Plot 4a, Plot 5a, Plot 7a), the exceptionally low calculated ferric content (Plot 3b-c) is more consistent with certain plutonic SSZ spinels. Boninites usually form in the early evolutionary stages of the arc from hydrous melting of metasomatized mantle above the subduction zones (e.g. Stern, 2010) and arc lavas like boninite have high fO_2 because the slab-derived fluids oxidize the mantle wedge source. According to Kamperman et al. (1996), Cr-spinel from subduction zones does not necessarily follow a stoichiometrical framework and consequently, the Fe^{2+}/Fe^{3+} ratios generated from the chemical compositions are often abnormally high. Subsolidus Fe^{3+} depletion can occur e.g. during talc-carbonate alteration at low temperatures and would add to the abnormally high Fe^{2+}/Fe^{3+} ratios but the effect should only be minor (see Barnes, 2000). If the rock only has been altered by greenschist grade metamorphism as suggested by Plot 1c, the effect would instead

potentially include a slight increase in Fe^{3+} (up to 20% higher; c.f. Barnes, 2000). However, during greenschist facies alteration, there is usually covariance in NiO, TiO_2 and Fe^{3+} and this was not observed in the data. Trettin (1998) noted that while the mineral assemblages in the West-central belt volcanics conform with regional lower greenschist facies metamorphism, it may be the result of hydrothermal alteration as neither volcanics nor associated limestone show evidence of metamorphic fabrics.

Three out of four volcanic samples that Trettin (1998) analyzed from the West-central belt were calc-alkaline and the forth medium-K alkali basalt, suggestive of a weakly extensional tectonic regime. Calc-alkaline rocks are strongly associated with arc volcanism (e.g. Stern, 2010) and the grain is strongly associated with a SSZ setting. The grain's composition is consistently affiliated with the field for serpentinized peridotite from the West Ethiopian Shield in the East African Orogen (Plot 3c, Plot 4c, Plot 5c, Plot 7b). This corroborates the accretionary prism hypothesis that was proposed by Bjørnerud (1991) based on observations of soft sediment structures. The TiO_2 content in the grain follows a Ti-enrichment trend like that of the pillow lava sample VP17-15, albeit on a significantly smaller scale (Plot 7). The small-scale Ti-enrichment trend may simply reflect the effects of fractional crystallization.

West-central belt deformed pillow lava (*OSv*) – VP17-15

Field observations and the vesicular, trachytic texture strongly indicate that the outcrop represents deformed pillow lava. Discreet lenticular structures in the groundmass and entrained volcanic lithic fragments with similar mineralogical compositions had differentiating size distributions and proportions of devitrified glass. The variable vesicle sizes in adjacent pillows (Figure 5d) and composite, lenticular structure of the groundmass in thin section may reflect differentiating rates of upwelling, which can result in fluctuating gas pressures, and a relatively heterogeneous melt. When primitive arc magmas ascend into the arc crust, they are often stored temporarily in magma reservoirs, where they may mix with other magmas and differentiate further (Stern, 2010). Island arc lavas are characteristically vesicular, porphyritic and fractionated as a testament of one or more magma reservoirs within the arc crust (Stern, 2010).

Strong, cryptic zoning has been preserved due to rapid cooling. The scale of the Ti and Fe^{3+} cryptic zoning within the grains (and generations) is variable but seemingly unrelated. This is significant because it suggests that the zoning is not the result of low T-alteration (see Barnes, 2000). The Ti zoning, which is on a much smaller scale in generation Z, is probably primary, and markedly decoupled from the small variations observed in Al and Cr within the generations. Generations Y and Z are chemically comparable in most senses (*cr#*, *mg#*, Fe^{2+}/Fe^{3+} ratios, MnO and relative proportions of Cr-Al-Fe^{3+}), but distinguished by the substantial contrast in Ti. The simple explanation for this striking resemblance is a genetic link between these compositions: Z could be derived from the advanced evolution of Y, following the MORB interaction trend (Plot 6), but transitional spinels that bridge the compositional gap in Ti would have to be recovered to confirm this hypothesis.

The compositional arrays resulting from the variable Ti in generations X and Y start roughly on the partial melting trend curve in Plot 6. Based on the morphology of the grains relative to the concentric cryptic zoning (e.g. 2D element distribution collage 9 and front page), the Ti trend in the compositional evolution is progressive; i.e. a Ti-enrichment trend as opposed to a Ti-depletion trend. The grains appear to have nucleated in a highly residual melt produced through >20% partial melting of FMM and thereafter evolved following the MORB interaction trend (Plot 6). The distinguishing *cr#* of compositions X and Y-Z suggests that they originated in a depleted mantle-derived residue at different degrees of partial melting, with the melt of generation X being the most refractory. Note that there are no transitional compositions connecting the *cr#* of generation X to Y-Z, which would be expected if the Y-Z spinels had stayed in the increasingly depleted residual melt and evolved parallel to X. Nonetheless, the linear MORB interaction trend suggests parallel chemical evolution.

Low Ti-spinels comparable to the most primitive compositions of X and Y are common in MORB-type peridotites (see abyssal perdotite and refractory abyssal peridotite fields in Plot 6). While abyssal basalt spinels may exhibit low TiO_2 contents similar to those of compositions X and Y, they are commonly much more enriched, which essentially is the basis for the horizontal MORB interaction trend in Plot 6. Progressive fractional crystallization produces a negative trend in spinel *cr#* (see Pearce et al., 2000) and so, cannot by itself explain the progressive Ti-enrichment in the pillow lava spinels, which is independent of *cr#*. Additionally, none of the spinels follow the magma-mantle reaction trend (Plot 5) that results from cooling of mantle-derived melts. It is here proposed that the conspicuous trend is the result of comingling of the residual melt(s) that produced the most primitive and depleted compositions and a more evolved MORB-like melt. For example, the spinels may have been injected into a magma chamber containing the evolved magma. Statistically, spinels from rocks of ophiolitic magma chamber locally have the highest TiO_2 in those ophiolites (see Barnes and Roeder, 2001). Based on the 50^{th} percentile data density field in Barnes and Roeder (2001), such spinels accommodate up to 0.3 wt.% TiO_2 while maintaining relatively low proportions of ferric iron. Fe^{3+} proportions can be expressed as the atomic fraction Fe^{3+} relative to total trivalent cations: $Y_{Fe3+} = Fe^{3+}/(Al^{3+} + Cr^{3+} + Fe^{3+}$. The ophiolitic magma chamber spinels in Barnes and Roeder (2001)'s dataset commonly displayed $Y_{Fe3+} < 0.10$. Correspondingly, the proportions of Fe^{3+} (Y_{Fe3+}) for the pillow lava spinels are in the order of 0.01-0.03 (Table 2) and the maximum TiO_2, which belongs to generation Z, is 0.33 wt.%. Alternatively, the magma chamber in which the spinels nucleated may have been replenished.

Pyroxene or amphibole enveloping one of the grains belonging to generation X was identified using EDS spot analysis (Microscope image 6d). Perhaps the generational gap in *cr#* between compositions X and Y-Z spinels is related to equilibration with different types of oikocrysts. Subsolidus equilibration processes between clinopyroxene and spinel that differ from those with olivine have been observed in high-pressure mantle nodules (Barnes and Roeder, 2001). A high- to low-pressure trend arises from significant amounts of Al being exsolved from clinopyroxene to form aluminous spinels at the high-pressure end of the spectrum (Barnes and Roeder, 2001). A drastic change in pressure might motivate the discreet gap in *cr#* between the compositions X

and Y-Z. This change in pressure would also be related to the diverging Fe^{2+}/Fe^{3+} ratios of composition X relative to Y-Z.

Composition X and the Kleybolte Fault Zone schist have many notable compositional similarities. Apart from the much lower Fe^{2+}/Fe^{3+} ratio and lack of the magma-mantle reaction trend in composition X, the data sometimes overlap (Plot 6, Plot 7). The sampling sites are presently separated by ca. 160 km but that may not have been the case in the Paleozoic, and the mantle may have been relatively homogenous over the paleo-distances between the magma reservoirs of the schist and the pillow lava. Assuming that the data representing the least altered compositions in the Kulutingwak Formation pyroxenite are those with the highest *mg#* and Fe^{2+}/Fe^{3+} ratios and the lowest Cr:Al, there are also some notable similarities between composition X and the Kulutingwak Formation pyroxenite. Two out of the six data points from the pyroxenite often plot close to composition X and the Kleybolte Fault Zone schist (Plot 1c, Plot 6, Plot 7). It should be noted that despite the altered state of the pyroxenite spinel, the pillow lava spinels appear to be more oxidized in comparison (Plot 3b-c).

All generations consistently conform with the data field defined by Wadi Bardah serpentinite in the Arabian-Nubian Shield in the East African Orogen that has been interpreted to represent seafloor spreading in the proto-forearc (Blades et al. 2017). Such seafloor spreading would indeed produce pillow lava. The Wadi Bardah serpentinite data field plots in the intersecting MORB- and SSZ-type peridotite data fields (Plot 5c, Plot 7b) and true to form, compositions X and Y are both affiliated with forearc peridotite (Izu-Bonin-Mariana and South Sandwich basin arc systems) in addition to abyssal (MORB-type) peridotite. Furthermore, compositions X and Y to a lesser extent also resemble the Semail ophiolite, known to possess geochemical characteristics of both mid-ocean ridge and island arc settings.

Kulutingwak Formation pyroxenite (*OK1*) – VP17-04b

The Kulutingwak Formation pyroxenite has been attributed to the older member of the formation, *OK1*, which consists of volcanics and minor marble. The Northeastern Kulutingwak Anticlinorium exposes both members of the Kulutingwak Formation juxtaposed the Phillips Inlet Formation (*SPI1* unit) at the center of the anticline. The Northwestern belt units perhaps represent relict ocean floor associated with an Ordovician island arc that likely predated the accretion of the Pearya terrane, as proposed by Klaper (1992). Associated deformation (e.g. the Kulutingwak Anticlinorium) and lower amphibolite facies metamorphism along the boundary zone between the Pearya terrane and the autochthonous crust (Trettin, 1991; Klaper and Ohta, 1993), and/or retrograde amphibolite facies following the classic path of subduction zone metamorphism, may unfortunately have altered the Kulutingwak Formation spinels.

Only three points on each grain were analyzed but the composition of point 1 on grain #1 is nearly identical to the composition of point 2 on grain #2. Incidentally, both of the analyzed spots were positioned near grain margins. It is possible that the two grains originally constituted a single crystal, which shattered during sample processing. Chemically, both grains are

moderately inhomogeneous (2D element distribution collages 6-7) and the irregular compositional zoning makes the grouping of data points relatively poor.

Based on the mineral assemblage observed in thin section and the metamorphic facies discrimination diagram (Plot 1c), the pyroxenite appears to have been subjected to lower amphibolite facies metamorphism, potentially resulting in extensive formation of chlorite (see Petrography). The presence of hydrous fluids and metamorphic temperatures higher than 550° C (see Barnes, 2000) are inferred from the formation of chlorite. The vertical spread in the data in Plot 6 and horizontal spread in Plot 7b may be a manifestation of metamorphic Al leaching during chlorite formation, and if that is the case, the least altered compositions should be those with the highest Al_2O_3 and lowest *cr#* (i.e. grain #1). If the spread in data is interpreted as the direct result of alteration, Plot 3b-c suggest that Al leaching was accompanied by elevated Fe^{3+}, which is consistent with this type of alteration (see Barnes, 2000). Barnes (2000) found that the main difference between greenschist and amphibolite facies altered spinel was statistically lower *mg#* associated with the latter. In their dataset, the amphibolite facies spinel seldom exceeded *mg#* ≈ 0.35. In comparison, the pyroxenite spinels cover an *mg#* range of 0.33-0.38 and so, they may still be acceptable tectonic indicators. Mg-depletion is, in the absence of carbonate, usually coupled with increasing amounts of MnO on account of the divalent substitution of Mg^{2+} -> Mn^{2+} but these somewhat altered Cr-spinels have seem to have maintained primitive amounts of MnO (Plot 1b) as the thin section encouragingly displayed a complete lack of carbonate.

While it seems like the pyroxenite has metamorphosed, the effects on the Cr-spinel appear to have been relatively moderate, as indicated by the positioning of the data in the gap of the metamorphic spinel array in the *cr#-mg#* plot. The ternary plots should still be reliable for tectonic interpretation (see Barnes, 2000) and potentially also the Ti plots, if some leeway in Al_2O_3/*cr#* is accounted for. Based on the ternary plot and the least altered compositions in the TiO_2 versus Al_2O_3 plot, the pyroxenite appears to be associated with forearc peridotites from the Izu-Bonin-Mariana and South Sandwich arc systems. Note that these are markedly more Ti-rich than the SSZ-peridotites from the East African Orogen, which the potentially coeval West-central belt spinels resemble, disregarding the pronounced Ti-enrichment by MORB interaction. TiO_2 enrichment could be a consequence of metamorphism, though it should be noted that diffusion rates of Ti in e.g. magnetite and Cr-spinel are slow and require very high temperatures (e.g. Barnes, 2000). High Ti in spinel from ultramafic plutonics can otherwise often be attributed to entrapment in intercumulus liquid in slow cooling cumulates (Barnes, 1998; Barnes 2000). Based on coarseness and orientations of the megacrysts in the pyroxenite (see Petrography), it is plausible that the pyroxenite (now amphibolite) was a slowly cooling cumulate prior to metamorphism but the metamorphic overprint makes this interpretation highly speculative. Right-hand displacement of the data in Plot 6 relative to the partial melting curve might indicate that the pyroxenite had a more fertile source than the source(s) of other samples or but it is perhaps more likely that the displacement represents entrapment and subsequent equilibration with intercumulus liquid during slow cooling.

The pyroxenite spinel compositions conform with the field for the tectonically stable forearc region along the Bonin Trench in the Izu-Bonin-Mariana arc system in e.g. Plot 3b. The field is represented by serpentinized rocks from the Torishima Seamount which, unlike the Conical Seamount, are not associated with actively venting fluids derived from slab hydration in the subduction zone (Parkinson & Pearce, 1998). Torishima Seamount has yielded more oxidized serpentinites than Conical Seamount and the serpentinites are thought to be (former) harzburgitic restites after extraction of arc magmas (Parkinson & Pearce, 1998). Modern arcs like the Izu-Bonin-Mariana, have a boundary layer at the base of the arc crust that separates it from the upper mantle, which appears to consists of pyroxenite, amphibolite and gabbro (Stern, 2010). If the West-central belt volcanics represent infant arc volcanism, the pyroxenite may represent a more mature stage in the arc evolution; potentially forming the boundary layer at the base of the crust.

Conclusion

- The phyric diabase dike that intrudes a dismembered fragment of the Pearya terrane and the serpentinized dunite from the Kleybolte Fault Zone yielded highly altered Cr-spinel that could not be interpreted in terms of tectonic settings
- The older member of the Kulutingwak Formation has been subjected to amphibolite facies metamorphism, which has affected the yielded Cr-spinels
- The Cr-spinel from the Kleybolte Fault Zone schist evolved through high degrees of partial melting or fractional crystallization
- The West-central belt exhibits a geochemical signature consistent with that of a supra-subduction zone in the infant evolutionary stage
- The now-deformed West-central belt pillow lava reflects proto-forearc seafloor spreading
- The West-central belt volcanic fragment xenocryst likely derived from an accretionary prism. The source of the xenocryst was highly restitic
- The depleted pillow lava source mingled with a Ti-enriched melt, producing a linear evolution of the spinels towards more MORB-like compositions
- The primitive sources of the pillow lava, the Kleybolte Fault Zone schist and the Kulutingwak Formation pyroxenite (prior to amphibolite facies metamorphism) were similar
- Rapid cooling rates are inferred from cryptic zoning in Cr-spinel from the West-central belt pillow lava and the Kleybolte Fault Zone schist spinels
- Collectively, the samples display a likeness to supra-subduction zone rocks from the East African Orogen and to a lesser extent, the Izu-Bonin-Mariana arc system

Acknowledgments

I would like to thank my supervisor, prof. Vicky Pease, for generously giving me the opportunity to perform this study and aiding me along the way; my family, for giving me the space I needed; Wanda Aylward at the Memorial University of Newfoundland for her skill, enthusiasm and total commitment as lab instructor; dr. Luke Beranek and Adam Wiest, also at the Memorial University of Newfoundland, for welcoming a complete stranger with open arms and taking the time to help me make the most of my stay; and last (but definitely not least!), my friends for their inexhaustible patience and unwavering support.

References

Cited works

Articles

Arai, S., Okamura, H., Kadoshima, K., Tanaka, C., Suzuki, K., & Ishimaru, S. (2011). Chemical characteristics of chromian spinel in plutonic rocks: implications for deep magma processes and discrimination of tectonic setting. *Island Arc, 20*(1), 125-137. doi: 10.1111/j.1440-1738.2010.00747.x

Arai, S., Shimizu, Y., Ismail, S. A., Ahmed, & A. H. (2006). Low-T formation of high-Cr spinel with apparently primary chemical characteristics within podiform chromitite from Rayat, northeastern Iraq. *Mineralogical Magazine, 70*(5), 499-508. doi: 10.1180/0026461067050353

Aswad, K. J., Aziz, N. R., & Koyi, H. A. (2011). Cr-spinel compositions in serpentinites and their implications for the petrotectonic history of the Zagros Suture Zone, Kurdistan Region, Iraq. *Geological magazine, 148*(5-6), 802-818. doi: 10.1017/S0016756811000422

Barnes, S. J. (1998). Chromite in komatiites, I. Magmatic controls on crystallization and composition. *Journal of Petrology, 39*(10), 1689-1720. doi: 10.1093/petroj/39.10.1689

Barnes, S. J. (2000). Chromite in komatiites, II. Modification during greenschist to mid-amphibolite facies metamorphism. *Journal of Petrology, 41*(3), 387-409. doi: 10.1093/petrology/41.3.387

Barnes, S. J., & Roeder, P. L. (2001). The range of spinel compositions in terrestrial mafic and ultramafic rocks. *Journal of petrology, 42*(12), 2279-2302. doi: 10.1093/petrology/41.3.387

Bjørnerud, M.G. (1991). Structural evolution of the Kulutingwak zone, northwestern Ellesmere Island: the northern edge of Paleozoic North America. *Current Research, Geological Survey of Canada*, *Part E*(91-1E), 187-195. doi: 10.4095/132643

Blades, M. L., Foden, J., Collins, A. S., Alemu, T., & Woldetinsae, G. (2017). The origin of the ultramafic rocks of the Tulu Dimtu Belt, western Ethiopia–do they represent remnants of the Mozambique Ocean? *Geological Magazine*, *156*(1), 1-21. doi:10.1017/S0016756817000802

Bloomer, S. H., & Hawkins, J. W. (1987). Petrology and geochemistry of boninite series volcanic rocks from the Mariana trench. *Contributions to Mineralogy and Petrology, 97*(3), 361-377. doi: 10.1007/BF00371999

Bridges, J., Prichard, H., & Meireles, C. (1995). Podiform chromitite-bearing ultrabasic rocks from the Braganca massif, northern Portugal: fragments of island arc mantle? *Geological Magazine, 132*(1), 39-49. doi: 10.1017/S0016756800011419

Dick, H. J., & Bryan, W. B. (1978). Variation of basalt phenocryst mineralogy and rock compositions in DSDP Hole 396B. *Initial Reports of the Deep Sea Drilling Project, 46*, 215-226. doi:10.2973/dsdp.proc.46.109.1979

Estrada, S., Piepjohn, K., Henjes-Kunst, F., & von Gosen, W. (2003). Geology, magmatism and structural evolution of the Yelverton Bay area, northern Ellesmere Island, Arctic Canada. *Polarforschung, 73*(2/3), 59-75. doi: 10.2312/polarforschung.73.2-3.59

Evans, B. W., & Frost, B. R. (1975). Chrome-spinel in progressive metamorphism—a preliminary analysis. *Geochimica et Cosmochimica Acta, 39*(6-7), 959-972. doi: 10.1016/0016-7037(75)90041-1

Evans, B. W., & Wright, T. L. (1972). Composition of liquidus chromite from the 1959 (Kilauea Iki) and 1965 (Makaopuhi) eruptions of Kilauea volcano, Hawaii. *American Mineralogist: Journal of Earth and Planetary Materials, 57*(1-2), 217-

230. Retrieved from https://pubs.geoscienceworld.org/

Freitas Suita, M. T. D., & Strieder, A. J. (1996). Cr-spinels from Brazilian mafic-ultramafic complexes: metamorphic modifications. *International Geology Review, 38*(3), 245-267. doi: 10.1080/00206819709465333

González-Jiménez, J.M., Kerestedjian, T., Proenza, J.A., & Gervilla, F. (2009). Metamorphism on Chromite Ores from the Dobromirtsi Ultramafic Massif, Rhodope Mountains (SE Bulgaria). *Geologica Acta*, *7,* 413-427. doi: 10.1344/104.000001447

Habtoor, A. M., Ahmed, A. H., Akizawa, N., Harbi, H., & Arai, S. (2017). Chemical homogeneity of high-Cr chromitites as indicator for widespread invasion of boninitic melt in mantle peridotite of Bir Tuluha ophiolite, Northern Arabian Shield, Saudi Arabia. *Ore Geology Reviews, 90*, 243-259. doi: 10.1016/j.oregeorev.2017.03.010

Hulbert, L. J. (1997). Geology and Metallogeny of the Kluane Mafic-ultramafic Belt, Yukon Territory, Canada: Eastern Wrangellia, a New Ni-Cu-PGE Metallogenic Terrane. *Bulletin, Geological Survey of Canada, 506,* 265. doi: 10.4095/208992

Irvine, T. (1965). Chromian spinel as a petrogenetic indicator: Part 1. Theory. *Canadian Journal of Earth Sciences, 2*(6), 648-672. doi: 10.1139/e65-046

Ishii, T. (1992). Petrological studies of peridotites from diapiric serpentinite seamounts in the Izu-Ogasawara-Mariana forearc, Leg 125. *Proceedings of the Ocean Drilling Program, scientific results, 125*, 401-414. doi: 10.2973/odp.proc.sr.125.129.1992

Jagoutz, O., Müntener, O., Ulmer, P., Pettke, T., Burg, J.-P., Dawood, H., & Hussain, S. (2007). Petrology and mineral chemistry of lower crustal intrusions: the Chilas Complex, Kohistan (NW Pakistan). *Journal of Petrology, 48*(10), 1895-1953. doi: 10.1093/petrology/egm044

Kamenetsky, V. S., Crawford, A. J., & Meffre, S. (2001). Factors controlling chemistry of magmatic spinel: an empirical study of associated olivine, Cr-spinel and melt inclusions from primitive rocks. *Journal of Petrology, 42*(4), 655-671. doi: 10.1093/petrology/42.4.655

Kamperman, M., Danyushevsky, L. V., Taylor, W. R., & Jablonski, W. (1996). Direct oxygen measurements of Cr-rich spinel; implications for spinel stoichiometry. *American Mineralogist, 81*(9–10), 1186–1194. doi: 10.2138/am-1996-9-1017

Kapsiotis, A., Rassios, A. E., Uysal, I., Grieco, G., Akmaz, R. M., Saka, S., & Bussolesi, M. (2017). Compositional fingerprints of chromian spinel from the refractory chrome ores of Metalleion, Othris (Greece): Implications for metallogeny and deformation of chromitites within a “hot” oceanic fault zone. *Journal of Geochemical Exploration, 185*, 14-32. doi: 10.1016/j.gexplo.2017.11.003

Kelemen, P., Hirth, G., Shimizu, N., Spiegelman, M., & Dick, H. (1997). A review of melt migration processes in the adiabatically upwelling mantle beneath oceanic spreading ridges. *Philosophical Transactions of the Royal Society of London. Series A: Mathematical, Physical and Engineering Sciences, 355*(1723), 283-318. doi: 10.1098/rsta.1997.0010

Khedr, M. Z., & Arai, S. (2017). Peridotite-chromitite complexes in the Eastern Desert of Egypt: Insight into Neoproterozoic sub-arc mantle processes. *Gondwana Research, 52*, 59-79. doi: 10.1016/j.gr.2017.09.001

Klaper, E. M. (1992). The Paleozoic tectonic evolution of the northern edge of North America: A structural study of northern Ellesmere Island, Canadian Arctic Archipelago. *Tectonics, 11*(4), 854-870. doi: 10.1029/92TC00277

Klaper, E. M., & Ohta, Y. (1993). Paleozoic metamorphism across the boundary between the Clements Markham fold belt and the Pearya terrane in northern Ellesmere Island, Canadian Arctic Archipelago. *Canadian Journal of Earth Sciences, 30*(4), 867-880. doi: 10.1139/e93-072

Lenaz, D., Adetunji, J., & Rollinson, H. (2014). Determination of $Fe^{3+}/\Sigma Fe$ ratios in chrome spinels using a combined Mössbauer and single-crystal X-ray approach: application to chromitites from the mantle section of the Oman ophiolite. *Contributions to Mineralogy and Petrology, 167*(1), 958. doi: 10.1007/s00410-013-0958-2

Malone, S. J., McClelland, W. C., von Gosen, W., & Piepjohn, K. (2018). Detrital zircon U-Pb and Lu-Hf analysis of Paleozoic sedimentary rocks from the Pearya terrane and Ellesmerian Fold Belt (northern Ellesmere Island): A comparison with Circum-Arctic datasets and their implications on terrane tectonics. *Circum-Arctic Structural Events: Tectonic Evolution of the Arctic Margins and Trans-Arctic Links with Adjacent Orogens, 541*, 231. doi: 10.1130/2018.2541(12)

Mattey, D. P, Marsh, N. G., & Tarney, J. (1981). The geochemistry, mineralogy, and petrology of basalts from the West Philippine and Parece Vela Basins and from the Palau-Kyushu and West Mariana Ridges, Deep Sea Drilling Project Leg 59. *Initial Reports of the Deep Sea Drilling Program Leg 59*, 753-800. doi: 10.2973/dsdp.proc.59.137.1981

Oze, C., Fendorf, S., Bird, D. K., & Coleman, R. G. (2004). Chromium geochemistry in serpentinized ultramafic rocks and serpentine soils from the Franciscan complex of California. *American Journal of Science, 304*(1), 67-101. doi: 10.2475/ajs.304.1.67

Pallister, J. S., & Hopson, C. A. (1981). Samail ophiolite plutonic suite: field relations, phase variation, cryptic variation and layering, and a model of a spreading ridge magma chamber. *Journal of Geophysical Research: Solid Earth, 86*(B4), 2593-2644. doi: 10.1029/JB086iB04p02593

Parkinson, I. J., & Pearce, J. A. (1998). Peridotites from the Izu-Bonin-Mariana Forearc (ODP Leg 125): Evidence for Mantle Melting and Melt-Mantle Interaction in a Supra-Subduction Zone Setting. *Journal of Petrology, 39*(9), 1577–1618. doi: 10.1093/petroj/39.9.1577

Pearce, J. A., Barker, P., Edwards, S., Parkinson, I., & Leat, P. (2000). Geochemistry and tectonic significance of peridotites from the South Sandwich arc–basin system, South Atlantic. *Contributions to Mineralogy and Petrology, 139*(1), 36-53. doi: 10.1007/s004100050572

Roeder, P. L., & Campbell, I. H. (1985). The effect of postcumulus reactions on composition of chrome-spinels from the Jimberlana intrusion. *Journal of Petrology, 26*(3), 763-786. doi: 10.1093/petrology/26.3.763

Saumur, B., & Hattori, K. (2013). Zoned Cr-spinel and ferritchromite alteration in forearc mantle serpentinites of the Rio San Juan Complex, Dominican Republic. *Mineralogical Magazine, 77*(1), 117-136. doi: 10.1180/minmag.2013.077.1.11

Schuchert, C. (1923). Sites and nature of the North American geosynclines. *Bulletin of the Geological Society of America, 34*(2), 151-229. doi: 10.1130/GSAB-34-151

Scowen, P., Roeder, P., & Helz, R. (1991). Reequilibration of chromite within Kilauea Iki lava lake, Hawaii. *Contributions to Mineralogy and Petrology, 107*(1), 8-20. doi: 10.1007/BF00311181

Sigurdsson, H., & Schilling, J.G. (1976). Spinels in Mid-Atlantic Ridge basalts: chemistry and occurrence. *Earth and Planetary Science Letters, 29*(1), 7-20. doi: 10.1016/0012-821X(76)90021-2

Sobolev, A. V., & Danyushevsky, L. V. (1994). Petrology and geochemistry of boninites from the north termination of the Tonga Trench: constraints on the generation conditions of primary high-Ca boninite magmas. *Journal of Petrology, 35*(5), 1183-1211. doi: 10.1093/petrology/35.5.1183

Stern, R. J. (2010). The anatomy and ontogeny of modern intra-oceanic arc systems. *Geological Society, London, Special Publications, 338*(1), 7-34. doi: 10.1144/SP338.2

Stevens, R. E. (1944). Composition of some chromites of the western hemisphere. *American Mineralogist: Journal of Earth and Planetary Materials, 29*(1-2), 1-34. Retrieved from https://pubs.geoscienceworld.org/

Surlyk, F., & Hurst, J. M. (1984). The evolution of the early Paleozoic deep-water basin of North Greenland. *Geological Society of America Bulletin, 95*(2), 131-154. doi: 10.1130/0016-7606(1984)95<131:TEOTEP>2.0.CO;2

Torsvik, T. H., Smethurst, M. A., Meert, J. G., van der Voo, R., McKerrow, W. S., Brasier, M. D., Sturt, B. A., & Walderhaug, H. J. (1996). Continental break-up and collision in the Neoproterozoic and Paleozoic: A tale of Baltica and Laurentia. *Earth Science Reviews*, 40, 229–258. doi:10.1016/0012-8252(96)00008-6.

Trettin, H. (1987). Pearya: a composite terrane with Caledonian affinities in northern Ellesmere Island. *Canadian Journal of Earth Sciences, 24*(2), 224-245. doi: 10.1139/e87-025

Trettin, H.P. (1998). Pre-Carboniferous geology of the northern part of the Arctic Islands Northern Heiberg fold belt, Clements Markham fold belt, and pearya; northern Axel Heiberg and Ellesmere Islands. *Bulletin, Geological Survey of Canadia, 425,* XI-239. doi: 10.4095/209572

Trettin, H. P., Parrish, R. R., & Roddick, J. C. (1992). New U-Pb and ^{40}Ar-^{39}Ar age determinations from northern Ellesmere and Axel Heiberg Islands, Northwest Territories and their tectonic significance. *Radiogenic Age and Isotopic Studies: Report 6, Geological Survey of Canada, Paper 92-2,* 3-30. doi: 10.4095/134161

Zheng, J., Griffin, W., O'Reilly, S. Y., Yu, C., Zhang, H., Pearson, N., & Zhang, M. (2007). Mechanism and timing of lithospheric modification and replacement beneath the eastern North China Craton: peridotitic xenoliths from the 100 Ma Fuxin basalts and a regional synthesis. *Geochimica et Cosmochimica Acta, 71*(21), 5203-5225. doi: 10.1016/j.gca.2007.07.028

Zheng, J., O'Reilly, S. Y., Griffin, W., Lu, F., Zhang, M., & Pearson, N. (2001). Relict refractory mantle beneath the eastern North China block: significance for lithosphere evolution. *Lithos, 57*(1), 43-66. doi: 10.1016/S0024-4937(00)00073-6

Books

Deer, W.A., Howie, R.A., & Zussman, J. (1992). *An introduction to the rock-forming minerals* (2nd ed.). Harlow: Longman

Fulay, P., & Lee, J.K. (2016). *Electronic, magnetic, and optical materials*. FL, USA: Crc Press

Lindsley, D. (1991). *Oxide minerals : petrologic and magnetic significance*. Washington, D.C: Mineralogical Society of America

Monroe, J., & Wicander, R. (2014). *The Changing Earth: Exploring Geology and Evolution* (7th ed.). CT, USA: Cengage Learning

O'Reilly, W. (2012). *Rock and mineral magnetism*. Germany: Springer Science & Business Media

Taylor, B. & Natland, J. (1995). *Active margins and marginal basins of the western Pacific*. Washington, DC: American Geophysical Union

Trettin, H. (1991). *Geology of the Innuitian Orogen and Arctic Platform of Canada and Greenland*. Ottawa, Canada: Geological Survey of Canada

Electronic documents

Malone, S. J. (2012). *Tectonic Evolution of Northern Ellesmere Island: Insights from the Pearya Terrane, Ellesmerian Clastic Wedge and Sverdrup Basin* (Ph. D. thesis, University of Iowa, Iowa City, USA). Retrieved from https://ir.uiowa.edu/etd/3496/

Raith M. M., Raase P., & Reinhardt J. (2012). *Guide to Thin Section Microscopy* (2nd ed.). Retrieved from http://www.minsocam.org/msa/openaccess_publications/

Stouge, S., Harper, D. A., Boyce, W. D., & Christiansen, I. K. L. (2012). *Development of the lower Cambrian–Middle Ordovician carbonate platform: North Atlantic Region.* doi: 10.1306/13331509M983508

Resources

Images

Pease, V. (Photographer). (2017, July 20). *Scenic photograph of the Franklinian Mobile Belt* [front page photograph]. Ellesmere Island, Canada: *(unpub.)*

GIS maps

Forbes Halldén, M. *Geologic map of the Audhild Bay sampling site on the Kleybolte Peninsula.* Canadian Geoscience Map 80. Preliminary version. Ottawa, Canada: Geological Survey of Canada, 2016. Using: *QGIS*. Version 2.18. Grüt, Schweiz: QGIS Development Team, Open Source Geospatial Foundation Project, 2019

Forbes Halldén, M. *Geologic map of the Yelverton Bay sampling site at the base of the Mitchell Point Peninsula.* Canadian Geoscience Map 80. Preliminary version. Ottawa, Canada: Geological Survey of Canada, 2016. Using: *QGIS*. Version 2.18. Grüt, Schweiz: QGIS Development Team, Open Source Geospatial Foundation Project, 2019

Related resources:

- Harrison, J.C., Lynds, T., Ford, A., and Rainbird, R.H. *Geology, Simplified tectonic assemblage map of the Canadian Arctic Islands, Northwest Territories–Nunavut.* Preliminary version. 1:2 000 000. Canadian Geoscience Map 80. Ottawa, Canada: Geological Survey of Canada, 2016*
- Porter, C.; Morin, P., Howat, I., Noh, M.J., Bates, B., Peterman, K., Keesey, S., Schlenk, M., Gardiner, J., Tomko, K., Willis, M., Kelleher, C., Cloutier, M., Husby, E., Foga, S., Nakamura, H., Platson, M., Wethington, M. Jr., Williamson, C., Bauer, G., Enos, J., Arnold, G., Kramer, W., Becker, P., Doshi, A., D'Souza, C., Cummens, P., Laurier, F., Bojesen, M. *ArcticDEM*. 10m resolution, alt. ≈ 300m. [MA, USA]: Harvard Dataverse, 2018**

Forbes Halldén, M. *Regional geologic map of Ellesmere Island.* Canadian Geoscience Map 80. Preliminary version. Ottawa, Canada: Geological Survey of Canada, 2016. Using: *QGIS*. Version 2.18. Grüt, Schweiz: QGIS Development Team, Open Source Geospatial Foundation Project, 2019

Forbes Halldén, M. *Topographical and structural map of a circa 150 km long strip of the northwestern Ellesmere Island coast.* Canadian Geoscience Map 80. Preliminary version. Ottawa, Canada: Geological Survey of Canada, 2016. ArcticDEM. MA, USA: Harvard Dataverse, 2018. Using: *QGIS*. Version 2.18. Grüt, Schweiz: QGIS Development Team, Open Source Geospatial Foundation Project, 2019

Forbes Halldén, M. *World map centered on Ellesmere Island and the northern North American plate.* Azimuthal ortographic

* doi:10.4095/297416
** https://www.pgc.umn.edu/data/arcticdem/ doi: 10.7910/DVN/OHHUKH

projection. Tectonic plates GIS data. CA, USA: Bird, P., Ahlenius, H., 2014. Natural Earth. USA: Patterson, T. Kelso, N. V., 2009. Using: *QGIS*. Version 2.18. Grüt, Schweiz: QGIS Development Team, Open Source Geospatial Foundation Project, 2019

Related resources:

- Bird, P. Ahlenius, H. *Tectonic plates GIS data.* 1.0. Sweden: Nordpil, 2014. (2014). CA, USA: Sweden: Nordpil[***]
- Bird, P. (2003). An updated digital model of plate boundaries. *Geochemistry, Geophysics, Geosystems*, *4*(3). doi: 10.1029/2001GC000252
- Patterson, T. Kelso, N.V. (2009). *Natural Earth*. USA: North American Cartographic Information Society (NACIS)[****]

Software

Ferracutti, G. R., Gargiulo, M. F., Ganuza, M. L., Bjerg, E. A., Castro, S. M. (2015). End Members Generator (8.0) [Computer software]. Buenos Aires, Argentina: VyGLab. Retrieved from: http://vyglab.cs.uns.edu.ar/

Related publications:

- Droop, G. (1987). A general equation for estimating Fe^{3+} concentrations in ferromagnesian silicates and oxides from microprobe analyses, using stoichiometric criteria. *Mineralogical magazine, 51*(361), 431-435. doi: 10.1180/minmag.1987.051.361.10
- Ferracutti, G. R., Gargiulo, M. F., Ganuza, M. L., Bjerg, E. A., Castro, S. M. (2015). Determination of the spinel group end-members based on electron microprobe analyses. *Mineralogy and Petrology, 109*(2), 153-160. doi: 10.1007/s00710-014-0363-1
- Weast, R. C. (1974). *Handbook of chemistry and physics.* OH, USA: CRC Press

Thompson, T. A., Baedke, S.J. (2009). TriPlot (4.1.2) [Computer software]. IN, USA: Todd Thompson Software. Retrieved from: http://mypage.iu.edu/~tthomps/programs/html/

[***] https://nordpil.com/resources/tectonic-plates-gis-data/
[****] https://www.naturalearthdata.com/

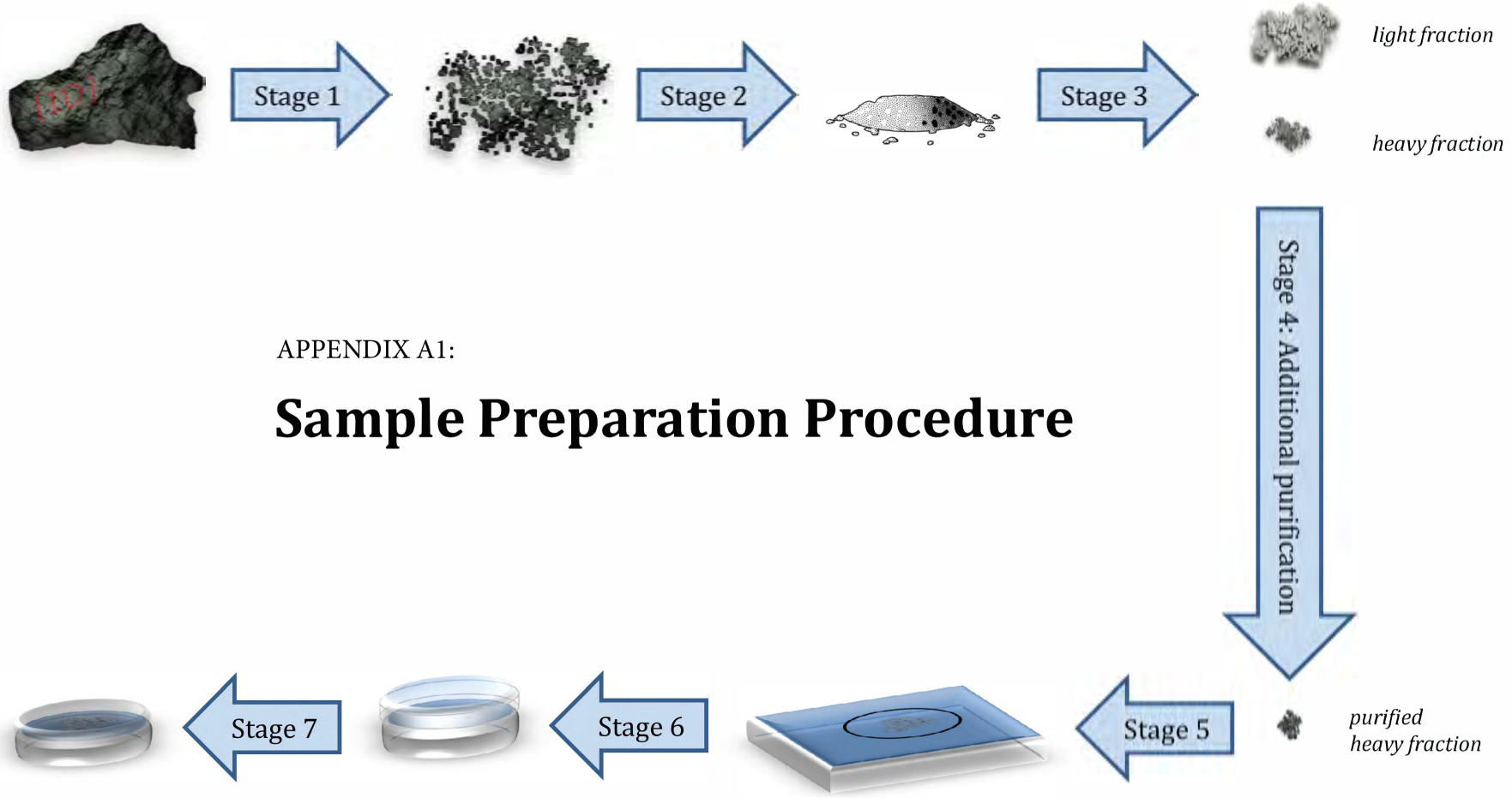

APPENDIX A1:

Sample Preparation Procedure

Stage 1 – Raw sample into gravel

If the ID-marked sample rocks consisted of pieces larger than Ø 9cm, which was often the case, these pieces were broken into more manageable sizes with a sledgehammer. If the rock was too compact to yield good-sized fragments this way, they were instead split using a wet diamond blade circle saw. When the sample volume allowed it, a small, representative hand sample was ID-marked and removed from the rest of the sample for archive purposes. Care was taken to only use rock fragments larger than gravel size (>2 cm) post breaking, that with full confidence could be identified as derivatives of the original sample rock.

Ø2- 9cm rocks were disintegrated into roughly gravel size fragments with a *Retsch* Jaw Crusher BB 200(image: left), equipped with stainless steel teeth. The jaw crusher was burnished with steel brushes and cleaned with deionized water and ethanol thoroughly between the handling of every sample to avoid metal shavings in the output gravel and cross contamination.

Photo: Retsch (n.d.). *Jaw Crusher BB 200.* From official website. Retrieved from: https://www.retsch.com/imgdb/-256x-max-alpha/sl/b4563ef8f4658fd86991e087a0118fd2.png

Stage 2 – Gravel into sand

The fresh gravel was handled using clean stainless-steel tools only. From the gravel, a portion was set aside for archive in an ID-marked plastic jar, and the rest ground into fine sand, using a *Retsch* Vibratory Disc Mill RS 200 equipped with a stainless-steel mortar(image: left). In the rare occasion of exceptionally small samples (17HSB-3 and 17HSB-4), no gravel was saved for the archive.

The rotation speed setting was chosen for each individual sample somewhere between 700-900 RPM based on the texture of the rock pieces, with higher speeds selected for the more unyielding rock types. Due to the limited volume of the mortar, the gravel had to be milled in portions and the running time varied between each sample. The adequacy of the particle size was assessed at intervals by pinch-sized spot tests of the sample in progress. The pinch of particles, initially removed from the mortar using tweezers, was discarded after the assessment.

The interior of the grinder and the mortar were cleaned between each sample to avoid metal shavings in the output sand and cross contamination. The interior of the grinder was wiped off with deionized water and dried with paper towels. The mortar and disc were burnished with steel brushes and thoroughly cleaned with deionized water and ethanol and thereafter air dried.

Photo: Retsch (n.d.). *Vibratory Disc Mill RS 200*. From official website. Retrieved from: https://www.retsch.com/imgdb/-256x-max-alpha/sl/4aa155ca98ff6df3511aeea8f1f0685c.png

Stage 3 – Mineral separation

A *Holman-Wilfley* 800 Shaking Table was used to separate the fine sand into light and heavy mineral fractions. All exposed surfaces of the table and the plastic containers used in the process were washed with warm water and dish soap before and after every use to avoid cross-contamination. Two different techniques were practiced at this stage; the scooping method (illustration: **A**) and the hanging bag method (illustration: **B**). Warm water was used for both techniques. Samples and the respective practiced techniques are specified in the table below.

The heavy mineral fraction was carefully washed with deionized water and ethanol before it was transferred to a marked Petri dish and left to dry overnight in an oven at a maximum temperature of 50° C to avoid aiding or enabling potential interfering chemical reactions. The light mineral fraction was also left in the oven to dry overnight and once dry, saved in a marked plastic bag for potential reiteration of the mineral separation if the yield of the heavy fraction was too small.

The dried heavy mineral fraction was transferred from the Petri dish onto waxing paper. The waxing papers were folded into a small envelopes and marked for storage before the contents of the envelopes were assessed using a *Leica* MZ12 stereomicroscope.

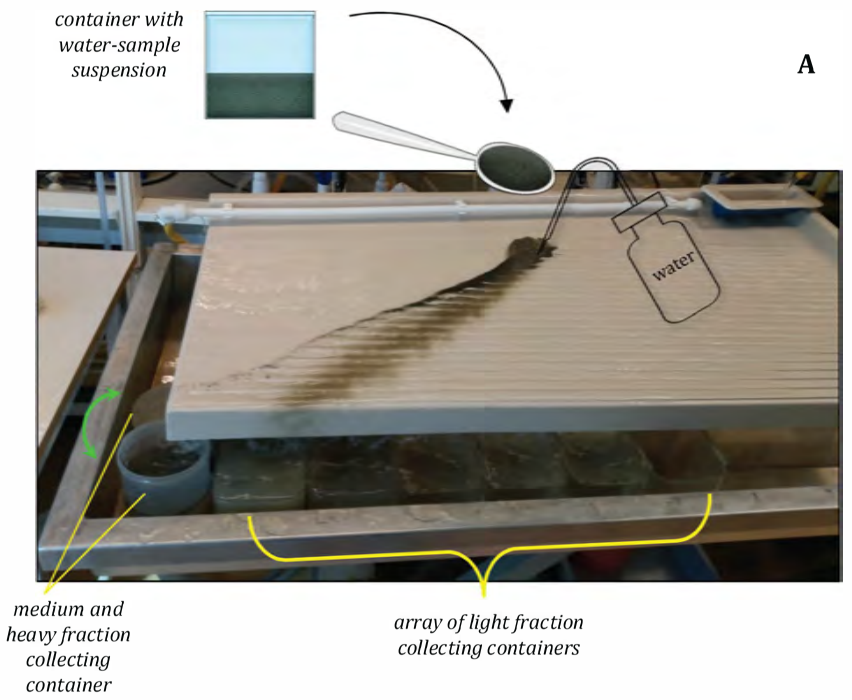

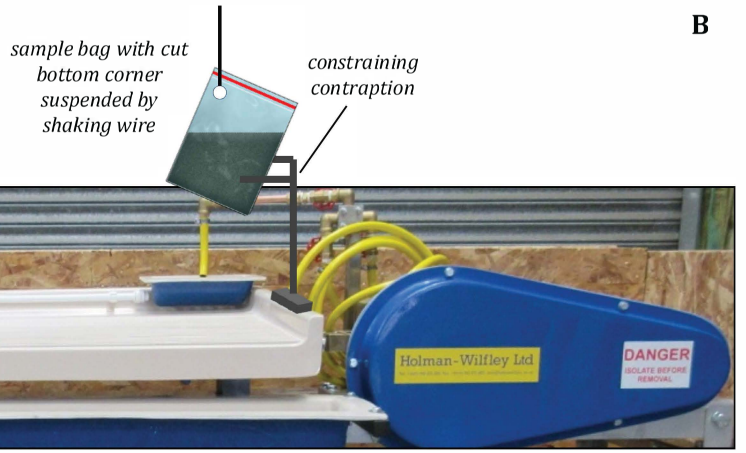

Sample	Scooping Method	Hanging Bag Method
17HSB-3	✔	
17HSB-4	✔	
VP17-01	✔	
VP17-04b		✔
VP17-05b		✔
VP17-15		✔

Photo: University of Washington (2017). *Holman-Wilfley Model 800 Table.* Retrieved from http://pita.ess.washington.edu/rockprep/wp-content/uploads/sites/5/2017/04/Wilfley_manual.pdf.

Stage 4 – Purification: Panning and magnetic separation

Panning: For the samples that contained significantly larger grains or grain aggregates of relatively low density, some purification was achieved through dry panning. Separation is achieved by applying the principles of granular segregation by the shaking of a disposable paper container that acted as working area and brushing off the unwanted low-density particles., which were more easily mobilized than the high-density counterparts. The low density particles were discarded. All samples but 17HSB-3 and 17HSB-4 were dry panned.

Magnetic separation: For the samples that contained significant proportions of metal shavings and unwanted pure magnetite spinel end-members, these unwanted particles were removed using a weak magnet covered in waxing paper. The sample particles were spread out in a Petri dish and the magnet lowered down to hover over the particles to attract the magnetic particles(illustration: **A**). When the magnet is moved away from the Petri dish, the purified non-magnetic fraction stays behind. The magnetic particles were transferred to a separate waxing paper envelope that was saved for future reference (illustration: **B**). The waxing paper that covered the magnet, which prevents any direct contact between magnet, was discarded after each use. The samples VP17-01, VP17-04b, VP17-05b and 17HSB-3 were separated this way.

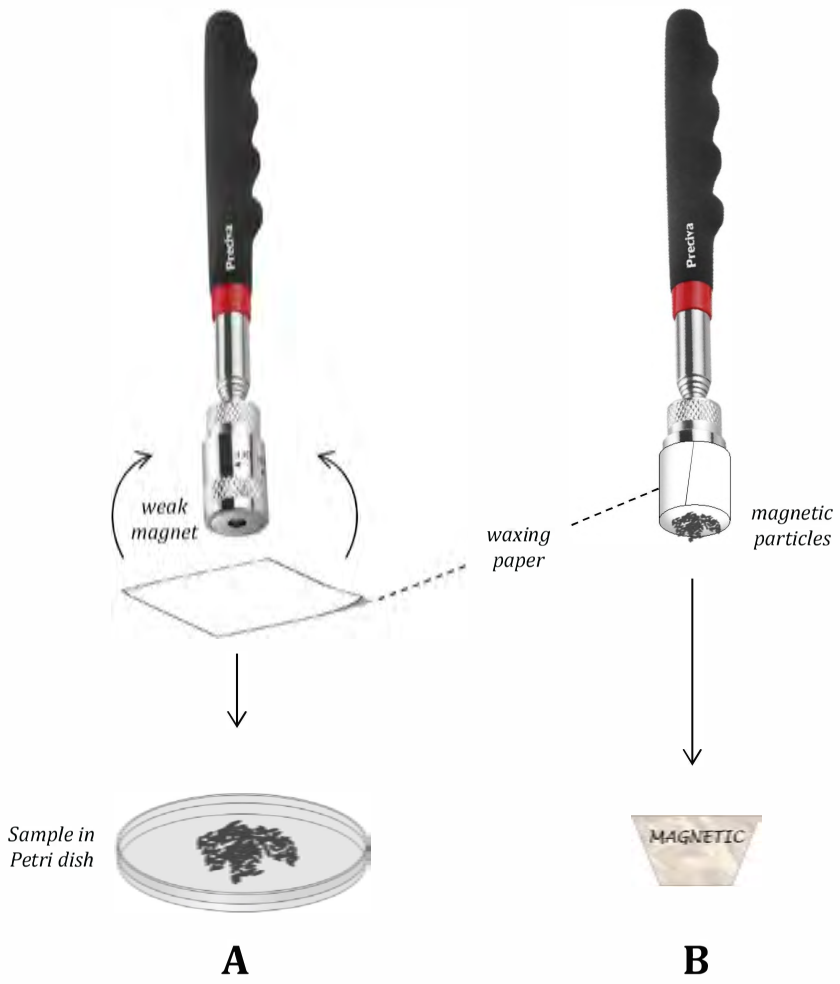

Stage 4 (continued) – Purification: Heavy liquid mineral separation

Some samples required more advanced purification that what could be achieved through simple panning and magnetic separation. These were purified by heavy liquid separation. A simplified illustration of how this technique utilized the gravity settling principle is provided to the right, omitting the mechanisms for recycling of the high-density liquid after trapping the heavy and light mineral fractions in filter papers (grade 00H; particle retention 1-2 µm). The recycling process used a switchable Buchner flask system with a motor for channelized suction. The liquid that was used as separation medium was 99+% stabilized diiodomethane with a density of 3.325 g/cm^3, and acetone was used for flushing excess liquid off of the separation funnel interior and washing the liquid off of the mineral grains. The acetone was dried off the filter papers under a fume hood before the fractions were transferred to separate, marked wax paper envelopes. VP17-04b and VP17-15 were purified using this technique.

A second assessment of the purified samples under the microscope was made before potential oxide grains were dry picked with the aid of the *Leica* MZ12 stereomicroscope for the Ø25 mm grain mounts.

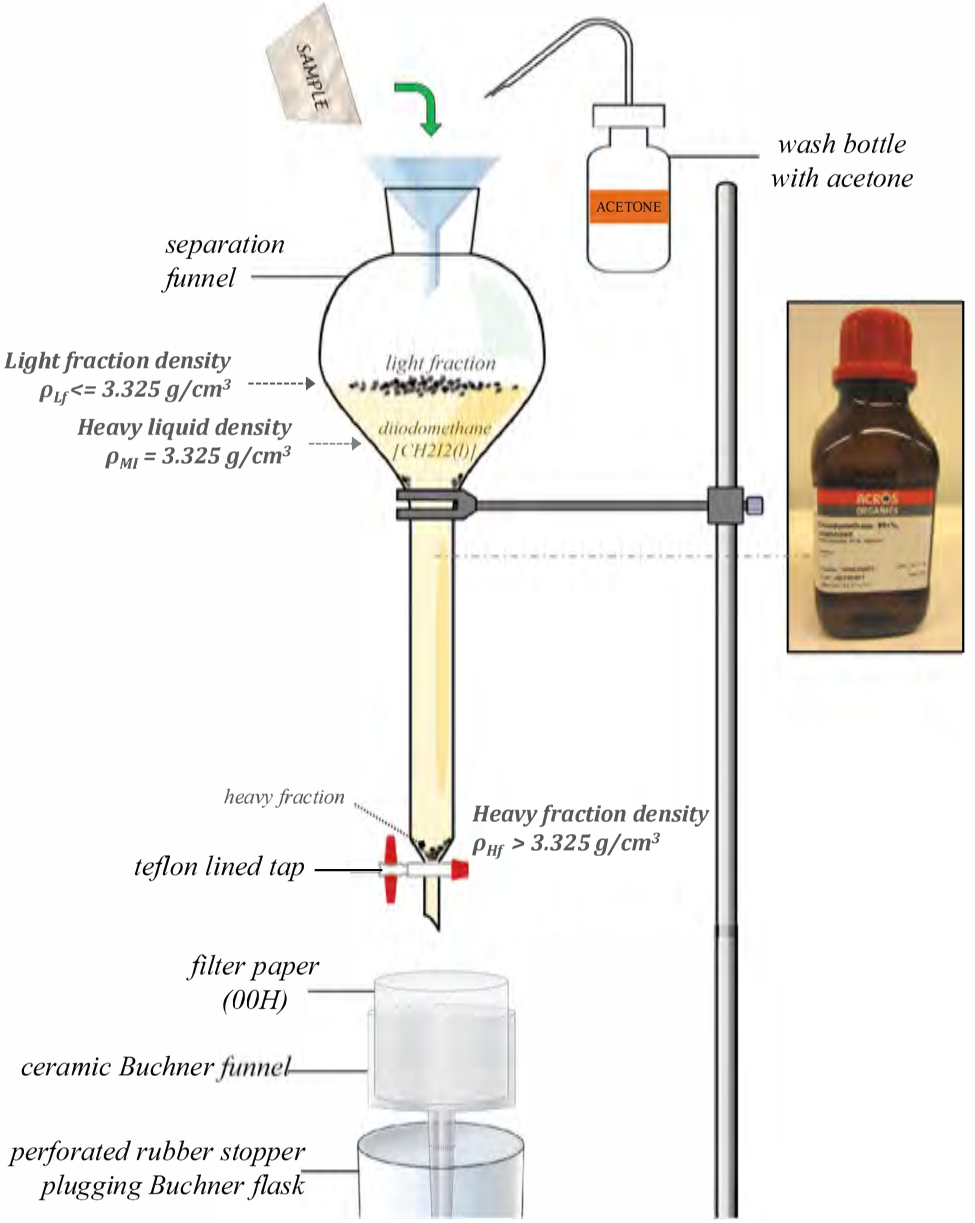

Stage 5 – Picking and mounting

Circular outlines of the grain mounts were drawn with a pen onto cut-out squares of *Plexiglas* prepared with a strip of double-sided tape. Allotted sample spaces were drawn on the tape inside the circular outline in a non-symmetric but systematic pattern so as to ensure the possibility of identification of the individual spaces from the shape of the pattern after the final processing when the ink from the pen has been polished off. Each *Plexiglas* square was marked with an identification number (1-2) and a map of the sample occupation of the spaces copied onto paper(images: top right).

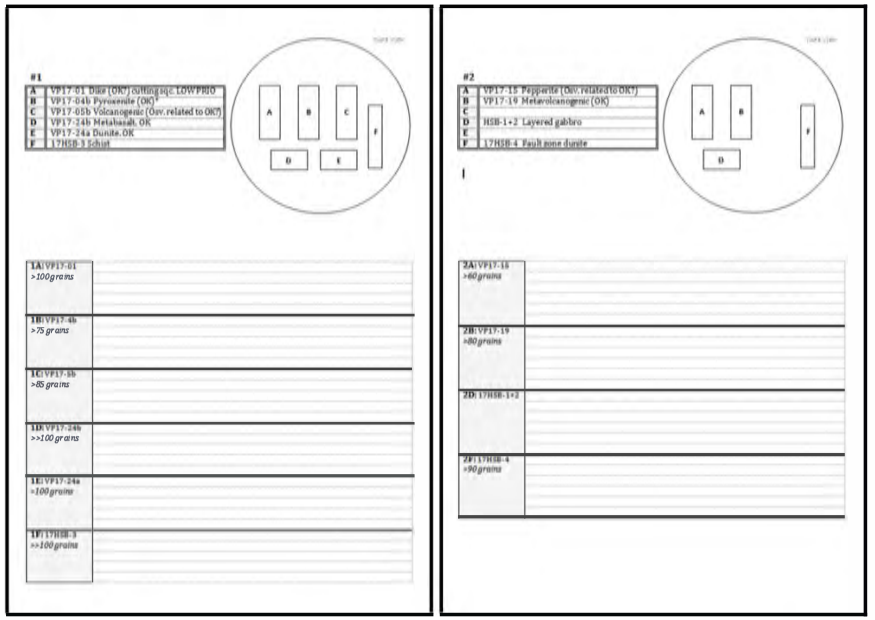

Ideally, only same-sized grains of similar hardness should be picked for each individual grain mount and the (relatively) smaller grains should be placed at the center of the mount, since the polishing procedure tends to grind down the edges of the mount to a larger extent than the center. Due to time pressure, material limitations and the heterogenetic nature of the samples themselves, some of these guidelines had to be overlooked when the grains were being picked and mounted.

Potential oxide grains were dry picked using single-hair brushes and carefully placed onto the sticky double-sided tape within the confinements of an allotted space. Each distribution map, marked with the identification number corresponding to the *Plexiglas* square, was additionally marked with an alphabetical space identifier (A-F) for each of the sample spaces, e.g. in sample space 1A: sample VP17-01, for mount 1, space A sample VP17-01.

The sticky surface was resealed with adhesive-protection wrap and the grains were vigorously pressed down into the adhesive and photographed (image: bottom right) before they were cast in epoxy resin during the next stage.

Stage 6 – Casting in epoxy

The casting was performed at the Swedish Museum of Natural History, using a *Struers* CitoVac vacuum impregnation unit (image: bottom right). 15 ml *EpoFix* Resin and 2 ml *EpoFix* Hardener were mixed in a tilted plastic cup in a circular motion with a wooden spatula for exactly 120 seconds to reduce bubbles in the epoxy mix. The essentially bubble-free mix was transferred with a syringe from the cup to a plastic tube connected to the impregnation unit, which pours the epoxy resin mix into the mold under vacuum to minimize bubbles. The epoxy resin was left to harden for more than 96 hours before the final polishing (image: top right).

Photo: Struers (n.d.). *CitoVac*. From official website. Retrieved from: https://cdnstruersproduction.azureedge.net/-/media/Struers-media-library/Products/Mounting/Mounting-equipment/CitoVac/CitoVac-Product-Overview-M28/CitoVac-1024x665-px.jpg?h=665&la=en&w=1024&hash=5E9C25BF3E4FB1E4365BF751D9A9863674AB79CB. Copyright 2019 by Struers.

Stage 7 – Polishing and final coating

The hardened mounts were hand-polished in the lab at the Memorial University of Newfoundland in Canada, sequentially from coarse grinding to fine polishing. Sandpaper (particle size: 9.2 µm), diamond film (particle size: 3 µm) and aluminum powder (particle size: 1 µm) were used as grit combined with deionized water. The mounts were systematically turned 90° at short time-constrained intervals during the polishing and frequently rinsed under a flow of tap water and in an ultrasonic bath.

The dried, polished mounts were carbon coated using a *Cressington* 208carbon High Vacuum Carbon Coater (image: right) and the thickness was monitored using the polished brass visual technique. By simultaneously coating a roundel of polished brass with the grain mounts, the thickness of the coat can be determined with good accuracy by the display of the interference color from the graphite film on the brass roundel in normal light. A thickness of approx. 200 Å to match the standards used for the chemical analysis was achieved when the interference color was somewhere between indigo red and blue.

APPENDIX A2:

Walkthrough of the stoichiometric algorithm for calculating ferric content from electron microprobe data: with worked example

The following walkthrough is largely based on an online exercise[1] published by Prof. John B. Brady (Smith College) using raw electron microprobe data from VP17-05b.

Any oxide i consists of a number of ionic species s of opposite electrostatic charge, in numbers henceforward referred to as the ideal number of cations c_i (+) and the ideal number of oxygen anions o_i (-). E.g for magnesium oxide MgO, $c_{MgO} = 1$ and $o_{MgO} = 1$. Index c refers to the inferred cation, i.e. Mg^{2+} (oxidation state $v = +2$) and index o to the anion O^{2-}.

The amount of substance $n_{s,i}$ of any faction of ionic species (cations or anions) in an oxide can be derived from the electron microprobe measurements using

$n_{s,i} = \frac{W_{\%,i} \cdot s_i}{M_i}$ where M_i is the molar mass $[g/mol]$ for the oxide.

ELECTRON MICROPROBE DATA: *VP17-05b Grain 1 Point 5*							
Oxide, *i*	**Weight percent, $W_{\%}$**	**Number of cations, *c***	**Number of anions, o**	**Cation valency, *v***	*** Molar mass, *M***		**Amount of cation substance, n_c**
NiO	0.0266	1	1	+2	74.6928		0.0004
MnO	0.3296	1	1	+2	70.9374		0.0046
TiO2	0.0256	1	2	+4	79.8658		0.0003
CaO	0.0031	1	1	+2	56.0774		0.0001
Al2O3	8.3550	2	3	+3	101.96128		0.1639
SiO2	0.0395	1	2	+4	60.0838		0.0007
MgO	9.7564	1	1	+2	40.3044		0.2421
FeO	18.2454	1	1	+2	71.8444		*0.2540*
Cr2O3	62.8911	2	3	+3	151.9904		0.8276
V2O3	0.1244	2	3	+3	149.8812		0.0017
Fe2O3	*0.0000*	2	3	+3	159.6882		*0.0000*
TOTAL:	*99.7967*					**Σn_s =**	1.4952

Table 1 Initial configuration begins with calculating cation substance of mass from raw electron microprobe data. **The atomic weights[2] used here are not the same as those used by the End-Member Generator 8.0 software*

[1] Brady, J. B. (2019, March 11). Mineral Formulae Recalculation. Retrieved March 16, 2019, from https://serc.carleton.edu/research_education/equilibria/mineralformulaerecalculation.html

[2] IUPAC Commission on Isotopic Abundances and Atomic Weights. (2017). ATOMIC WEIGHTS OF THE ELEMENTS 2017. Retrieved January 1, 2019, from http://www.qmul.ac.uk/sbcs/iupac/AtWt/

The electron microprobe initially assumes that $W_{\%,Fe2O3} = 0$ (i.e. $n_{c,Fe2O3} = 0$), even though this may not actually be accurate. To test this, the calculated cation charge from the measured mass is checked against the ideal spinel formula unit. In the formula unit, there are 3 cations with an electrostatic charge sum of +8 and 4 oxygen anions, with an electrostatic charge sum of -8, which balance each other out.

The general formula for calculating the electrostatic charge e from mass for any ionic species is

$$e_{s,i} = v_{s,i} \cdot n_{s,i}$$

But for the purpose of these calculations, this formula is only applied to cations, since the number of oxygen anions present was assumed as per one of the stated initial conditions, and was never measured in any way. For this reason, the anionic charge must be assumed to be equivalent to, but of the opposite sign of, the corresponding cation charge.

Ideal stoichiometry is assumed but reality is seldom ideal. Since whole spots are analyzed as opposed to individual molecules, small heterogeneities at any given spot will shift the results away from the ideal and this will also most likely be reflected in the sum of cation charges $\sum_i e_c$ calculated from the measurements. To account for this, the amount of substance is substituted with a combined factor of atomic proportions of the individual cation's amount of substance to the total amount of cation substance multiplied by the ideal amount of substance of cations in the spinel formula unit:

$$p_{c,i} = \frac{C \cdot n_{c,i}}{\sum_{i \neq Fe2O3} n_{c,i}} \text{ where } C = 3\ mol$$

As indicated by the summation index, this formula is not applied to the ferric oxide component, which hitherto has been ignored. Since the amount of ferric substance has been assigned a zero value, the equation will generate a zero value result. Additionally, the value generated for Fe^{2+} in FeO is only preliminary in the sense that it currently accounts for all iron content, not only ferrous iron, but this value will be corrected later on when the ferric portion has been deducted.

	Amount of cation substance, n_c	Cation species	Cation proportions, p_c
	0.0004	Ni^{2+}	0.0007
	0.0046	Mn^{2+}	0.0093
	0.0003	Ti^{4+}	0.0006
	0.0001	Ca^{2+}	0.0001
	0.1639	Al^{3+}	0.3288
	0.0007	Si^{4+}	0.0013
	0.2421	Mg^{2+}	0.4857
	0.2540	Fe^{2+}	*0.5096*
	0.8276	Cr^{3+}	1.6605
	0.0017	V^{3+}	0.0033
	0.0000	Fe^{3+}	
Σn_s =	1.4952	**Σp_c =**	3.0000

Table 2 The amounts of substances of cations n_c are adjusted to their corresponding amounts when ideal stoichiometry is assumed in the form of the proportion factor p_c.

The proportion factor $p_{c,i}$ can now be substituted into the equation that calculates the sum of electrostatic cation charge, which will be compared to respective sum in the ideal spinel formula unit, +8.

$$\sum_i e_c = \sum_i v_{c,i} \cdot p_{c,i}$$

The oxide Fe_2O_3 can be assumed to be present ($W_{\%,Fe2O3} \subseteq W_{\%,FeO}$) if the conditions *a)-e)* are met, in proportions that are equal to the derived difference in condition *e).*

a) iron is the only cation with variable valency,

b) oxygen is the only type of anion present,

c) the measured point is electrostatically balanced,

d) each point of measurement contains only negligible amounts of elements not measured

and

e) $8 - \sum_i e_c > 0$

Additional calculations must then be performed to correct for the ferric content that is present. Thus, charge balance is instituted when $p_{c,Fe2O3} = 8 - \sum e_{c,i}$ and $p_{c,FeO}^{recalculated} = p_{c,FeO} - p_{c,Fe2O3}$. These proportions can then be used to calculate a new value for the weight percentages $W_{\%}$ of FeO and Fe_2O_3.

Cation species		**Cation proportions, p_c**
Ni^{2+}		0.0007
Mn^{2+}		0.0093
Ti^{4+}		0.0006
Ca^{2+}		0.0001
Al^{3+}		0.3288
Si^{4+}		0.0013
Mg^{2+}		0.4857
Fe^{2+}		**0.5061**
Cr^{3+}		1.6605
V^{3+}		0.0033
Fe^{3+}		**0.0034**
$\Sigma e_{c,i}$ =	7.9966	

Table 3 The difference between the calculated and ideal charge sums is used to calculate new proportions factors for the iron oxides to achieve charge balance.

Because the relationship between the derived amounts of substances $n_{c,i}$ and the calculated proportion factor $p_{c,i}$ should be equal for all oxides, this relationship is ultimately used to calculate the new weight percentages for the two iron oxides (hereafter referenced to with index x). For batch calculations, it is prudent to choose an ubiquitous oxide, such as Al_2O_3, since the relationship cannot be used if an oxide is absent ($W_{\%,i} = 0$) and attempting to do so will most likely generate a false zero value for $W_{\%,x}$.

The relationship can thus be expressed as $\frac{n_{c,i}}{p_{c,i}} = \frac{n_{c,x}}{p_{c,x}}$ where e.g. $i = Al_2O_3$ would be an appropriate choice.

Because weight percent $W_{\%,i}$ can also be expressed as $\frac{m_i}{\sum m} \cdot 100\%$, the general formula for calculating the amount of substance $n_i = \frac{m_i}{M_i}$ can be rewritten for the cationic species in an oxide as $\frac{W_{\%,i} \cdot c_i}{100\% \cdot M_i}$. By substituting this into the previously defined relationship with e.g. Al_2O_3, $W_{\%,x}$ can be factored out:

$$\frac{n_{c,Al2O3}}{p_{c,Al2O3}} = \frac{n_{c,x}}{p_{c,x}} \xrightarrow{substitute} \frac{\frac{W_{\%,Al2O3} \cdot c_{Al2O3}}{100\% \cdot M_{Al2O3}}}{p_{c,Al2O3}} = \frac{\frac{W_{\%,x} \cdot c_x}{100\% \cdot M_x}}{p_{c,x}}$$

$$\xrightarrow{simplify} \frac{W_{\%,x} \cdot c_x}{\cancel{100\%} \cdot M_x} = \frac{W_{\%,Al2O3} \cdot c_{Al2O3} \cdot p_{c,x}}{p_{c,Al2O3} \cdot \cancel{100\%} \cdot M_{Al2O3}}$$

$$\xrightarrow{factor\ out} W_{\%,x} = \left[\frac{W_{\%,Al2O3} \cdot c_{Al2O3}}{p_{c,Al2O3} \cdot M_{Al2O3}}\right] \cdot \frac{p_{c,x} \cdot M_x}{c_x}$$

Due to the updated the weight percentage values of the iron oxides, the total weight percent will also change as a result:

Oxide, *i*	Weight percent, $W_{\%}$
NiO	0.0266
MnO	0.3296
TiO2	0.0256
CaO	0.0031
Al2O3	8.3550
SiO2	0.0395
MgO	9.7564
FeO	**18.1223**
Cr2O3	62.8911
V2O3	0.1244
Fe2O3	**0.1368**
TOTAL:	**99.8104**

Table 4 The new weight percentages for the iron oxides and total weight percent.

APPENDIX B1: Petrography - *Microscope images*

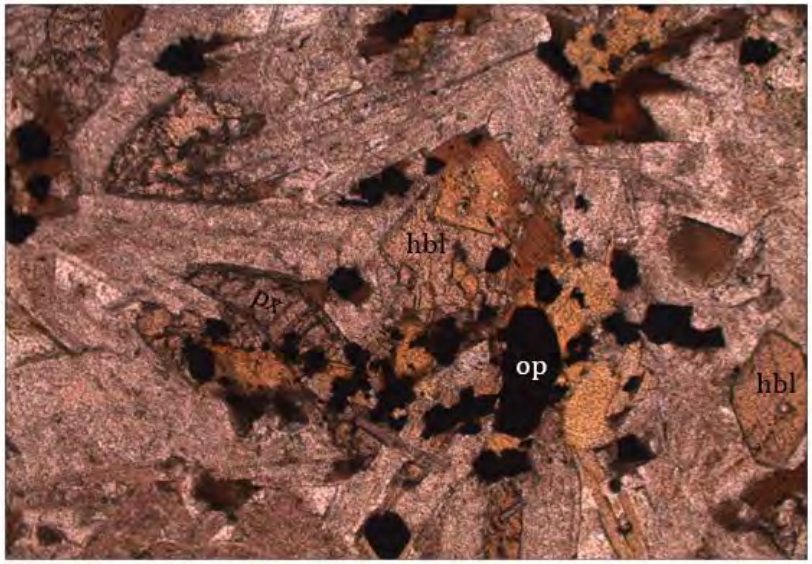

VP17-01 ***PPL*** *FOV: 1.40 mm*

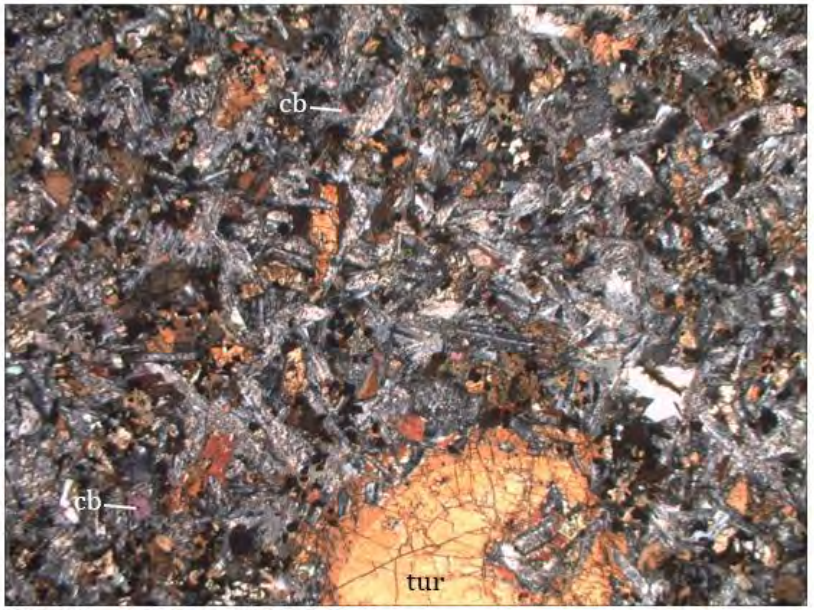

VP17-01 ***XPL*** *FOV: 5.60 mm*

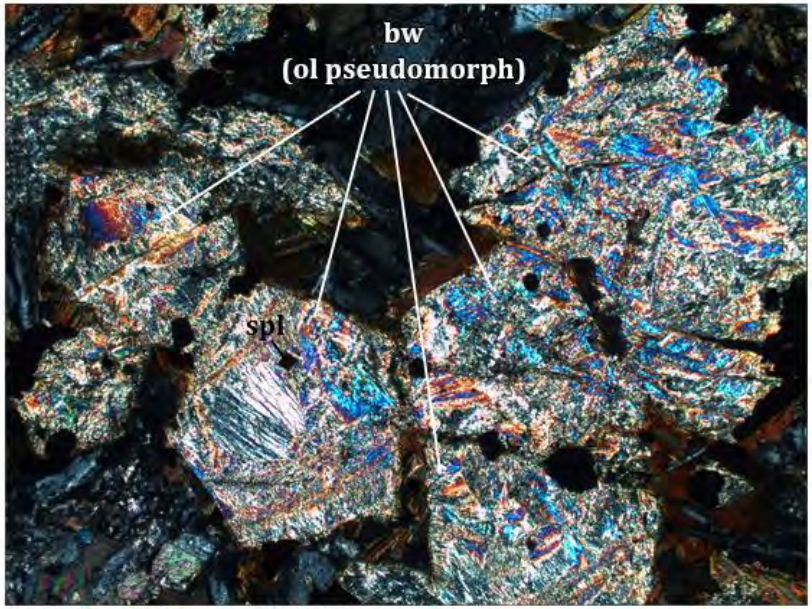

VP17-01 ***XPL*** *FOV: 1.40 mm*

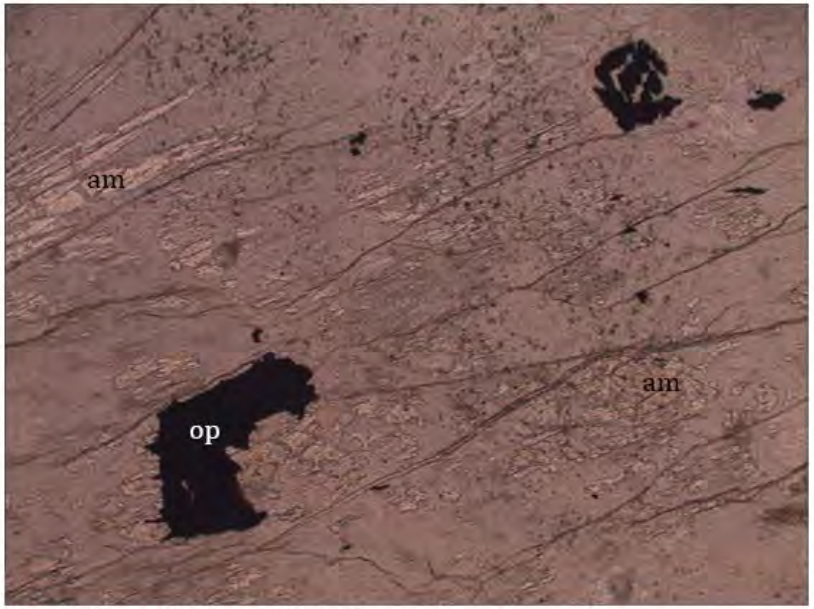

VP17-04b ***PPL*** *FOV: 0.70 mm*

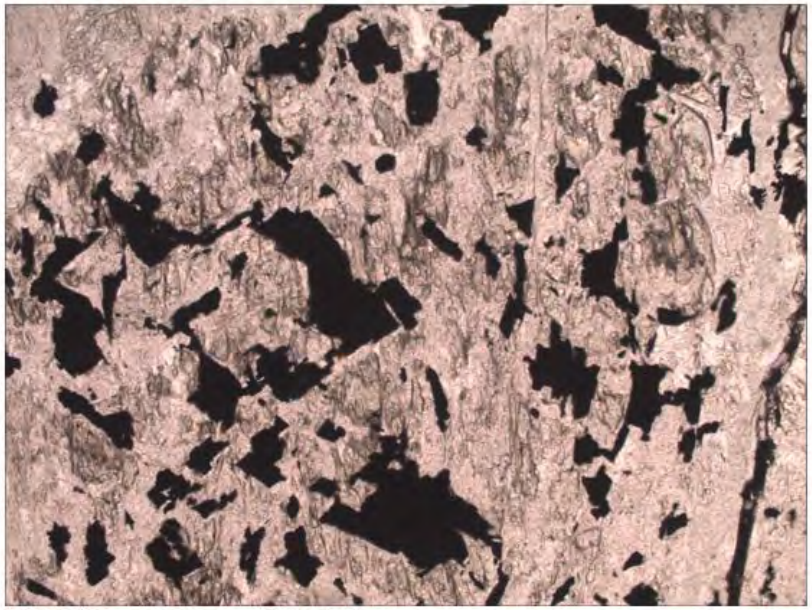

VP17-04b ***PPL*** *FOV: 0.70 mm*

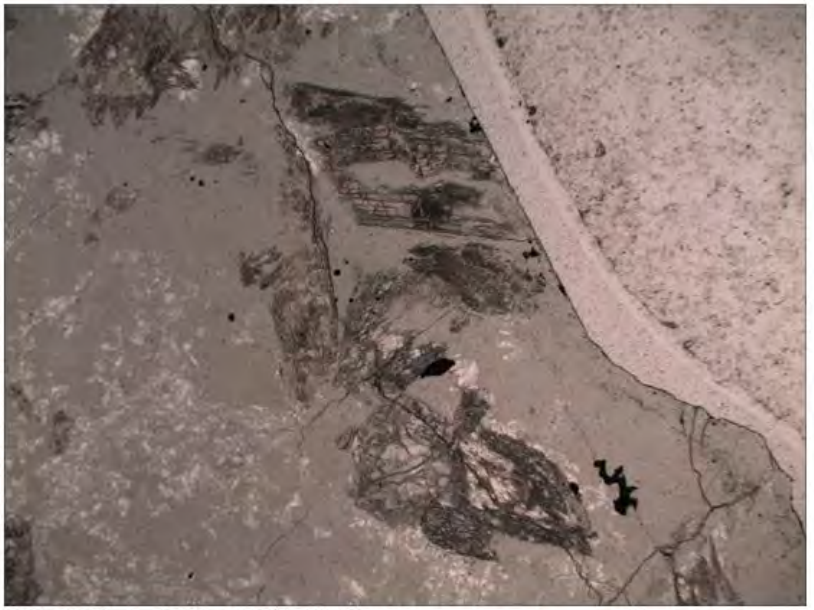

VP17-04b ***PPL*** *FOV: 1.40 mm*

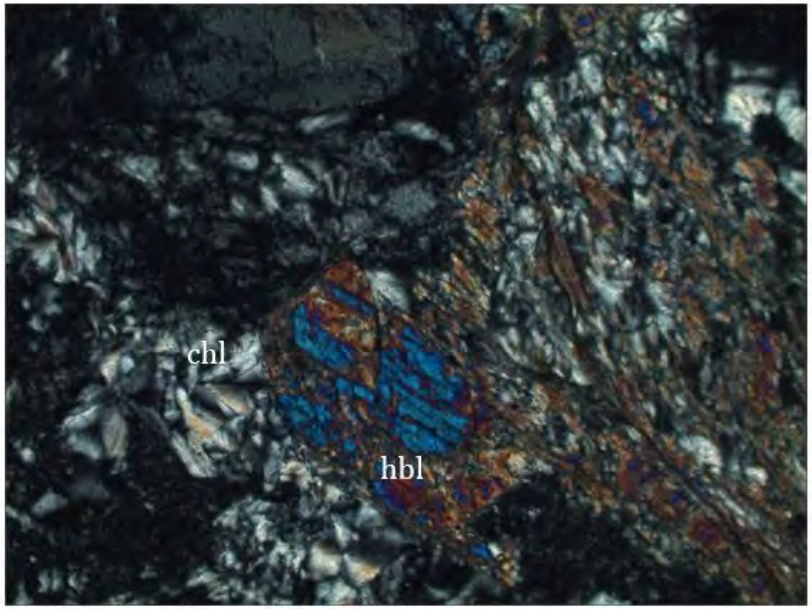

VP17-04b ***XPL*** *FOV: 0.70 mm*

VP17-04b ***PPL*** *FOV: 0.70 mm*

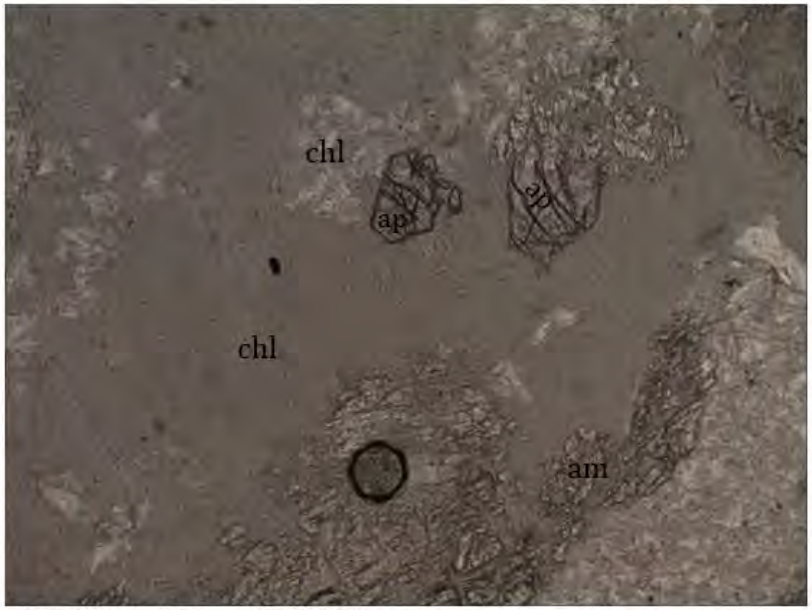

VP17-04b ***PPL*** *FOV: 0.70 mm*

VP17-15 ***XPL*** *FOV: 1.40 mm*

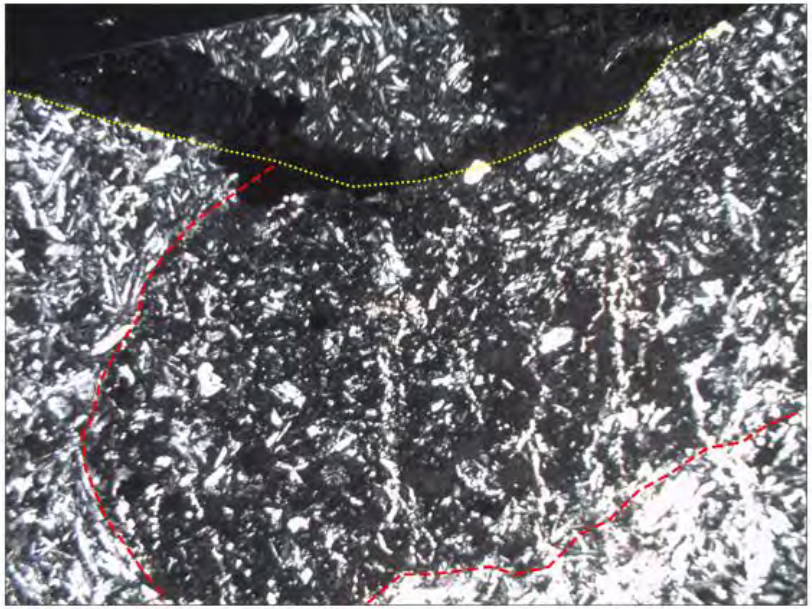

VP17-15 ***XPL*** *FOV: 1.40 mm*

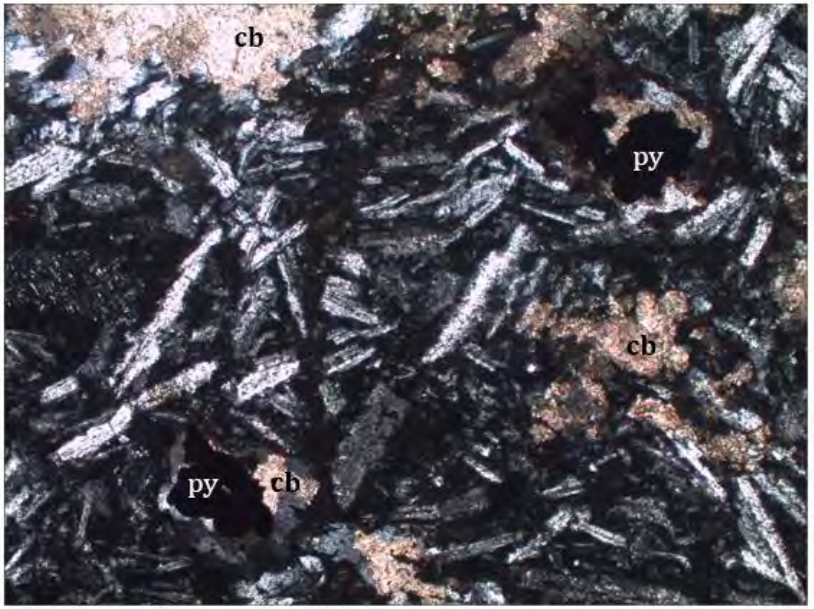

VP17-15 ***XPL*** *FOV: 0.70 mm*

2D element distribution collage 10.
VP17-01 Grain #2

MAJOR ELEMENT X-RAY MAPS

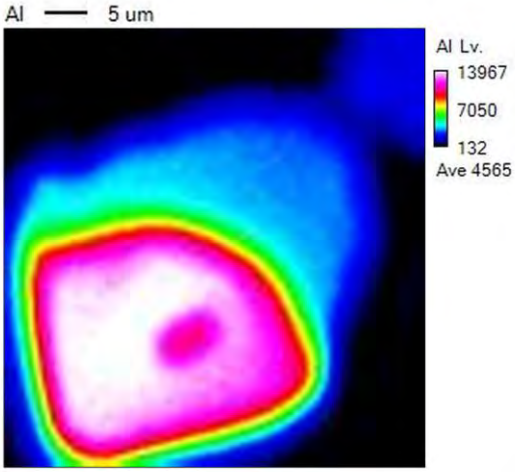

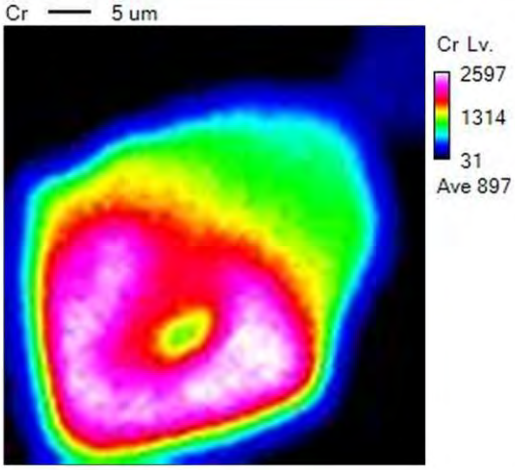

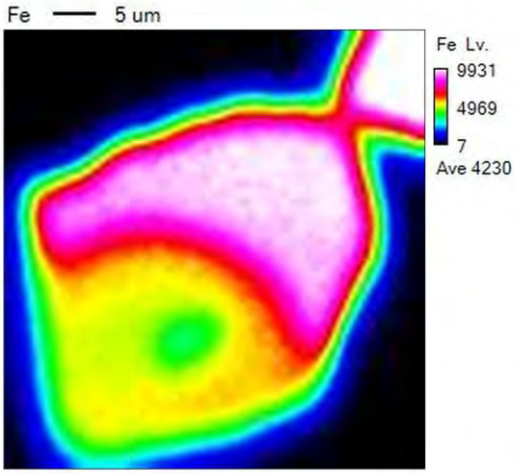

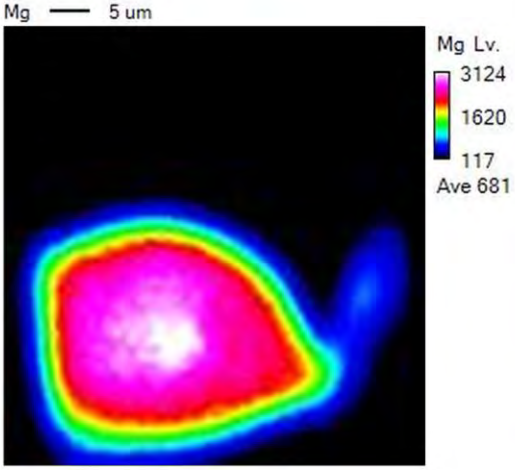

Backscatter electron image of compositional variations

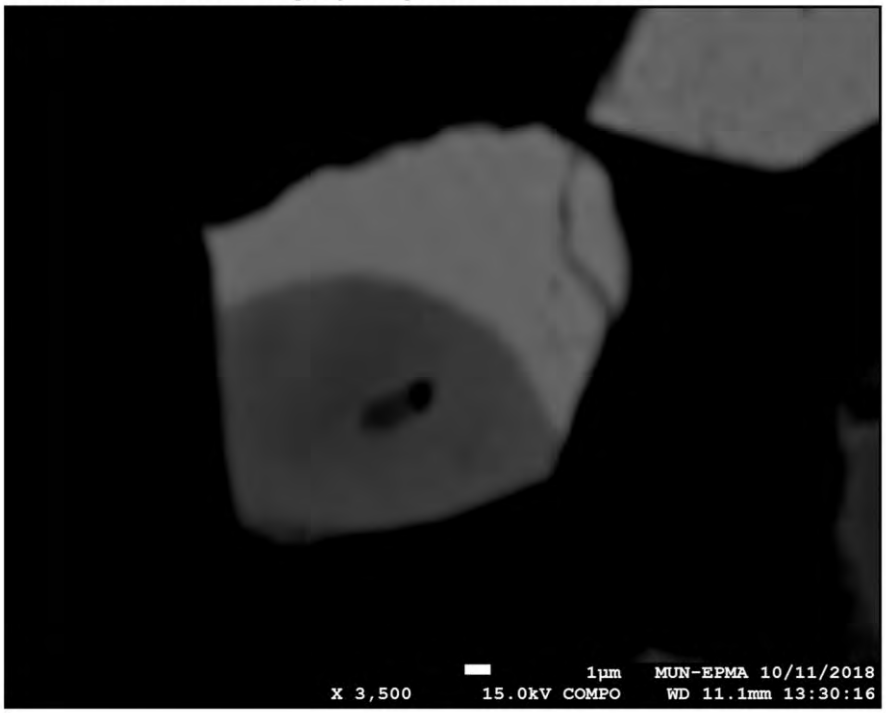

Secondary electron image (topography) with spot analyses positions

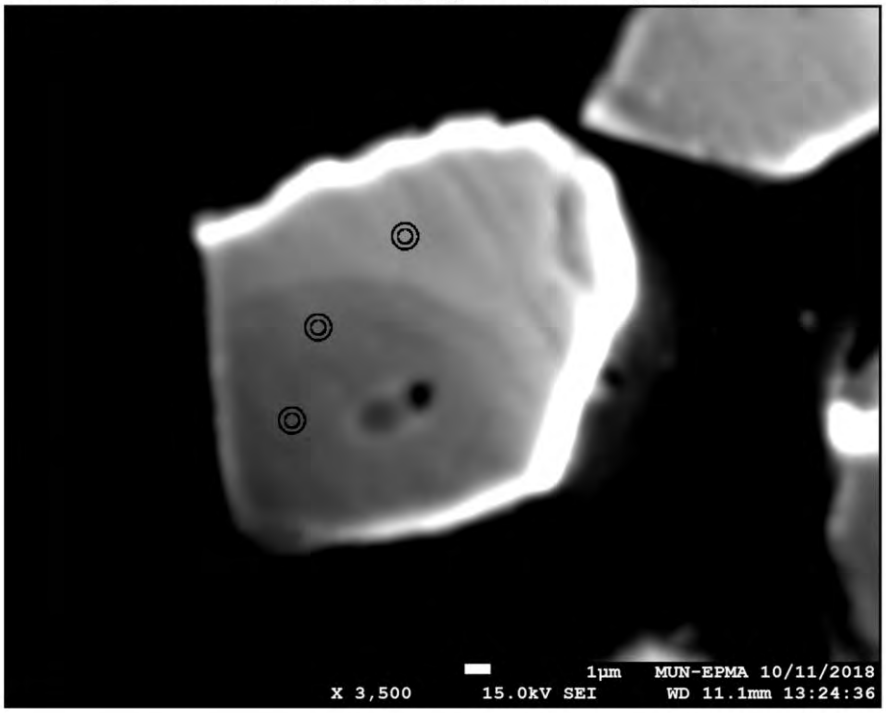

MINOR ELEMENT X-RAY MAPS

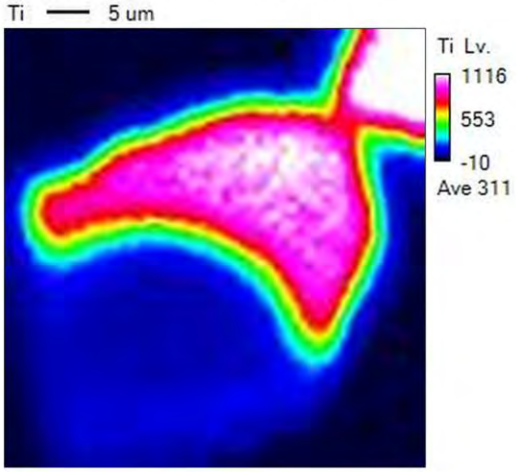

2D element distribution collage 11.
VP17-15 Grain #4 (generation Z)

Backscatter electron image of compositional variations

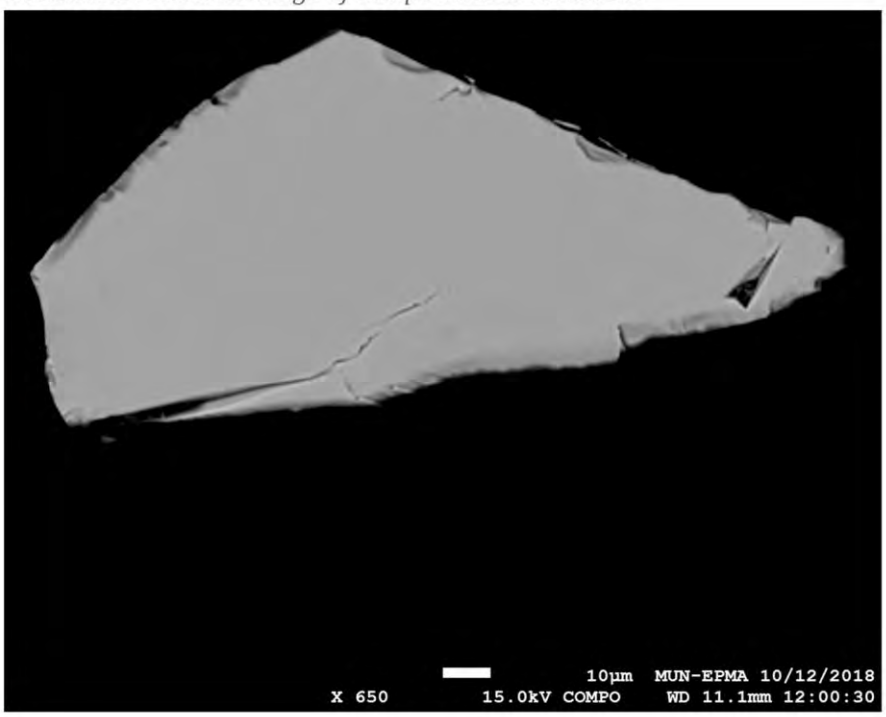

Secondary electron image (topography) with spot analyses positions

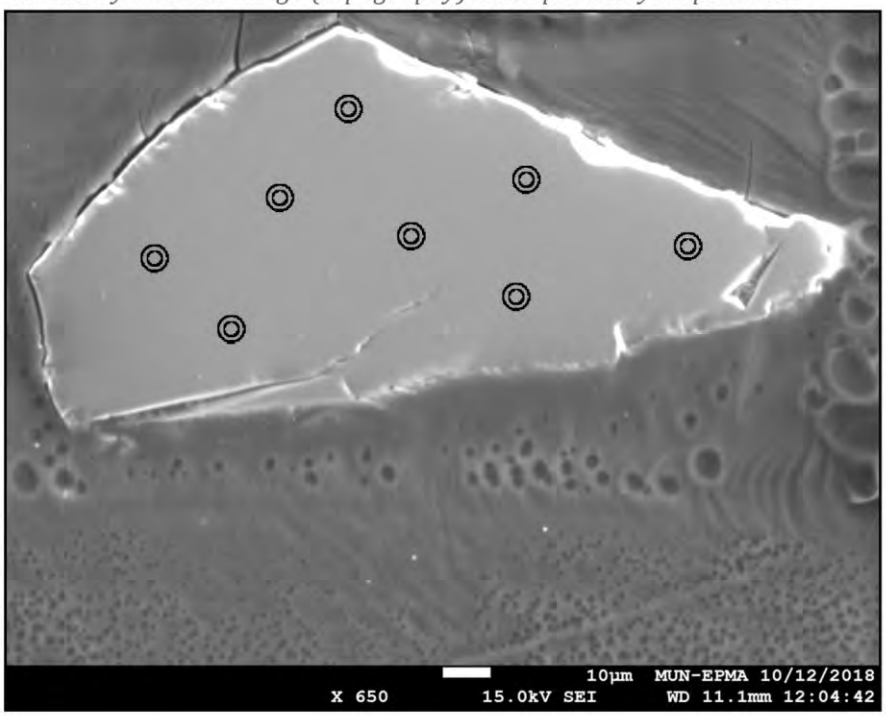

MAJOR ELEMENT X-RAY MAPS

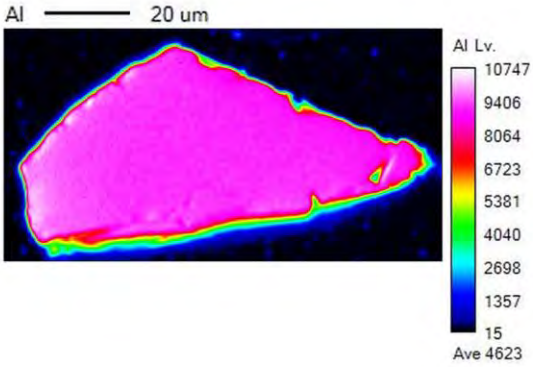

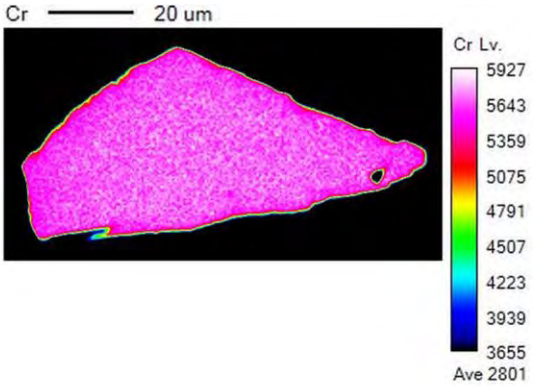

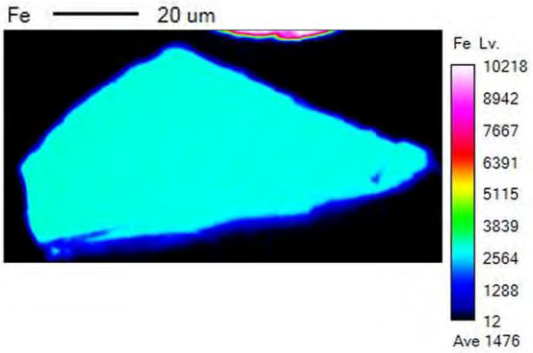

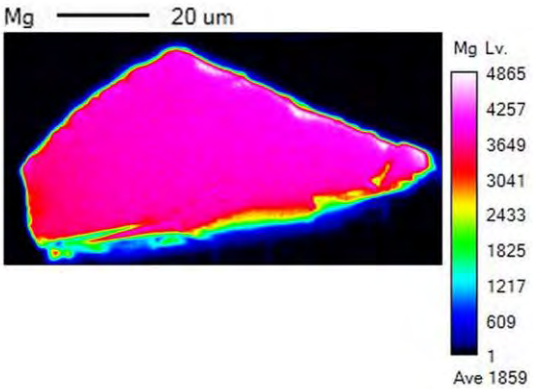

MINOR ELEMENT X-RAY MAPS

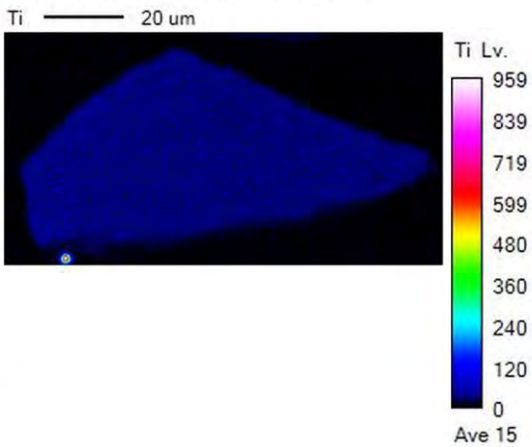

2D element distribution collage 12.
VP17-15 Grain #5 (generation Y)

MAJOR ELEMENT X-RAY MAPS

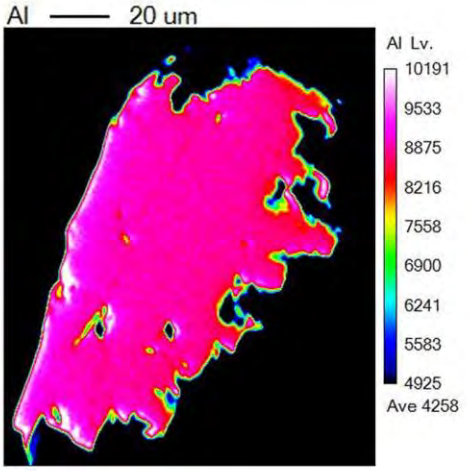

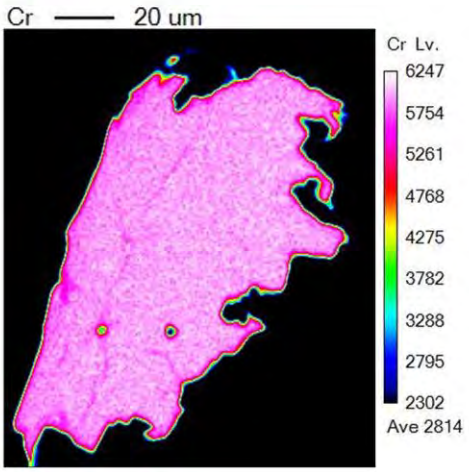

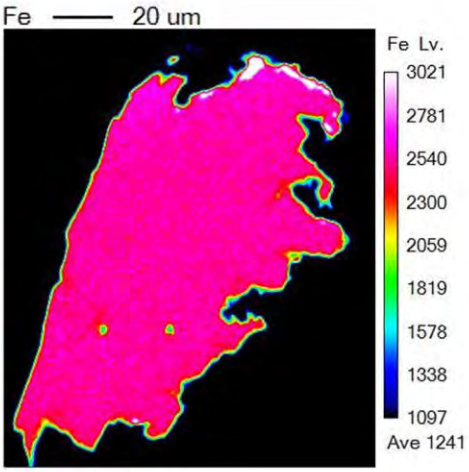

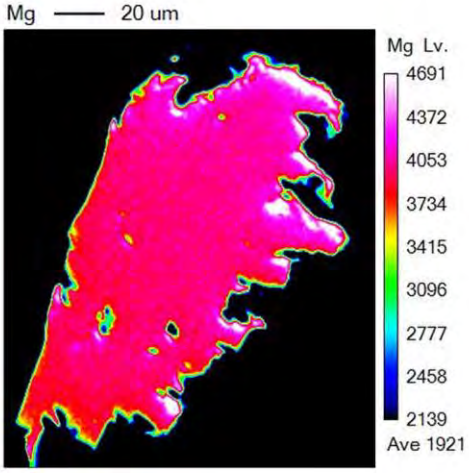

Backscatter electron image of compositional variations

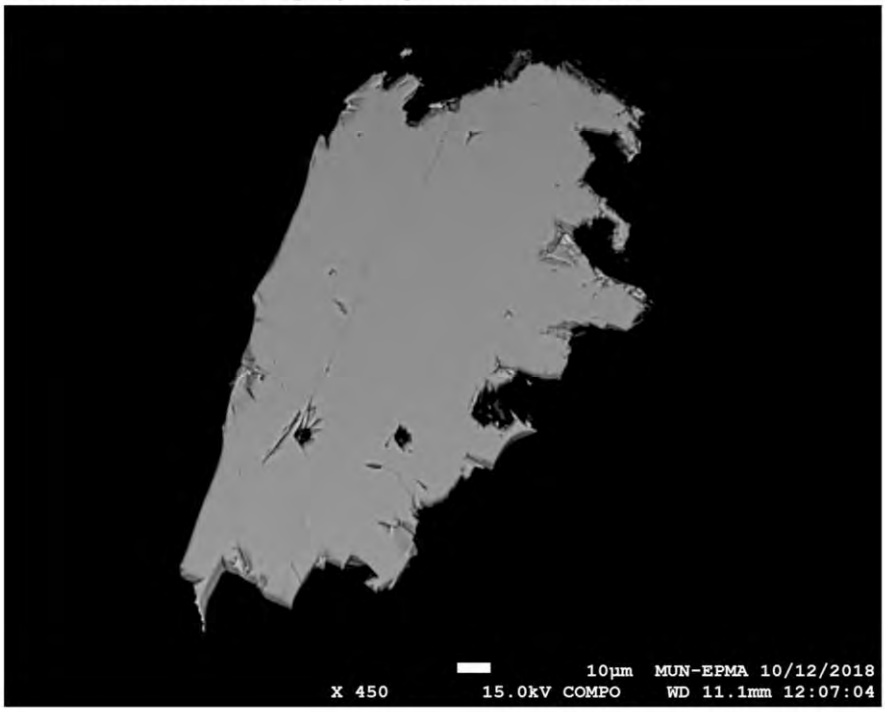

Secondary electron image (topography) with spot analyses positions

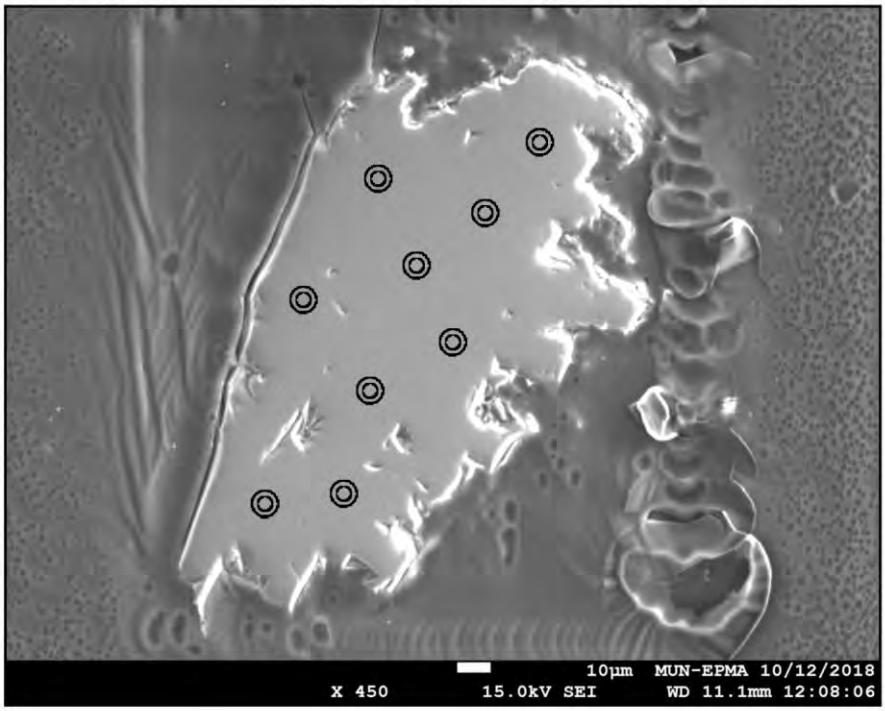

MINOR ELEMENT X-RAY MAPS

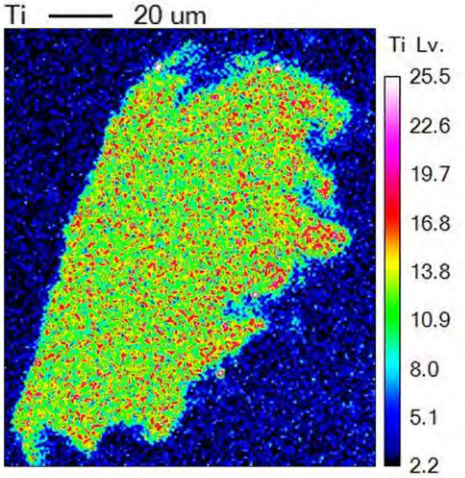

2D element distribution collage 13.
VP17-15 Grain #6 (generation Y)

MAJOR ELEMENT X-RAY MAPS

Al ——— 50 um

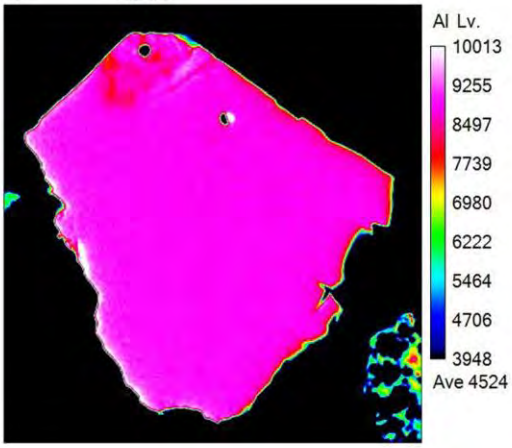

Cr ——— 50 um

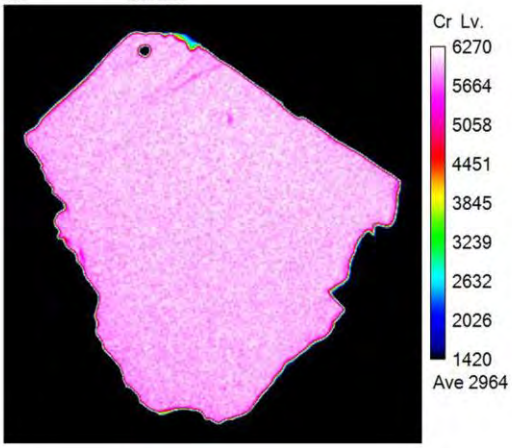

Fe ——— 50 um

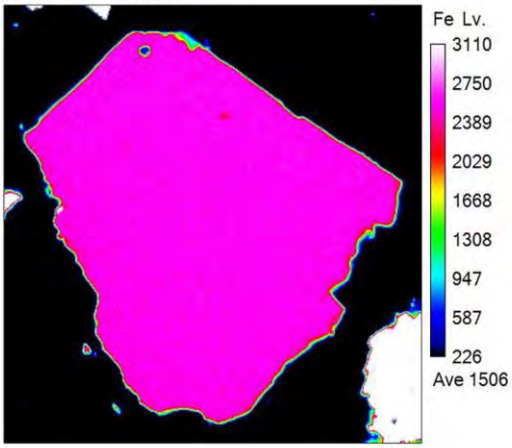

Mg ——— 50 um

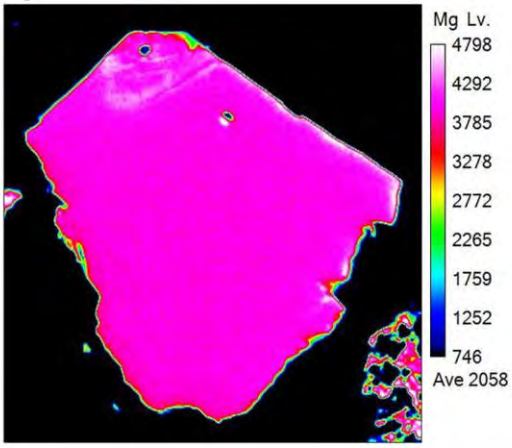

Backscatter electron image of compositional variations

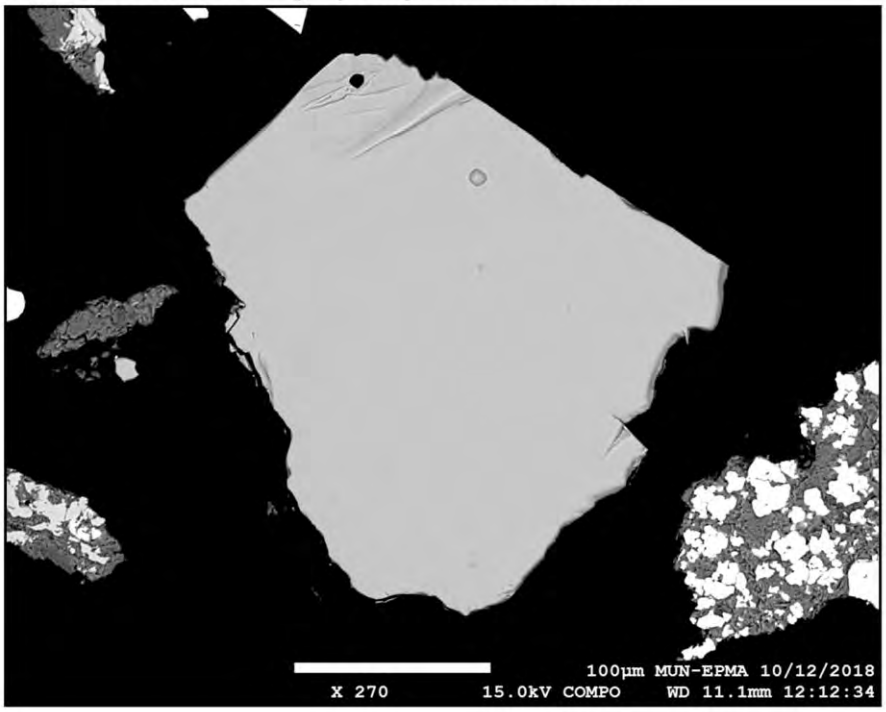

Secondary electron image (topography) with spot analyses positions

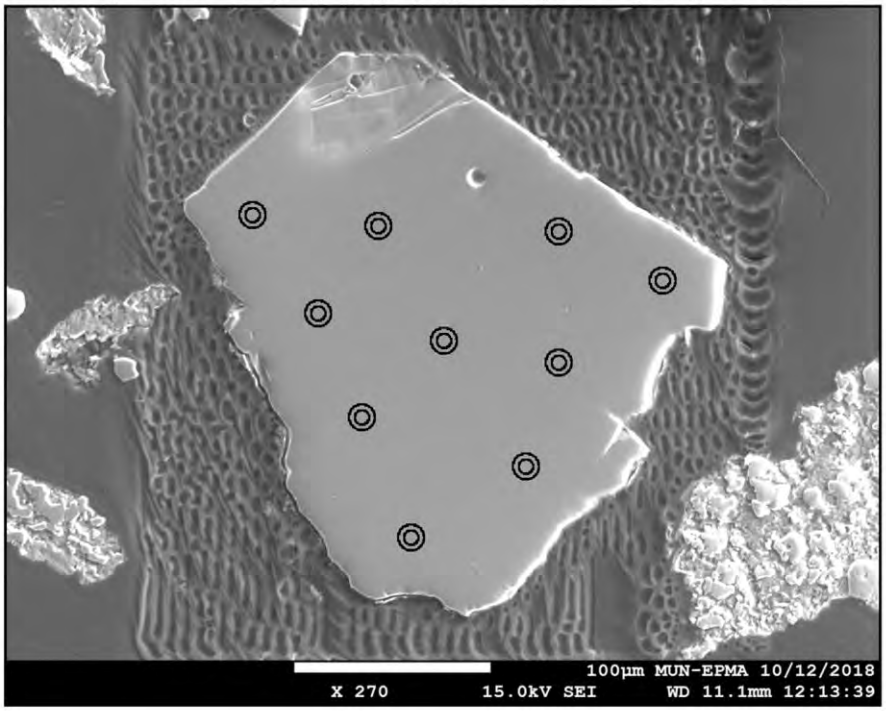

MINOR ELEMENT X-RAY MAPS

Ti ——— 50 um

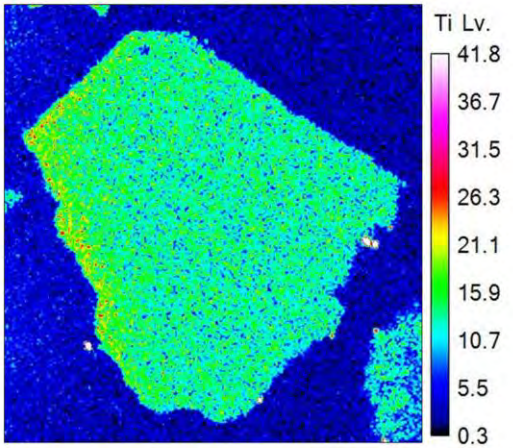

APPENDIX B3:

Chemical data from electron microprobe analysis (extended)

		Measured oxide wt.% by electron microprobe analysis											Computed values																
		major components				*minor components*							*oxide wt.% by EMG 8.0*			*cations per 4 oxygen atoms by EMG 8.0*													
Sample ID Grain no.	**Point**	Al_2O_3	MgO	FeO_T	Cr_2O_3	TiO_2	V_2O_3	MnO	NiO	CaO	SiO_2	Total	FeO	Fe_2O_3	Total	Al^{3+}	Mg^{2+}	Cr^{3+}	Ti^{4+}	V^{3+}	Mn^{2+}	Ni^{2+}	Ca^{2+}	Si^{4+}	Fe^{2+}	Fe^{3+}	Fe^{2+}/Fe^{3+}	Y_{Fe3+}	*cr#*	*mg#*
17HSB-3																														
#1																														
ferritchromite	*1*	2.75	2.53	45.75	40.84	0.06	0.17	2.22	0.20	bdl	0.00	94.51	24.91	23.16	96.83	0.122	0.142	1.214	0.002	0.005	0.071	0.006	-	-	0.783	0.655	1.195	0.329	0.909	0.154
Cr-magnetite	*2*	0.15	0.26	86.72	3.12	bdl	0.02	0.08	1.55	bdl	0.04	91.96	28.66	64.52	98.42	0.007	0.015	0.096	-	0.001	0.003	0.049	-	0.001	0.935	1.893	0.494	0.948	0.932	0.016
ferritchromite	*3*	1.67	1.14	64.82	21.21	0.03	0.08	1.00	0.94	0.01	0.05	90.95	26.58	42.50	95.21	0.077	0.067	0.659	0.001	0.002	0.033	0.030	-	0.002	0.873	1.256	0.695	0.631	0.895	0.071
ferritchromite	*4*	2.20	3.39	45.21	39.61	0.05	0.18	2.95	0.27	bdl	0.01	93.87	22.51	25.23	96.40	0.098	0.190	1.179	0.001	0.005	0.094	0.008	-	-	0.709	0.715	0.992	0.359	0.923	0.211
ferritchromite	*5*	2.22	3.09	45.48	40.10	0.03	0.14	2.05	0.23	0.01	0.02	93.36	23.75	24.15	95.78	0.099	0.175	1.203	0.001	0.004	0.066	0.007	-	0.001	0.754	0.690	1.093	0.346	0.924	0.188
#2																														
ferritchromite	*1*	0.69	2.52	45.45	43.62	0.14	0.22	1.81	0.14	bdl	0.24	94.83	25.53	22.14	97.05	0.031	0.142	1.306	0.004	0.007	0.058	0.004	-	0.009	0.808	0.631	1.281	0.321	0.977	0.149
ferritchromite	*2*	1.02	1.70	51.29	37.35	0.15	0.16	1.49	0.30	0.00	0.31	93.78	26.86	27.15	96.50	0.046	0.097	1.133	0.004	0.005	0.048	0.009	-	0.012	0.862	0.784	1.099	0.399	0.961	0.101
ferritchromite	*3*	0.61	1.39	48.59	39.80	0.11	0.19	1.39	0.38	0.01	0.90	93.34	27.82	23.08	95.66	0.028	0.080	1.218	0.003	0.006	0.045	0.012	-	0.035	0.901	0.672	1.341	0.350	0.978	0.082
Cr-magnetite	*4*	0.04	0.03	87.84	0.93	bdl	0.03	0.02	1.64	bdl	0.02	90.55	28.54	65.91	97.16	0.002	0.002	0.029	-	0.001	0.001	0.052	-	0.001	0.946	1.966	0.481	0.984	0.935	0.002
Cr-magnetite	*5*	0.03	0.06	88.72	0.55	bdl	0.01	bdl	1.28	bdl	0.02	90.67	28.90	66.48	97.33	0.001	0.004	0.017	-	-	-	0.041	-	0.001	0.956	1.979	0.483	0.991	0.944	0.004
#3																														
ferritchromite	*1*	0.76	1.92	49.79	38.14	0.06	0.22	1.95	0.32	bdl	bdl	93.16	25.32	27.20	95.88	0.034	0.110	1.165	0.002	0.007	0.064	0.010	-	-	0.818	0.791	1.034	0.397	0.972	0.119
ferritchromite	*2*	0.73	2.09	50.47	37.90	0.06	0.24	2.19	0.48	bdl	0.01	94.18	25.01	28.30	97.01	0.033	0.119	1.143	0.002	0.007	0.071	0.015	-	0.001	0.798	0.812	0.983	0.408	0.972	0.130
ferritchromite	*3*	0.15	0.37	62.50	27.41	bdl	0.09	1.00	0.91	0.01	0.07	92.50	27.98	38.36	96.34	0.007	0.021	0.851	-	0.003	0.033	0.029	-	0.003	0.919	1.134	0.810	0.569	0.992	0.022
ferritchromite	*4*	0.73	2.25	49.56	37.44	0.07	0.22	2.27	0.38	bdl	0.06	92.96	24.45	27.90	95.76	0.033	0.129	1.142	0.002	0.007	0.074	0.012	-	0.002	0.789	0.810	0.974	0.408	0.972	0.141
ferritchromite	*5*	0.80	1.86	49.60	38.05	0.07	0.24	2.27	0.47	0.01	0.00	93.37	25.02	27.31	96.10	0.036	0.107	1.160	0.002	0.008	0.074	0.015	-	-	0.807	0.792	1.019	0.398	0.970	0.117
ferritchromite	*6*	0.84	0.77	52.65	35.87	0.03	0.19	1.52	0.63	0.00	0.05	92.55	27.07	28.42	95.39	0.039	0.045	1.111	0.001	0.006	0.050	0.020	-	0.002	0.887	0.838	1.058	0.422	0.966	0.048
#4																														
ferritchromite	*1*	0.82	2.23	48.01	41.06	0.22	0.18	1.65	0.21	0.01	bdl	94.40	25.75	24.74	96.88	0.037	0.127	1.236	0.006	0.006	0.053	0.007	-	-	0.820	0.709	1.157	0.358	0.971	0.134
ferritchromite	*2*	1.09	2.40	47.65	40.26	0.17	0.18	1.44	0.22	0.01	bdl	93.40	25.38	24.75	95.88	0.049	0.137	1.221	0.005	0.005	0.047	0.007	-	-	0.814	0.715	1.138	0.360	0.961	0.144
ferritchromite	*3*	0.94	1.97	50.41	38.00	0.17	0.18	1.76	0.30	0.01	0.07	93.83	25.86	27.28	96.56	0.042	0.112	1.150	0.005	0.006	0.057	0.009	0.001	0.003	0.828	0.786	1.053	0.397	0.965	0.119
#5																														
ferritchromite	*1*	0.44	2.25	43.71	45.85	0.15	0.18	2.87	0.17	0.01	0.04	95.66	24.80	21.02	97.77	0.020	0.126	1.367	0.004	0.005	0.092	0.005	-	0.001	0.782	0.597	1.310	0.301	0.986	0.139
ferritchromite	*2*	0.44	3.32	41.29	44.76	0.15	0.20	3.39	0.17	bdl	0.18	93.90	22.25	21.15	96.02	0.020	0.188	1.346	0.004	0.006	0.109	0.005	-	0.007	0.708	0.606	1.168	0.307	0.985	0.210
ferritchromite	*3*	0.59	0.37	66.36	25.01	0.03	0.08	0.88	1.10	0.01	0.06	94.47	28.68	41.87	98.66	0.027	0.021	0.758	0.001	0.002	0.028	0.034	-	0.002	0.919	1.207	0.761	0.606	0.966	0.022
#6																														
ferritchromite	*1*	0.53	2.24	45.65	42.92	0.11	0.19	2.07	0.18	0.06	bdl	93.95	24.95	23.00	96.26	0.024	0.128	1.301	0.003	0.006	0.067	0.006	0.003	-	0.800	0.663	1.207	0.334	0.982	0.138
ferritchromite	*3*	0.59	2.58	46.97	41.44	0.10	0.22	2.37	0.22	0.16	bdl	94.64	24.23	25.26	97.17	0.026	0.145	1.241	0.003	0.007	0.076	0.007	0.006	-	0.768	0.720	1.067	0.362	0.979	0.159
ferritchromite	*4*	0.60	2.13	51.09	36.27	0.09	0.14	1.96	0.30	0.36	0.01	92.96	24.56	29.49	95.92	0.027	0.122	1.106	0.003	0.004	0.064	0.009	0.015	-	0.792	0.856	0.925	0.430	0.976	0.133
ferritchromite	*5*	0.68	2.20	47.64	41.23	0.13	0.18	1.52	0.24	0.10	0.03	93.96	25.56	24.54	96.42	0.030	0.126	1.248	0.004	0.006	0.049	0.007	0.004	0.001	0.818	0.707	1.157	0.356	0.977	0.133
#7																														
ferritchromite	*1*	0.48	2.84	45.20	42.64	0.13	0.20	2.88	0.24	0.01	0.05	94.65	23.54	24.07	97.07	0.021	0.161	1.276	0.004	0.006	0.092	0.007	-	0.002	0.745	0.686	1.086	0.346	0.984	0.178
ferritchromite	*2*	0.56	2.99	47.45	41.69	0.10	0.19	2.01	0.25	0.01	bdl	95.26	24.32	25.71	97.84	0.025	0.168	1.237	0.003	0.006	0.064	0.008	-	-	0.763	0.726	1.051	0.365	0.980	0.180
ferritchromite	*3*	0.61	3.05	44.49	41.28	0.07	0.22	2.90	0.28	bdl	0.04	92.94	22.57	24.36	95.37	0.027	0.175	1.254	0.002	0.007	0.095	0.009	-	0.002	0.725	0.704	1.030	0.355	0.979	0.194
ferritchromite	*4*	0.52	2.85	46.95	41.41	0.14	0.21	1.95	0.22	0.00	0.06	94.32	24.43	25.02	96.83	0.023	0.161	1.243	0.004	0.006	0.063	0.007	-	0.002	0.776	0.715	1.085	0.361	0.982	0.172
ferritchromite	*5*	0.49	2.10	49.71	41.01	0.11	0.20	0.93	0.22	0.00	0.00	94.78	26.66	25.62	97.35	0.022	0.119	1.232	0.003	0.006	0.030	0.007	-	-	0.847	0.733	1.156	0.369	0.982	0.123
ferritchromite	*6*	0.49	2.29	47.64	42.50	0.11	0.21	1.77	0.20	0.01	0.01	95.22	25.67	24.42	97.66	0.022	0.129	1.270	0.003	0.006	0.057	0.006	-	-	0.812	0.695	1.168	0.350	0.983	0.137
#8																														
ferritchromite	*1*	0.51	2.06	48.99	40.55	0.07	0.23	2.09	0.28	bdl	0.02	94.80	25.49	26.12	97.41	0.023	0.117	1.218	0.002	0.007	0.067	0.009	-	0.001	0.810	0.747	1.084	0.376	0.981	0.126
#9																														
ferritchromite	*1*	1.32	2.09	51.85	37.83	0.16	0.20	0.68	0.27	0.00	0.01	94.41	26.97	27.65	97.18	0.059	0.118	1.136	0.004	0.006	0.022	0.008	-	-	0.856	0.790	1.084	0.398	0.951	0.121
ferritchromite	*2*	1.51	2.52	50.05	38.13	0.17	0.19	0.84	0.23	0.01	0.03	93.67	26.00	26.73	96.34	0.068	0.143	1.148	0.005	0.006	0.027	0.007	-	0.001	0.828	0.766	1.081	0.386	0.944	0.147
ferritchromite	*3*	1.46	2.22	51.07	38.28	0.13	0.19	0.86	0.25	bdl	0.02	94.47	26.64	27.15	97.19	0.065	0.125	1.147	0.004	0.006	0.028	0.008	-	0.001	0.844	0.774	1.090	0.390	0.946	0.129
ferritchromite	*4*	1.38	3.01	48.02	39.33	0.16	0.20	1.67	0.21	bdl	0.01	93.98	24.48	26.16	96.60	0.062	0.170	1.177	0.004	0.006	0.053	0.007	-	-	0.775	0.745	1.040	0.376	0.950	0.180
#10																														
Cr-magnetite	*1*	0.09	0.69	78.08	12.25	0.03	0.05	0.37	1.32	0.00	0.30	93.18	28.53	55.06	98.69	0.004	0.040	0.373	0.001	0.002	0.012	0.041	-	0.011	0.919	1.597	0.575	0.809	0.989	0.042
ferritchromite	*3*	0.56	1.56	50.36	39.85	0.11	0.17	1.64	0.27	bdl	0.05	94.58	26.76	26.23	97.20	0.025	0.089	1.204	0.003	0.005	0.053	0.008	-	0.002	0.855	0.754	1.134	0.380	0.980	0.094
ferritchromite	*4*	0.66	2.70	45.30	44.18	0.09	0.17	1.80	0.15	0.01	0.05	95.12	25.03	22.52	97.38	0.029	0.152	1.318	0.003	0.005	0.058	0.005	-	0.002	0.790	0.639	1.236	0.322	0.978	0.161
ferritchromite	*7*	0.57	2.55	44.84	43.12	0.08	0.19	1.90	0.20	0.02	0.46	93.92	25.23	21.79	96.10	0.025	0.145	1.303	0.002	0.006	0.061	0.006	0.001	0.017	0.806	0.627	1.285	0.321	0.981	0.152
#11																														
ferritchromite	*1*	0.03	0.33	83.78	3.24	0.02	0.03	0.01	1.26	bdl	0.25	88.95	28.20	61.77	95.14	0.001	0.020	0.103	0.001	0.001	-	0.041	-	0.010	0.950	1.873	0.507	0.947	0.990	0.021
ferritchromite	*2*	0.22	0.21	83.84	1.68	0.02	0.02	0.03	1.13	bdl	0.20	87.35	27.94	62.13	93.57	0.011	0.013	0.054	-	0.001	0.001	0.037	-	0.008	0.958	1.917	0.500	0.967	0.831	0.013
ferritchromite	*4*	1.19	2.09	79.52	6.26	0.01	0.03	0.14	0.92	0.01	1.66	91.84	28.53	56.68	97.52	0.053	0.119	0.189	-	0.001	0.005	0.028	0.001	0.064	0.911	1.629	0.559	0.871	0.781	0.116
Cr-magnetite	*5*	0.52	0.87	50.04	39.07	0.06	0.18	1.36	0.37	0.00	0.22	92.69	27.52	25.02	95.20	0.024	0.051	1.211	0.002	0.006	0.045	0.012	-	0.009	0.902	0.738	1.222	0.374	0.981	0.054
ferritchromite	*6*	bdl	0.03	86.91	1.94	0.01	0.01	bdl	1.03	0.01	0.05	89.99	28.97	64.39	96.44	-	0.002	0.061	-	-	-	0.033	-	0.002	0.967	1.934	0.500	0.969	1.000	0.002
ferritchromite	*8*	0.11	0.19	87.49	1.18	0.01	bdl	0.01	1.00	bdl	0.16	90.15	28.98	65.02	96.67	0.005	0.011	0.037	-	-	-	0.032	-	0.006	0.963	1.944	0.495	0.979	0.881	0.011
ferritchromite	*11*	0.02	0.20	83.91	2.47	0.01	0.01	0.01	1.28	0.01	0.18	88.08	27.98	62.16	94.31	0.001	0.012	0.080	-	-	-	0.042	-	0.007	0.953	1.905	0.500	0.959	0.988	0.012
#12																														
ferritchromite	*1*	0.51	2.99	45.77	40.35	0.13	0.21	3.33	0.29	0.00	0.01	93.59	22.45	25.92	96.18	0.023	0.170	1.218	0.004	0.006	0.108	0.009	-	-	0.717	0.745	0.962	0.375	0.981	0.192
ferritchromite	*2*	0.49	2.34	45.60	43.35	0.08	0.20	2.68	0.25	0.01	0.10	95.10	24.64	23.29	97.43	0.022	0.132	1.297	0.002	0.006	0.086	0.008	-	0.004	0.780	0.663	1.176	0.335	0.983	0.145
ferritchromite	*3*	0.43	2.88	43.73	44.49	0.07	0.19	2.84	0.18	bdl	bdl	94.80	23.49	22.49	97.05	0.019	0.162	1.331	0.002	0.006	0.091	0.005	-	-	0.743	0.640	1.161	0.322	0.986	0.179
ferritchromite	*4*	0.40	2.55	45.18	43.11	0.11	0.23	2.65	0.21	bdl	0.02	94.47	24.12	23.40	96.81	0.018	0.145	1.297	0.003	0.007	0.085	0.006	-	0.001	0.767	0.670	1.145	0.338	0.986	0.159
ferritchromite	*5*	0.69	3.86	43.90	39.58	0.11	0.21	2.79	0.24	0.01	0.05	91.42	21.08	25.36	93.96	0.032	0.223	1.212	0.003	0.006	0.092	0.007	-	0.002	0.683	0.739	0.924	0.373	0.974	0.246
ferritchromite	*6*	0.43	2.78	46.24	41.99	0.11	0.22	2.50	0.17	bdl	0.09	94.54	24.10	24.61	97.00	0.019	0.157	1.259	0.003	0.007	0.080	0.005	-	0.003	0.764	0.702	1.088	0.355	0.985	0.170
ferritchromite	*7*	0.49	2.76	44.79	43.70	0.09	0.16	2.02	0.16	0.00	0.02	94.19	24.38	22.68	96.46	0.022	0.157	1.316	0.003	0.005	0.065	0.005	-	0.001	0.777	0.650	1.195	0.327	0.984	0.168
ferritchromite	*8*	0.50	2.62	45.05	43.82	0.08	0.19	2.02	0.16	bdl	0.01	94.44	24.64	22.68	96.72	0.022	0.149	1.318	0.002	0.006	0.065	0.005	-	-	0.784	0.649	1.208	0.326	0.984	0.160
Cr-magnetite	*9*	bdl	0.08	87.30	2.71	bdl	0.03	0.08	1.11	0.00	0.20	91.50	29.42	64.32	97.94	-	0.004	0.084	-	0.001	0.003	0.035	-	0.008	0.966	1.899	0.509	0.958	1.000	0.004
Cr-magnetite	*10*	bdl	0.05	85.42	4.59	bdl	0.01	0.10	1.09	0.01	0.04	91.31	29.17	62.52	97.57	-	0.003	0.143	-	-	0.003	0.034	-	0.002	0.961	1.853	0.519	0.928	1.000	0.003
Cr-magnetite	*11*	0.03	0.02	88.41	0.97	0.03	0.02	0.02	1.63	0.00	0.02	91.15	28.78	66.27	97.79	0.001	0.001	0.030	0.001	0.001	0.001	0.052	-	0.001	0.948	1.964	0.483	0.984	0.968	0.001
ferritchromite	*12*	0.47	1.86	48.93	39.01	0.11	0.24	2.37	0.29	bdl	0.04	93.31	25.09	26.49	95.96	0.021	0.107	1.192	0.003	0.007	0.078	0.009	-	0.001	0.811	0.770	1.053	0.388	0.983	0.117
Cr-magnetite	*13*	0.06	0.77	86.38	1.13	bdl	0.03	0.02	1.30	0.01	0.89	90.60	28.84	63.95	97.00	0.003	0.045	0.035	-	0.001	0.001	0.041	-	0.035	0.948	1.891	0.501	0.980	0.921	0.045
#13																														
Cr-magnetite	*4*	0.17	1.35	83.80	1.31	bdl	0.01	0.01	0.95	0.01	1.40	89.02	28.45	61.51	95.18	0.008	0.080	0.041	-	-	-	0.030	-	0.056	0.945	1.839	0.514	0.974	0.837	0.078
Cr-magnetite	*5*	0.03	0.13	79.45	10.15	bdl	0.05	0.35	1.62	0.01	0.01	91.79	28.30	56.84	97.48	0.001	0.007	0.315	-	0.001	0.012	0.051	-	0.001	0.930	1.681	0.553	0.842	0.997	0.007
Cr-magnetite	*6*	0.03	0.07	87.50	0.23	0.02	0.02	bdl	1.55	0.00	0.02	89.44	28.23	65.87	96.04	0.002	0.004	0.007	-	0.001	-	0.050	-	0.001	0.947	1.988	0.476	0.995	0.778	0.004
Cr-magnetite	*7*	0.18	0.13	83.01	5.49	bdl	0.02	0.21	1.06	bdl	0.08	90.18	28.64	60.42	96.23	0.008	0.008	0.173	-	0.001	0.007	0.034	-	0.003	0.954	1.812	0.526	0.909	0.956	0.008
ferritchromite	*8*	0.59	2.80	41.97	46.40	0.06	0.20	3.09	0.13	0.01	0.02	95.26	23.55	20.47	97.31	0.026	0.157	1.382	0.002	0.006	0.099	0.004	-	0.001	0.742	0.581	1.277	0.292	0.982	0.175
ferritchromite	*9*	0.54	1.48	47.26	44.05	0.10	0.15	1.97	0.22	0.01	0.00	95.79	26.82	22.72	98.07	0.024	0.084	1.318	0.003	0.005	0.063	0.007	-	-	0.849	0.647	1.312	0.325	0.982	0.090
ferritchromite	*10*	0.61	0.75	50.92	39.42	0.10	0.22	1.42	0.35	0.01	0.03	93.84	27.84	25.66	96.40	0.028	0.043	1.208	0.003	0.007	0.047	0.011	-	0.001	0.903	0.749	1.206	0.377	0.977	0.045
ferritchromite	*11*	0.52	1.70	47.19	43.12	0.11	0.19	2.03	0.20	0.01	0.01	95.06	26.24	23.28	97.39	0.023	0.096	1.297	0.003	0.006	0.065	0.006	-	-	0.835	0.667	1.252	0.336	0.983	0.103
#14																														
ferritchromite	*1*	0.41	0.68	57.86	32.28	0.06	0.20	1.31	0.77	0.01	0.02	93.60	27.63	33.60	96.97	0.019	0.039	0.989	0.002	0.006	0.043	0.024	0.001	0.001	0.896	0.980	0.914	0.493	0.981	0.042
ferritchromite	*2*	0.37	1.61	57.85	31.76	0.11	0.17	1.77	0.68	bdl	0.03	94.35	26.16	35.22	97.88	0.017	0.091	0.958	0.003	0.005	0.057	0.021	-	0.001	0.835	1.011	0.826	0.509	0.983	0.098
ferritchromite	*3*	0.61	2.51	50.72	36.94	0.11	0.19	2.93	0.32	bdl	0.01	94.35	23.88	29.83	97.33	0.027	0.142	1.108	0.003	0.006	0.094	0.010	-	-	0.758	0.852	0.890	0.429	0.976	0.158
ferritchromite	*4*	0.84	2.56	50.19	36.74	0.11	0.19	2.06	0.33	bdl	0.01	93.02	24.27	28.80	95.91	0.038	0.146	1.116	0.003	0.006	0.067	0.010	-	0.001	0.780	0.833	0.936	0.419	0.967	0.158
Cr-magnetite	*6*	bdl	0.19	88.70	1.71	bdl	bdl	0.03	1.37	0.00	0.02	92.03	29.00	66.35	98.68	-	0.011	0.053	-	-	0.001	0.043	-	0.001	0.945	1.946	0.486	0.973	1.000	0.012
Cr-magnetite	*7*	0.22	0.52	74.29	15.08	0.03	0.07	0.69	1.26	0.00	0.07	92.24	27.89	51.56	97.40	0.010	0.031	0.465	0.001	0.002	0.023	0.040	-	0.003	0.911	1.515	0.601	0.761	0.979	0.033
#15																														
ferritchromite	*1*	0.55	2.92	45.54	42.45	0.04	0.17	2.78	0.24	bdl	0.01	94.70	23.43	24.57	97.16	0.025	0.165	1.268	0.001	0.005	0.089	0.007	-	-	0.741	0.699	1.060	0.351	0.981	0.182
ferritchromite	*2*	0.50	2.76	45.95	42.60	0.05	0.20	2.71	0.25	0.00	0.06	95.09	23.93	24.47	97.54	0.022	0.155	1.270	0.002	0.006	0.087	0.008	-	0.002	0.754	0.694	1.086	0.349	0.983	0.171
ferritchromite	*3*	0.50	2.74	45.76	42.16	0.06	0.18	2.76	0.33	bdl	0.02	94.51	23.62	24.61	96.98	0.022	0.155	1.264	0.002	0.005	0.089	0.010	-	0.001	0.749	0.702	1.067	0.353	0.983	0.171
ferritchromite	*4*	0.54	3.19	46.01	42.01	bdl	0.20	2.68	0.31	0.00	0.18	95.12	23.37	25.16	97.64	0.024	0.178	1.246	-	0.006	0.085	0.009	-	0.007	0.734	0.710	1.034	0.359	0.981	0.195
ferritchromite	*5*	0.50	2.63	45.91	41.80	0.08	0.20	2.60	0.26	bdl	0.05	94.02	23.89	24.47	96.47	0.022	0.150	1.261	0.002	0.006	0.084	0.008	-	0.002	0.762	0.703	1.084	0.354	0.983	0.164
ferritchromite	*6*	0.64	3.04	43.92	40.45	0.02	0.19	2.96	0.28	bdl	0.07	91.57	22.09	24.26	94.00	0.029	0.176	1.247	0.001	0.006	0.098	0.009	-	0.003	0.720	0.712	1.011	0.358	0.977	0.196
#16																														
Cr-spinel	*1*	22.71	7.63	23.23	43.65	0.02	0.20	0.43	0.03	0.00	0.01	97.92	22.89	0.39	97.96	0.867	0.368	1.117	-	0.005	0.012	0.001	-	-	0.620	0.009	68.889	0.005	0.563	0.372
Cr-spinel	*2*	24.23	8.30	22.76	43.88	bdl	0.20	0.42	0.03	0.00	bdl	99.83	22.70	0.07	99.84	0.900	0.390	1.093	-	0.005	0.011	0.001	-	-	0.598	0.002	299.000	0.001	0.548	0.395
Cr-spinel	*3*	25.46	8.82	22.38	43.59	0.03	0.22	0.42	0.05	bdl	0.02	100.99	22.39	0.00	100.99	0.928	0.407	1.066	0.001	0.006	0.011	0.001	-	0.001	0.579	-	-	0.000	0.535	0.413
Cr-spinel	*4*	24.68	8.50	22.58	44.00	bdl	0.23	0.42	0.03	bdl	bdl	100.45	22.58	0.00	100.45	0.909	0.396	1.087	-	0.006	0.011	0.001	-	-	0.590	-	-	0.000	0.545	0.402
Cr-spinel	*5*	27.25	9.59	22.22	43.63	0.01	0.19	0.41	0.03	0.01	0.02	103.36	22.22	0.00	103.36	0.963	0.429	1.034	-	0.004	0.010	0.001	-	0.001	0.557	-	-	0.000	0.518	0.435
Cr-spinel	*6*	24.57	8.32	22.64	43.66	bdl	0.21	0.40	0.02	0.00	0.01	99.83	22.64	0.00	99.83	0.911	0.390	1.086	-	0.005	0.011	-	-	-	0.596	-	-	0.000	0.544	0.396
Cr-spinel	*7*	22.72	7.49	22.99	43.11	0.02	0.20	0.44	0.06	bdl	bdl	97.02	22.78	0.23	97.05	0.875	0.365	1.113	-	0.005	0.012	0.001	-	-	0.622	0.006	103.667	0.003	0.560	0.370
Cr-spinel	*8*	23.97	8.11	22.59	43.93	0.02	0.19	0.43	0.03	0.00	bdl	99.27	22.59	0.00	99.27	0.896	0.384	1.102	0.001	0.005	0.011	0.001	-	-	0.600	-	-	0.000	0.552	0.390
#17																														
ferritchromite	*1*	0.95	2.47	48.17	41.97	0.07	0.19	1.97	0.20	0.01	0.01	96.02	25.50	25.20	98.54	0.042	0.138	1.239	0.002	0.006	0.062	0.006	-	-	0.796	0.708	1.124	0.356	0.967	0.148
ferritchromite	*2*	1.11	2.25	52.20	38.83	0.07	0.21	0.78	0.25	0.00	bdl	95.72	26.94	28.07	98.53	0.049	0.126	1.150	0.002	0.006	0.025	0.008	-	-	0.844	0.791	1.067	0.397	0.959	0.130
ferritchromite	*3*	2.73	2.50	50.02	39.42	0.07	0.17	0.62	0.22	bdl	0.01	95.76	26.99	25.59	98.33	0.119	0.138	1.157	0.002	0.005	0.019	0.007	-	-	0.838	0.715	1.172	0.359	0.907	0.141
ferritchromite	*4*	1.88	2.39	50.63	38.61	0.09	0.19	0.60	0.24	0.02	0.01	94.64	26.70	26.60	97.30	0.083	0.134	1.151	0.003	0.006	0.019	0.007	0.001	-	0.842	0.755	1.115	0.380	0.933	0.137
ferritchromite	*5*	1.33	2.40	50.07	36.77	0.05	0.18	0.76	0.28	bdl	0.04	91.88	25.53	27.27	94.61	0.061	0.139	1.130	0.001	0.006	0.025	0.009	-	0.001	0.830	0.798	1.040	0.401	0.949	0.143
ferritchromite	*6*	2.18	2.25	50.77	39.17	0.06	0.15	0.61	0.29	0.00	0.01	95.49	27.15	26.25	98.12	0.096	0.125	1.157	0.002	0.005	0.019	0.009	-	-	0.848	0.738	1.149	0.371	0.923	0.128
ferritchromite	*7*	1.52	2.66	47.45	40.76	0.09	0.19	1.30	0.23	0.00	0.49	94.69	26.13	23.69	97.06	0.067	0.150	1.214	0.003	0.006	0.041	0.007	-	0.018	0.823	0.671	1.227	0.344	0.948	0.154
ferritchromite	*8*	1.16	1.69	56.73	35.05	0.07	0.22	0.63	0.35	0.01	0.00	95.92	27.99	31.94	99.12	0.051	0.095	1.038	0.002	0.007	0.020	0.011	-	-	0.877	0.900	0.974	0.452	0.953	0.098
#18																														
ferritchromite	*1*	0.38	2.22	50.78	39.16	0.07	0.17	1.13	0.23	0.01	0.02	94.18	26.07	27.46	96.93	0.017	0.126	1.182	0.002	0.005	0.037	0.007	-	0.001	0.833	0.789	1.056	0.397	0.986	0.131
ferritchromite	*3*	0.55	3.67	45.44	39.05	0.04	0.21	2.79	0.23	bdl	0.02	92.00	21.47	26.65	94.67	0.025	0.211	1.191	0.001	0.006	0.091	0.007	-	0.001	0.693	0.774	0.895	0.389	0.979	0.233
#19																														
ferritchromite	*1*	0.50	3.15	43.51	41.65	0.06	0.16	3.49	0.20	bdl	0.02	92.75	21.79	24.14	95.17	0.022	0.181	1.268	0.002	0.005	0.114	0.006	-	0.001	0.702	0.699	1.004	0.351	0.983	0.205
ferritchromite	*3*	0.27	0.85	64.59	24.17	0.06	0.08	1.11	0.85	bdl	0.01	91.99	27.10	41.66	96.17	0.013	0.049	0.750	0.002	0.003	0.037	0.027	-	0.001	0.889	1.230	0.723	0.617	0.983	0.052
#20																														
ferritchromite	*1*	0.53	3.02	45.65	40.46	0.15	0.21	2.77	0.23	0.00	0.01	93.03	22.87	25.32	95.57	0.024	0.173	1.228	0.004	0.007	0.090	0.007	-	-	0.734	0.732	1.003	0.369	0.981	0.191
ferritchromite	*3*	0.56	2.81	48.20	38.87	0.08	0.19	2.02	0.37	bdl	0.02	93.11	23.83	27.09	95.82	0.025	0.161	1.180	0.002	0.006	0.066	0.011	-	0.001	0.765	0.783	0.977	0.394	0.979	0.174
#21																														
ferritchromite	*1*	0.52	1.94	46.45	39.85	0.12	0.17	1.61	0.39	0.00	1.38	92.44	27.04	21.57	94.60	0.024	0.112	1.225	0.003	0.005	0.053	0.012	-	0.054	0.879	0.631	1.393	0.336	0.981	0.113
ferritchromite	*3*	0.53	1.82	48.16	40.11	0.10	0.17	1.89	0.32	0.01	0.05	93.16	25.54	25.14	95.67	0.024	0.105	1.228	0.003	0.005	0.062	0.010	-	0.002	0.827	0.733	1.128	0.369	0.981	0.113
#22																														
ferritchromite	*1*	0.48	2.50	48.66	38.42	0.04	0.17	2.93	0.40	0.01	0.33	93.94	23.95	27.46	96.69	0.022	0.142	1.158	0.001	0.005	0.095	0.012	-	0.012	0.764	0.788	0.970	0.400	0.981	0.157
ferritchromite	*3*	0.11	0.16	71.43	17.90	0.03	0.09	0.69	1.09	0.00	0.06	91.55	28.31	47.91	96.35	0.005	0.009	0.560	0.001	0.003	0.023	0.035	-	0.003	0.936	1.426	0.656	0.716	0.991	0.010
17HSB-4																														
#1																														
Cr-magnetite	*1*	0.03	0.03	89.81	1.49	0.02	0.01	0.02	0.41	0.01	0.01	91.84	30.15	66.31	98.48	0.002	0.001	0.046	-	-	0.001	0.013	0.001	-	0.985	1.950	0.505	0.976	0.958	0.001
Cr-magnetite	*2*	0.01	0.34	85.87	4.93	bdl	0.03	0.04	0.40	0.01	0.31	91.94	29.99	62.09	98.16	-	0.020	0.152	-	0.001	0.001	0.012	0.001	0.012	0.978	1.822	0.537	0.923	1.000	0.020
Cr-magnetite	*3*	bdl	0.04	88.49	3.95	bdl	0.03	0.03	0.19	0.02	0.13	92.87	30.75	64.17	99.30	-	0.003	0.121	-	0.001	0.001	0.006	0.001	0.005	0.995	1.868	0.533	0.939	1.000	0.003
Cr-magnetite	*4*	0.29	0.81	82.15	1.89	0.01	0.02	0.02	0.19	0.03	0.66	86.05	28.05	60.11	92.08	0.014	0.050	0.062	-	0.001	0.001	0.006	0.001	0.027	0.969	1.869	0.518	0.961	0.816	0.049
Cr-magnetite	*5*	0.04	bdl	86.72	4.93	bdl	0.03	0.06	0.22	0.01	0.04	92.05	30.36	62.64	98.32	0.002	-	0.152	-	0.001	0.002	0.007	0.001	0.002	0.992	1.842	0.539	0.923	0.987	0.000
Cr-magnetite	*6*	bdl	bdl	91.20	1.28	bdl	0.04	bdl	0.30	0.01	0.02	92.85	30.65	67.29	99.59	-	-	0.039	-	0.001	-	0.009	-	0.001	0.991	1.958	0.506	0.980	1.000	0.000
Cr-magnetite	*7*	bdl	0.01	90.64	1.34	0.01	0.05	bdl	0.30	0.01	0.01	92.36	30.46	66.88	99.06	-	0.001	0.041	-	0.001	-	0.009	-	-	0.990	1.956	0.506	0.979	1.000	0.001
high *cr#* spinel	*8*	4.58	2.65	33.26	54.67	0.06	0.47	1.42	0.01	0.01	0.02	97.18	26.60	7.40	97.92	0.197	0.145	1.580	0.002	0.014	0.044	-	0.001	0.001	0.813	0.204	3.985	0.103	0.889	0.151
ferritchromite	*9*	1.25	0.64	68.44	22.34	0.02	0.10	0.36	0.09	0.03	0.53	93.79	30.26	42.43	98.04	0.056	0.036	0.676	0.001	0.003	0.012	0.003	0.001	0.020	0.969	1.223	0.792	0.626	0.923	0.036
#2																														
ferritchromite	*3*	4.43	0.62	52.62	34.60	0.05	0.08	0.77	0.10	0.07	0.40	93.74	29.87	25.29	96.27	0.199	0.035	1.041	0.001	0.002	0.025	0.003	0.003	0.015	0.951	0.724	1.314	0.369	0.840	0.035
#3																														

Cr-magnetite	1	0.01	0.02	87.82	3.28	bdl	0.04	0.01	0.18	0.03	0.07	91.46	30.27	63.96	97.87	0.001	0.001	0.102	-	0.001	-	0.006	0.001	0.003	0.994	1.891	0.526	0.948	0.990	0.001
ferritchromite	2	1.42	0.80	58.37	31.35	0.06	0.16	0.59	0.12	0.02	0.59	93.47	29.63	31.94	96.67	0.064	0.046	0.955	0.002	0.005	0.019	0.004	0.001	0.023	0.955	0.926	1.031	0.476	0.937	0.046
Cr-magnetite	3	0.01	bdl	89.52	1.53	bdl	0.03	0.02	0.35	0.01	0.04	91.52	30.16	65.96	98.12	0.001	-	0.048	-	0.001	0.001	0.011	0.001	0.002	0.990	1.947	0.508	0.975	0.980	0.000
#4																														
Cr-magnetite	1	0.32	0.10	82.10	9.17	0.01	0.05	0.13	0.15	0.02	0.10	92.16	30.27	57.60	97.93	0.015	0.006	0.283	-	0.001	0.004	0.005	0.001	0.004	0.988	1.692	0.584	0.850	0.950	0.006
high *cr#* spinel	2	3.39	0.97	44.55	45.67	0.02	0.18	0.76	0.03	0.02	0.40	95.99	29.86	16.33	97.63	0.150	0.054	1.353	0.001	0.005	0.024	0.001	0.001	0.015	0.936	0.461	2.030	0.235	0.900	0.055
Cr-magnetite	3	0.28	1.26	83.42	5.99	0.01	0.05	0.05	0.21	0.04	1.39	92.69	30.37	58.95	98.59	0.012	0.072	0.181	-	0.001	0.002	0.006	0.002	0.053	0.972	1.698	0.572	0.898	0.938	0.069
Cr-magnetite	4	bdl	bdl	82.74	8.95	0.03	0.05	0.15	0.21	0.02	0.06	92.21	30.30	58.29	98.05	-	-	0.277	0.001	0.001	0.005	0.007	0.001	0.002	0.991	1.715	0.578	0.861	1.000	0.000
#5																														
Cr-magnetite	1	0.02	1.10	87.96	0.54	bdl	0.05	0.02	0.43	0.02	0.85	90.99	29.26	65.24	97.52	0.001	0.064	0.017	-	0.001	0.001	0.013	0.001	0.033	0.954	1.915	0.498	0.991	0.944	0.063
Cr-magnetite	2	0.01	0.04	83.97	5.63	bdl	0.04	0.09	0.42	0.05	0.08	90.32	29.50	60.53	96.38	-	0.002	0.177	-	0.001	0.003	0.013	0.002	0.003	0.983	1.815	0.542	0.911	1.000	0.002
Cr-magnetite	3	bdl	0.03	88.15	1.90	bdl	0.05	0.04	0.50	0.02	0.01	90.71	29.61	65.05	97.23	-	0.002	0.059	-	0.002	0.001	0.016	0.001	0.001	0.980	1.938	0.506	0.970	1.000	0.002
Cr-magnetite	4	0.05	0.51	85.01	1.89	bdl	0.02	0.01	0.31	0.06	1.37	89.24	30.29	60.81	95.33	0.003	0.031	0.060	-	0.001	-	0.010	0.003	0.055	1.012	1.827	0.554	0.967	0.952	0.030
Cr-magnetite	5	bdl	0.02	88.05	1.50	0.02	0.04	bdl	0.57	0.03	bdl	90.22	29.44	65.13	96.74	-	0.001	0.047	-	0.001	-	0.018	0.001	-	0.980	1.951	0.502	0.976	1.000	0.001
Cr-magnetite	6	bdl	0.02	89.37	0.70	bdl	0.02	bdl	0.41	0.02	0.13	90.67	29.92	66.07	97.28	-	0.001	0.022	-	0.001	-	0.013	0.001	0.005	0.990	1.967	0.503	0.989	1.000	0.001
#6																														
Cr-magnetite	1	0.13	1.51	86.25	3.02	0.01	0.04	0.02	0.21	0.03	1.17	92.39	29.68	62.86	98.69	0.006	0.086	0.091	-	0.001	0.001	0.006	0.001	0.045	0.950	1.811	0.525	0.949	0.938	0.083
ferritchromite	3	2.03	0.53	60.46	28.60	0.05	0.16	0.52	0.06	0.02	0.69	93.12	30.30	33.52	96.48	0.093	0.031	0.873	0.001	0.005	0.017	0.002	0.001	0.027	0.978	0.973	1.005	0.502	0.904	0.031
#7																														
ferritchromite	1	1.61	0.40	50.10	43.01	0.04	0.18	0.74	0.09	0.06	0.16	96.39	30.30	22.01	98.59	0.072	0.022	1.283	0.001	0.006	0.024	0.003	0.002	0.006	0.956	0.625	1.530	0.316	0.947	0.022
ferritchromite	2	4.01	1.09	51.71	37.40	0.04	0.20	0.57	0.11	0.01	0.42	95.55	29.93	24.21	97.98	0.176	0.060	1.104	0.001	0.006	0.018	0.003	-	0.016	0.934	0.680	1.374	0.347	0.863	0.060
#8																														
ferritchromite	2	4.21	0.61	51.53	36.74	0.07	0.10	0.76	0.07	0.07	0.36	94.52	30.07	23.84	96.91	0.188	0.034	1.099	0.002	0.003	0.024	0.002	0.003	0.014	0.952	0.679	1.402	0.345	0.854	0.034
#9																														
Cr-magnetite	1	0.02	0.23	87.46	1.49	bdl	0.04	bdl	0.23	0.08	0.50	90.05	29.96	63.90	96.45	0.001	0.014	0.047	-	0.001	-	0.007	0.003	0.020	0.996	1.911	0.521	0.975	0.979	0.014
Cr-magnetite	2	0.03	0.07	88.26	3.02	bdl	0.02	0.02	0.20	0.09	0.25	91.96	30.49	64.20	98.39	0.001	0.004	0.093	-	0.001	0.001	0.006	0.004	0.010	0.995	1.885	0.528	0.953	0.989	0.004
ferritchromite	3	0.92	1.14	64.15	24.11	0.02	0.13	0.44	0.09	0.08	1.30	92.38	29.77	38.21	96.21	0.042	0.066	0.738	0.001	0.004	0.015	0.003	0.003	0.050	0.964	1.114	0.865	0.588	0.946	0.064
#10																														
Cr-magnetite	1	0.02	0.13	84.85	5.27	bdl	0.02	0.07	0.42	0.03	0.11	90.91	29.63	61.36	97.05	0.001	0.008	0.165	-	0.001	0.002	0.013	0.001	0.004	0.980	1.825	0.537	0.917	0.994	0.008
Cr-magnetite	2	0.02	0.04	85.41	5.58	0.02	0.01	0.05	0.33	0.02	0.02	91.51	29.99	61.59	97.68	0.001	0.002	0.174	0.001	-	0.002	0.011	0.001	0.001	0.986	1.822	0.541	0.912	0.994	0.002
Cr-magnetite	3	0.01	0.21	89.86	0.60	bdl	0.01	bdl	0.21	0.02	0.74	91.65	30.92	65.49	98.21	-	0.012	0.019	-	-	-	0.006	0.001	0.029	1.009	1.923	0.525	0.990	1.000	0.012
Cr-magnetite	4	bdl	0.02	88.57	2.77	0.02	0.04	0.03	0.30	0.02	0.02	91.79	30.20	64.87	98.29	-	0.001	0.086	-	0.001	0.001	0.010	0.001	0.001	0.988	1.911	0.517	0.957	1.000	0.001
Cr-magnetite	5	bdl	0.01	85.38	6.18	bdl	0.01	0.08	0.33	0.01	0.01	92.03	30.14	61.39	98.18	-	0.001	0.191	-	-	0.003	0.010	0.001	0.001	0.986	1.807	0.546	0.904	1.000	0.001
Cr-magnetite	6	bdl	0.01	89.60	0.98	0.02	0.02	bdl	0.22	0.02	0.08	90.95	30.17	66.04	97.56	-	-	0.031	0.001	0.001	-	0.007	0.001	0.003	0.996	1.961	0.508	0.984	1.000	0.000
Cr-magnetite	7	bdl	0.24	84.71	5.02	bdl	0.01	0.07	0.22	0.03	0.51	90.80	30.14	60.64	96.87	-	0.014	0.157	-	-	0.002	0.007	0.001	0.020	0.996	1.803	0.552	0.920	1.000	0.014
#11																														
ferritchromite	1	1.27	0.54	58.61	32.21	0.02	0.34	0.54	0.15	0.03	0.05	93.76	29.36	32.50	97.01	0.058	0.031	0.983	-	0.011	0.017	0.005	0.001	0.002	0.948	0.944	1.004	0.476	0.944	0.032
high *cr#* spinel	2	1.77	0.44	44.47	45.29	0.03	0.46	0.70	0.06	0.06	0.11	93.40	29.21	16.96	95.10	0.081	0.025	1.396	0.001	0.015	0.023	0.002	0.002	0.004	0.952	0.498	1.912	0.252	0.945	0.026
Cr-magnetite	3	bdl	0.01	89.45	1.23	0.03	bdl	bdl	0.29	0.06	0.03	91.09	30.03	66.04	97.71	-	0.001	0.038	0.001	-	-	0.009	0.002	0.001	0.989	1.958	0.505	0.981	1.000	0.001
#12																														
high *cr#* spinel	1	2.39	0.68	42.13	47.43	0.08	0.18	0.71	0.03	0.05	0.27	93.95	29.35	14.20	95.37	0.109	0.039	1.448	0.002	0.005	0.023	0.001	0.002	0.010	0.948	0.413	2.295	0.210	0.930	0.040
altered Cr-spinel	2	7.32	1.04	38.30	48.66	0.12	0.16	0.77	0.03	0.03	0.04	96.47	29.99	9.24	97.39	0.317	0.057	1.413	0.003	0.005	0.024	0.001	0.001	0.001	0.921	0.255	3.612	0.128	0.817	0.058
Cr-magnetite	3	0.01	0.02	88.61	0.88	0.01	0.03	0.02	0.27	0.03	0.01	89.90	29.63	65.55	96.47	0.001	0.001	0.028	-	0.001	0.001	0.009	0.001	-	0.989	1.969	0.502	0.985	0.966	0.001
Cr-magnetite	4	bdl	0.04	84.22	6.30	bdl	0.03	0.07	0.31	0.06	0.03	91.06	29.77	60.51	97.12	-	0.002	0.197	-	0.001	0.002	0.010	0.003	0.001	0.984	1.800	0.547	0.901	1.000	0.002
#13																														
Cr-magnetite	1	bdl	0.03	89.34	2.64	bdl	0.05	0.01	0.25	0.06	0.03	92.42	30.41	65.49	98.98	-	0.002	0.081	-	0.002	-	0.008	0.003	0.001	0.988	1.915	0.516	0.959	1.000	0.002
Cr-magnetite	2	bdl	0.02	85.78	6.32	bdl	0.02	0.04	0.27	0.03	0.02	92.50	30.37	61.58	98.67	-	0.001	0.194	-	0.001	0.001	0.008	0.001	0.001	0.988	1.803	0.548	0.903	1.000	0.001
Cr-magnetite	3	bdl	bdl	87.92	3.39	bdl	0.05	0.03	0.29	0.05	0.02	91.74	30.17	64.18	98.17	-	-	0.105	-	0.002	0.001	0.009	0.002	0.001	0.988	1.892	0.522	0.947	1.000	0.000
#14																														
Cr-magnetite	1	0.39	0.10	73.64	17.35	0.03	0.12	0.31	0.18	0.05	0.12	92.27	29.98	48.53	97.13	0.018	0.006	0.537	0.001	0.004	0.010	0.006	0.002	0.005	0.982	1.430	0.687	0.720	0.968	0.006
Cr-magnetite	2	bdl	0.01	86.19	5.96	bdl	0.05	0.05	0.33	0.03	0.02	92.63	30.37	62.03	98.84	-	0.001	0.183	-	0.002	0.002	0.010	0.001	0.001	0.987	1.814	0.544	0.908	1.000	0.001
high *cr#* spinel	3	2.66	0.75	39.48	50.46	0.07	0.35	0.75	0.03	0.04	0.17	94.76	29.32	11.29	95.89	0.120	0.043	1.527	0.002	0.011	0.024	0.001	0.002	0.007	0.939	0.325	2.889	0.165	0.927	0.044
#15																														
high *cr#* spinel	1	2.16	0.57	44.31	44.04	0.03	0.32	0.68	0.06	0.09	0.16	92.43	28.81	17.23	94.16	0.100	0.034	1.367	0.001	0.010	0.023	0.002	0.004	0.006	0.945	0.509	1.857	0.258	0.932	0.035
Cr-magnetite	2	0.27	0.24	77.30	12.69	bdl	0.11	0.21	0.11	0.03	0.33	91.29	29.93	52.65	96.57	0.013	0.014	0.396	-	0.003	0.007	0.003	0.001	0.013	0.987	1.562	0.632	0.792	0.968	0.014
Cr-magnetite	3	0.04	0.02	80.50	10.07	bdl	0.08	0.17	0.26	0.01	0.03	91.17	29.79	56.35	96.81	0.002	0.001	0.315	-	0.002	0.006	0.008	-	0.001	0.986	1.678	0.588	0.841	0.994	0.001
Cr-magnetite	4	bdl	0.21	81.87	7.76	0.02	0.05	0.11	0.27	0.01	0.20	90.51	29.59	58.10	96.33	-	0.013	0.244	0.001	0.002	0.004	0.009	0.001	0.008	0.983	1.737	0.566	0.877	1.000	0.013
#16																														
Cr-magnetite	1	bdl	0.11	83.52	5.98	bdl	0.03	0.07	0.29	0.07	0.08	90.15	29.43	60.10	96.17	-	0.006	0.189	-	0.001	0.002	0.009	0.003	0.003	0.982	1.804	0.544	0.905	1.000	0.006
Cr-magnetite	2	0.06	0.90	85.77	2.52	bdl	0.02	0.01	0.17	0.05	1.11	90.62	29.96	62.02	96.83	0.003	0.053	0.078	-	0.001	-	0.005	0.002	0.044	0.983	1.831	0.537	0.958	0.963	0.051
Cr-magnetite	3	0.02	0.54	76.41	11.69	0.02	0.03	0.23	0.25	0.04	0.70	89.93	29.32	52.33	95.17	0.001	0.032	0.369	0.001	0.001	0.008	0.008	0.002	0.028	0.979	1.572	0.623	0.809	0.997	0.032
#17																														
Cr-magnetite	1	0.05	0.04	86.79	3.11	bdl	0.05	0.05	0.23	0.02	0.09	90.42	29.85	63.28	96.76	0.002	0.002	0.098	-	0.001	0.002	0.007	0.001	0.004	0.992	1.891	0.525	0.950	0.980	0.002
Cr-magnetite	2	0.03	0.13	78.39	11.68	0.04	0.05	0.20	0.21	0.02	0.17	90.90	29.72	54.09	96.32	0.002	0.007	0.366	0.001	0.001	0.007	0.007	0.001	0.007	0.986	1.615	0.611	0.814	0.995	0.007
#18																														
high *cr#* spinel	1	2.16	1.55	34.19	55.71	0.08	0.19	1.52	0.05	0.03	0.03	95.53	27.25	7.71	96.30	0.097	0.088	1.670	0.002	0.006	0.049	0.002	0.001	0.001	0.864	0.220	3.927	0.111	0.945	0.092
high *cr#* spinel	2	2.60	1.01	37.46	52.77	0.07	0.20	0.79	0.04	0.03	0.68	95.65	29.79	8.53	96.50	0.116	0.057	1.580	0.002	0.006	0.025	0.001	0.001	0.026	0.943	0.243	3.881	0.125	0.932	0.057
Cr-magnetite	3	bdl	0.09	87.74	2.13	bdl	0.03	0.04	0.27	0.02	0.18	90.49	29.89	64.28	96.93	-	0.006	0.067	-	0.001	0.001	0.009	0.001	0.007	0.991	1.918	0.517	0.966	1.000	0.006
Cr-magnetite	4	bdl	0.01	87.14	3.22	0.01	0.03	0.05	0.21	0.03	0.16	90.87	30.14	63.34	97.22	-	0.001	0.101	-	0.001	0.002	0.007	0.001	0.006	0.996	1.884	0.529	0.949	1.000	0.001
Cr-magnetite	5	bdl	bdl	88.40	2.79	bdl	0.03	0.02	0.30	0.03	bdl	91.57	30.12	64.76	98.05	-	-	0.087	-	0.001	0.001	0.009	0.001	-	0.988	1.913	0.516	0.957	1.000	0.000
#19																														
Cr-magnetite	1	0.23	1.72	76.54	11.36	0.01	0.06	0.22	0.18	0.04	1.63	91.99	29.47	52.31	97.22	0.010	0.099	0.346	-	0.002	0.007	0.006	0.002	0.063	0.949	1.516	0.626	0.810	0.972	0.094
Cr-magnetite	2	0.46	1.00	71.73	16.54	0.03	0.08	0.31	0.15	0.09	0.88	91.26	29.23	47.23	95.99	0.021	0.058	0.513	0.001	0.002	0.010	0.005	0.004	0.034	0.958	1.393	0.688	0.723	0.961	0.057
#20																														
Cr-magnetite	1	0.12	0.24	81.46	7.84	0.01	0.05	0.13	0.23	0.04	0.41	90.52	29.80	57.41	96.27	0.005	0.014	0.246	-	0.002	0.004	0.007	0.002	0.016	0.989	1.714	0.577	0.872	0.980	0.014
Cr-magnetite	2	0.02	0.09	88.31	1.48	bdl	0.06	0.01	0.22	0.02	0.12	90.31	29.86	64.95	96.82	0.001	0.005	0.047	-	0.002	-	0.007	0.001	0.005	0.992	1.941	0.511	0.976	0.979	0.005
high *cr#* spinel	3	3.16	1.67	38.93	46.87	0.12	0.55	0.78	0.07	0.03	1.44	93.61	29.26	10.74	94.68	0.142	0.095	1.416	0.004	0.017	0.025	0.002	0.001	0.055	0.935	0.309	3.026	0.166	0.909	0.092
high *cr#* spinel	4	3.54	2.02	38.70	46.38	0.10	0.55	0.77	0.07	0.03	1.78	93.94	29.32	10.43	94.98	0.158	0.114	1.388	0.003	0.017	0.025	0.002	0.001	0.067	0.928	0.297	3.125	0.161	0.898	0.109
#21																														
Cr-magnetite	1	0.46	1.60	78.03	11.42	bdl	0.07	0.20	0.15	0.04	1.65	93.63	30.31	53.03	98.94	0.021	0.091	0.342	-	0.002	0.006	0.004	0.002	0.063	0.959	1.510	0.635	0.806	0.942	0.087
ferritchromite	2	1.08	0.44	50.18	41.55	0.06	0.13	0.73	0.07	0.03	0.50	94.79	30.15	22.26	97.02	0.049	0.025	1.262	0.002	0.004	0.024	0.002	0.001	0.019	0.968	0.643	1.505	0.329	0.963	0.025
ferritchromite	3	1.36	0.22	62.90	27.06	0.03	0.12	0.43	0.15	0.01	0.08	92.37	29.67	36.94	96.07	0.063	0.013	0.837	0.001	0.004	0.014	0.005	0.001	0.003	0.971	1.088	0.892	0.547	0.930	0.013
#22																														
Cr-magnetite	1	0.01	0.06	89.45	3.76	bdl	0.08	0.01	0.26	0.01	0.13	93.78	30.97	64.99	100.28	-	0.004	0.114	-	0.002	-	0.008	0.001	0.005	0.992	1.874	0.529	0.943	1.000	0.004
Cr-magnetite	3	0.02	0.03	89.39	1.91	0.02	0.05	0.02	0.29	0.03	0.00	91.78	30.19	65.79	98.37	0.001	0.002	0.059	0.001	0.002	0.001	0.009	0.001	-	0.988	1.937	0.510	0.970	0.983	0.002
high *cr#* spinel	4	4.21	1.48	36.48	53.71	0.04	0.38	1.08	0.04	0.02	0.07	97.52	28.81	8.52	98.38	0.182	0.081	1.563	0.001	0.011	0.034	0.001	0.001	0.003	0.886	0.236	3.754	0.119	0.896	0.084
ferritchromite	5	1.62	0.50	50.93	41.18	bdl	0.17	0.68	0.09	0.04	0.28	95.48	30.07	23.18	97.81	0.073	0.028	1.238	-	0.005	0.022	0.003	0.002	0.011	0.956	0.663	1.442	0.336	0.944	0.028
high *cr#* spinel	6	2.99	1.42	35.92	55.82	0.05	0.31	1.11	0.02	0.02	0.03	97.68	28.71	8.01	98.49	0.130	0.078	1.632	0.001	0.009	0.035	0.001	0.001	0.001	0.888	0.223	3.982	0.112	0.926	0.081
#23																														
Cr-magnetite	1	bdl	bdl	90.09	1.18	bdl	0.02	0.02	0.28	0.03	0.01	91.63	30.21	66.55	98.29	-	-	0.037	-	0.001	0.001	0.009	0.001	-	0.990	1.962	0.505	0.981	1.000	0.000
Cr-magnetite	2	0.01	0.01	90.41	1.14	bdl	0.03	bdl	0.25	0.05	0.01	91.90	30.29	66.80	98.59	-	0.001	0.035	-	0.001	-	0.008	0.002	-	0.989	1.963	0.504	0.982	1.000	0.001
Cr-magnetite	3	bdl	0.02	90.88	0.49	bdl	0.01	bdl	0.28	0.06	bdl	91.73	30.21	67.43	98.48	-	0.001	0.015	-	-	-	0.009	0.002	-	0.988	1.985	0.498	0.993	1.000	0.001
Cr-magnetite	4	bdl	0.09	89.09	2.47	bdl	0.02	0.01	0.25	0.04	0.05	92.01	30.26	65.39	98.56	-	0.005	0.076	-	0.001	-	0.008	0.001	0.002	0.987	1.920	0.514	0.962	1.000	0.005
Cr-magnetite	5	bdl	0.08	89.93	2.22	bdl	0.03	0.01	0.30	0.05	0.11	92.72	30.51	66.03	99.34	-	0.005	0.068	-	0.001	-	0.009	0.002	0.004	0.988	1.923	0.514	0.966	1.000	0.005
Cr-magnetite	6	0.63	0.11	76.39	17.37	0.03	0.06	0.26	0.15	0.03	0.04	95.08	30.92	50.54	100.15	0.028	0.006	0.521	0.001	0.002	0.008	0.005	0.001	0.001	0.982	1.444	0.680	0.725	0.949	0.006
Cr-magnetite	7	0.16	0.10	85.56	5.27	bdl	0.04	0.06	0.30	0.06	0.07	91.62	29.98	61.77	97.81	0.008	0.006	0.163	-	0.001	0.002	0.010	0.002	0.003	0.983	1.823	0.539	0.914	0.953	0.006
#24																														
Cr-magnetite	1	0.45	0.24	75.97	12.15	0.03	0.08	0.16	0.27	0.01	0.60	89.96	29.80	51.31	95.10	0.021	0.015	0.384	0.001	0.003	0.005	0.009	-	0.024	0.996	1.543	0.645	0.792	0.948	0.015
Cr-magnetite	2	0.02	0.02	86.87	4.32	bdl	0.04	0.04	0.30	0.01	0.02	91.64	30.12	63.07	97.96	0.001	0.001	0.134	-	0.001	0.001	0.009	0.001	0.001	0.988	1.862	0.531	0.932	0.993	0.001
Cr-magnetite	3	0.02	0.06	88.37	1.56	0.02	0.04	0.03	0.24	0.01	0.06	90.42	29.83	65.06	96.94	0.001	0.003	0.049	-	0.001	0.001	0.008	0.001	0.002	0.990	1.943	0.510	0.975	0.980	0.003
#25																														
ferritchromite	1	0.22	0.13	67.20	23.89	0.03	0.03	0.41	0.11	0.10	0.17	92.29	29.76	41.61	96.46	0.010	0.008	0.743	0.001	0.001	0.014	0.004	0.004	0.007	0.979	1.231	0.795	0.620	0.987	0.008
high *cr#* spinel	2	3.85	1.41	40.53	47.06	0.02	0.17	0.72	0.03	0.14	0.79	94.70	29.20	12.59	95.96	0.171	0.079	1.405	0.001	0.005	0.023	0.001	0.005	0.030	0.922	0.358	2.575	0.185	0.891	0.079
ferritchromite	3	6.49	2.61	41.87	37.87	0.03	0.14	0.68	0.08	2.76	1.28	93.81	25.09	18.64	95.67	0.281	0.143	1.102	0.001	0.004	0.021	0.002	0.109	0.047	0.772	0.516	1.496	0.272	0.797	0.156
#26																														
Cr-magnetite	1	0.21	0.34	82.51	8.70	0.02	0.11	0.14	0.21	0.04	0.30	92.58	30.21	58.12	98.40	0.010	0.020	0.267	0.001	0.003	0.005	0.006	0.001	0.012	0.980	1.696	0.578	0.860	0.964	0.020
Cr-magnetite	2	0.01	0.30	88.46	2.37	bdl	0.06	0.03	0.18	0.04	0.34	91.79	30.27	64.67	98.26	-	0.018	0.073	-	0.002	0.001	0.006	0.002	0.013	0.988	1.898	0.521	0.963	1.000	0.018
Cr-magnetite	3	0.05	0.49	84.96	4.68	bdl	0.02	0.03	0.14	0.05	0.76	91.19	30.29	60.76	97.27	0.002	0.029	0.145	-	0.001	0.001	0.004	0.002	0.030	0.993	1.793	0.554	0.924	0.986	0.028
Cr-magnetite	4	0.04	0.05	86.74	4.84	bdl	0.04	0.07	0.19	0.04	0.10	92.12	30.37	62.65	98.40	0.002	0.003	0.149	-	0.001	0.002	0.006	0.002	0.004	0.991	1.840	0.539	0.924	0.987	0.003
#27																														
high *cr#* spinel	1	3.10	0.88	34.48	56.18	0.03	0.41	0.93	0.05	0.04	0.04	96.14	29.15	5.92	96.74	0.138	0.050	1.677	0.001	0.012	0.030	0.001	0.002	0.002	0.920	0.168	5.476	0.085	0.924	0.052
high *cr#* spinel	2	5.05	2.82	34.31	54.16	0.03	0.47	1.45	0.03	0.03	0.02	98.36	26.73	8.43	99.21	0.214	0.151	1.541	0.001	0.014	0.044	0.001	0.001	0.001	0.804	0.228	3.526	0.115	0.878	0.158
high *cr#* spinel	3	3.90	0.94	37.35	52.26	0.06	0.38	0.82	0.04	0.04	0.46	96.26	29.94	8.23	97.08	0.172	0.053	1.547	0.002	0.011	0.026	0.001	0.002	0.017	0.937	0.232	4.039	0.119	0.900	0.054
high *cr#* spinel	4	2.77	0.43	34.63	54.72	0.02	0.34	0.81	bdl	0.06	0.08	93.86	29.25	5.98	94.46	0.127	0.025	1.680	0.001	0.011	0.027	-	0.002	0.003	0.950	0.175	5.429	0.088	0.930	0.026
Cr-magnetite	5	0.04	0.03	88.68	3.31	0.01	0.07	0.03	0.25	0.03	0.02	92.46	30.44	64.71	98.94	0.002	0.002	0.102	-	0.002	0.001	0.008	0.001	0.001	0.989	1.892	0.523	0.948	0.981	0.002
#28																														
high *cr#* spinel	1	3.23	1.05	36.12	52.77	0.04	0.46	0.99	0.05	0.02	0.07	94.79	28.53	8.43	95.64	0.145	0.060	1.591	0.001	0.014	0.032	0.002	0.001	0.003	0.910	0.242	3.760	0.122	0.916	0.062
Cr-magnetite	2	0.24	0.19	87.23	4.96	bdl	0.05	0.07	0.22	0.03	0.24	93.23	30.72	62.80	99.52	0.011	0.011	0.151	-	0.002	0.002	0.007	0.001	0.009	0.988	1.818	0.543	0.918	0.932	0.011
high *cr#* spinel	3	3.69	1.32	37.86	52.50	0.05	0.38	1.12	0.08	0.06	0.12	97.17	28.84	10.02	98.17	0.161	0.073	1.537	0.001	0.011	0.035	0.002	0.002	0.004	0.893	0.279	3.201	0.141	0.905	0.076
high *cr#* spinel	4	3.17	0.56	37.32	54.67	0.05	0.42	0.85	0.04	0.03	0.03	97.13	30.10	8.03	97.93	0.140	0.031	1.617	0.001	0.013	0.027	0.001	0.001	0.001	0.942	0.226	4.168	0.114	0.920	0.032
ferritchromite	5	1.97	0.86	55.80	35.34	0.03	0.23	0.51	0.09	0.02	0.50	95.34	30.13	28.52	98.19	0.087	0.048	1.055	0.001	0.007	0.016	0.003	0.001	0.019	0.952	0.811	1.174	0.415	0.924	0.048
high *cr#* spinel	6	3.16	1.05	42.54	48.96	0.05	0.34	0.79	0.09	0.03	0.29	97.31	29.86	14.10	98.72	0.138	0.058	1.435	0.001	0.010	0.025	0.003	0.001	0.011	0.925	0.393	2.354	0.200	0.912	0.059
Cr-magnetite	7	0.01	0.02	89.65	2.23	bdl	0.04	bdl	0.23	0.03	bdl	92.20	30.41	65.84	98.79	-	0.001	0.069	-	0.001	-	0.007	0.001	-	0.991	1.930	0.513	0.965	1.000	0.001
#29																														
Cr-magnetite	1	0.08	1.44	85.37	2.71	bdl	0.02	0.01	0.31	0.09	1.09	91.12	29.10	62.53	97.38	0.004	0.084	0.083	-	0.001	-	0.010	0.004	0.042	0.945	1.828	0.517	0.955	0.954	0.082
Cr-magnetite	2	0.05	0.58	85.49	0.59	0.01	0.03	bdl	0.23	0.22	0.57	87.76	28.61	63.22	94.09	0.002	0.035	0.019	-	0.001	-	0.008	0.009	0.023	0.971	1.931	0.503	0.989	0.905	0.035
Cr-magnetite	3	bdl	0.03	88.68	2.06	bdl	0.04	bdl	0.40	0.05	0.01	91.26	29.90	65.32	97.80	-	0.002	0.064	-	0.001	-	0.013	0.002	-	0.984	1.934	0.509	0.968	1.000	0.002
Cr-magnetite	4	0.03	0.04	85.78	4.26	0.02	0.02	0.03	0.43	0.03	0.03	90.67	29.66	62.37	96.92	0.001	0.002	0.134	0.001	0.001	0.001	0.014	0.001	0.001	0.983	1.861	0.528	0.932	0.993	0.002
#30																														
Cr-magnetite	1	0.02	0.00	81.45	9.36	0.01	0.05	0.16	0.24	0.05	0.11	91.45	30.00	57.18	97.18	0.001	-	0.292	-	0.002	0.005	0.008	0.002	0.004	0.989	1.697	0.583	0.853	0.997	0.000
high *cr#* spinel	2	9.99	1.18	40.23	42.16	0.02	0.19	0.64	0.04	0.04	0.05	94.55	29.65	11.76	95.72	0.434	0.065	1.229	-	0.006	0.020	0.001	0.002	0.002	0.914	0.326	2.804	0.164	0.739	0.066
#31																														
high *cr#* spinel	1	5.01	2.33	33.61	55.52	0.07	0.41	1.24	0.04	0.02	0.04	98.29	27.69	6.58	98.95	0.214	0.126	1.589	0.002	0.012	0.038	0.001	0.001	0.001	0.838	0.179	4.682	0.090	0.881	0.131
high *cr#* spinel	2	4.03	2.30	34.10	55.76	0.04	0.39	1.63	0.04	0.04	0.04	98.39	27.17	7.71	99.16	0.173	0.125	1.601	0.001	0.011	0.050	0.001	0.002	0.001	0.825	0.211	3.910	0.106	0.902	0.132
high *cr#* spinel	3	2.87	0.93	36.33	56.52	0.04	0.30	0.90	0.04	0.02	0.14	98.09	29.88	7.17	98.81	0.125	0.052	1.654	0.001	0.009	0.028	0.001	0.001	0.005	0.925	0.200	4.625	0.101	0.930	0.053
high *cr#* spinel	4	4.38	4.45	29.61	57.87	0.06	0.45	1.43	0.01	0.02	0.04	98.32	24.18	6.04	98.92	0.184	0.237	1.634	0.002	0.013	0.043	-	0.001	0.001	0.722	0.162	4.457	0.082	0.899	0.247
Cr-magnetite	5	0.05	bdl	88.05	5.47	bdl	0.03	0.04	0.19	0.01	0.09	93.93	31.09	63.30	100.27	0.002	-	0.166	-	0.001	0.001	0.006	-	0.003	0.996	1.824	0.546	0.916	0.988	0.000
Cr-magnetite	6	bdl	0.03	80.19	11.54	bdl	0.05	0.13	0.36	0.01	0.04	92.35	30.07	55.70	97.93	-	0.002	0.357	-	0.002	0.004	0.011	0.001	0.001	0.983	1.639	0.600	0.821	1.000	0.002
#32																														
Cr-magnetite	1	0.02	bdl	89.06	2.18	bdl	0.03	bdl	0.29	0.00	bdl	91.58	30.21	65.40	98.13	0.001	-	0.068	-	0.001	-	0.009	-	-	0.991	1.931	0.513	0.966	0.986	0.000
Cr-magnetite	2	bdl	bdl	87.84	3.38	bdl	0.03	0.03	0.16	0.01	0.09	91.56	30.37	63.88	97.95	-	-	0.105	-	0.001	0.001	0.005	0.001	0.004	0.997	1.887	0.528	0.947	1.000	0.000
Cr-magnetite	3	bdl	bdl	90.24	1.30	0.02	0.05	0.02	0.33	0.01	0.01	91.99	30.32	66.59	98.66	-	-	0.040	0.001	0.002	0.001	0.010	0.001	0.001	0.990	1.956	0.506	0.980	1.000	0.000
Cr-magnetite	4	bdl	bdl	90.96	2.05	0.02	0.05	0.01	0.30	0.01	0.02	93.43	30.84	66.82	100.12	-	-	0.062	0.001	0.002	-	0.009	0.001	0.001	0.991	1.933	0.513	0.969	1.000	0.000
Cr-magnetite	5	0.01	bdl	89.18	3.64	0.01	0.03	0.02	0.15	0.02	0.11	93.18	30.94	64.72	99.66	0.001	-	0.111	-	0.001	0.001	0.005	0.001	0.004	0.998	1.878	0.531	0.944	0.991	0.000
Cr-magnetite	6	bdl	0.03	85.19	8.57	0.04	0.05	0.15	0.13	0.02	0.11	94.29	31.10	60.11	100.32	-	0.002	0.259	0.001	0.002	0.005	0.004	0.001	0.004	0.994	1.729	0.575	0.870	1.000	0.002
Cr-magnetite	7	bdl	0.02	89.68	3.21	bdl	0.03	0.02	0.23	0.01	0.03	93.23	30.76	65.48	99.79	-	0.001	0.098	-	0.001	0.001	0.007	-	0.001	0.991	1.899	0.522	0.951	1.000	0.001
high *cr#* spinel	8	2.93	2.05	39.59	47.85	bdl	0.17	0.79	0.04	0.01	1.70	95.13	29.42	11.30	96.26	0.130	0.115	1.419	-	0.005	0.025	0.001	-	0.064	0.923	0.319	2.893	0.171	0.916	0.111
high *cr#* spinel	9	3.14	1.34	37.76	53.90	0.03	0.27	0.97	0.02	0.01	0.10	97.54	29.07	9.65	98.51	0.137	0.074	1.577	0.001	0.008	0.030	0.001	-	0.004	0.900	0.269	3.346	0.136	0.920	0.076

#33																														
Cr-magnetite	*1*	0.03	0.01	90.10	0.90	bdl	0.03	bdl	0.31	0.03	0.01	91.43	30.12	66.65	98.10	0.001	-	0.028	-	0.001	-	0.010	0.001	0.001	0.989	1.969	0.502	0.985	0.966	0.000
Cr-magnetite	*2*	0.07	0.32	87.38	3.34	bdl	0.05	0.03	0.31	0.01	0.22	91.74	29.97	63.81	98.13	0.003	0.019	0.103	-	0.002	0.001	0.010	0.001	0.009	0.979	1.875	0.522	0.946	0.972	0.019
Cr-magnetite	*3*	bdl	bdl	90.86	1.22	bdl	bdl	0.01	0.28	0.01	0.02	92.39	30.51	67.07	99.11	-	-	0.037	-	-	-	0.009	0.001	0.001	0.991	1.961	0.505	0.981	1.000	0.000
Cr-magnetite	*4*	0.01	0.01	88.11	3.70	bdl	0.03	0.02	0.30	0.03	0.01	92.24	30.33	64.22	98.67	-	0.001	0.114	-	0.001	0.001	0.010	0.001	0.001	0.988	1.883	0.525	0.943	1.000	0.001
Cr-magnetite	*5*	bdl	0.07	84.07	7.60	bdl	0.05	0.15	0.19	0.02	0.07	92.21	30.23	59.83	98.20	-	0.004	0.235	-	0.001	0.005	0.006	0.001	0.003	0.987	1.758	0.561	0.882	1.000	0.004
Cr-magnetite	*6*	bdl	0.02	84.28	7.29	0.01	0.02	0.08	0.30	0.01	0.01	92.02	30.15	60.16	98.05	-	0.001	0.226	-	0.001	0.003	0.009	-	-	0.987	1.772	0.557	0.887	1.000	0.001
Cr-magnetite	*7*	0.01	0.02	89.97	1.09	bdl	0.02	bdl	0.40	0.03	0.02	91.55	30.07	66.57	98.22	-	0.001	0.034	-	-	-	0.013	0.001	0.001	0.986	1.964	0.502	0.983	1.000	0.001
#34																														
altered Cr-spinel	*1*	11.73	2.94	33.50	46.06	0.03	0.24	0.86	0.06	0.05	0.08	95.56	27.27	6.93	96.25	0.495	0.157	1.304	0.001	0.007	0.026	0.002	0.002	0.003	0.817	0.187	4.369	0.094	0.725	0.161
ferritchromite	*2*	5.23	0.88	47.46	38.97	0.08	0.36	0.68	0.08	0.03	0.05	93.82	29.27	20.22	95.84	0.234	0.050	1.169	0.002	0.011	0.022	0.003	0.001	0.002	0.929	0.577	1.610	0.291	0.833	0.051
altered Cr-spinel	*3*	8.44	2.71	36.09	47.87	0.03	0.26	1.07	0.06	0.02	0.04	96.59	27.27	9.81	97.57	0.358	0.145	1.364	0.001	0.008	0.033	0.002	0.001	0.001	0.822	0.266	3.090	0.134	0.792	0.150
Cr-magnetite	*4*	0.02	0.03	81.50	8.47	0.02	0.03	0.14	0.42	0.05	0.19	90.87	29.75	57.51	96.63	0.001	0.002	0.266	0.001	0.001	0.005	0.013	0.002	0.008	0.986	1.716	0.575	0.865	0.996	0.002
#35																														
Cr-magnetite	*1*	0.34	0.90	83.75	5.97	0.03	0.04	0.09	0.20	0.06	0.77	92.14	29.92	59.82	98.13	0.015	0.052	0.183	0.001	0.001	0.003	0.006	0.002	0.030	0.967	1.740	0.556	0.898	0.924	0.051
ferritchromite	*2*	1.73	0.59	58.87	29.55	0.03	0.20	0.54	0.13	0.08	0.27	91.99	29.05	33.14	95.31	0.080	0.035	0.915	0.001	0.006	0.018	0.004	0.003	0.010	0.951	0.976	0.974	0.495	0.920	0.035
#36																														
Cr-magnetite	*1*	0.01	0.05	88.93	3.50	0.02	0.05	0.03	0.26	bdl	0.03	92.88	30.60	64.83	99.37	-	0.003	0.107	0.001	0.002	0.001	0.008	-	0.001	0.990	1.887	0.525	0.946	1.000	0.003
altered Cr-spinel	*2*	18.64	6.58	26.72	45.98	0.01	0.20	0.85	0.04	0.01	0.03	99.05	23.86	3.18	99.37	0.721	0.322	1.193	-	0.005	0.024	0.001	-	0.001	0.655	0.079	8.291	0.040	0.623	0.330
altered Cr-spinel	*3*	19.05	5.62	28.07	44.13	0.01	0.17	1.04	0.01	0.01	0.03	98.15	24.95	3.47	98.50	0.746	0.279	1.160	-	0.005	0.029	-	-	0.001	0.693	0.087	7.966	0.044	0.609	0.287
#37																														
Cr-magnetite	*1*	bdl	0.02	89.96	2.25	bdl	0.05	bdl	0.29	0.01	0.02	92.59	30.53	66.04	99.21	-	0.001	0.069	-	0.001	-	0.009	-	0.001	0.990	1.928	0.513	0.965	1.000	0.001
Cr-magnetite	*3*	0.02	0.05	86.20	4.52	bdl	0.02	0.05	0.29	0.01	0.08	91.24	30.00	62.45	97.49	0.001	0.003	0.141	-	0.001	0.002	0.009	0.001	0.003	0.989	1.852	0.534	0.929	0.993	0.003
#38																														
Cr-magnetite	*1*	0.04	bdl	89.25	2.54	0.01	0.02	0.01	0.31	0.01	0.03	92.23	30.41	65.38	98.77	0.002	-	0.078	-	0.001	-	0.010	0.001	0.001	0.991	1.916	0.517	0.960	0.975	0.000
altered Cr-spinel	*2*	0.01	0.18	88.79	1.54	bdl	0.04	0.01	0.26	0.01	0.31	91.15	30.19	65.11	97.67	0.001	0.010	0.048	-	0.001	-	0.008	-	0.012	0.993	1.926	0.516	0.975	0.980	0.010
VP17-01																														
#1																														
Cr-spinel (core)	*1*	37.93	11.00	24.70	25.97	0.83	0.15	0.30	0.14	0.03	0.09	101.13	22.03	2.96	101.43	1.296	0.475	0.595	0.018	0.003	0.007	0.003	0.001	0.002	0.534	0.065	8.215	0.033	0.315	0.471
Cr-spinel (core)	*2*	38.56	11.82	23.60	26.15	0.75	0.12	0.26	0.16	0.02	0.09	101.53	20.95	2.94	101.83	1.303	0.505	0.593	0.016	0.003	0.006	0.004	0.001	0.002	0.503	0.063	7.984	0.032	0.313	0.501
Cr-spinel (core)	*3*	38.92	10.76	25.82	26.16	0.75	0.11	0.30	0.18	0.02	0.08	103.10	23.09	3.04	103.40	1.306	0.457	0.589	0.016	0.002	0.007	0.004	-	0.002	0.550	0.065	8.462	0.033	0.311	0.454
Cr-spinel (core)	*4*	38.85	8.50	29.87	24.71	0.91	0.10	0.41	0.12	0.01	0.08	103.59	26.78	3.44	103.93	1.317	0.365	0.562	0.020	0.002	0.010	0.003	-	0.002	0.644	0.074	8.703	0.038	0.299	0.362
Cr-spinel (core)	*5*	39.37	9.72	27.70	25.35	0.88	0.13	0.33	0.14	0.02	0.14	103.77	25.16	2.82	104.05	1.321	0.412	0.570	0.019	0.003	0.008	0.003	0.001	0.004	0.599	0.060	9.983	0.031	0.301	0.408
titanomagnetite (rim)	*6*	4.71	0.02	60.31	4.12	21.14	0.44	0.40	0.01	0.06	0.06	91.27	48.85	12.73	92.55	0.219	0.001	0.129	0.628	0.014	0.013	-	0.003	0.002	1.613	0.378	4.267	0.521	0.371	0.001
titanomagnetite (rim)	*8*	3.77	0.02	62.97	2.62	22.03	0.46	0.41	0.01	0.07	0.08	92.43	49.91	14.51	93.89	0.174	0.001	0.081	0.648	0.014	0.014	-	0.003	0.003	1.634	0.427	3.827	0.626	0.318	0.001
titanomagnetite (rim)	*9*	7.39	0.01	58.14	9.42	16.72	0.39	1.40	bdl	0.03	0.06	93.55	45.09	14.50	95.00	0.331	0.001	0.283	0.478	0.012	0.045	-	0.001	0.002	1.433	0.415	3.453	0.403	0.461	0.001
#2																														
Cr-spinel (core)	*1*	43.22	9.70	29.51	14.07	1.05	0.13	0.28	0.12	0.08	0.25	98.41	24.41	5.66	98.98	1.487	0.422	0.325	0.023	0.003	0.007	0.003	0.003	0.007	0.596	0.124	4.806	0.064	0.179	0.415
Cr-spinel (core)	*3*	39.55	7.41	35.33	12.95	2.81	0.21	0.40	0.06	0.07	0.16	98.96	28.96	7.08	99.67	1.394	0.330	0.306	0.063	0.005	0.010	0.001	0.002	0.005	0.724	0.159	4.553	0.086	0.180	0.313
titanomagnetite (rim)	*4*	10.28	0.05	56.28	5.27	17.86	0.53	1.16	0.05	0.07	0.05	91.60	45.98	11.45	92.74	0.464	0.003	0.159	0.514	0.016	0.038	0.001	0.003	0.002	1.471	0.330	4.458	0.346	0.255	0.002
VP17-04b																														
#1																														
Cr-spinel	*1*	21.45	6.89	26.73	44.49	0.10	0.34	0.30	0.13	0.00	bdl	100.44	24.76	2.19	100.66	0.809	0.328	1.125	0.002	0.009	0.008	0.003	-	-	0.662	0.053	12.491	0.027	0.582	0.331
Cr-spinel	*2*	25.44	7.90	25.20	41.17	0.09	0.34	0.29	0.11	0.01	0.01	100.56	23.90	1.44	100.70	0.936	0.368	1.017	0.002	0.009	0.008	0.003	-	-	0.624	0.034	18.353	0.017	0.521	0.371
Cr-spinel	*3*	25.94	8.22	24.99	41.08	0.11	0.33	0.30	0.12	0.02	0.02	101.13	23.67	1.46	101.28	0.946	0.379	1.005	0.003	0.008	0.008	0.003	0.001	0.001	0.613	0.034	18.029	0.017	0.515	0.382
#2																														
Cr-spinel	*1*	19.64	7.46	25.89	47.12	0.15	0.35	0.33	0.07	0.01	bdl	101.00	23.86	2.26	101.23	0.739	0.355	1.190	0.004	0.009	0.009	0.002	-	-	0.637	0.054	11.796	0.027	0.617	0.358
Cr-spinel	*2*	21.46	6.99	27.22	44.90	0.12	0.34	0.29	0.07	0.00	bdl	101.39	25.00	2.46	101.63	0.802	0.330	1.125	0.003	0.009	0.008	0.002	-	-	0.663	0.059	11.237	0.030	0.584	0.332
Cr-spinel	*3*	19.17	7.37	25.88	47.26	0.08	0.34	0.30	0.09	bdl	bdl	100.50	23.72	2.41	100.74	0.727	0.354	1.202	0.002	0.009	0.008	0.002	-	-	0.638	0.058	11.000	0.029	0.623	0.357
VP17-05b																														
#1																														
Cr-spinel	*1*	8.43	9.82	18.26	63.22	0.03	0.15	0.33	0.02	0.00	0.03	100.30	18.20	0.07	100.30	0.330	0.486	1.661	0.001	0.004	0.009	0.001	-	0.001	0.506	0.002	253.000	0.001	0.834	0.490
Cr-spinel	*2*	8.56	9.97	18.21	62.78	0.02	0.15	0.35	0.03	0.00	0.02	100.08	17.88	0.37	100.12	0.335	0.494	1.649	0.001	0.004	0.010	0.001	-	0.001	0.497	0.009	55.222	0.005	0.831	0.498
Cr-spinel	*3*	8.60	10.00	17.96	63.00	0.02	0.15	0.33	0.02	0.01	0.02	100.11	17.85	0.12	100.12	0.337	0.495	1.654	0.001	0.004	0.009	-	-	0.001	0.496	0.003	165.333	0.002	0.831	0.499
Cr-spinel	*4*	8.48	9.84	18.15	63.10	0.03	0.13	0.35	0.04	0.00	0.02	100.15	18.07	0.10	100.16	0.332	0.488	1.659	0.001	0.004	0.010	0.001	-	0.001	0.502	0.002	251.000	0.001	0.833	0.493
Cr-spinel	*5*	8.35	9.76	18.25	62.89	0.03	0.12	0.33	0.03	0.00	0.04	99.79	18.12	0.14	99.81	0.329	0.486	1.661	0.001	0.003	0.009	0.001	-	0.001	0.506	0.004	126.500	0.002	0.835	0.490
VP17-15																														
#1																														
Cr-spinel - gen X	*1*	26.18	15.03	15.91	43.77	0.03	0.19	0.20	0.18	0.01	0.03	101.53	13.43	2.75	101.80	0.910	0.661	1.021	0.001	0.004	0.005	0.004	-	0.001	0.331	0.061	5.426	0.031	0.529	0.666
Cr-spinel - gen X	*2*	26.35	15.03	16.11	43.47	0.04	0.19	0.22	0.17	bdl	0.04	101.62	13.51	2.89	101.91	0.915	0.660	1.012	0.001	0.005	0.005	0.004	-	0.001	0.333	0.064	5.203	0.032	0.525	0.665
Cr-spinel - gen X	*3*	26.41	15.25	16.08	43.57	0.07	0.18	0.21	0.18	0.01	0.03	102.00	13.32	3.07	102.31	0.913	0.666	1.010	0.002	0.004	0.005	0.004	-	0.001	0.327	0.068	4.809	0.034	0.525	0.671
Cr-spinel - gen X	*4*	26.35	14.92	15.67	43.35	0.03	0.19	0.21	0.18	0.01	0.03	100.92	13.41	2.51	101.17	0.920	0.659	1.016	0.001	0.004	0.005	0.004	-	0.001	0.332	0.056	5.929	0.028	0.525	0.665
Cr-spinel - gen X	*5*	26.41	15.10	15.91	43.83	0.02	0.21	0.20	0.16	0.01	0.03	101.87	13.48	2.70	102.14	0.915	0.661	1.018	0.001	0.005	0.005	0.004	-	0.001	0.331	0.060	5.517	0.030	0.527	0.666
Cr-spinel - gen X	*6*	26.35	14.87	15.97	43.45	0.05	0.21	0.20	0.19	0.00	0.03	101.31	13.63	2.59	101.57	0.918	0.655	1.015	0.001	0.005	0.005	0.004	-	0.001	0.337	0.058	5.810	0.029	0.525	0.660
#2																														
Cr-spinel - gen X	*1*	27.77	14.02	18.53	43.11	0.03	0.20	0.23	0.18	bdl	0.04	104.12	16.05	2.75	104.40	0.946	0.604	0.985	0.001	0.005	0.006	0.004	-	0.001	0.388	0.060	6.467	0.030	0.510	0.609
Cr-spinel - gen X	*2*	26.77	13.83	18.10	43.33	0.04	0.17	0.20	0.18	0.00	0.04	102.66	15.75	2.62	102.92	0.927	0.606	1.007	0.001	0.004	0.005	0.004	-	0.001	0.387	0.058	6.672	0.029	0.521	0.610
Cr-spinel - gen X	*3*	27.23	13.99	18.18	43.16	0.03	0.21	0.23	0.17	0.01	0.04	103.26	15.72	2.73	103.53	0.936	0.608	0.995	0.001	0.005	0.006	0.004	-	0.001	0.384	0.060	6.400	0.030	0.515	0.613
Cr-spinel - gen X	*4*	26.68	14.40	17.74	43.57	0.03	0.21	0.22	0.18	bdl	0.03	103.07	14.96	3.10	103.38	0.918	0.627	1.006	0.001	0.005	0.005	0.004	-	0.001	0.365	0.068	5.368	0.034	0.523	0.632
Cr-spinel - gen X	*5*	26.89	15.09	16.53	43.79	0.03	0.22	0.19	0.20	bdl	0.01	102.95	13.85	2.98	103.25	0.921	0.654	1.007	0.001	0.005	0.005	0.005	-	-	0.337	0.065	5.185	0.033	0.522	0.660
Cr-spinel - gen X	*6*	27.78	15.56	16.63	43.81	0.05	0.18	0.21	0.19	bdl	0.04	104.44	13.82	3.12	104.75	0.935	0.662	0.989	0.001	0.004	0.005	0.004	-	0.001	0.330	0.067	4.925	0.034	0.514	0.667
Cr-spinel - gen X	*7*	26.97	14.52	17.33	43.20	0.03	0.19	0.23	0.18	0.00	0.04	102.69	14.69	2.93	102.98	0.929	0.633	0.998	0.001	0.004	0.006	0.004	-	0.001	0.359	0.064	5.609	0.032	0.518	0.638
#3																														
Cr-spinel - gen X	*1*	25.95	14.75	16.04	43.92	0.05	0.20	0.20	0.15	0.00	0.04	101.30	13.81	2.48	101.55	0.906	0.652	1.029	0.001	0.005	0.005	0.004	-	0.001	0.342	0.055	6.218	0.028	0.532	0.656
Cr-spinel - gen X	*2*	26.79	15.28	16.03	43.76	0.11	0.23	0.22	0.18	bdl	0.02	102.63	13.54	2.77	102.91	0.920	0.664	1.008	0.002	0.005	0.005	0.004	-	0.001	0.330	0.061	5.410	0.031	0.523	0.668
Cr-spinel - gen X	*3*	26.40	15.12	16.01	43.94	0.03	0.22	0.23	0.17	0.00	0.03	102.16	13.49	2.79	102.44	0.912	0.661	1.018	0.001	0.005	0.006	0.004	-	0.001	0.331	0.062	5.339	0.031	0.527	0.666
Cr-spinel - gen X	*4*	26.11	15.16	15.83	44.10	0.03	0.21	0.21	0.18	0.00	0.01	101.85	13.27	2.84	102.13	0.905	0.665	1.025	0.001	0.005	0.005	0.004	-	-	0.326	0.063	5.175	0.032	0.531	0.671
Cr-spinel - gen X	*5*	26.06	14.77	16.10	43.55	0.07	0.18	0.21	0.16	0.01	0.04	101.16	13.73	2.64	101.43	0.911	0.653	1.021	0.002	0.004	0.005	0.004	-	0.001	0.340	0.059	5.763	0.030	0.528	0.658
Cr-spinel - gen X	*6*	26.24	14.98	16.08	43.85	0.04	0.18	0.21	0.18	0.01	0.05	101.82	13.62	2.74	102.09	0.910	0.657	1.020	0.001	0.004	0.005	0.004	-	0.001	0.335	0.061	5.492	0.031	0.528	0.662
Cr-spinel - gen X	*7*	26.35	15.11	16.05	44.08	bdl	0.19	0.19	0.18	bdl	0.04	102.19	13.55	2.78	102.46	0.910	0.660	1.021	-	0.005	0.005	0.004	-	0.001	0.332	0.061	5.443	0.031	0.529	0.665
Cr-spinel - gen X	*8*	26.91	15.75	15.95	43.89	0.04	0.20	0.21	0.21	0.01	0.01	103.18	12.91	3.37	103.52	0.917	0.679	1.003	0.001	0.005	0.005	0.005	-	-	0.312	0.073	4.274	0.037	0.522	0.685
Cr-spinel - gen X	*9*	27.13	15.57	15.91	43.80	0.06	0.20	0.22	0.20	bdl	0.03	103.12	13.26	2.95	103.41	0.925	0.671	1.002	0.001	0.005	0.005	0.005	-	0.001	0.321	0.064	5.016	0.032	0.520	0.676
#4																														
Cr-spinel - gen Z	*1*	33.27	15.40	16.25	37.03	0.27	0.21	0.19	0.15	0.01	0.04	102.81	14.62	1.80	102.99	1.113	0.651	0.831	0.006	0.005	0.005	0.003	-	0.001	0.347	0.038	9.132	0.019	0.427	0.652
Cr-spinel - gen Z	*2*	32.53	15.09	16.30	37.15	0.31	0.23	0.20	0.16	bdl	0.02	102.00	14.74	1.73	102.17	1.100	0.645	0.843	0.007	0.005	0.005	0.004	-	0.001	0.354	0.037	9.568	0.019	0.434	0.646
Cr-spinel - gen Z	*3*	33.24	15.48	16.37	36.86	0.31	0.21	0.19	0.17	0.01	0.03	102.86	14.53	2.05	103.06	1.111	0.654	0.826	0.007	0.005	0.005	0.004	-	0.001	0.344	0.044	7.818	0.022	0.426	0.655
Cr-spinel - gen Z	*4*	32.77	15.17	16.43	37.33	0.30	0.20	0.21	0.15	bdl	0.05	102.61	14.87	1.73	102.78	1.101	0.645	0.841	0.006	0.005	0.005	0.003	-	0.001	0.355	0.037	9.595	0.019	0.433	0.645
Cr-spinel - gen Z	*5*	33.11	15.19	16.53	36.83	0.33	0.20	0.23	0.15	bdl	0.03	102.61	14.87	1.84	102.80	1.111	0.645	0.829	0.007	0.005	0.006	0.004	-	0.001	0.354	0.039	9.077	0.020	0.427	0.646
Cr-spinel - gen Z	*6*	32.79	15.04	16.54	37.23	0.30	0.23	0.21	0.17	bdl	0.04	102.54	15.03	1.67	102.71	1.103	0.640	0.840	0.006	0.005	0.005	0.004	-	0.001	0.359	0.036	9.972	0.018	0.432	0.641
Cr-spinel - gen Z	*7*	32.08	14.40	16.90	36.91	0.31	0.21	0.20	0.15	0.00	0.02	101.18	15.46	1.60	101.34	1.098	0.624	0.847	0.007	0.005	0.005	0.004	-	0.001	0.375	0.035	10.714	0.018	0.435	0.625
Cr-spinel - gen Z	*8*	32.32	14.47	16.72	36.85	0.32	0.21	0.20	0.15	bdl	0.03	101.27	15.44	1.42	101.41	1.104	0.625	0.844	0.007	0.005	0.005	0.003	-	0.001	0.374	0.031	12.065	0.016	0.433	0.626
#5																														
Cr-spinel - gen Y	*1*	31.63	15.54	14.62	39.50	0.06	0.17	0.21	0.18	0.01	0.03	101.97	13.63	1.11	102.08	1.071	0.665	0.897	0.001	0.004	0.005	0.004	-	0.001	0.327	0.024	13.625	0.012	0.456	0.670
Cr-spinel - gen Y	*2*	31.85	15.67	14.83	39.59	0.07	0.18	0.18	0.19	bdl	0.03	102.58	13.71	1.25	102.70	1.071	0.666	0.893	0.001	0.004	0.004	0.004	-	0.001	0.327	0.027	12.111	0.014	0.455	0.671
Cr-spinel - gen Y	*3*	31.94	15.63	14.74	39.13	0.06	0.17	0.21	0.18	0.01	0.05	102.13	13.61	1.25	102.25	1.078	0.667	0.886	0.001	0.004	0.005	0.004	-	0.001	0.326	0.027	12.074	0.014	0.451	0.672
Cr-spinel - gen Y	*4*	32.12	15.86	14.78	39.61	0.08	0.17	0.19	0.19	bdl	0.03	103.03	13.59	1.33	103.16	1.074	0.671	0.889	0.002	0.004	0.005	0.004	-	0.001	0.322	0.028	11.500	0.014	0.453	0.676
Cr-spinel - gen Y	*5*	31.69	15.60	14.66	39.09	0.04	0.17	0.19	0.19	0.01	0.04	101.68	13.46	1.34	101.82	1.074	0.669	0.889	0.001	0.004	0.005	0.004	-	0.001	0.324	0.029	11.172	0.015	0.453	0.674
Cr-spinel - gen Y	*6*	32.02	15.73	14.89	39.44	0.09	0.19	0.20	0.21	bdl	0.04	102.83	13.70	1.33	102.96	1.074	0.667	0.887	0.002	0.004	0.005	0.005	-	0.001	0.326	0.029	11.241	0.015	0.452	0.672
Cr-spinel - gen Y	*7*	31.92	15.58	14.85	39.44	0.05	0.16	0.21	0.18	bdl	0.02	102.41	13.76	1.22	102.53	1.075	0.664	0.891	0.001	0.004	0.005	0.004	-	0.001	0.329	0.026	12.654	0.013	0.453	0.669
Cr-spinel - gen Y	*8*	31.98	15.78	14.82	38.99	0.08	0.16	0.18	0.20	bdl	0.03	102.23	13.44	1.54	102.39	1.077	0.672	0.881	0.002	0.004	0.004	0.005	-	0.001	0.321	0.033	9.727	0.017	0.450	0.677
Cr-spinel - gen Y	*9*	32.58	16.10	14.99	39.08	0.08	0.17	0.19	0.19	0.00	0.03	103.41	13.42	1.74	103.58	1.083	0.677	0.871	0.002	0.004	0.005	0.004	-	0.001	0.317	0.037	8.568	0.019	0.446	0.681
#6																														
Cr-spinel - gen Y	*1*	31.99	15.74	15.02	39.17	0.07	0.17	0.21	0.20	bdl	0.02	102.59	13.57	1.61	102.75	1.075	0.669	0.883	0.001	0.004	0.005	0.005	-	0.001	0.324	0.035	9.257	0.018	0.451	0.674
Cr-spinel - gen Y	*2*	31.84	15.61	14.79	39.36	0.06	0.21	0.21	0.19	bdl	0.02	102.29	13.66	1.26	102.41	1.074	0.666	0.890	0.001	0.005	0.005	0.004	-	0.001	0.327	0.027	12.111	0.014	0.453	0.671
Cr-spinel - gen Y	*3*	31.78	15.79	14.92	39.26	0.07	0.17	0.20	0.18	bdl	0.03	102.40	13.45	1.64	102.56	1.070	0.672	0.886	0.001	0.004	0.005	0.004	-	0.001	0.321	0.035	9.171	0.018	0.453	0.677
Cr-spinel - gen Y	*4*	31.59	15.66	14.83	39.38	0.07	0.18	0.22	0.19	0.01	0.03	102.17	13.50	1.48	102.32	1.067	0.669	0.892	0.002	0.004	0.005	0.004	-	0.001	0.323	0.032	10.094	0.016	0.455	0.674
Cr-spinel - gen Y	*5*	31.95	15.63	15.01	39.63	0.06	0.22	0.20	0.17	0.00	0.04	102.91	13.88	1.26	103.03	1.072	0.663	0.892	0.001	0.005	0.005	0.004	-	0.001	0.330	0.027	12.222	0.014	0.454	0.668
Cr-spinel - gen Y	*6*	31.96	15.78	14.85	39.38	0.06	0.20	0.20	0.17	bdl	0.03	102.65	13.56	1.44	102.79	1.073	0.670	0.887	0.001	0.005	0.005	0.004	-	0.001	0.323	0.031	10.419	0.016	0.453	0.675
Cr-spinel - gen Y	*7*	32.05	15.85	14.92	39.61	0.06	0.18	0.18	0.18	bdl	0.02	103.04	13.60	1.46	103.18	1.072	0.671	0.889	0.001	0.004	0.004	0.004	-	0.001	0.323	0.031	10.419	0.016	0.453	0.675
Cr-spinel - gen Y	*8*	31.54	15.86	15.01	39.55	0.04	0.16	0.21	0.17	0.01	0.03	102.59	13.33	1.86	102.77	1.061	0.674	0.892	0.001	0.004	0.005	0.004	-	0.001	0.318	0.040	7.950	0.020	0.457	0.679
Cr-spinel - gen Y	*9*	31.58	15.64	15.05	39.59	0.07	0.18	0.20	0.17	bdl	0.02	102.50	13.67	1.54	102.66	1.064	0.667	0.895	0.002	0.004	0.005	0.004	-	0.001	0.327	0.033	9.909	0.017	0.457	0.671
Cr-spinel - gen Y	*10*	31.91	15.59	14.78	39.57	0.10	0.19	0.20	0.18	bdl	0.04	102.57	13.86	1.03	102.67	1.074	0.664	0.893	0.002	0.004	0.005	0.004	-	0.001	0.331	0.022	15.045	0.011	0.454	0.667
#7																														
Cr-spinel - gen X	*1*	26.22	14.91	15.84	43.64	0.08	0.19	0.21	0.18	bdl	0.04	101.31	13.58	2.51	101.56	0.914	0.657	1.020	0.002	0.004	0.005	0.004	-	0.001	0.336	0.056	6.000	0.028	0.527	0.662
Cr-spinel - gen X	*2*	26.41	14.96	15.93	43.52	0.04	0.19	0.22	0.15	0.01	0.03	101.46	13.56	2.63	101.73	0.918	0.658	1.015	0.001	0.004	0.005	0.004	-	0.001	0.335	0.058	5.776	0.029	0.525	0.663
Cr-spinel - gen X	*3*	27.18	15.30	16.01	43.84	0.04	0.19	0.21	0.18	0.01	0.03	103.00	13.64	2.63	103.26	0.929	0.662	1.005	0.001	0.005	0.005	0.004	-	0.001	0.331	0.057	5.807	0.029	0.520	0.667
Cr-spinel - gen X	*4*	26.63	15.19	15.97	43.77	0.04	0.20	0.20	0.17	0.00	0.02	102.20	13.46	2.79	102.48	0.918	0.663	1.013	0.001	0.005	0.005	0.004	-	-	0.329	0.061	5.393	0.031	0.525	0.668
Cr-spinel - gen X	*5*	26.51	14.89	15.88	43.81	0.05	0.23	0.22	0.19	bdl	0.03	101.81	13.77	2.35	102.05	0.919	0.653	1.019	0.001	0.005	0.005	0.005	-	0.001	0.339	0.052	6.519	0.026	0.526	0.658
Cr-spinel - gen X	*6*	26.47	15.17	16.00	43.74	0.03	0.17	0.18	0.17	0.01	0.04	101.98	13.44	2.85	102.26	0.915	0.663	1.014	0.001	0.004	0.004	0.004	-	0.001	0.330	0.063	5.238	0.032	0.526	0.668
Cr-spinel - gen X	*7*	26.43	15.07	16.17	44.08	0.03	0.21	0.21	0.19	bdl	0.03	102.43	13.68	2.77	102.70	0.911	0.657	1.020	0.001	0.005	0.005	0.004	-	0.001	0.335	0.061	5.492	0.031	0.528	0.662
Cr-spinel - gen X	*8*	26.84	15.41	15.82	43.69	0.04	0.18	0.20	0.18	bdl	0.04	102.40	13.24	2.86	102.69	0.922	0.670	1.007	0.001	0.004	0.005	0.004	-	0.001	0.323	0.063	5.127	0.032	0.522	0.675
Cr-spinel - gen X	*9*	27.50	15.69	15.91	43.84	0.06	0.22	0.20	0.16	0.00	0.04	103.63	13.35	2.84	103.92	0.932	0.673	0.997	0.001	0.005	0.005	0.004	-	0.001	0.321	0.062	5.177	0.031	0.517	0.677

[T] generated value by electron microprobe software assuming 100% FeO

End-Member Generator (EMG 8.0) assumes ideal stoichiometry: A_3O_4

cr# = $Cr^{3+}/Cr^{3+} + Al^{3+}$ a.p.f

mg# = $Mg^{2+}/Mg^{2+} + Fe^{2+}$ a.p.f

bdl = below detection limit